MATERIALS FOR ELECTROANALYSIS BASED ON ADVANCED FRAMEWORKS

EDITED BY: Baiqing Yuan, Dong Liu, Huajie Yin and Daojun Zhang
PUBLISHED IN: Frontiers in Chemistry

frontiers Research Topics

frontiers

ISSN 1664-8714
ISBN 978-2-88966-619-5
DOI 10.3389/978-2-88966-619-5

About Frontiers

Frontiers is more than just an open-access publisher of scholarly articles: it is a pioneering approach to the world of academia, radically improving the way scholarly research is managed. The grand vision of Frontiers is a world where all people have an equal opportunity to seek, share and generate knowledge. Frontiers provides immediate and permanent online open access to all its publications, but this alone is not enough to realize our grand goals.

Frontiers Journal Series

The Frontiers Journal Series is a multi-tier and interdisciplinary set of open-access, online journals, promising a paradigm shift from the current review, selection and dissemination processes in academic publishing. All Frontiers journals are driven by researchers for researchers; therefore, they constitute a service to the scholarly community. At the same time, the Frontiers Journal Series operates on a revolutionary invention, the tiered publishing system, initially addressing specific communities of scholars, and gradually climbing up to broader public understanding, thus serving the interests of the lay society, too.

Dedication to Quality

Each Frontiers article is a landmark of the highest quality, thanks to genuinely collaborative interactions between authors and review editors, who include some of the world's best academicians. Research must be certified by peers before entering a stream of knowledge that may eventually reach the public - and shape society; therefore, Frontiers only applies the most rigorous and unbiased reviews.
Frontiers revolutionizes research publishing by freely delivering the most outstanding research, evaluated with no bias from both the academic and social point of view. By applying the most advanced information technologies, Frontiers is catapulting scholarly publishing into a new generation.

What are Frontiers Research Topics?

Frontiers Research Topics are very popular trademarks of the Frontiers Journals Series: they are collections of at least ten articles, all centered on a particular subject. With their unique mix of varied contributions from Original Research to Review Articles, Frontiers Research Topics unify the most influential researchers, the latest key findings and historical advances in a hot research area! Find out more on how to host your own Frontiers Research Topic or contribute to one as an author by contacting the Frontiers Editorial Office: frontiersin.org/about/contact

MATERIALS FOR ELECTROANALYSIS BASED ON ADVANCED FRAMEWORKS

Topic Editors:
Baiqing Yuan, Ludong University, China
Dong Liu, Jiangsu University, China
Huajie Yin, Griffith University, Australia
Daojun Zhang, Anyang Normal University, China

Citation: Yuan, B., Liu, D., Yin, H., Zhang, D., eds. (2021). Materials for Electroanalysis Based on Advanced Frameworks. Lausanne: Frontiers Media SA. doi: 10.3389/978-2-88966-619-5

Table of Contents

frontiers in Chemistry

EDITORIAL
published: 15 February 2021
doi: 10.3389/fchem.2021.638338

Editorial: Materials for Electroanalysis Based on Advanced Frameworks

Baiqing Yuan[1], Dong Liu[2], Huajie Yin[3] and Daojun Zhang[4]*

[1]School of Chemistry and Materials Science, Ludong University, Yantai, China, [2]Key Laboratory of Modern Agricultural Equipment and Technology, Ministry of Education, School of Agricultural Equipment Engineering, Jiangsu University, Zhenjiang, China, [3]Centre for Clean Environment and Energy, Griffith University, Southport, QLD, Australia, [4]Henan Province Key Laboratory of New Optoelectronic Functional Materials, College of Chemistry and Chemical Engineering, Anyang Normal University, Anyang, China

Keywords: covalent organic frameworks (COFs), metal-organic frameworks (MOFs), electrochemical sensors/sensing, electrical conductivity, photoelectric conversion, near-infrared phosphorescence, nanoscale

Editorial on the Research Topic

Materials for Electroanalysis Based on Advanced Frameworks

Covalent organic frameworks (COFs) and metal-organic frameworks (MOFs) are two emerging classes of extended porous structures, which seek to develop the reticular chemistry beyond molecules and open up new horizons for compositions, structures, properties, and applications (Yaghi, 2019; Lyu et al., 2020). Like MOFs that extend inorganic metal complexes into 2D and 3D frameworks, COFs extend organic chemistry from molecules and polymers into 2D and 3D organic structures (Diercks and Yaghi, 2017). MOFs/COFs are built with the aim of extending porous frameworks through strong bonds (coordinate/covalent interactions) between molecular building blocks (metal-containing unit-organic linker/organic-organic monomer) based on topological guides. The advantages of these approaches include controllable synthesis, pre-designable structures, and manageable functionality (Geng et al., 2020). In addition to possessing high surface area and tunable pores, both MOFs and COFs display a lot of intriguing properties including layered crystalline structures through π-π stacking and high stability which is only exhibited in graphene (Fritz and Coskun, 2020) owing to the presence of strong covalent bonds. However, metal-free COFs far from meet the growing demands of numerous fields where the role of metal in the framework structure is emphasized. This includes applications such as gas adsorption and separation, heterogeneous catalysis, electronics, electrocatalysis, and electrochemical energy storage. An effective way to address these challenges is to introduce targeted metal ions into COFs frameworks to form metal-covalent organic frameworks (MCOFs) (Dong et al., 2020). Compared with metal-free COFs, MCOFs not only have superior electrocatalytic activity but also display higher intrinsic conduction due to the involvement of the metal component. Developing distinctive synthesis methods/strategies to achieve novel MOFs and COFs holds much promise toward promoting their application. For instance, flexible and free-standing pure COFs membranes were prepared by liquid-liquid interfacial polymerization at room temperature and atmospheric pressure, which solves a major problem since COFs are generally insoluble and unprocessable powders (Liu et al., 2020). A vast number of organic monomers have been reported to date with infinite possibilities of functionalization in their resulting structures. This leads to "digital reticular chemistry" based on laboratory robotics and artificial intelligence (AI), which could achieve high-throughput experiments involving synthesis and characterization. This approach is poised to make the discoveries in MOFs and COFs more significant and easily achievable (Lyu et al., 2020).

Since the first report in 1962 for the detection of glucose using glucose oxidase, electrochemical sensing has been well accepted as a powerful tool in a variety of fields where high sensitivity, simple operation, rapid response, and low cost are necessary. Electrochemical sensing is especially suited for miniaturization, and therefore offers multiple construction merits for manufacturing flexible, disposable, and cheap devices (Amiri et al., 2018). The introduction of novel elements into MOFs and COFs brings enhanced scope for electrochemical sensing, which promise to be a major boost toward their synthesis.

OPEN ACCESS

Edited and reviewed by:
Tony D. James,
University of Bath, United Kingdom

****Correspondence:***
Baiqing Yuan
baiqingyuan1981@126.com

Specialty section:
This article was submitted to Supramolecular Chemistry, a section of the journal Frontiers in Chemistry

Received: *06 December 2020*
Accepted: *04 January 2021*
Published: *15 February 2021*

Citation:
Yuan B, Liu D, Yin H and Zhang D (2021) Editorial: Materials for Electroanalysis Based on Advanced Frameworks. Front. Chem. 9:638338. doi: 10.3389/fchem.2021.638338

For example, MOFs and COFs possess highly ordered porous structures, adjustable holes, and manageable functionality, thereby providing an efficient and powerful platform to anchor electroactive molecules, biomolecules, and nanoparticles. Yet, there are still many key issues regarding MOFs and COFs that need to be urgently resolved before they can be successfully applied in electrochemical sensing. In this context, Yuan et al. presented a critical review on the recent advances regarding COFs and their applications in electrochemical sensing, with a focus on the mechanism and methods/strategies for improving electrical conductivity, the immobilization of COFs on different substrates, device miniaturization, and application in electrochemical sensors. On this Research Topic, we present eight original research articles and one review article to showcase the recent advances in MOFs and COFs explored for electrochemical sensing.

A key problem regarding the application of MOFs and COFs in electrochemical sensing is the inherent low conductivity of bulk MOFs and COFs. It essentially implies that porosity and high surface area do not coexist with excellent electrical conductivity which is indispensable for fast electron transfer in electro-analysis. However, most of these framework materials are typically poor electrical conductors owing to the lack of transport channels for the charge carriers. Neither hopping transport nor band transport pathways are feasible. This result mainly originates from the intrinsically insulating character of the organic ligands, as well as the poor energetic and orbital overlap between the ligands and metal-oxo nodes (e.g., π−d interactions) (Sun et al., 2016; Pratik et al., 2020). The types of linkages (e.g., imine, imide, and boroxine) that are formed while building conventional COFs decides that the charge transport in COFs follows an interlayer hopping mechanism rather than an in-plane mechanism, resulting in wide band gaps and low in-plane conduction. In-plane conduction is improved by conducting polydisperse 1D graphene nanoribbons (GNRs)-based COFs via interfacial polymerization (Veber et al., 2020). Luo et al. report a 2D conductive nano-MOF (NiCu-CAT) composed of a 2, 3, 6, 7, 10, 11-hexahydroxytriphenylene ligand that shows high electrocatalytic activity toward the oxidation of paracetamol. The full in-plane charge delocalization is achieved by π-π stacking, which contributes to the excellent electrical conductivity. A conductive Ni_3 (2, 3, 6, 7, 10, 11-hexaiminotriphenylene)$_2$ MOF is explored by Wu et al. as an electrochemical sensing platform with long-term stability, for the detection of glucose. Another efficient strategy to enhance electrical conductivity is to mix conductive materials with MOFs or COFs to form conductive composites. For instance, Song et al. fabricated conductive COFs composites based on nitrogen-contained carbon derived from kenaf stem. The conductive composites are demonstrated to immobilize acetylcholinesterase for the detection of organophosphorus pesticides over a wide linear range, with a low detection limit (0.067 ng/ml). Karimi-Maleh et al. report the development of a highly sensitive electrochemical biosensor for analyzing the mitoxantrone anti-cancer drug by using DNA as a recognition moiety based on ZIF-8/ionic liquid carbon paste electrodes. The presence of ZIF-8 helps in the high loading of ds-DNA, and BMIM serves as the conductive binder for improving the electrical conductivity and sensitivity of the sensor. Combination of porosity and high electrical conductivity can also be accomplished by derivatization of MOFs or COFs. Derived MOFs or COFs can also enhance the structural stability. Pang et al. demonstrate Ni/NiO heterostructure nanobelts derived from Ni-based MOF for use as an electrochemical platform for the sensitive detection of glucose. This derived MOF exhibits an interleaved 3D reticulated structure with high mechanical stability. Besides, ultrafine Ni nanoparticles decorated on the NiO nanobelt enhance the electrical conductivity and active sites.

MOFs-based materials possessing both strong enrichment ability and high electrocatalytic activity are demonstrated by Shirsat et al. The incorporation of Au nanoparticles in CuBTC MOFs is used for the sensitive detection of Pb^{2+}. Other contributions are about the synthesis of a redox-active UV-11 MOF and its characterization by cyclic voltammetry, by Cobos-Murcia et al., and near-infrared phosphorescence emission by binuclear Mn(II)-based MOFs for efficient photoelectric conversion, by Zhang et al.

Though limited articles are collected in this topical issue due to the COVID-19 pandemic, we hope that this Research Topic will serve as a guide for the novel design and modification of frameworks explored in the field of electrochemical sensing. We think the following research/challenges highlighted in this issue may be of interest to readers in terms of the application of frameworks or their composites/derivatives in electrochemical sensing: structures with both large porosity and high conductivity, simple immobilization methods/strategies developed for MOFs/COFs on different conductive substrates, hydrogels/aerogels/flexible films to overcome intrinsic fragility and powdered crystalline states of MOFs/COFs, nanoscale MOFs/COFs, encapsulation of biomolecules in MOFs/COFs to enhance thermal, chemical, and mechanical stability, structures possessing enzyme-mimicking activity, stimuli-responsive frameworks, and enantioselective/chiral sensing. Finally, we would like to thank all the authors for their contributions to this collection. We also appreciate the referees and the editorial staff of Frontiers in Chemistry for their efforts toward in the publication of this topical issue.

AUTHOR CONTRIBUTIONS

BY writing-original draft and manuscript revision/review/editing. DL, HY, and DZ manuscript revision/review/editing

FUNDING

This work was funded by the Natural Science Foundation of Shandong Province (No.ZR2020MB058).

REFERENCES

Amiri, M., Bezaatpour, A., Jafari, H., Boukherroub, R., and Szunerits, S. (2018). Electrochemical methodologies for the detection of pathogens. *ACS Sens.* 3, 1069–1086. doi:10.1021/acssensors.8b00239

Diercks, C. S., and Yaghi, O. M. (2017). The atom, the molecule, and the covalent organic framework. *Science* 355, eaal1585. doi:10.1126/science.aal1585

Dong, J. Q., Han, X., Liu, Y., Li, H. Y., and Cui, Y. (2020). Metal-covalent organic frameworks (MCOFs): a bridge between metal-organic frameworks and covalent organic frameworks. *Angew Chem. Int. Ed. Engl.* 59, 13722–13733. doi:10.1002/anie.202004796

Fritz, P. W., and Coskun, A. (2020). COFs meet graphene nanoribbons. *Inside Chem.* 6, 1046–1048. doi:10.1016/j.chempr.2020.04.011

Geng, K., He, T., Liu, R., Dalapati, S., Tan, K. T., Li, Z. P., et al. (2020). Covalent organic frameworks: design, synthesis, and functions. *Chem. Rev.* 120, 8814–8933. doi:10.1021/acs.chemrev.9b00550

Liu, J., Han, G., Zhao, D. L., Lu, K. J., Gao, J., and Chung, T. S. (2020). Self-standing and flexible covalent organic framework (COF) membranes for molecular separation. *Sci. Adv.* 6, eabb1110. doi:10.1126/sciadv.abb1110

Lyu, H., Ji, Z., Wuttke, S., and Yaghi, O. M. (2020). Digital reticular chemistry. *Inside Chem.* 6, 2219–2241. doi:10.1016/j.chempr.2020.08.008

Pratik, S. M., Gagliardi, L., and Cramer, C. J. (2020). Engineering electrical conductivity in stable zirconium-based PCN-222 MOFs with permanent mesoporosity. *Chem. Mater.* 32, 6137–6149. doi:10.1021/acs.chemmater.0c01847

Sun, L., Campbell, M. G., and Dincă, M. (2016). Electrically conductive porous metal-organic frameworks. *Angew Chem. Int. Ed. Engl.* 55, 3566–3579. doi:10.1002/anie.201506219

Veber, G., Diercks, C. S., Rogers, C., Perkins, W. S., Ciston, J., Lee, K., et al. (2020). Reticular growth of graphene nanoribbon 2D covalent organic frameworks. *Inside Chem.* 6, 1125–1133. doi:10.1016/j.chempr.2020.01.022

Yaghi, O. M. (2019). Reticular chemistry in all dimensions. *ACS Cent. Sci.* 5, 1295–1300. doi:10.1021/acscentsci.9b00750

Conflict of Interest: The authors declare that the research was conducted in the absence of any commercial or financial relationships that could be construed as a potential conflict of interest.

frontiers in Chemistry

ORIGINAL RESEARCH
published: 23 April 2020
doi: 10.3389/fchem.2020.00330

Ultrathin Ni-MOF Nanobelts-Derived Composite for High Sensitive Detection of Nitrite

Xiangren Meng[1,2*†], *Xiao Xiao*[3†] *and Huan Pang*[3*]

[1] School of Tourism and Culinary Science, Yangzhou University, Yangzhou, China, [2] Jiangsu Huai-yang Cuisine Engineering Center, Yangzhou University, Yangzhou, China, [3] School of Chemistry and Chemical Engineering, Yangzhou University, Yangzhou, China

In this paper, the Ni/NiO ultrathin nanobelts were successively synthesized by a facile in suit conversion process using pre-synthesized Ni-based metal-organic frameworks (MOFs) nanobelts as parent materials to detect the nitrite ($NaNO_2$). The synthesized Ni/NiO composites have the advantages in structure, as follows: (I) Interleaved 3D reticulated structure has strong mechanical stability; (II) Ultrathin nanobelt structures allow more active sites to be exposed and make the transfer of charge faster; (III) A large number of ultrafine Ni nanoparticles decorate the building blocks of the NiO nanobelt and enhance the electrical conductivity. Ni/NiO/GCE has an obvious oxidation peak at 0.78 V, when the concentration is between 0.5 and 1000 μM, the oxidation peak current of $NaNO_2$ is linearly related to the concentration, and the sensitivity is 1.5319 μA mM^{-1} cm^{-2} (S/N = 3). Moreover, the experimental results also concluded that the Ni/NiO ultrathin nanobelts not only indicated wonderful reproducibility in the determination of $NaNO_2$ in the pickled pork samples, but also could be well-recovered and keep stable for a long time.

Keywords: in suit conversion method, Ni/NiO ultrathin nanobelt, metal nanoparticle, metal organic framework, nitrite

OPEN ACCESS

Edited by:
Baiqing Yuan,
Ludong University, China

Reviewed by:
Guoxing Zhu,
Jiangsu University, China
Sujuan Li,
Anyang Normal University, China

***Correspondence:**
Xiangren Meng
xrmeng@yzu.edu.cn
Huan Pang
huanpangchem@hotmail.com;
panghuan@yzu.edu.cn

† These authors have contributed equally to this work

Specialty section:
This article was submitted to Supramolecular Chemistry, a section of the journal Frontiers in Chemistry

Received: *15 February 2020*
Accepted: *31 March 2020*
Published: *23 April 2020*

Citation:
Meng X, Xiao X and Pang H (2020) Ultrathin Ni-MOF Nanobelts-Derived Composite for High Sensitive Detection of Nitrite. Front. Chem. 8:330. doi: 10.3389/fchem.2020.00330

INTRODUCTION

Metal-organic frameworks (MOFs) are expected to play a significant role in energy applications (Lin et al., 2015; Xia et al., 2015; Tan et al., 2017; Liang et al., 2018; Wu et al., 2019; Yang et al., 2019; Zhao Y. et al., 2019). Because the micro/nanoscale structure has a great potential to overcome the disadvantages of low specific surface area (SSAs) and poor contacts of active materials with electrolyte/pollutants compared to conventional bulks or aggregate materials. Therefore, it is considered as a promising electrode material (Du et al., 2014, 2017; Bosch et al., 2017; Chen et al., 2017; Shi et al., 2017; Li Y.-P. et al., 2019; Xiao et al., 2020). In recent years, since it has been noted that various processes such as thermodynamics and kinetics of various reactions occurring at the interface are significantly affected by the surface energy of micro/nanocrystals, MOF-derived materials have become a research hotspot (Yang et al., 2008; Larsson et al., 2009; Du et al., 2014, 2017; Bosch et al., 2017; Chen et al., 2017; Shi et al., 2017; Liu et al., 2019; Li Y.-P. et al., 2019; Xiao et al., 2020). Many studies have focused on designing and controlling their different morphologies. On the basis of keeping the original geometry of the micro/nanostructure unchanged, the derivatization can improve the low conductivity and enhance the structural stability of the original MOFs (Chen et al., 2012; Liu et al., 2014; Ma et al., 2017; Shi et al., 2017; Wang et al., 2018; Zou et al., 2018).

Because of its great importance in catalysis, metal nanoparticles are rapidly attracting widespread interest (Han et al., 2010; Zhang et al., 2010, 2012, 2014; Xu et al., 2014; Li Q. Y. et al., 2019; Zhu et al., 2019). However, the high surface energy of metal nanoparticles makes them thermodynamically unstable during the process of catalytic reaction, and it is easy to aggregate, resulting in reduced activity. Therefore, whether the size, shape and dispersion of metal nanoparticles can be controlled properly is the key factor to determine whether the stability activity can be improved. To the end, small metal nanoparticles with specific shapes are generally prepared from many surface capping agents including dendrimers, oleamide, and polyethylenepyrrolidone (PVP) (Cho et al., 2016; Zhao et al., 2016; Li et al., 2018; Zhang et al., 2019; Zhao R. B. et al., 2019). Although this surface capping agent is considered effective, in most cases, it is not ideal to attach molecules to metal nanoparticles with strong chemical interactions and inhibit the catalytic reaction. In order to produce surface-clean and well-dispersed metal nanoparticles, limiting them within porous materials, such as porous silica, zeolites, as well as porous carbons are currently common methods. Through the porous materials, the pore-responsive substrates/products can be transferred, porous materials can also avoid the aggregation and growth of metal nanoparticles, all of which are attributed to its inherent conditions for spatial confinement (Zhan and Zeng, 2016, 2018; Chen and Xu, 2017; Xu et al., 2017; Li et al., 2018; Geng et al., 2019). MOFs and MOF-derived materials can stand out among numerous porous materials and become excellent choices because (1) they have diverse pore sizes and shapes to meet the special requirements of metal nanoparticles; (2) They have high porosity and specific surface areas to carry metal nanoparticles; (3) Understanding catalysis requires defining the MOF structure distinctly and ensuring that the pore structure is easily tailored in order to assure that the surrounding environment of metal nanoparticles is easily identified (Mukoyoshi et al., 2015; Tang et al., 2018; Chen et al., 2019; Li Y.-P. et al., 2019).

Nitrite, mainly sodium nitrite ($NaNO_2$), is often used as a preservative and a food additive in daily life. The high content of nitrite in the human body not only causes hemoglobin to be irreversibly oxidized to high-iron hemoglobin, but also reacts with dietary components to produce nitrosamines, leading to cancer and high blood pressure (Yue et al., 2011; Lin Z. et al., 2015). Therefore, eating meat products, sauces and spoiled vegetables with higher levels of nitrate or nitrite, or the drinking water containing nitrate or nitrite can cause poisoning (Li et al., 2012; Zou et al., 2017). In this work, we report that, with pre-synthesized ultrathin Ni-MIL-77 nanobelts as parent materials, a facile *in situ* conversion way (O_2-protected annealing process) has been demonstrated to fabricate metal nickel nanoparticle functionalized NiO composites (Ni/NiO ultrathin nanobelts). An excellent electrochemical performance of the Ni/NiO ultrathin nanobelts with large surface area and metal Ni nanoparticles generated by *in situ* conversion method is exhibited during the oxidation of $NaNO_2$. In addition, $NaNO_2$ in pickled pork was determined by the Ni/NiO materials, and good recovery was achieved.

RESULTS AND DISCUSSION

Synthesis Strategy

In this work, we used Ni-MIL-77 as the precursor because it presented a chiral structure that has large cross channels (**Figure S1**). The Ni/NiO composite reported here was made by using an in suit conversion process. Two steps are included in the preparation of Ni-functionalized NiO ultrathin nanobelts (**Figure 1A**). In step I, we successfully synthesized Ni-MIL-77 ultrathin nanobelts under solvothermal conditions (Xiao et al., 2017, 2018, 2019). In step II, we used a method that anneals the nickel-based ultrathin nanobelts in air at an elevated temperature to make it converted into Ni/NiO heterostructure nanobelts *in situ*. There are many structural features of the obtained Ni/NiO composite (**Figure 1B**): (I) interleaved 3D reticulated structure has strong mechanical stabilities; (II) More active sites are exposed and the charge transfer process is also promoted due to ultrathin nanobelt structures; (III) A large number of ultrafine Ni nanoparticles decorate the building blocks of the NiO nanobelt and enhance the electrical conductivity.

Characterizations of Ni/NiO Heterostructure

The thermogravimetric (TG) curve of Ni-MIL-77 that shows two obvious weight losses is given in **Figure S2**. In the temperature range of 25 to100°C is the first step of the weight loss (a 6% drop), which is equivalent to the decrease of the adsorbed solvent molecules. While the temperature reaches 400°C, since the Ni-MIL-77 skeleton is decomposed and glutaric acid ($HOOC(CH_2)_3COOH$) ligands turn into gas, weight loses 40.1%. Therefore, we can obtain Ni/NiO heterostructures at 350°C.

The morphology of the samples can be observed using transmission electron microscopy (TEM) and field emission scanning electron microscopy (FESEM). The typical low-magnification SEM images in **Figure S3** and TEM images in **Figure S4** show that the morphology of Ni-MOF and Ni/NiO composites are ultrathin nanobelts. The results show that the thickness of Ni/NiO nanobelts is about 3 nm (**Figure S5**). Further understanding of the architecture of the Ni/NiO composites is shown in **Figure 2**. It can be clearly seen from **Figures 2a,b** that the Ni metal nanoparticles have been *in situ* generate. These small metal particles are uniformly distributed on the NiO-based surface, forming a stable Ni/NiO composite (**Figure 2c**). The rational elemental constituents (e.g., Ni, and O) of the product is shown in the energy-dispersive X-ray spectrum (EDX)-mapping without impurities in Ni/NiO ultrathin nanobelts (**Figures 2d–g**).

We used XRD to test the phase purity as well as the crystallographic structure of the experimental product. By calcining Ni-MIL-77 at 350°C, we found two kinds of diffraction peaks (Ni and NiO) in the **Figure 2i** and **Figure S6**. Five well-defined diffraction peaks at 37.248, 43.286, 62.852, 75.404, and 79.372 are assigned to the (101), (012), (110), (113), and (202) facets of NiO, respectively. And three well-defined diffraction peaks at 44.507, 51.846, and 76.370 are distributed to the (111), (200), and (220) facets of Ni, respectively. The diffraction peaks

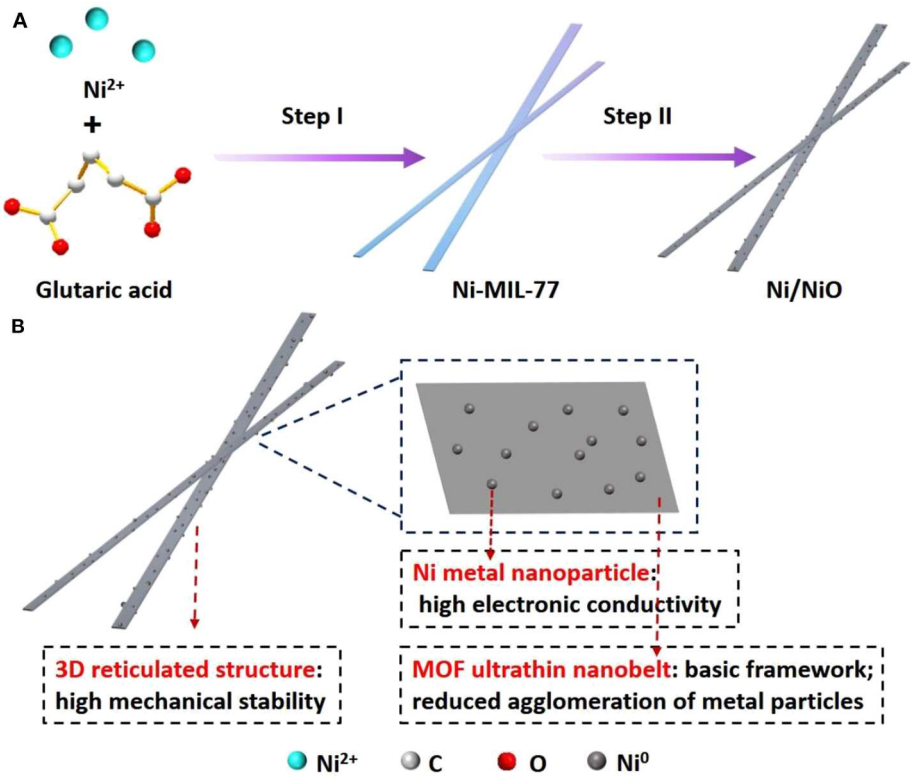

FIGURE 1 | (A) Schematic illustration of the synthesis of Ni/NiO ultrathin nanobelts. Step I: hydrothermal treatment of Ni-MIL-77 ultrathin nanobelts; Step II: annealing the Ni-MOF ultrathin nanobelts in air. **(B)** Schematic illustration of the detailed Ni/NiO ultrathin nanobelts.

can be easily assigned to the standard NiO phase (JCPDS 44-1159) as well as Ni phase (JCPDS 04-0850) (Tang et al., 2018; Zhao L. et al., 2019).

An effective method that can distinguish functional groups in the products is X-ray photoelectron spectroscopy (XPS). **Figure 3** shows the XPS spectra of Ni-MOF nanobelts and Ni/NiO nanobelts and their survey spectra. The survey spectra (**Figure 3A**) show three apparent peaks at 282.63 (C 1s), 530.29 (O 1s), and 856.37 (Ni 2p), respectively, which implied that Ni-MIL-77 nanobelts and Ni/NiO nanobelts were successfully formed. Ni oxidation states are determined through performing Ni 2p XPS spectrum. Two peaks in the Ni 2p region of the XPS spectra for Ni-MIL-77 that centered at 856.1 ($2p_{3/2}$) and 873.8 ($2p_{1/2}$) eV corresponded to the Ni^{2+} ions in Ni-MIL-77 (**Figure 3B**). In addition to these peaks, a new pair of spin-orbit splitting peaks is generated at 852.8 ($2p_{3/2}$) and 870.0 eV ($2p_{1/2}$) (**Figure 3C**), corresponding to the formation of Ni nanoparticles, and the results are consistent with PXRD. **Figures S7a**, **S8a** shows the high-resolution XPS spectrum of C 1s, and it can be deconvoluted well into two surface carbon components at ≈284.3 eV (nonoxygenated carbon: C-C), as well as 288.1 eV (carboxyl carbon: O=C-O). **Figures S7b, S8b** shows the high-resolution XPS spectrum of O 1s.

Determination of $NaNO_2$ on the Ni/NiO/GCE

Figure S9 showed the cyclic voltammograms (CVs) of different electrodes (Ni-MOF/GCE, Ni/NiO/GCE) in 5.0 mM $K_3Fe(CN)_6$ containing 1 M KCl solution at a scan rate of 50 mV s^{-1}. As displayed in **Figure S9**, the Ni/NiO /GCE exhibited an increase in the anodic peak current (192.66 μA) compared to Ni-MIL-77/GCE (108.23 μA).

We know that studying the effect of scanning rate on the peak current and oxidation peak potential can be used to judge electrode reaction kinetics. **Figure 4** and **Figure S10** represented at different scan rates (20–200 mV s^{-1}), the CVs of Ni/NiO/GCE and Ni-MIL-77/GCE in 0.1 M PBS solution with 5 mM $NaNO_2$, respectively. The anodic peak currents for Ni/NiO/GCE increase linearly with the scan rate as well as the calibration equation is I_{pa} (μA) = 0.046465υ (mV s^{-1}) + 1.35653 (R^2 = 0.948) (**Figure 4B**). This property indicates that the electron transfer for $NaNO_2$ at Ni/NiO/GCE is controlled by an adsorption process. Moreover, it can be seen that the redox peak potential changes slightly with the increase of scan rate, and the linear regression equation of E_{pa} and log of scan rate in **Figure 4C** is represented by E_{pa} = 0.04951lg ν + 0.69305 (R^2 = 0.993). The electron transfer number (n) is calculated according to the Laviron's equation (Yang et al., 2014, 2015). It was found by calculation that there

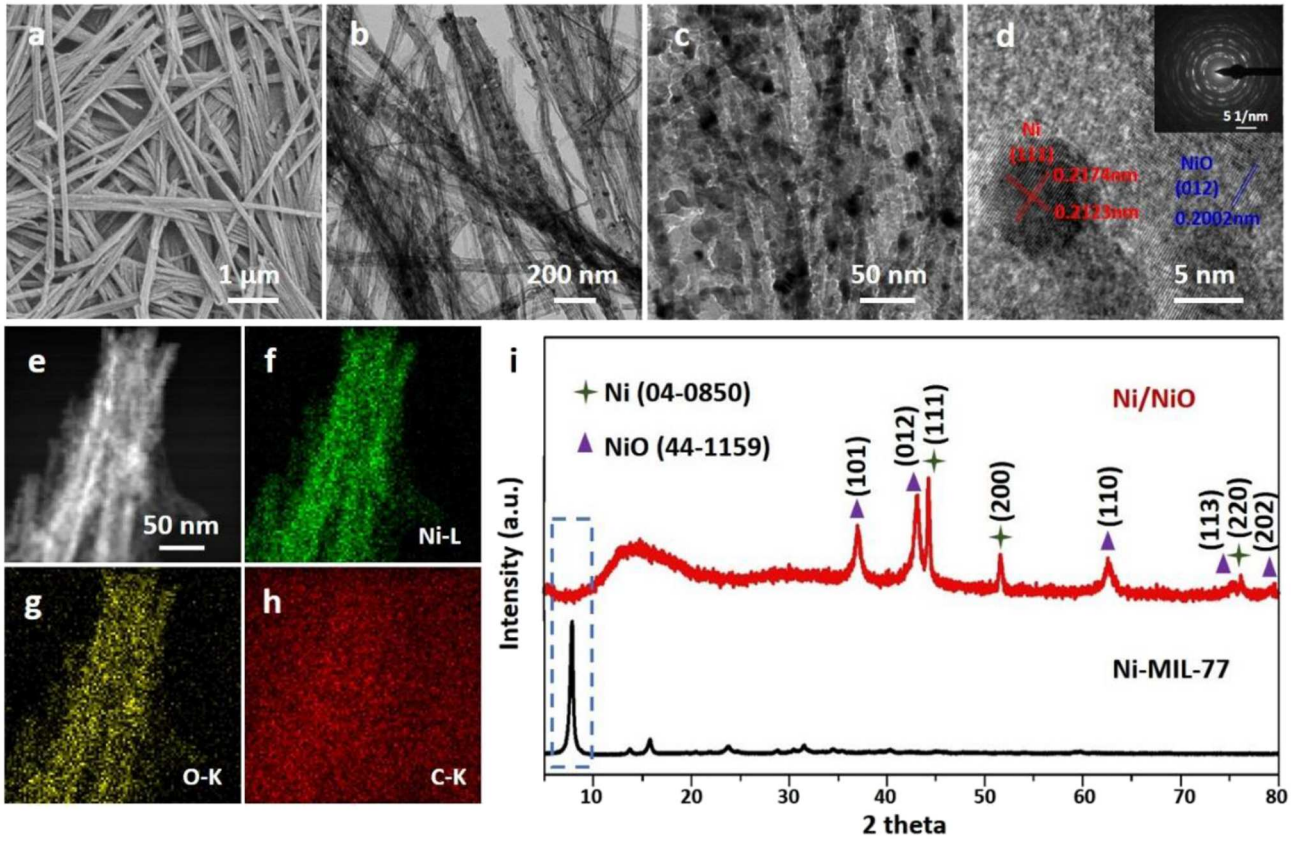

FIGURE 2 | Morphology and structure characterization of Ni/NiO ultrathin nanobelts. **(a)** SEM, **(b,c)** TEM, **(d)** HRTEM (insert: SAED patterns) and **(e–h)** elemental mapping images of Ni/NiO ultrathin nanobelts. **(i)** XRD patterns of the Ni-MIL-77 and Ni/NiO.

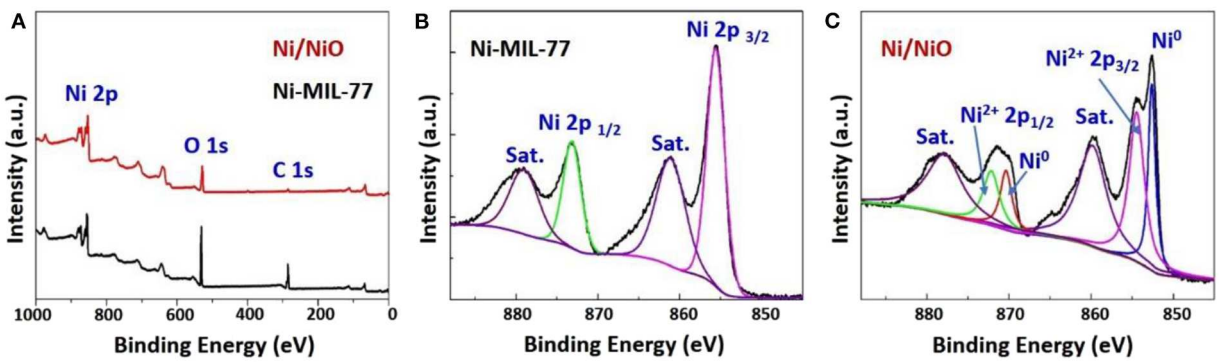

FIGURE 3 | (A) XPS survey of the Ni-MOF and Ni/NiO; Ni $2p_{3/2}$ XPS spectra of **(B)** Ni-MOF **(C)** and Ni/NiO.

are $2e^-$ involved in the irreversible reaction of $NaNO_2$, and it is consistent with Equation.

$$NO_2^- + H_2O \rightarrow NO_3^- + 2H^+ + 2e^-$$

Figures S11, **S12** describe the effect of pH on the response of 5 mM $NaNO_2$ CVs with a pH range of 4.0–8.0 (scanning rate of 50 mV s^{-1}). As seen from **Figure S11a**, the peak anode current reaches its maximum at pH 7.0. As reported by Brylev et al. (2007) N_2O generation may lead to a decrease in peak current at low pH values. In addition, the oxidation peak of $NaNO_2$ shifted in a very negative direction as pH increases, so we chose pH 7.0 as the optimal pH for our experiment.

The linear working range of Ni/NiO/GCE was determined by recording the amperometric response as a function of $NaNO_2$ concentration. **Figure 5A** shows the typical current time curve of the modified Ni/NiO nanobelt electrode and $NaNO_2$

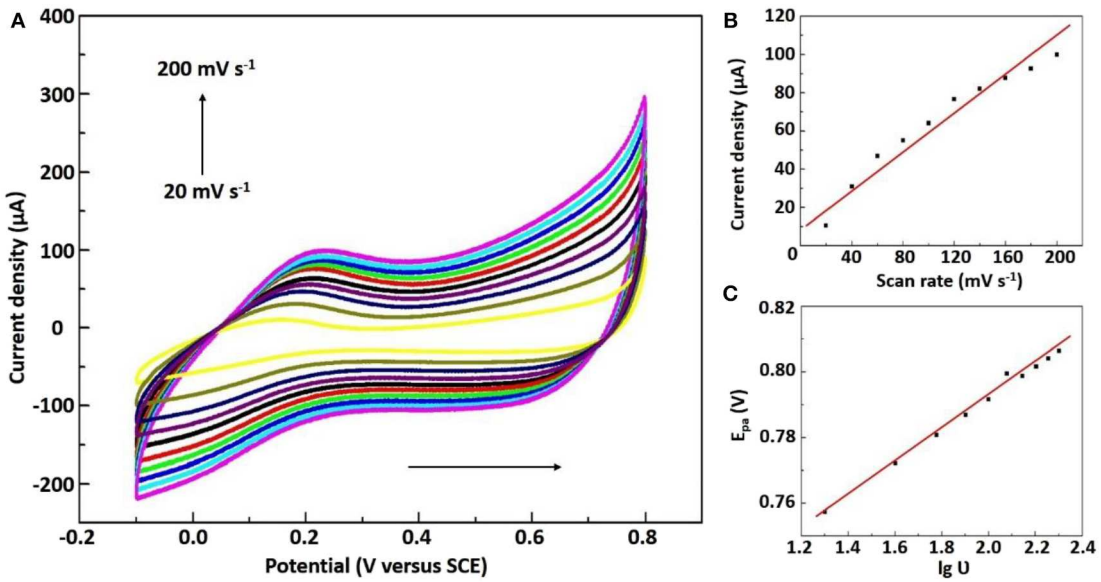

FIGURE 4 | (A) CVs of the Ni/NiO/GCE in 0.1 M PBS solution containing 5 mM $NaNO_2$ (20 to 200 mV s^{-1}). **(B)** The plots of scan rates to the anodic peak currents. **(C)** lg ν vs. anodic peak potentials.

solution with continuous injection concentrations from 0.5 μM to 1,000 μM. An obvious reaction occurs when $NaNO_2$ solution concentration is as low as 0.5 μM. **Figure 5B** exhibits that Ni/NiO/GCE electrode displays a sensitive increase in current response after successive increments of $NaNO_2$ in 0.1 M PBS (pH = 7) solution. After each increase of $NaNO_2$, the current response increases sensitively and rapidly, which shows a nice linear dependence. Two linear working ranges can be seen from **Figure 5B**. Notably, from the plots of electrocatalytic current versus $NaNO_2$ concentration in the range of 2–100 mM (**Figure 5B**), the simulated linear equation of the Ni/NiO/GCE is found to be: I (mA) = 0.117C (mM) + 0.25324, R = 0.9982, and the calculated sensitivity is 1.5420 mA mM^{-1} cm^{-2}. The illustrations in **Figure 5B** shows a good linear response in the range of 2.0∼10.0 mM $NaNO_2$ with a relation coefficient of 0.99926.

In the complex biological environments, the ability to identify target molecules and interference molecules is very important for sensors. Therefore, we further investigated the effects of some electroactive substances on the Ni/NiO/GCE electrode response. **Figure 5C** shows the amperometric response of the sensor to the consecutive addition of $NaNO_2$, KNO_3, $NaSO_4$, $NaClO_4$, and KCl to the solution. Only the current response of $NaNO_2$ is remarkable. These results show that GCE modified by Ni/NiO ultrathin nanoribends can be used for selective and sensitive detection of $NaNO_2$ without interference from KNO_3, $NaSO_4$, $NaClO_4$ and KCl.

In addition, the stability of the Ni/NiO/GCE electrode was tested. The amperometric response to determining stability is shown in **Figure 5D**. The result exhibits that 96.72% of the current response remained unchanged for a long period of 5 h, indicating good stability in the measurement process. As shown in **Figure S13**, Ni-MIL-77 also exhibits good stability over a long period of 5 h, and a current response of 96.51% remains unchanged. In order to further appraise the properties of the Ni/NiO/GCE, a correlative reference is shown in **Table S1**.

The advantages of Ni/NiO composites can be summarized as follows:

(1) The study shows that the standard electrode potential decreases ∼100 mV when the electrode material size is 1 nm. Therefore, the ultrathin nanobelt structure not only allows more active sites to be exposed, but also promotes charge transfer.
(2) MOF derivative support can effectively avoid agglomeration of ultrafine Ni nanoparticles, and ultrafine Ni nanoparticles can effectively improve the conductivity of MOF materials.
(3) Interleaved 3D reticulated structure has strong mechanical stability.

Determination of $NaNO_2$ in Real Samples

To illustrate the feasibility and application potential of the electrode, the Ni/NiO/GCE was applied to determine $NaNO_2$ from pickled pork using the standard addition technique. The collected pickled pork was disposed and the spiked $NaNO_2$ concentrations were 10, 20, and 30 mg kg^{-1}, respectively. As shown in **Table 1**, the recovery rates were 98.3, 100.3, and 99.5%, respectively. The results show that the method has good recovery rates and good practical value.

CONCLUSIONS

In summary, Ni/NiO ultrathin nanobelts were prepared by a facile in suit conversion method (O_2-protected annealing

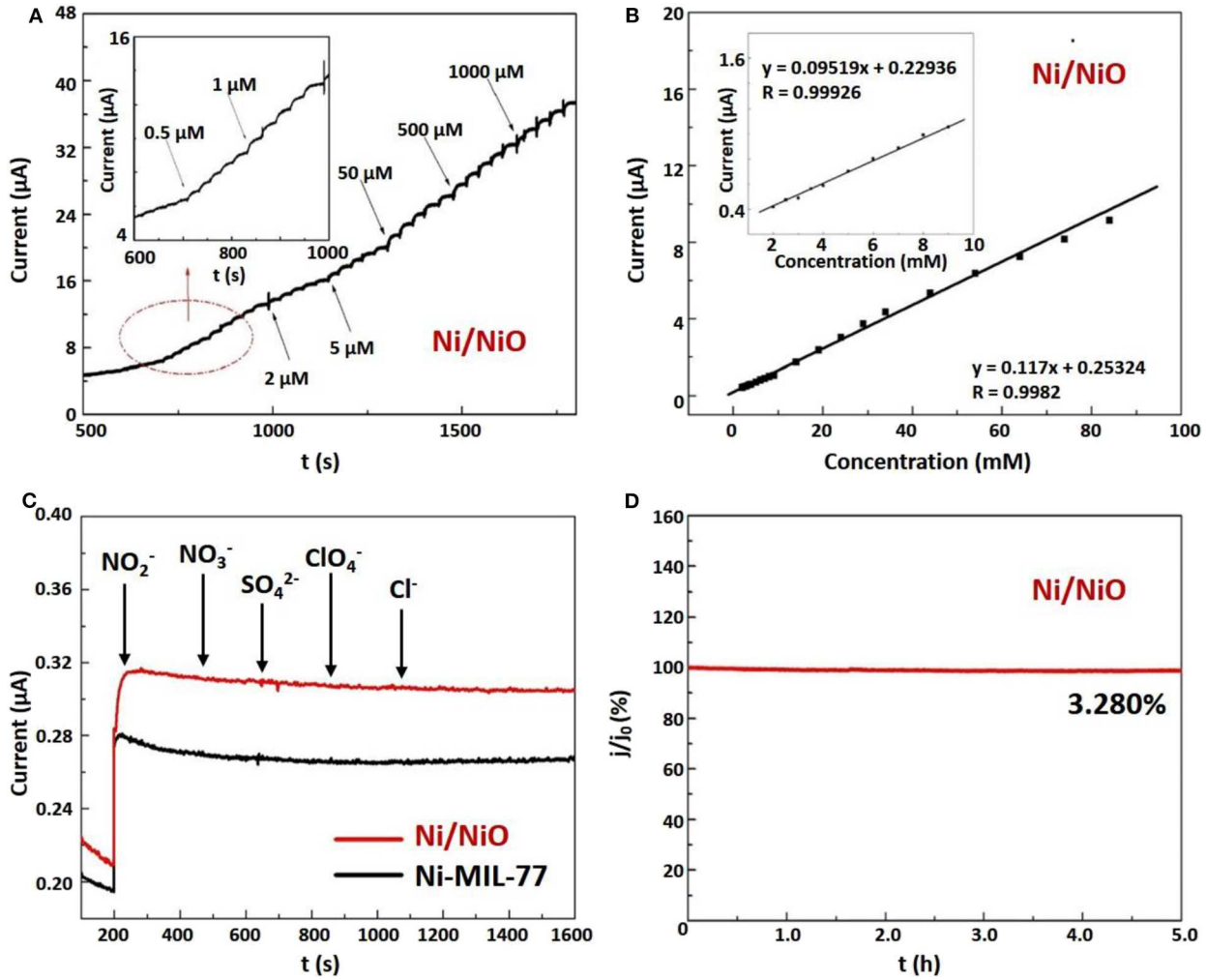

FIGURE 5 | Electrochemical performances of the Ni/NiO ultrathin nanobelts modified electrode. **(A)** Amperometric responses of the Ni/NiO/GCE electrode to the successive injection of $NaNO_2$ in 0.1 M PBS (inset: carefully observe the response currents of several micromolar $NaNO_2$). **(B)** The calibration curve of current vs. $NaNO_2$ concentration of 2∼100 mM. Inset: calibration curve with $NaNO_2$ concentration of 2∼10 mM. **(C)** Amperometric response of Ni/NiO /GCE to NO_2^- in the presence of NO_2^-, NO_3^-, SO_4^-, ClO_4^-, Cl^-. **(D)** Stability of Ni/NiO/GCE over 5 h.

TABLE 1 | Determination of various concentrations of nitrite in pickled pork.

Samples	Content (mg kg^{-1})	Added (mg kg^{-1})	Found (mg kg^{-1})	Recovery (%)	R.S.D (%, n=10)
1	10.2	15	24.8	98.3	2.8
2	10.2	25	35.3	100.3	2.6
3	10.2	35	45.0	99.5	3.2

process). The ultrathin nanobelts with large surface area and *in situ* generated metal Ni particles exhibit outstanding electrochemical performance. During the oxidation of $NaNO_2$, the Ni/NiO ultrathin nanobelts exhibit excellent stability, special reproducibility, and strong anti-interference ability. Moreover, Ni/NiO composites also obtained a good recovery rate when it was applied to the determination of $NaNO_2$ in marinated pork. Compared with other methods, the electrochemical method is inexpensive, simple, which is suitable for practical applications.

DATA AVAILABILITY STATEMENT

All datasets generated for this study are included in the article/**Supplementary Material**.

AUTHOR CONTRIBUTIONS

XM and XX conducted all the major experiments, designed the study, and wrote the manuscript. HP provided valuable inputs for the study's development and helped with manuscript writing. All authors agree to be accountable for the content of the work.

FUNDING

This work was supported by the National Natural Science Foundation of China (NSFC-U1904215, 21671170, and 21673203), the Top-notch Academic Programs Project of Jiangsu Higher Education Institutions (TAPP), Changjiang scholars program of the ministry of Education (Q2018270), and Program for New Century Excellent Talents of the University in China (NCET-13-0645), the Six Talent Plan (2015-XCL-030), Qinglan Project of Jiangsu, Qinglan Project of Yangzhou University. Project supported by the Natural Science Foundation for Young Scientists of Jiangsu Province, China (Grant nos. BK20190903 and 19KJB430043). Postgraduate Research & Practice Innovation Program of Jiangsu Province (KYCX19-2100).

ACKNOWLEDGMENTS

The authors acknowledge the Jiangsu Huai-yang Cuisine Engineering Center, Priority Academic Program Development of Jiangsu Higher Education Institutions, and the technical support we received at the Testing Center of Yangzhou University.

SUPPLEMENTARY MATERIAL

The Supplementary Material for this article can be found online at: https://www.frontiersin.org/articles/10.3389/fchem.2020.00330/full#supplementary-material

REFERENCES

Bosch, M., Yuan, S., Rutledge, W., and Zhou, H. C. (2017). Stepwise synthesis of metal-organic frameworks. *Acc. Chem. Res.* 50, 857–865. doi: 10.1021/acs.accounts.6b00457

Brylev, O., Sarrazin, M., Roué, L., and Bélanger, D. (2007). Nitrate and nitrite electrocatalytic reduction on Rh-modified pyrolytic graphite electrodes. *Electrochim. Acta* 52, 6237–6247. doi: 10.1016/j.electacta.2007.03.072

Chen, D. M., Zhang, N. N., Tian, J. Y., Liu, C. S., and Du, M. (2017). Pore modulation of metal-organic frameworks towards enhanced hydrothermal stability and acetylene uptake via incorporation of different functional brackets. *J. Mater. Chem. A* 5, 4861–4867. doi: 10.1039/C6TA10785K

Chen, F. F., Shen, K., Chen, J. Y., Yang, X. F., Cui, J., and Li, Y. W. (2019). General immobilization of ultrafine alloyed nanoparticles within metal-organic frameworks with high loadings for advanced synergetic catalysis. *ACS Cent. Sci.* 5, 176–185. doi: 10.1021/acscentsci.8b00805

Chen, L.-F., and Xu, Q. (2017). Converting MOFs into amination catalysts. *Science* 358, 304–305. doi: 10.1126/science.aap8004

Chen, M., Wu, B. H., Yang, J., and Zheng, N. F. (2012). Small adsorbate-assisted shape control of Pd and Pt nanocrystals. *Adv. Mater.* 24, 862–879. doi: 10.1002/adma.201104145

Cho, K., Han, S., and Suh, M. P. (2016). Copper-organic framework fabricated with CuS nanoparticles: synthesis, electrical conductivity, and electrocatalytic activities for oxygen reduction reaction. *Angew. Chemie Int. Ed.* 128, 15527–15531. doi: 10.1002/ange.201607271

Du, M., Chen, M., Yang, X. G., Wen, J., Wang, X., Fang, S. M., et al. (2014). A channel-type mesoporous In(iii)-carboxylate coordination framework with high physicochemical stability for use as an electrode material in supercapacitors. *J. Mater. Chem. A* 2, 9828–9834. doi: 10.1039/C4TA00963K

Du, T. Y., Zhao, C. Q., ur Rehman, F., Lai, L. M., Li, X. Q., Sun, Y., et al. (2017). *In situ* multimodality imaging of cancerous cells based on a selective performance of Fe^{2+} -adsorbed zeolitic imidazolate framework-8. *Adv. Funct. Mater.* 27:1603926. doi: 10.1002/adfm.201603926

Geng, P. B., Cao, S., Guo, X. T., Ding, J. W., Zheng, S. S., Zheng, M. B., et al. (2019). Polypyrrole coated hollow metal-organic framework composites for lithium-sulfur batteries. *J. Mater. Chem. A* 7, 19465–19470. doi: 10.1039/C9TA05812E

Han, J., Li, L. Y., and Guo, R. (2010). Novel approach to controllable synthesis of gold nanoparticles supported on polyaniline nanofibers. *Macromolecules* 43, 10636–10644. doi: 10.1021/ma102251e

Larsson, E. M., Langhammer, C., Zoric, I., and Kasemo, B. (2009). Nanoplasmonic probes of catalytic reactions. *Science* 326, 1091–1094. doi: 10.1126/science.1176593

Li, F.-L., Shao, Q., Huang, X., and Lang, J.-P. (2018). Nanoscale trimetallic metal-organic frameworks enable efficient oxygen evolution electrocatalysis. *Angew. Chemie Int. Ed.* 57, 1888–1892. doi: 10.1002/anie.201711376

Li, Q. Y., Zhang, L., Xu, Y. X., Li, Q., Xue, H. G., and Pang, H. (2019). Smart Yolk/Shell ZIF-67@POM hybrids as efficient electrocatalysts for the oxygen evolution reaction. *ACS Sustain. Chem. Eng.* 7, 5027–5033. doi: 10.1021/acssuschemeng.8b05744

Li, X.-R., Kong, F.-Y., Liu, J., Liang, T.-M., Xu, J.-J., and Chen, H.-Y. (2012). Synthesis of potassium-modified graphene and its application in nitrite-selective sensing. *Adv. Funct. Mater.* 22, 1981–1988. doi: 10.1002/adfm.201103025

Li, Y.-P., Wang, Y., Xue, Y.-Y., Li, H.-P., Zhai, Q.-G., Li, S.-N., et al. (2019). Ultramicroporous building units as a path to bi-microporous metal-organic frameworks with high acetylene storage and separation performance. *Angew. Chemie Int. Ed.* 58, 13590–13595. doi: 10.1002/anie.201908378

Liang, Z. B., Qu, C., Xia, D. G., Zou, R. Q., and Xu, Q. (2018). Atomically dispersed metal sites in MOF-based materials for electrocatalytic and photocatalytic energy conversion. *Angew. Chemie Int. Ed.* 57, 9604–9633. doi: 10.1002/anie.201800269

Lin, M.-C., Gong, M., Lu, B. G., Wu, Y. P., Wang, D.-Y., Guan, M. Y., et al. (2015). An ultrafast rechargeable aluminium-ion battery. *Nature* 520, 324–328. doi: 10.1038/nature14340

Lin, Z., Dou, X. N., Li, H. F., Ma, Y., and Lin, J.-M. (2015). Nitrite sensing based on the carbon dots-enhanced chemiluminescence from peroxynitrous acid and carbonate. *Talanta* 132, 457–462. doi: 10.1016/j.talanta.2014.09.046

Liu, G., Yang, H. G., Pan, J., Yang, Y. Q., Lu, G. Q. M., and Cheng, H.-M. (2014). Titanium dioxide crystals with tailored facets. *Chem. Rev.* 114, 9559–9612. doi: 10.1021/cr400621z

Liu, G. Y., Sheng, Y., Ager, J. W., Kraft, M., and Xu, R. (2019). Research advances towards large-scale solar hydrogen production from water. *Energy Chem* 1:100014. doi: 10.1016/j.enchem.2019.100014

Ma, J. L., Ren, F. Z., Wang, G. X., Xiong, Y., Li, Y. Q., and Wen, J. B. (2017). Electrochemical performance of melt-spinning Al-Mg-Sn based anode alloys. *Int. J. Hydrogen Energy* 42, 11654–11661. doi: 10.1016/j.ijhydene.2017.02.185

Mukoyoshi, M., Kobayashi, H., Kusada, K., Hayashi, M., Yamada, T., Maesato, M., et al. (2015). Hybrid materials of Ni NP@MOF prepared by a simple synthetic method. *Chem. Commun.* 51, 12463–12466. doi: 10.1039/C5CC04663G

Shi, D., Zheng, R., Sun, M.-J., Cao, X., Sun, C.-X., Cui, C.-J., et al. (2017). Semiconductive copper(I)-organic frameworks for efficient light-driven hydrogen generation without additional photosensitizers and cocatalysts. *Angew. Chemie Int. Ed.* 56, 14637–14641. doi: 10.1002/anie.201709869

Tan, C. L., Cao, X. H., Wu, X.-J., He, Q. Y., Yang, J., Zhang, X., et al. (2017). Recent advances in ultrathin two-dimensional nanomaterials. *Chem. Rev.* 117, 6225–6331. doi: 10.1021/acs.chemrev.6b00558

Tang, C. J., Liu, Y. N., Xu, C., Zhu, J. X., Wei, X. J., Zhou, L., et al. (2018). Ultrafine nickel-nanoparticle-enabled SiO_2 hierarchical hollow spheres for high-performance lithium storage. *Adv. Funct. Mater.* 28:1704561. doi: 10.1002/adfm.201704561

Wang, F., Liu, Y., Zhao, Y. F., Wang, Y., Wang, Z. J., Zhang, W. H., et al. (2018). Facile synthesis of two-dimensional porous $MgCo_2O_4$ nanosheets as anode for lithium-ion batteries. *Appl. Sci.* 8:22. doi: 10.3390/app8010022

Wu, Y. P., Tian, J. W., Liu, S., Li, B., Zhao, J., Ma, L. F., et al. (2019). Bi-Microporous metal-organic frameworks with cubane $[M_4(OH)_4]$ (M=Ni, Co) clusters and pore-space partition for electrocatalytic methanol oxidation reaction. *Angew. Chemie Int. Ed.* 58, 12185–12189. doi: 10.1002/anie.201907136

Xia, W., Mahmood, A., Zou, R. Q., and Xu, Q. (2015). Metal-organic frameworks and their derived nanostructures for electrochemical energy storage and conversion. *Energy Environ. Sci.* 8, 1837–1866. doi: 10.1039/C5EE00762C

Xiao, X., Li, Q., Yuan, X. Y., Xu, Y. X., Zheng, M. B., and Pang, H. (2018). Ultrathin nanobelts as an excellent bifunctional oxygen catalyst: insight into the subtle changes in structure and synergistic effects of bimetallic metal-organic framework. *Small Methods* 2:1800240. doi: 10.1002/smtd.201800240

Xiao, X., Zhang, G. X., Yuan, Y. X., Zhang, H. L., Guo, X. T., Liu, Y., et al. (2019). A new strategy for the controllable growth of MOF@PBA architectures. *J. Mater. Chem. A* 7, 17266–17271. doi: 10.1039/C9TA05409J

Xiao, X., Zheng, S. S., Li, X. R., Zhang, G. X., Guo, X. T., Xue, H. G., et al. (2017). Facile synthesis of ultrathin Ni-MOF nanobelts for high-efficiency determination of glucose in human serum. *J. Mater. Chem. B* 5, 5234–5239. doi: 10.1039/C7TB00180K

Xiao, X., Zou, L. L., Pang, H., and Xu, Q. (2020). Synthesis of micro/nanoscaled metal–organic frameworks and their direct electrochemical applications. *Chem. Soc. Rev.* 49, 301–331. doi: 10.1039/C7CS00614D

Xu, G. Y., Nie, P., Dou, H., Ding, B., Li, L. Y., and Zhang, X. G. (2017). Exploring metal organic frameworks for energy storage in batteries and supercapacitors. *Mater. Today* 20, 191–209. doi: 10.1016/j.mattod.2016.10.003

Xu, Q., Gu, S.-X., Jin, L. Y., Zhou, Y. E., Yang, Z. J., Wang, W., et al. (2014). Graphene/polyaniline/gold nanoparticles nanocomposite for the direct electron transfer of glucose oxidase and glucose biosensing. *Sensors Actuators B Chem.* 190, 562–569. doi: 10.1016/j.snb.2013.09.049

Yang, B. B., Wang, H. W., Du, J., Fu, Y. Z., Yang, P., and Du, Y. K. (2014). Direct electrodeposition of reduced graphene oxide on carbon fiber electrode for simultaneous determination of ascorbic acid, dopamine and uric acid. *Colloids Surf. A Physicochem. Eng. Asp.* 456, 146–152. doi: 10.1016/j.colsurfa.2014.05.029

Yang, B. B., Wang, J., Bin, D., Zhu, M. S., Yang, P., and Du, Y. K. (2015). A three dimensional Pt nanodendrite/graphene/MnO_2 nanoflower modified electrode for the sensitive and selective detection of dopamine. *J. Mater. Chem. B* 3, 7440–7448. doi: 10.1039/C5TB01031D

Yang, H. G., Sun, C. H., Qiao, S. Z., Zou, J., Liu, G., Smith, S. C., et al. (2008). Anatase TiO_2 single crystals with a large percentage of reactive facets. *Nature* 453, 638–641. doi: 10.1038/nature06964

Yang, X. G., Ma, L. F., and Yan, D. P. (2019). Facile synthesis of 1D organic-inorganic perovskite micro-belts with high water stability for sensing and photonic applications. *Chem. Sci.* 10, 4567–4572. doi: 10.1039/C9SC00162J

Yue, R., Lu, Q., and Zhou, Y. K. (2011). A novel nitrite biosensor based on single-layer graphene nanoplatelet-protein composite film. *Biosens. Bioelectron.* 26, 4436–4441. doi: 10.1016/j.bios.2011.04.059

Zhan, G. W., and Zeng, H. C. (2016). Synthesis and functionalization of oriented metal-organic-framework nanosheets: toward a series of 2D catalysts. *Adv. Funct. Mater.* 26, 3268–3281. doi: 10.1002/adfm.201505380

Zhan, G. W., and Zeng, H. C. (2018). Hydrogen spillover through Matryoshka-type $(ZIFs@)_{n-1}ZIFs$ nanocubes. *Nat. Commun.* 9:3778. doi: 10.1038/s41467-018-06269-z

Zhang, S., Zhao, Y. X., Shi, R., Waterhouse, G. I. N., and Zhang, T. R. (2019). Photocatalytic ammonia synthesis: recent progress and future. *Energy Chem.* 1:100013. doi: 10.1016/j.enchem.2019.100013

Zhang, Y. C., Du, Z. N., Li, S. Y., and Zhang, M. (2010). Novel synthesis and high visible light photocatalytic activity of SnS2 nanoflakes from $SnCl_2{\cdot}2H_2O$ and S powders. *Appl. Catal. B Environ.* 95, 153–159. doi: 10.1016/j.apcatb.2009.12.022

Zhang, Y. C., Li, J., and Xu, H. Y. (2012). One-step in situ solvothermal synthesis of SnS2/TiO2 nanocomposites with high performance in visible light-driven photocatalytic reduction of aqueous Cr(VI). *Appl. Catal. B Environ.* 123–124, 18–26. doi: 10.1016/j.apcatb.2012.04.018

Zhang, Y. C., Yao, L., Zhang, G. S., Dionysiou, D. D., Li, J., and Du, X. H. (2014). One-step hydrothermal synthesis of high-performance visible-light-driven SnS_2/SnO_2 nanoheterojunction photocatalyst for the reduction of aqueous Cr(VI). *Appl. Catal. B Environ.* 144, 730–738. doi: 10.1016/j.apcatb.2013.08.006

Zhao, L., Zhang, Y., Zhao, Z. L., Zhang, Q.-H., Huang, L.-B., Gu, L., et al. (2019). Steering elementary steps towards efficient alkaline hydrogen evolution via size-dependent Ni/NiO nanoscale heterosurfaces. *Natl. Sci. Rev.* 7, 27–36. doi: 10.1093/nsr/nwz145

Zhao, R. B., Xie, H. T., Chang, L., Zhang, X. X., Zhu, X. J., Tong, X., et al. (2019). Recent progress in the electrochemical ammonia synthesis under ambient conditions. *EnergyChem* 1:100011. doi: 10.1016/j.enchem.2019.100011

Zhao, S. L., Wang, Y., Dong, J. C., He, C.-T., Yin, H. J., An, P. F., et al. (2016). Ultrathin metal-organic framework nanosheets for electrocatalytic oxygen evolution. *Nat. Energy* 1:16184. doi: 10.1038/nenergy.2016.184

Zhao, Y., Wang, Y. J., Wang, N., Zheng, P., Fu, H. R., Han, M. L., et al. (2019). Tetraphenylethylene-decorated metal-organic frameworks as energy-transfer platform for the detection of nitro-antibiotics and white-light emission. *Inorg. Chem.* 58, 12700–12706. doi: 10.1021/acs.inorgchem.9b01588

Zhu, R. M., Ding, J. W., Jin, L., and Pang, H. (2019). Interpenetrated structures appeared in supramolecular cages, MOFs, COFs. *Coord. Chem. Rev.* 389, 119–140. doi: 10.1016/j.ccr.2019.03.002

Zou, C. E., Yang, B. B., Bin, D., Wang, J., Li, S. M., Yang, P., et al. (2017). Electrochemical synthesis of gold nanoparticles decorated flower-like graphene for high sensitivity detection of nitrite. *J. Colloid Interface Sci.* 488, 135–141. doi: 10.1016/j.jcis.2016.10.088

Zou, L. L., Hou, C.-C., Liu, Z., Pang, H., and Xu, Q. (2018). Superlong single-crystal metal-organic framework nanotubes. *J. Am. Chem. Soc.* 140, 15393–15401. doi: 10.1021/jacs.8b09092

Conflict of Interest: The authors declare that the research was conducted in the absence of any commercial or financial relationships that could be construed as a potential conflict of interest.

The reviewer GZ declared a past co-authorship with one of the authors HP to the handling editor.

frontiers in Chemistry

CORRECTION
published: 28 July 2020
doi: 10.3389/fchem.2020.00631

Corrigendum: Ultrathin Ni-MOF Nanobelts-Derived Composite for High Sensitive Detection of Nitrite

Xiangren Meng[1,2*†], *Xiao Xiao*[3†] *and Huan Pang*[3*]

[1] School of Tourism and Culinary Science, Yangzhou University, Yangzhou, China, [2] Jiangsu Huai-yang Cuisine Engineering Center, Yangzhou University, Yangzhou, China, [3] School of Chemistry and Chemical Engineering, Yangzhou University, Yangzhou, China

Keywords: in suit conversion method, Ni/NiO ultrathin nanobelt, metal nanoparticle, metal organic framework, nitrite

OPEN ACCESS

Edited and reviewed by:
Baiqing Yuan,
Ludong University, China

***Correspondence:**
Xiangren Meng
xrmeng@yzu.edu.cn
Huan Pang
huanpangchem@hotmail.com;
panghuan@yzu.edu.cn

†These authors have contributed equally to this work

Specialty section:
This article was submitted to Supramolecular Chemistry, a section of the journal Frontiers in Chemistry

Received: *12 June 2020*
Accepted: *17 June 2020*
Published: *28 July 2020*

Citation:
Meng X, Xiao X and Pang H (2020) Corrigendum: Ultrathin Ni-MOF Nanobelts-Derived Composite for High Sensitive Detection of Nitrite. Front. Chem. 8:631. doi: 10.3389/fchem.2020.00631

A Corrigendum on

Ultrathin Ni-MOF Nanobelts-Derived Composite for High Sensitive Detection of Nitrite
by Meng, X., Xiao, X., and Pang, H. (2020). Front. Chem. 8:330. doi: 10.3389/fchem.2020.00330

In the original article, there was a mistake in Figure S9 as published. When processing the CV curves, we misarranged the order of Ni/NiO and Ni-MIL-77 in Figure S9, resulting in errors.

Figure S9 shows the cyclic voltammograms (CVs) of different electrodes (Ni-MOF/GCE, Ni/NiO/GCE) in 5.0 mM $K_3Fe(CN)_6$ containing 1 M KCl solution at a scan rate of 50 mV s^{-1}. As displayed in Figure S9, the Ni/NiO /GCE exhibited an increase in the anodic peak current (117.64 μA) compared to Ni-MIL-77/GCE (68.96 μA).

The authors apologize for this error and state that this does not change the scientific conclusions of the article in any way. The original article has been updated.

frontiers in Chemistry

ORIGINAL RESEARCH
published: 04 August 2020
doi: 10.3389/fchem.2020.00617

Synthesis of UV-11 MOF and Its Characterization by Cyclic Voltammetry

Ingrid Guadalupe Meza-Pardo[1], *Alfredo A. Morales-Tapia*[2], *María Aurora Veloz Rodríguez*[1†], *Victor Esteban Reyes-Cruz*[1], *Miguel Perez-Labra*[1], *Gustavo Urbano-Reyes*[1], *José María Rivera-Villanueva*[2] *and Jose Angel Cobos-Murcia*[1*]

[1] *Laboratory Electrochemistry Process, Institute of Basic Sciences and Engineering, Academic Area of Earth Sciences and Materials, Autonomous University of the State of Hidalgo, Pachuca, Mexico,* [2] *LADISER Organic Chemistry, Faculty of Chemical Sciences, Universidad Veracruzana, Orizaba, Mexico*

In this work a Metal–Organic Framework (MOF) was prepared using a solvothermal method, taking as precursors 1. 2-di-(4-pyridyl)-ethylene, 1.2.4.5-benzenetetracarboxylic acid and $Co(No_3)_2$-$6H_2O$. This MOF was called UV-11 and was evaluated using microscopic, spectroscopic and electrochemical techniques. According to the obtained results, the melting point of the compound is located in a higher interval than its precursors. Stereoscopic microscopy analysis shows the presence of pink crystals in the form of needles. MEB technique displays a laminar morphology as well as crystals with approximate sizes (36 mm wide and 150 mm long). EDS analysis corroborated the presence of precursor elements such as cobalt, carbon and oxygen. Furthermore, the XRD technique shows the cobalt-related phases in the sample, which is cobalt bis (pyridine-6-carboxylic-2-carboxylate). A modified carbon paste electrode was prepared using MOF UV-11 and by cyclic voltammetry electrochemical technique, semi-reversible redox processes are identified, as well as thermodynamic and kinetic parameters were obtained with the Laviron equation, and electrochemical performance properties from the cyclic voltammetry experimental data.

Keywords: characterization-analysis, electroanalysis, MOF (Metal–Organic Framework), interface mechanical behavior, micro supercapacitor, electrochemistry (cyclic voltametry)

OPEN ACCESS

Edited by:
Daojun Zhang,
Anyang Normal University, China

Reviewed by:
Zhiyong Guo,
Fuzhou University, China
Xiaodong Zhuang,
Shanghai Jiao Tong University, China

****Correspondence:***
Jose Angel Cobos-Murcia
jose_cobos@uaeh.edu.mx

†ORCID:
María Aurora Veloz Rodríguez
orcid.org/0000-0002-3453-1227

Specialty section:
This article was submitted to Supramolecular Chemistry, a section of the journal Frontiers in Chemistry

Received: *28 April 2020*
Accepted: *11 June 2020*
Published: *04 August 2020*

Citation:
Meza-Pardo IG, Morales-Tapia AA, Veloz Rodríguez MA, Reyes-Cruz VE, Perez-Labra M, Urbano-Reyes G, Rivera-Villanueva JM and Cobos-Murcia JA (2020) Synthesis of UV-11 MOF and Its Characterization by Cyclic Voltammetry. Front. Chem. 8:617. doi: 10.3389/fchem.2020.00617

INTRODUCTION

Since ancient times, a variety of porous materials have been used, for instance: cell membranes, porous polymers, and some natural materials such as rocks, foams and soils (clays), which are classified as low- or medium-porosity materials (Zdravkov et al., 2007). Nowadays, there are materials with excellent microstructural characteristics (high porosity), such as MOF (metal–organic frameworks); which are crystalline materials with high porosity, belonging to hybrid-material classification, due to the presence of chemical bonds between metal and ligand ions (Zhou et al., 2012), constituting coordination links and the ability to grow in different dimensions such as 2D and 3D (Wang et al., 2005).

MOF have been of great interest due to the wide amount of applications, for instance, catalysis (Shen et al., 2016), magnetism (Tian et al., 2014), luminescence (Allendorf et al., 2009), gas detection (Drobek et al., 2016), water purification (Ma et al., 2017), gas storage (Li and Yang, 2007), adsorption properties (Kaur et al., 2019), and supercapacitors (Lee et al., 2009).

The latter is another great advantage of MOF, since the structural flexibility vs. external stimuli (changes in temperature and pressure), that varies their porosity. For this reason, it is possible to promote their use as molecular sieves (Bux et al., 2010) and drug-releasing capsules (Orellana-Tavra et al., 2016), among other things. This versatility in their application is due to the properties such as the high specific surface area of >1,000 m2/g, a regular and adjustable pore texture, flexibility in surface chemistry, and high chemical and thermal stability (Xia, 2011).

MOF are porous structures that can also be called Porous Coordination Polymers (PCPs), Microporous Coordination Polymers (MCPs) or Porous Coordination Networks (PCNs). These materials are known as hybrids because their structure is composed of inorganic nodes and organic linkers through covalent coordination (Vogel, 2012), which allows for different MOF to be designed.

Various techniques are used in their synthesis, notably mechanochemistry (Klimakow et al., 2010), electrochemical (Van Assche et al., 2012), sonochemistry (Son et al., 2008), microwave (Topologies et al., 2012) and solvothermal techniques (Mulyati et al., 2015). The main advantages these techniques promote are the high crystallinity, short-time reaction, and larger crystal size (Li et al., 2009).

On the other hand, the metallic ion used in MOF synthesis has evolved over time and crystals have been made with different metals such as Cu, Rh, Ru, Mo, Cr, Fe, W, Zn, Cu, Mn, Zr, and Co. However, according to the Cambridge Structural Database (CSD), cobalt is the least used element (1%) in the synthesis of MOF (Wang, 2006). However, cobalt in the metallic center of the MOF could contribute with different properties like a high reactivity through the oxygen interaction with the ligands (Betteridge, 1980), allowing many possibilities of application, such as in magnetic and supercapacitors field. This manner, synthesis of MOF with cobalt represents a theme of great interest in the scientific community.

Thus, to synthesize and characterize MOF with cobalt is the main objective of this work. It was synthesized and reported by our work group in October 2015 (Alfonso-Herrera et al., 2018) in the Cambridge Crystallographic Data Center (CCDC) under the number 1434259, called IUPAC catena-[bis(μ-benzene-1,2,4,5-tetracarboxylate)-tris(μ-4-(2-(pyridin-4-yl)vinyl)pyridine]-tetra-cobalt N,N-dimethylformamide solvate (here called MOF UV-11). However, a full characterization for this MOF has not been reported, in spite of it has already been used by other research groups in the post synthesis of this compound for photocatalytic applications in hydrogen evolution degradation of indigo carmine dye (Alfonso-Herrera et al., 2018).

In this work the MOF UV-11 synthesis through a solvothermal technique using cobalt metal ions was carried out, as well as the analytical characterization using electrochemical voltammetry to elude the pathways of the redox electron transfer process, while the faradaic reaction occurs. In particular, because this type of reaction is used to design and build sensors. So, the voltammetry is useful in elucidating mechanisms and estimate thermodynamic, kinetic and electrochemical performance properties.

EXPERIMENTAL

Synthesis of MOF UV-11

For MOF UV-11 synthesis, all the used analytical grade reagents were provided by Sigma-Aldrich. The precursors were weighed in a RADWAG XA220 analytical balance, firstly, 0.2743 mmol of 1,2-di-(4-pyridyl)-ethylene, 0.5486 mmol of $Co(NO_3)_2$-$6H_2O$, and 0.2743 mmol of 1,2,4,5-benzenetetracarboxylic; subsequently, they were dissolved in 5 ml of Dimethyl Formamide (DMF). In addition, the resulting solution was placed in stainless steel-coated Teflon reactors, being heated inside of a muffle furnace at 90°C for 72 h. Then, all of the reactors were cooled to room temperature and a filtering process was carried out, whereby obtaining the MOF crystals. Finally, MOF UV-11 activation was performed in agitation for 30 min in ethanol. The activation of the MOF is necessary so that it can have a permanent pore size thus avoiding host molecules, this without affecting the structural capacity (Mondloch et al., 2013). Crystals obtained this manner are higher than that of the mechanical synthesis.

Characterization

Melting point characterization was conducted using Electrothermal fusiometer IA-9200 model 10034137/01. The Z potential of MOF UV-11 was carried out with Zetasizer Nano series from Malvern Instruments. PH solutions were prepared with different values (4, 5, 6 and 7) using an approximate concentration of 185 ppm of MOF UV-11. Stereoscopic microscopy technique was performed using a Motic stereo microscope trinocular model bA310 Pol. For microscopic characterization and energy dispersive spectroscopy (MEB/EDS), JEOL model IT-JSM-300 equipment was utilized with an Oxford X-MaxN model 51-XMX1181 detector. X-ray diffraction was obtained using an INEL EQUINOX 2000 model with a [CoK_α = 1.78901 Å] wavelength, Diffraction spectra were obtained in a range of 10–50° for 2θ, with an incremental step size of 0.02°. The data acquisition time constituted 2 s. To make a comparison of the experimental diffractogram, a theoretical simulated model with Mercury 4.3.1 software, was used.

Preparation of Britton–Robinson Buffer Electrolyte

For the preparation of the supporting electrolyte, a buffer solution called Britton–Robinson was used, which is also known as "universal buffer," due to the wide pH damping range between 2 and 12. Acid H_3BO_4 0.01 M, phosphoric acid H_3PO_4 0.01 M, and acetic acid CH_3COOH 0.01 M were utilized at a ratio of 1:1:1, respectively; all of which were of the J.T. Baker brand with 99.5% purity. The pH dissolution was adjusted to 7 with a solution comprising sodium hydroxide 0.01 M; this solution was made using Reasol brand reagent 0.01 M with 97% purity. NaCl 0.001 M was added to the obtained supporting electrolyte, this solution was made using Sigma-Aldrich with 99% purity and deionized water.

Electrode Preparation

The carbon paste electrode represents one of the most convenient materials for modified electrodes preparation, due to their high homogenization capacity, their easy preparation and modification by different methods (Kalcher, 1990; Taylor et al., 2010). The Carbon Paste Electrodes (CPEs) were prepared using graphite powder with a particle size of <20 microns and Nujol oil as a binder, both of which are produced by Sigma-Aldrich. A 2:1 ratio of graphite and binder was utilized. For the preparation of Modified Carbon Paste Electrodes (MCPEs), the same proportion as the CPEs was used, but 3%$_{w/w}$ of MOF UV-11 was incorporated.

Voltammetry Characterization

Electrochemical analysis was conducted on an Autolab PGSTAT30 Potentiostat-Galvanostat with NOVA 2.0 software, using a typical three-electrode array. A saturated calomel electrode was used as reference electrode, a platinum bar as counter electrode, and CPEs and MCPEs as the working electrodes. Cyclic voltammetry scan started with a zero current potential of $E_i = 0$ and in an anodic direction, at three different potential scanning rates: 25, 50, and 100 mVs^{-1}. In addition, the inversion potential evaluation was undertaken from 750 mV (every 50 mV) until reaching the maximum limit of 1,200 mV.

Thermodynamic, Kinetic and Electrochemical Performance Parameters

For thermodynamic and kinetic parameters determination of the modified electrode, it was used experimentally adjusting data to the mathematical parameterised model, according to the Laviron equation (Huang et al., 2010) with the Levenberg–Marquardt iteration, in Origin v. 9.1 software.

$$E_p = E^0 + \frac{2.303RT}{\alpha nF}\left[log\left(\frac{RT}{\alpha nF}(k_s)\right) - log\ (v)\right] \quad (1)$$

$$E_p = A + B\left[C - log\ (v)\right] \quad (2)$$

$$A = E^0 \quad (3)$$

$$B = \frac{2.303RT}{\alpha nF} \quad (4)$$

$$C = \left[log\left(\frac{RT}{\alpha nF}(k_s)\right) - log\ (v)\right] \quad (5)$$

$$ip = \frac{nFQv}{4R\Gamma} \quad (6)$$

Where: α is the electron transfer coefficient, *Ks* is the standard velocity constant of the reaction surface, v is the potential scan rate, n is the electron transfer number, F is the Faraday constant, and E_0 is the formal potential.

The electrochemical assessment of the modified electrode from voltammetry data was performed in a potential range from E_{OCP} to 0.7 V and was calculated using the Equation (1); where, CA is the specific areal capacitance, v is the scan rate, E_f y E_i are the final and initial potential of discharge, j is the current density and E the potential. On the other hand, the Ragone graph was drawn to show and compare results of EMPC against EPC and evaluate the electrochemical performance of the modified electrode. The specific areal energy density (E_A) and the specific areal power density (P_A), was calculated using the Equations (8) and (9) respectively (Yang et al., 2017).

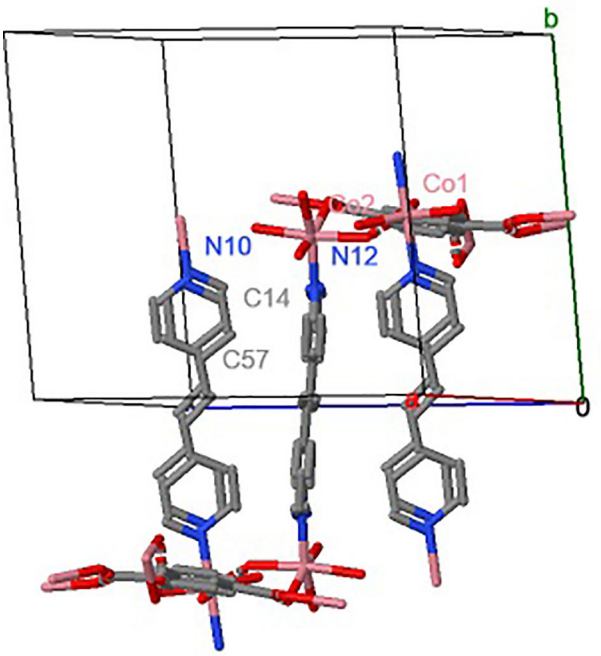

FIGURE 1 | MOF UV-11 unit cell simulation.

$$C_A = \frac{1}{v(E_f - E_i)}\int_{E_i}^{E_f} jdE \quad (7)$$

$$E_A = \frac{C_A^*(E_f - E_i)}{2} \quad (8)$$

$$P_A = \frac{E_A}{(E_f - E_i)/v} \quad (9)$$

RESULTS AND DISCUSSION

Characterization of MOF-UV 11

The method used has a synthesis yield of 72% of the MOF UV-11, and previously activation demonstrated to be necessary in order to keep a permanent pore size to avoid host molecules, without affecting the structural capacity (Farha and Hupp, 2010). The synthesized compound presented a melting point of 292–293°C and show a zeta potential of -10.47 ± 0.99, -8.86 ± 0.81, -10.70 ± 0.49 and -14.60 ± 0.46 mV, for pH of 4, 5, 6, and 7 respectively.

Figure 1 shows the MOF UV-11 unit cell simulation, corresponding to the molecule simulated using Mercury 4.3.1 software. In the **Figure 1** the hydrogen atoms were omitted for better visualization of the molecule structure. The structure of the compound has two cobalt ions. Firstly, the Co1 ion is coordinated with two nitrogen atoms and three oxygen atoms. Meanwhile, the Co2 ion is coordinated with five oxygen atoms and one nitrogen

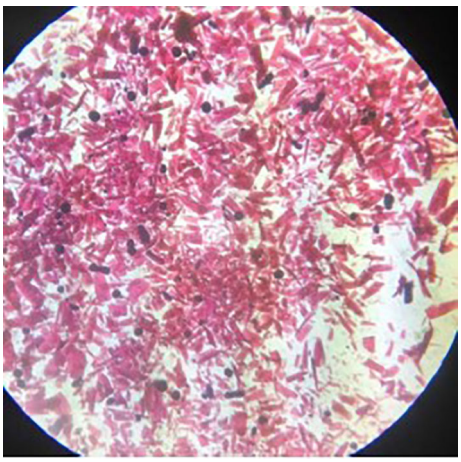

FIGURE 2 | Stereoscopic microscopy of MOF.

atom; therefore, the structure and the form of coordination have a triclinic crystalline system and a volume unit cell of 1922 Å.

To corroborate the correct synthesis of the MOF UV-11, a melting point was evaluated, which is different from that of the precursors; being assumed the presence of greater stability in comparison of the precursors, because its high melting point and crystalline structure. On the other hand, the results of Z potential indicate that all over the range of pH evaluated, there is not significant variability, presenting an average of−10 mV; this implies that the MOF is stable in the range evaluated because of the lack of interaction with the electrolyte. This is consistent with the MOF's prime requirements showing structural stability to changes in the pH values (Howarth et al., 2016). These values are attributable to the molecule structure that has functional groups such as carbonyls and aromatic groups, which cause the polar molecule behavior and do not present repulsion toward the molecules in the electrode interface. Also, at this range of pH, the carbonic groups have their acid constant pK_a uniform.

Figure 2 shows the stereoscopic micrograph of MOF UV-11 crystals, which have an elongated morphology with pink-violet colouration; this tone is attributed to the presence of cobalt in the metal–organic framework.

The crystals shown have different sizes and thicknesses, attributed to the solvothermal production method. In contrast to other techniques such as the mechanochemical, the smaller crystal dimensions are due to the interaction between mechanical elements and produce results presenting a decrease in magnitudes. The melting point of 1,2-di-(4-pyridyl)-ethylene is in the range of 148–152°C. Moreover, the 1,2,4,5-benzenetetracarboxylic acid is in the range of 281–284°C and $Co(NO_3)2\text{-}6H_2O$ does not exceed 56°C.

Figure 3 shows micrograph with a 200x magnification at 20 KV (3a) and an EDS analysis of MOF crystals (3b). **Figure 3a** shows the presence of agglomerates of different sizes fluctuating between 25 and 55 μm.

On the other hand, MOF UV-11 shows microscopic properties such as a rectangular form of the crystal with dimensions of approximately 173 μm in length and 40 μm in width, with a contact surface area of 6932 m^2. In addition, the EDS analysis corroborated that the MOF crystal (**Figure 3b**) contains the precursor elements. These components are joined in the metal–organic framework, constituting a mass ratio proportion of 55.9%$_{w/w}$ of carbon, 28.4%$_{w/w}$ of oxygen, and 15.8%$_{w/w}$ of cobalt and according to the simulation shown in **Figure 1**. The structure and the coordination form have a triclinic crystalline system and an unit cell of 1922 Å volume.

Figure 4 shows the DRX results, **Figure 4A** shows MOF UV-11 experimental results. Meanwhile, **Figure 4B** corresponds to the theoretical diffractogram collected from the Cambridge Crystallographic Data Center (CCDC).

According to XRD analysis, it was found that it is in agreement to the experimental diffractogram (**Figure 4A**), with the theoretical diffractogram (**Figure 4B**), respect to 2θ at: 11.51°, 14.91°, 18.15°, 18.80°, 22.87°, 24.86° and 31.58°. Likewise, Herrera et al. in 2018, reported the theoretical diffractogram (**Figure 4B**), obtaining the same angles reported here. On the other hand, it is possible to corroborate the peaks absence of cobalt nitrate hexahydrate, used as a precursor, according to the PDF-25-1219 card (Glaspell et al., 2007).

Voltammetry Characterization

Figure 5 shows the cyclic voltammetry comparison of the Carbon Paste Electrode (CPE), that works as a control of the electrochemical response in the absence of the MOF, and the modified carbon paste electrode with MOF UV-11 (MCPE, solid line), with a potential range from −0.4 to 1.2 V at a scan rate of 25 mVs^{-1} and starting in an anodic direction. The inset box shows the redox process expansion that occurs in the range of 0.2–1.1 V.

It is observed that CPE response presents an oxidation process with a higher potential of 0.8 V, which is attributed to the oxygen evolution process. By reversing the scan potential direction, a shoulder is observed at −0.1 V and, subsequently, a reduction process, associated with hydrogen adsorption and evolution, respectively.

On the other hand, the MCPE response shows an oxidation peak (I_{OX}) with 0.730 V of potential, attributable to the oxidation of the acid organic linking 1,2,4,5-benzenetetracarboxylic present in MOF UV-11, which matches the oxidation potential range reported in the literature (Talbi et al., 2001) which describes the different modifications in the carboxylic groups induced by electrochemical oxidation, continuing with the potential scan in the anodic-direction process corresponding to the oxygen evolution. Reversing the potential scan to cathodic direction a peak reduction (I_{RED}) in 0.670 V can be seen, which is attributed to the carbonyl group reduction of the organic ligand present in the structure of the MOF ($RCOO^- \leftrightarrow RCOO^{\bullet}$).

In addition, it is important to mention that due to the evaluated potential range, it is not possible to observe the corresponding redox processes of the 1,2-di-(4-piridil) ligand, as these are presented at high reduction potential values (Peroff et al., 2016). This functional group is only an electrical conductor that allows the conduction between the carboxylic and metallic centre groups.

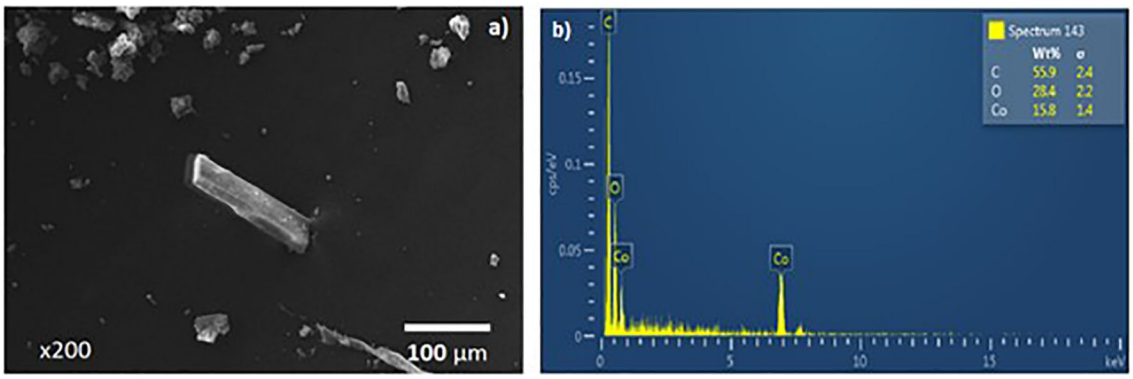

FIGURE 3 | MOF micrograph **(a)** and dispersed electron spectrum **(b)**.

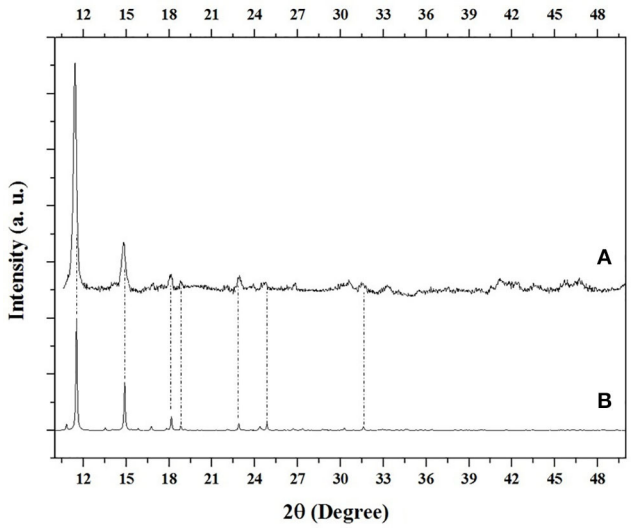

FIGURE 4 | MOF theoretical diffraction comparison **(A)** experimental and **(B)** theoretical.

Likewise, the associated processes with oxidation and reduction of Co^{2+} and Co^{3+} are not observed. According to Matheus et al., oxidation is present in a range from 0 to 0.5 V, with a reduction of 0.12 V (Matheus et al., 2008), which is due to the coordination that cobalt presents with the ligands. However, the coordination orbitals of Cobalt allow the storage of the charge received by the carbonyl group. The electron can be stored and subsequently released, by oxidation and reduction of the metal centre that is bound to the ligands.

From results of MCPE it is possible to obtain the corresponding voltammogram through the difference of oxidation peaks (I_{OX}) and a reduction (I_{RED}) ($\Delta E = E_C - E_A$) with a value of 0.030 V and the analysis using the Nernst equation indicates two electrons with a standard potential reduction of 0.775 V, for the ligand reduction process.

Figure 6 shows the cyclic voltammetry comparison at a scanning rate of 25 mVs^{-1} and with different inversion potentials with 50 mV intervals between each and using an electroactive range between 0.350 and 1.2 V.

The results of the investment potential study (**Figure 6**) indicate that the redox processes correspond to the same chemical species, since both the anodic and cathodic peaks depend on the inversion potential value (see insert), with a correlation coefficient of 0.918. It is important pointing out that voltammetry studies show the stability of the MOF in the modified electrode under the potential conditions evaluated because they show reproducibility and repeatability of the redox process.

Figure 7 shows the comparison of cyclic voltammetry at different scan rates (25, 50, and 100 mVs^{-1}) using the Modified Carbon Paste Electrode (MCPE), in a potential range from −0.4 to 1.2 V, starting the scan towards anodic direction. It is noticed that there is no significant difference in the anodic capacitive charge when changing the scan rate in the potential range of 0.2–0.7 V and it is also noticeable that the potential of the oxidation peak (I_{OX}) begins to happen at the same value. This is because the electroactive species is on the surface of the electrode. It is observed that increasing the scan rate increases the current value of the oxidation (I_{OX}) and reduction (I_{RED}) peaks. This can be described using the Laviron model (Equation 1), which shows the dependence of potential and current peaks at the scanning rate for processes occurring in confined spaces within an electrode (Thomas et al., 2015).

To obtain the values of the electrochemical parameters the parameterisation of Equation (1) is considered, and broken down in Equation (2); furthermore, each parameter is expressed in Ec. 3–5. Ec. 6 shows the dependence of the current on the scanning rate in terms of the average superficial reaction of the electrode ip. The extension of **Figure 7** shows the linear dependence on the value of the anodic peak (I_{OX}) and the cathode ($I_{RED)}$ potential value to the scan rate logarithm. The function describes that the behavior of the anodic peak potential is Ep = 0.663–0.033 V (5.411 + log v), with a linear correlation of 0.9643 of the data. Meanwhile, for the potential of the cathode peak at Ep = 0.830–0.0498 V (6.54 × 10^{-6} + log v), there is a linear correlation of 0.9999,

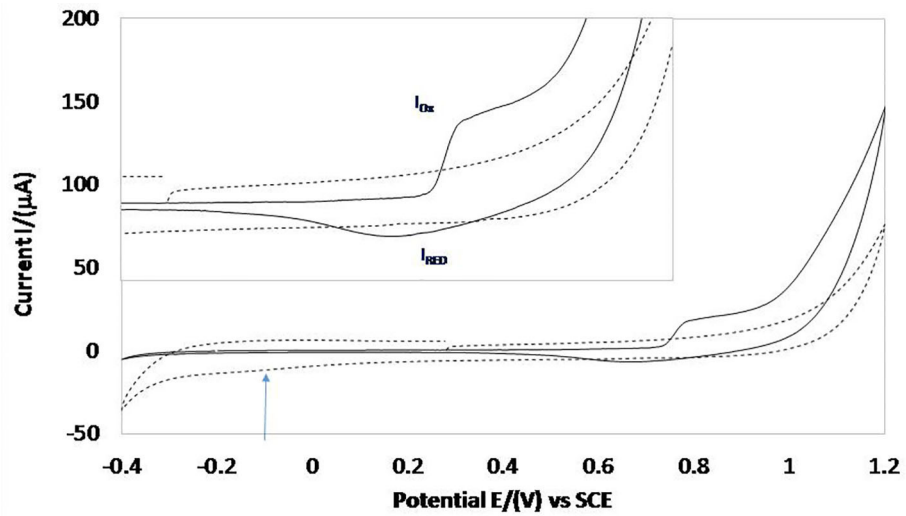

FIGURE 5 | Cyclic voltammetry comparison of MCPE electrode (solid line) and CPE (discontinued line) at a scan rate of 25 mVs^{-1}.

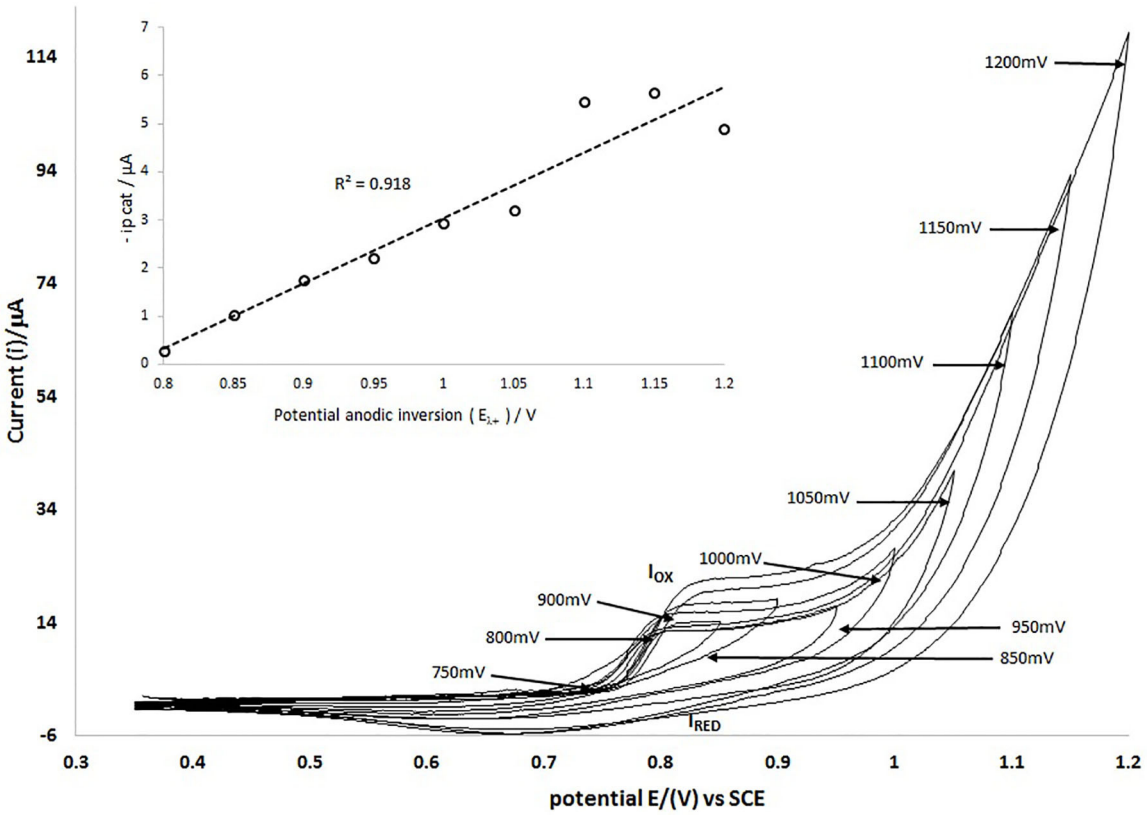

FIGURE 6 | Cyclic voltammetry of MCPE with different positive inversion potentials ($E_{\lambda+}$) in an electroactive range of 350–1200 mV, evaluating every 50 mV, at a scan rate of 25 mVs^{-1}.

which may indicate that there are diffusion mechanisms in the electrode.

With the parameters obtained by the iteration adjustment using the Levenberg–Marquardt algorithm, the thermodynamic and kinetic values of the redox processes described are obtained, as shown in **Table 1**. With an anodic peak potential (E_{pa}) of 0.624 V and a cathodic peak (E_{PC}) of 0.662 V, there exists a standard redox potential of 0.787 V. This indicates that there

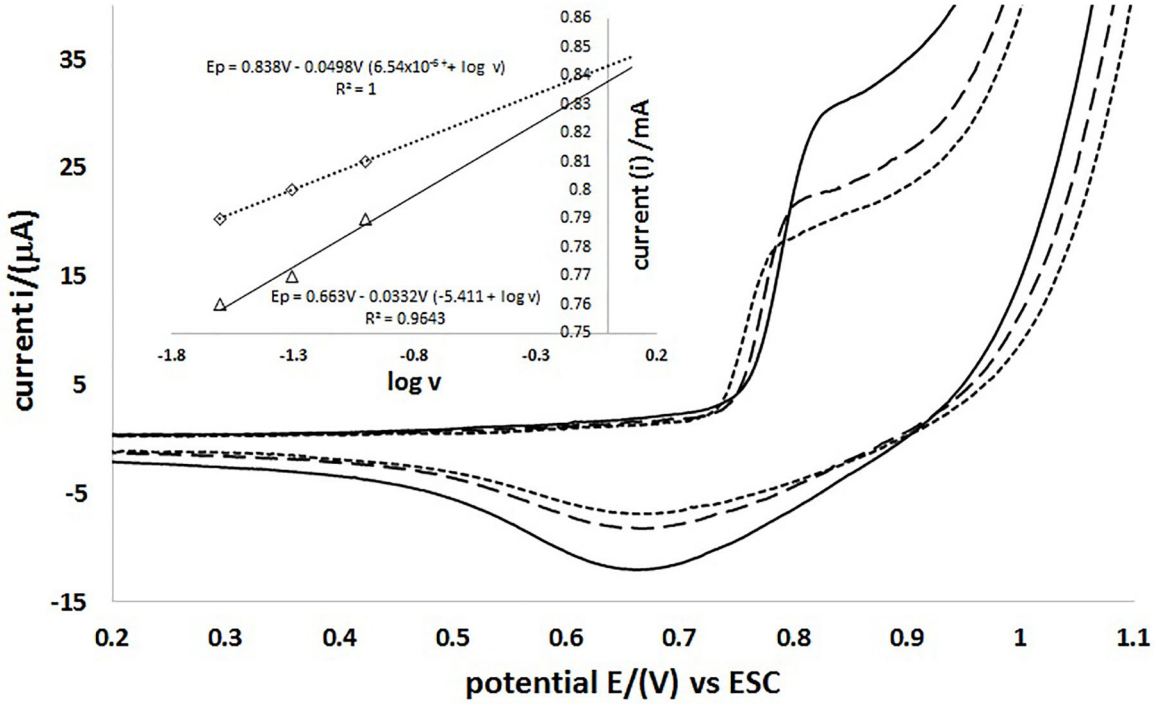

FIGURE 7 | MCPE cyclic voltammetry at different scanning rates vs. SCE 100 mVs^{-1} (—), 50 mVs^{-1} (- - -) and 25 mVs^{-1} (· · ·). The insert shows the current dependency to the logarithm of scan rate.

is a semi-reversible process, since there is a potential difference (ΔE) between the anodic peak and the 0.027 V cathode and the coefficient of the current is 2.706. The standard velocity constant of the reaction surface (ks) obtained was 0.4978 and 0.275 s^{-1} for the anodic and cathodic processes, respectively; with values of the electronic transfer coefficient (α) of the anodic and cathodic processes being 0.47 and 0.79, respectively. The average surface concentration of the electrode reaction was also calculated, constituting 1.012×10^{-7} mol*cm^{-2}, which describes the average of the slope of the maximum peak current vs. the scan rate.

Therefore, the described processes do not depend on the linear diffusion of the electrolyte to the electrode, but the electroactive species is on the electrode and the process is governed by the rapid transfer species into the same electrode, considering that the higher scanning rate presents a transfer increase of two to three electrons.

On the other hand, the results shown in the voltammetric study indicate the capacitive and resistive behavior on the surface of the modified electrode. It is possible to observe that the current of the capacitive process of the MCPE is lower than that obtained with the CPE. Likewise, the current associated with the hydrogen evolution process in the MCPE is attributable to the electrode conductivity increased and decrease the resistance due to the MOF presence.

Figure 8 shows the comparison of the specific areal capacitance responses of MCPE electrode (solid line) and CPE (discontinued line) to the change of the scan rate (**Figure 8A**). **Figure 8B** shows the Ragone plot of the electrochemical performance. The electrochemical performance of the MCPE using voltammetry data, (a) response of the specific areal Capacitance vs. Scan rate and (b) the Ragone plot of the electrochemical performance.

The specific areal capacitance of the MCPE it is lower than the CPE, and both show a diminution of capacitance while the scan rate is increasing. So, its capacitance is lower while increasing the speed of electronic transfer; which favors faradaic processes that can be associated with the electrons in the coordinated orbitals of the metal and pyridyl)-ethylene ligand. These results of CPE are similar with those found for the capacitance and power density on graphite sheet (Mandal et al., 2019). Likewise, their electrodes modified with metal oxides have a capacitance and power density higher than MCPE (Mijangos et al., 2017). The order of energy and power implies that MPCE is an electrochemical microsupercapacitor, which are material useful to miniaturized energy storage systems, like the graphene-based electrochemical microsupercapacitors. These values of energy and power are due to the abundance of active and accessible sites in the interface (Yang and Lu, 2016).

Figure 9 shows the cyclic voltammogram repeating the potential scan program 20 times (cycles 1, 5, 10, 15, and 20 are shown). It is observed that the peak current is increased logarithmically according to the number of cycles, with a coefficient correlation of 0.9865 and 0.9964 for anodic and cathodic peaks, respectively. However, from the last three cycles, significant changes are not observed; which may be attributable to MOF crystalline framework activation over the electrode and

TABLE 1 | Thermodynamic values and modeled kinetic parameters using Laviron equation adjustment.

	E/V=	E°/V=	ΔE	k_s / s^{-1}	α	i_C/i_A	Γ/mol cm^{-2}
Anodic	0.624	0.787	0.027	0.4978	0.47	2.706	1.012E-07
Cathodic	0.662			0.2754	0.79		

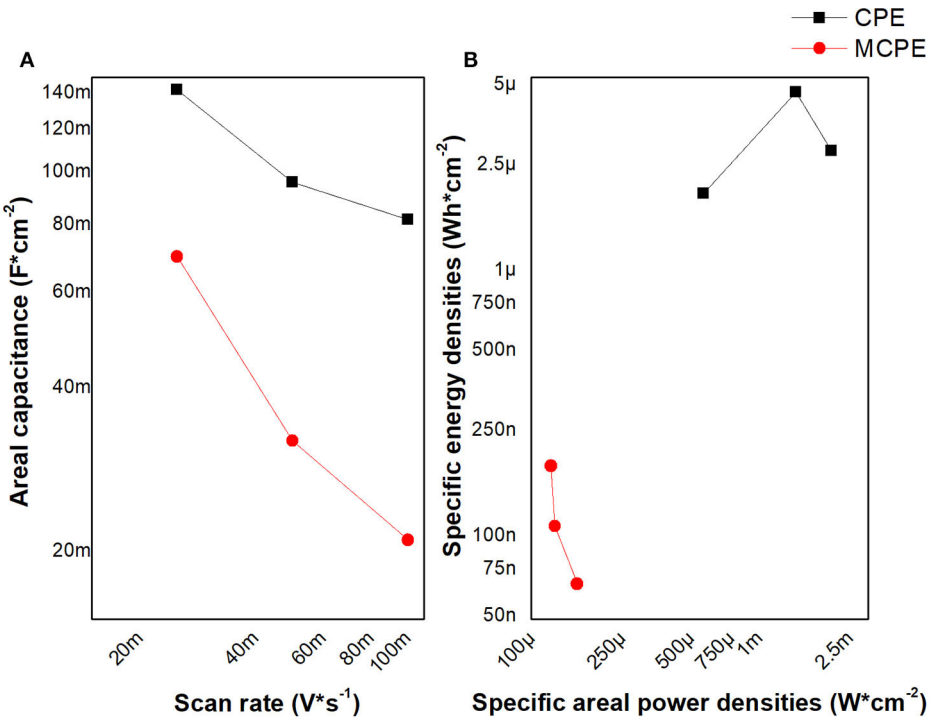

FIGURE 8 | The electrochemical performance of the MCPE using voltammetry data, **(A)** response of the specific areal Capacitance vs. Scan rate and **(B)** the Ragone plot of the electrochemical performance.

could be associated with improved conductivity and decreased interface capacitance of the electrode on its surface.

In the **Figure 9** it is observed that the peak current is increased logarithmically according to the number of cycles, with a coefficient correlation of 0.9865 and 0.9964 for anodic and cathodic peaks respectively. However, from the last three cycles, significant changes are not observed, which may be attributable to MOF crystalline framework activation over the electrode and could be associated with improved conductivity and decreased interface capacitance of the surface electrode. Likewise, when the program of the voltammetry scanning potential is repeated, the signals are shown in the same potential like the first cycle and do not disappear. In the same way, the current signals grow indicating that the MOF in the modified electrode continues transfer the charge and the redox process.

CONCLUSIONS

The porous coordination polymer obtained using a solvothermal method with a cobalt metal centre (MOF UV-11) presents a melting point in an interval of 292–293°C, which is greater than that of its precursors. Pink crystals (~173 µm in length and 40 µm in width) with a laminar morphology demonstrated the presence of elements such as cobalt, carbon and oxygen. The XRD analysis corroborated the existence of cobalt phase peaks (PDF-00-054-2464) as cobalt bis (pyridine-6-carboxylic-2-carboxylate) supporting the obtaining of MOF UV-11, whose evaluation has not been reported in the literature.

Electrochemical techniques show that MOF UV-11 presents an oxidation peak with a potential of 0.73 V and a reduction peak at 0.67 V, resulting in a semi-reversible process between oxidation and reduction peaks. The voltammetric study at different scanning rates allowed determining thermodynamic values such as the average anodic peak potential at 0.624 V and the cathodic peak at 0.662 V, presenting a formal potential of 0.787 V. There is a difference of potential between the anodic and cathodic peaks of 0.0276 V and the coefficient of the current is 2.706, as well as the kinetic values of the standard speed constant of the anodic process reaction surface of 0.4978 s^{-1} and the cathodic process at 0.275 s^{-1}. The electronic transfer coefficient for the anodic and cathodic processes constituted 0.47 and 0.79 values, respectively, and the average concentration surface reaction of the electrode 1.012 × 10-7 mol*cm^{-2}. These parameters allowed establishing that the process was governed by the electronic transfer of

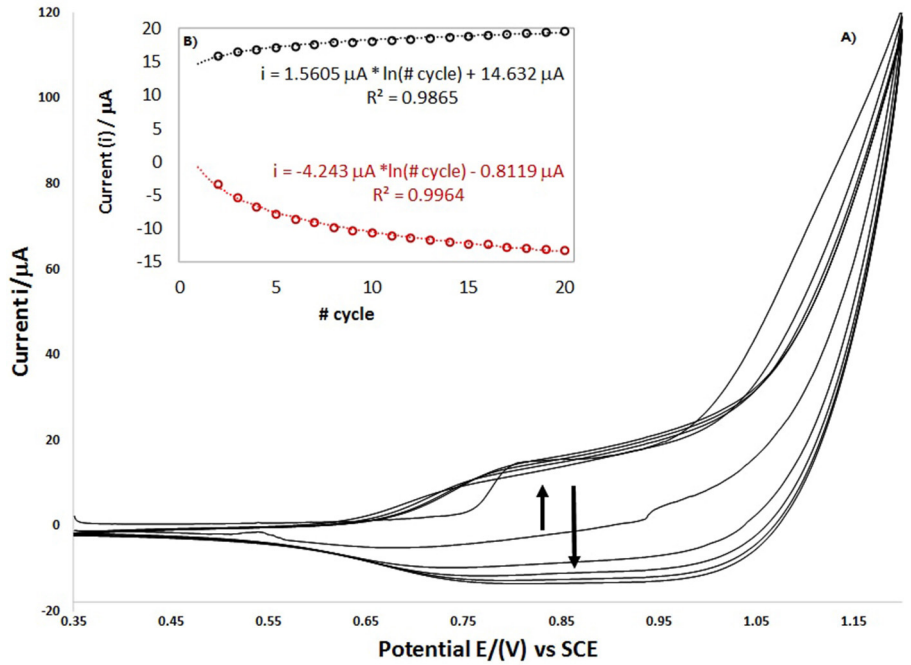

FIGURE 9 | The electrochemical performance of the MCPE using voltammetry data, **(A)** response of the specific areal Capacitance vs. Scan rate and **(B)** the Ragone plot of the electrochemical performance.

two electrons and the possible electrochemical activation of the MOF structure within the electrode after several voltammetric cycles. The electrochemical performance of the MCPE showed energy and power of an electrochemical micro supercapacitor, useful to miniaturized energy storage systems with a specific areal Capacitance of 40 $mFcm^{-2}$ and a specific areal Energy density of 100 $nWh*cm^{-2}$ with a specific areal power density of 120 $\mu W*cm^{-2}$.

DATA AVAILABILITY STATEMENT

All datasets presented in this study are included in the article.

AUTHOR CONTRIBUTIONS

IM-P carried out the organic characterization and synthesis of the materials, as well as the writing of the manuscript. AM-T carried out the organic synthesis and purification of the MOF. MV performed the experimental design and electrochemical tests. VR-C conducted the discussion of the results of the electrochemical characterization. MP-L performed the review and discussion of the results of the characterization by XRD and microscopy. GU-R carried out the design for the preparation of modified electrodes with MOFs. JR-V reviewed and discussed results on MOF synthesis and material characterization. JC-M coordinated the experimental work, discussion of results and writing of the manuscript. All authors contributed to the article and approved the submitted version.

FUNDING

This work was supported with a scholarship by CONACyT (grant 605132) and financed by PRODEP (511-6/19-8268).

ACKNOWLEDGMENTS

The author IM-P is thankful to CONACYT for the scholarship. JC-M is thankful to PRODEP for financing.

REFERENCES

Alfonso-Herrera, L. A., Huerta-Flores, A. M., Torres-Martínez, L. M., Rivera-Villanueva, J. M., and Ramírez-Herrera, D. J. (2018). Hybrid SrZrO3-MOF heterostructure: surface assembly and photocatalytic performance for hydrogen evolution and degradation of indigo carmine dye. *J. Mater. Sci. Mater. Electron.* 29, 10395–10410. doi: 10.1007/s10854-018-9096-y

Allendorf, M. D., Bauer, C. A., Bhakta, R. K., and Houk, R. J. T. (2009). Luminescent metal-organic frameworks. *Chem. Soc. Rev.* 38, 1330–1352. doi: 10.1039/b802352m

Betteridge, W. (1980). The properties of metallic cobalt. *Prog. Mater. Sci.* 24, 51–142. doi: 10.1016/0079-6425(79)90004-5

Bux, H., Chmelik, C., Van Baten, J. M., Krishna, R., and Caro, J. (2010). Novel MOF-membrane for molecular sieving predicted by IR-diffusion studies and molecular modeling. *Adv. Mater.* 22, 4741–4743. doi: 10.1002/adma.201002066

Drobek, M., Kim, J. H., Bechelany, M., Vallicari, C., Julbe, A., and Kim, S. S. (2016). MOF-based membrane encapsulated ZnO nanowires for enhanced gas sensor selectivity. *ACS Appl. Mater. Interfaces* 8, 8323–8328. doi: 10.1021/acsami.5b12062

Farha, O. K., and Hupp, J. T. (2010). Rational design, synthesis, purification, and activation of metal-organic framework materials. *Acc. Chem. Res*. 43, 1166–1175. doi: 10.1021/ar1000617

Glaspell, G. P., Jagodzinski, P. W., and Manivannan, A. (2007). Formation of cobalt nitrate hydrate, cobalt oxide, and cobalt nanoparticles using laser vaporization controlled condensation. *J. Phys. Chem. B* 108, 9604–9607. doi: 10.1021/jp0370831

Howarth, A. J., Liu, Y., Li, P., Li, Z., Wang, T. C., Hupp, J. T., et al. (2016). Chemical, thermal and mechanical stabilities of metal-organic frameworks. *Nat. Rev. Mater*. 1, 1–15. doi: 10.1038/natrevmats.2015.18

Huang, K. J., Sun, J. Y., Niu, D. J., Xie, W. Z., and Wang, W. (2010). Direct electrochemistry and electrocatalysis of hemoglobin on carbon ionic liquid electrode. *Colloids Surfaces B Biointerfaces* 78, 69–74. doi: 10.1016/j.colsurfb.2010.02.014

Kalcher, K. (1990). Chemically modified carbon paste electrodes in voltammetric analysis. *Electroanalysis* 2, 419–433. doi: 10.1002/elan.1140020603

Kaur, R., Kaur, A., Umar, A., Anderson, W. A., and Kansal, S. K. (2019). Metal organic framework (MOF) porous octahedral nanocrystals of Cu-BTC: synthesis, properties and enhanced absorption properties. *Mater. Res. Bull*. 109, 124–133. doi: 10.1016/j.materresbull.2018.07.025

Klimakow, M., Klobes, P., Thünemann, A. F., Rademann, K., and Emmerling, F. (2010). Mechanochemical synthesis of metal-organic frameworks: a fast and facile approach toward quantitative yields and high specific surface areas. *Chem. Mater*. 22, 5216–5221. doi: 10.1021/cm1012119

Lee, J., Farha, O. K., Roberts, J., Scheidt, K. A., Nguyen, S. T., and Hupp, J. T. (2009). Metal-organic framework materials as catalysts. *Chem. Soc. Rev*. 38, 1450–1459. doi: 10.1039/b807080f

Li, J., Cheng, S., Zhao, Q., Long, P., and Dong, J. (2009). Synthesis and hydrogen-storage behavior of metal-organic framework MOF-5. *Int. J. Hydrogen Energy* 34, 1377–1382. doi: 10.1016/j.ijhydene.2008.11.048

Li, Y., and Yang, R. T. (2007). Gas adsorption and storage in metal-organic framework MOF-177. *Langmuir* 23, 12937–12944. doi: 10.1021/la702466d

Ma, J., Guo, X., Ying, Y., Liu, D., and Zhong, C. (2017). Composite ultrafiltration membrane tailored by MOF@GO with highly improved water purification performance. *Chem. Eng. J*. 313, 890–898. doi: 10.1016/j.cej.2016.10.127

Mandal, D., Routh, P., Mahatoa, A. K., and Nandi, A. K. (2019). Electrochemically modified graphite paper as an advanced electrode substrate for supercapacitor application. *J. Mater. Chem. A*. 7, 17547–17560. doi: 10.1039/C9TA04496E

Matheus, P. R., Abad, J. M., Fernández, L., Velandria, O. M., and Fernández, V. M. (2008). Influencia del estado de oxidación del ión cobalto en la estabilidad de electrodos modificados con monocapas SAM-TOA-ANTA-Con+-HRP-NHis. Av. *En Química* 3, 69–77. Available online at: https://www.redalyc.org/articulo.oa?id=93330205

Mijangos, E., Roy, S., Pullen, S., Lomoth, R., and Ott, S. (2017). Evaluation of two- and three-dimensional electrode platforms for the electrochemical characterization of organometallic catalysts incorporated in non-conducting metal-organic frameworks. *Dalt. Trans*. 46, 4907–4911. doi: 10.1039/C7DT00578D

Mondloch, J. E., Karagiaridi, O., Farha, O. K., and Hupp, J. T. (2013). Activation of metal-organic framework materials. *Cryst. Eng. Comm*. 15, 9258–9264. doi: 10.1039/c3ce41232f

Mulyati, T. A., Ediati, R., and Rosyidah, A. (2015). Influence of solvothermal temperatures and times on crystallinity and morphology of MOF-5. *Indones. J. Chem* 2, 101–107. doi: 10.22146/ijc.21202

Orellana-Tavra, C., Mercado, S. A., and Fairen-Jimenez, D. (2016). Endocytosis mechanism of nano metal-organic frameworks for drug delivery. *Adv. Healthc. Mater*. 5, 2261–2270. doi: 10.1002/adhm.201600296

Peroff, A. G., Weitz, E., and Van Duyne, R. P. (2016). Mechanistic studies of pyridinium electrochemistry: alternative chemical pathways in the presence of CO_2. *Phys. Chem. Chem. Phys*. 18, 1578–1586. doi: 10.1039/C5CP04757A

Shen, K., Chen, X., Chen, J., and Li, Y. (2016). Development of MOF-derived carbon-based nanomaterials for efficient catalysis. *ACS Catal*. 6, 5887–5903. doi: 10.1021/acscatal.6b01222

Son, W. J., Kim, J., Kim, J., and Ahn, W. S. (2008). Sonochemical synthesis of MOF-5. *Chem. Commun*. 6336–6338. doi: 10.1039/b814740j

Talbi, H., Billaud, D., Louarn, G., and Pron, A. (2001). *In-situ* spectroscopic investigations of the redox behavior of poly(indole-5-carboxylic-acid) modified electrodes in acidic aqueous solutions. *Spectrochim. Acta Part A Mol. Biomol. Spectrosc*. 57, 423–433. doi: 10.1016/S1386-1425(00)00356-5

Taylor, P., Švancara, I., Vyt, K., and Svancara, I. (2010). Critical reviews in analytical chemistry carbon paste electrodes in modern electroanalysis electroanalysis. *Crit. Rev. Anal. Chem*. 31, 37–41. doi: 10.1080/10408341076785

Thomas, D., Rasheed, Z., Jagan, J. S., and Kumar, K. G. (2015). Study of kinetic parameters and development of a voltammetric sensor for the determination of butylated hydroxyanisole (BHA) in oil samples. *J. Food Sci. Technol*. 52, 6719–6726. doi: 10.1007/s13197-015-1796-1

Tian, Y., Cong, J., Shen, S., Chai, Y., Yan, L., Wang, S., et al. (2014). Electric control of magnetism in a multiferroic metal-organic framework. *Phys. Status Solidi Rapid Res. Lett*. 8, 91–94. doi: 10.1002/pssr.201308230

Topologies, M. O. F., Stock, N., and Biswas, S. (2012). Synthesis of metal-organic frameworks (MOFs): routes to various MOF topologies, morphologies, and composites. *Chem. Rev*. 2012, 112, 933–969. doi: 10.1021/cr200304e

Van Assche, T. R. C., Desmet, G., Ameloot, R., De Vos, D. E., Terryn, H., and Denayer, J. F. M. (2012). Electrochemical synthesis of thin HKUST-1 layers on copper mesh. *Microporous Mesoporous Mater*. 158, 209–213. doi: 10.1016/j.micromeso.2012.03.029

Vogel, N. (2012). *Surface Patterning with Colloidal Monolayers*. Springer Science & Business Media.

Wang, Y. L., Yuan, D. Q., Bi, W. H., Li, X., Li, X. J., Li, F., et al. (2005). Syntheses and characterizations of two 3D cobalt-organic frameworks from 2D honeycomb building blocks. *Cryst. Growth Des*. 5, 1849–1855. doi: 10.1021/cg0501128

Wang, Z. (2006). *Design of Metal-Organic Framework Materials Based upon Inorganic Clusters and Polycarboxylates* Graduate Theses and Dissertations. Available online at: https://scholarcommons.usf.edu/etd/2747

Xia, W. (2011). *Fabrication of Metal-Organic Framework Derived Nanomaterials and Their Electrochemical Applications*. Springer Nature Singapore Pte Ltd. doi: 10.1007/978-981-10-6811-9

Yang, C., Schellhammer, K. S., Ortmann, F., Sun, S., Dong, R., Karakus, M., et al. (2017). Coordination polymer framework-based on-chip microsupercapacitors with AC line-filtering performance. *Angew. Chem. Int*. 56, 1–6. doi: 10.1002/anie.201700679

Yang, H., and Lu, W. (2016). "Graphene-based electrochemical microsupercapacitors for miniaturized energy storage applications," in *Nanomaterials for Sustainable Energy*, ed Q. Li (Cham: NanoScience and Technology. Springer), 271–291. doi: 10.1007/978-3-319-32023-6_8

Zdravkov, B. D., Cermák, J. J., Šefara, M., and Janku, J. (2007). Pore classification in the characterization of porous materials: a perspective. *Cent. Eur. J. Chem*. 5, 385–395. doi: 10.2478/s11532-007-0017-9

Zhou, H.-C., Long, J. R., and Yaghi, O. M. (2012). Introduction to metal–organic frameworks. *Chem. Rev*. 112, 673–674. doi: 10.1021/cr300014x

Conflict of Interest: The authors declare that the research was conducted in the absence of any commercial or financial relationships that could be construed as a potential conflict of interest.

frontiers in Chemistry

ORIGINAL RESEARCH
published: 28 August 2020
doi: 10.3389/fchem.2020.00643

Preparation of a Sensor Based on Biomass Porous Carbon/Covalent-Organic Frame Composites for Pesticide Residues Detection

Yali Liu[1†], *Mingyue Zhou*[1†], *Chen Jin*[1], *Jinxiang Zeng*[1], *Chao Huang*[1], *Qiuye Song*[2] *and Yonggui Song*[1*]

[1] *Laboratory Animal Science and Technology Center, College of Science and Technology, Jiangxi University of Traditional Chinese Medicine, Nanchang, China,* [2] *Pharmacy Department of Zhangjiagang, First People's Hospital, Suzhou, China*

In this work, a covalent-organic framework with high carbon and nitrogen content microstructures (named COF-LZU1), assisted by 3D nitrogen-containing kenaf stem composites (represented as COF-LZU1/3D-KSCs), was constructed. Moreover, it was utilized for immobilizing acetylcholinesterase (AChE) for identifying trichlorfon, a commonly applied organophosphorus (OP) pesticide. The development of COF-LZU1/3D-KSC was affirmed by SEM, PXRD, and EDXS. The findings confirmed that COF-LZU1 microstructures were uniformly developed on 3D-KSC holes using a one-step synthesis approach, which can substantially enhance the effective surface area. Also, the COF-LZU1/3D-KSC composite contains not only the nitrogen element in COF-LZU1 but also the nitrogen element in 3D-KSC, which will greatly improve the biocompatibility of the material. The AChE/COF-LZU1/3D-KSC integrated electrode was fabricated by directly fixing a large amount of AChE on the composite. At the same time, the integrated electrode had good detection efficiency for trichlorfon. Improved stabilization, a wide-linear-range (0.2–19 ng/mL), and a lower detection limit (0.067 ng/mL) have been displayed by the sensor. Therefore, this sensor can be used as an important platform for the on-site detection of OP residue.

Keywords: sensor, AChE, integrated electrode, biomass carbon materials, detecting

OPEN ACCESS

Edited by:
Daojun Zhang,
Anyang Normal University, China

Reviewed by:
Jiahuan Luo,
Anyang Institute of Technology, China
Wenbo Lu,
Shanxi Normal University, China

***Correspondence:**
Yonggui Song
songyonggui1999@163.com

†These authors have contributed equally to this work

Specialty section:
This article was submitted to Supramolecular Chemistry, a section of the journal Frontiers in Chemistry

Received: *07 May 2020*
Accepted: *22 June 2020*
Published: *28 August 2020*

Citation:
Liu Y, Zhou M, Jin C, Zeng J, Huang C, Song Q and Song Y (2020) Preparation of a Sensor Based on Biomass Porous Carbon/Covalent-Organic Frame Composites for Pesticide Residues Detection. Front. Chem. 8:643. doi: 10.3389/fchem.2020.00643

INTRODUCTION

Organophosphorus pesticides (OPs), such as Trichlorfon, have been thoroughly used in agriculture due to their powerful insecticidal ability (Ma et al., 2018). However, due to its inhibition of acetylcholinesterase (AChE), the key enzyme of nerve conduction (Baldissera et al., 2019), it also poses a major threat to overall health (Soreq and Seidman, 2001; Shi et al., 2016b). Consequently, quick and sensitive probes of OPs in food production have turned out to be of considerable importance. Conventional analytical techniques, like HPLC and gas chromatography, mostly combined with mass-selective detectors (Liu et al., 2017; Song et al., 2019a), are slow and costly. These approaches are still carried out in laboratories (Shi et al., 2016a; Liu et al., 2017; Su et al., 2018) butthey are not appropriate for quick field detection (Su et al., 2014; Song et al., 2019b). Therefore, the fabrication of rapid and sensitive OPs

detection strategies with fewer limitations are increasingly desired by the food industry and for environmental monitoring.

An electrochemical AChE biosensor has the potential to replace traditional methods due to its higher sensitivity, fast response, and tiny volume (Zeng et al., 2019). According to the inhibition of OPS on AChE, even smaller concentrations of pesticide can be determined accurately. The sensitiveness and limit of detection of such biosensors is dependent on the amount of enzyme (Zhang et al., 2019), so enzyme immobilization on the electrode surface is a key step for biosensor activity.

In order to firmly immobilize the enzyme, many smart materials, such as carbon nanotubes (Sotiropoulou and Chaniotakis, 2005) and gold nanoparticles, were employed to fabricate an enzyme-entrapped matrix (Wang et al., 2003; Shi et al., 2019). The incorporation of enzymes in new nanomaterials effectively increased the stability, sensibility, and detection threshold of enzymatic biosensors. Nevertheless, several proteases will stack on the surface of these nanomaterials, which will affect the transmission of electrons and reduce the performance of sensors (Khalilzadeh et al., 2016). Therefore, it is very important to discover an electrode material that can modify a large number of proteases without the stacking effect while maintaining good biocompatibility. Carbon biomass materials have good electrical conductivity and biocompatibility and are very suitable for the preparation of electrode materials for enzyme biosensors (Song et al., 2015; Khalilzadeh et al., 2016; Su et al., 2020). However, due to the large pore size of the biomass carbon material, the transmission of electrons will be affected. Therefore, for bioelectrochemical enzyme sensors, it is crucial to modify micro-materials with good conductivity and biocompatibility in the holes.

In this study, metal-free frame microstructures utilizing a covalent organic framework (named COF-LZU1) through the (3D N-containing kenaf stem) composites were formed using a one-step method. The COF-LZU1s may spread over the pores of 3D-KSC, and also had good biocompatibility because they contain no metal elements and only carbon, nitrogen, and oxygen elements. The COF-LZU1sshowed pitted surfaces, which, when superimposed with the 3D porous structure of KSC, can be employed to entrap more AChE molecules. Furthermore, AChE molecules were added in the COF-LZU1s by using pits of COFs, that efficiently prevented the agglomeration of enzymes at the electrode surface. Moreover, COF-LZU1s material also has good conductivity (Liu et al., 2016; Song et al., 2016a), which can improve the proton transportability of the whole integrated electrode. Thus, the developed trichlorfon sensor based upon the AChE/COF-LZU1/3D-KSC composites showed a wide-range linearity, lower detection limitations, and good stability.

EXPERIMENTAL SECTION

Materials and Reagents

The kenaf stems (KS) were collected from the Futian farm in Ji'an, Jiangxi Province. Graphite powder (99.95% and 325 mesh) and paraffin were acquired from Aladdin. DMFc, 1,3,5-triformylbenzene, acetylthiocholine chloride (ATCl), 1,4-diaminobenzene, and Acetylcholinesterase (1,000 U/mg), were obtained from Sigma-Aldrich (USA). Trichlorfon was bought from Kanghe Yinong Biotechnology Co., Ltd. Other reagents utilized were of analytical grades and procured from Shanghai Guoyao Group Chemical Reagent (China). Distilled water (18.2 MΩ cm) was employed for making all the solutions and purged by nitrogen prior to experiments. PBS was freshly made using dihydrogen phosphate and sodium disodium hydrogen phosphate.

Instruments

Cyclic voltammetry (CVS) and differential pulse voltammetry (DPVS) were carried out on the CHI660E electrochemical analyzer. A three-electrodes system with a platinum wire (auxiliary electrode), a saturated calomel electrode (SCE) (reference electrode), and AChE/COF -LZU1/3D-KSCE was adopted as a working electrode. CVs and DPVs were carried out in 10 mL (0.2 M PBS of pH 7.0) under 25°C. SEM was done employing an XL30 ESEM-FEG SEM using accelerating voltage (20 kV) provided with a Phoenix (EDXA). The PXRD data was gathered over a (D/Max 2,500 V/PC) diffractometer via Cu Kα radiation info ($\lambda = 0.154056$ nm, 40 kV, and 200 mA).

Preparation of COF-LZU1/3D-KSCs Composite

The carbonization of dried KS synthesized the 3D-KSC in a high-heating furnace following protocol from our former project (Song et al., 2015; Khalilzadeh et al., 2016). The carbonization procedure was executed in a quartz reactor in an N_2 environment on heating (5°C min^{-1}) and annealing (2 h at 900°C). 3D-KSC was split up to a cylindrical shape, with the exterior diameter equivalent to the inner diameter of a used pipette tip. Therefore, the cylindrical 3D-KSC can be immobilized firmly in the already treated pipette tip. The prepared 3D-KSC was treated with dilute hydrochloric acid (2 M) for 24 h, and distilled water (24 h) to eliminate the inorganic contaminants, and afterwards was cleaned with ethanol and purified water successively, dried out normally, and placed in a beaker. Subsequently, 1,3,5-Triformylbenzene (0.30 mmol) and 1,4-dia-minobenzene (0.45 mmol) were measured and solubilized in 3 mL of 1,4-dioxane. After that 3D-KSCs were immersed in the solution, shifted in a glass vial (volume 20 mL), and then 0.6 mL of 3 mol L^{-1} dilute acetic acid was added to the mixture. The glass vial was flash-frozen in liquified nitrogen, subjected to a 19 mbar of internal pressure and flame-sealed, decreasing 10 cm in length. After attaining 25°C, the suspension was kept inside an oven uninterrupted for 3 days at 120°C, resulting in a yellow solid forming across the tube. The modified 3D-KSCs which were obtained after centrifugation were washed with N, N-dimethylformamide (3 × 10 mL) and tetrahydrofuran (3 × 10 mL), and then dried at 80°C in a vacuum for (2 h to produce COF-LZU1, a yellow-colored powder (90% yield), and produce the COF-LZU1-modified 3D-KSCs (COF-LZU1/3D-KSCs). Following our previous work,[14,15] 3D-KSC were developed by carbonizing dried KS in a higher heating system. The procedure is explained as follows: in a tubular quartz reactor, carbonization is conducted at a rate of 5°C min^{-1} in an N_2 atmosphere, and annealing is carried out

at 900°C for 2 h. The 3D-KSC is made into a cylinder such that the outer diameter corresponds to the inner diameter of a processed pipette tip so that the cylindrical 3d-ksc can be firmly fixed on the treated pipette tip. After treatment, the 3D-KSCs were treated with diluted hydrochloric acid (2 M) and distilled water for 24 h to eliminate inorganic impurities, and after that were washed alternately with ethanol and ultrapure water, then dried and placed in a beaker. Then, 1,3,5-trimethyl benzene (0.30 mmol) and 1,4-diaminobenzene (0.45 mmol) were put in vials and dissolved within 3 mL 1,4-dioxane. Then 3D-KSCs was immersed in the solution, the mixture transferred to a glass ampoule (vol 20 ml), and 0.6 ml of 3.0 mol L^{-1} water acetic acid was added to the mixture. The glass ampoules were quickly frozen in a liquified nitrogen bath, vacuumed to 19 mbar interior pressure, and flame-sealed to reduce the entire length by 10 cm. After the suspension was heated to room temperature, it was put in an oven at 120°C for 3 d. The yellow solid was generated along the test tube. The modified 3D-KSCs were separated by centrifugation, and afterwards washed with N, N-dimethylformamide (3 × 10 mL) and tetrahydrofuran (3 × 10 mL). After vacuum drying at (80°C) for 12 h, the yellow powder COF -LZU1 (90% yield) was obtained. The modified 3D-KSCs of COF -LZU1 (COF -LZU1/3D-KSC s) were obtained.

Preparation of Integrated AChE/COF -LZU1/3D-KSC Electrodes

The COF-LZU1/3D-KSC were incorporated within the processed pippete tip. After that, 0.25 g liquid paraffin was mixed with 1 g powder of graphite and homogenized for 20 min in the agate mortar. Then, the mixture was packed inside the upper portion of the pipette tip to touch the base of COF-LZU1/3D-KSC. Then, a copper wire was inserted into the end of the pipette tip, and connected with the COF-LZU1/3D-KSC at the tip through graphite paste. After the paste was naturally dried at room temperature, as depicted in **Figure S1**, the copper wire was further fixed with a sealing film or epicote. The AChE/COF-LZU1/3D-KSC electrode was fabricated by dropping a 5 μL AChE solution with various concentrations upon the electrode surface, followed by dessication. The entire preparation process was illustrated by **Figure S1**, including **Scheme 1**. Lastly, the modified electrode was washed with purified water to eliminate loosely bounded materials and kept at 4°C, intended for further usage. The obtained AChE/COF-LZU1/3D-KSC electrode was denoted as AChE/COF-LZU1/3D-KSCE.

Inhibition Measurement of AChE Biosensor

The trichlorfon assay process was illustrated in detail in **Scheme 1**. Regarding inhibitory tests, the first (DPV) signal was ($I_{P,control}$) recorded in 0.1 M PBS of pH 7 alongwith 1 mM ATCl. After that, the electrode was cleaned with distilled water, then placed inside an aqueous solution having a preferred concentration of trichlorfon for about 10 min. Afterwards, residual signal ($I_{P,exp}$) was also observed in a similar state. The rate of trichlorfon inhibition was computed below:

In **Scheme 1**, the analysis process of trichlorfon was described in detail. For the inhibition test, the original (DPV) signal ($I_{P,control}$) was determined in 0.1 M PBS (pH 7) and 1 mM ATCI. The electrodes were then cleaned by water and stored within an aqueous solution having the required amount of trichlorfon for 10 min. Following an incubation period, residual signals ($I_{P,exp}$) were recorded under the same conditions. The inhibition rate of trichlorfon was estimated as below:

$$\text{Inhibition (\%)} = 100\% \times \frac{I_{P,control} - I_{P,exp}}{I_{P,control}} \quad (2.1)$$

RESULTS AND DISCUSSION

Characterization of AChE/COF-LZU1/3D-KSC Electrodes

Figures 1A–C shows the SEM images of 3D-KSC and COF-LZU1/3D-KSC composites. 3D-KSC have a 3D macroporous inner structure (**Figure 1A**) (Song et al., 2015; Shan et al., 2019). After the growth of COF-LZU1, the procured electrode surface was adequately coated with the COF-LZU1 microstructures (**Figures 1B,C**). As depicted in **Figure 1C**, the spherical COF-LZU1 microstructures size is about 150 nm (inset of **Figure 1C**). The high magnification image in **Figure 1C** shows a special bumpy morphology, which significantly enhances the surface of electrode and the mass transfer. The EDX spectrums of COF-LZU1 and COF-LZU1/3D-KSC indicate the higher pureness of the composite, containing only O, N, and C (**Figure 1D**). Simultaneously, it can be seen that not only KSC but also COF-LZU1 contain nitrogen, which may greatly increase the biocompatibility of the composites. **Figure 1F** displays the XRD pattern of COF-LZU1 and also COF-LZU1/3D-KSC, which shows a microcrystalline solid with a long-range structure. Moreover, diffraction peaks around 4.9, 8.0, 9.4, and 12.1 according to 100, 110, 200, and 210 crystal planes, in accordance with the reported literature (Song et al., 2016b). Also, the XRD diffraction pattern of COF-LZU1/3D-KSC coincides with that of COF-LZU1, which indicates that COF-LZU1/3D-KSC has the same crystal structure as that of a single COF-LZU1 material. When AChE molecules were collected on the COF-LZU1/3D-KSC electrode, the interior wall of pores in the COF-LZU1/3D-KSC electrode became rough and irregular, comprising of an opaque film of a fuzzy-like material which might have resulted from the adsorption of AChE molecules at the inner side of pores (**Figure 1E**). Furthermore, the structure of AChE molecules could be damaged whenever an electron beam pierced the protein, and consequently, the pore surfaces of the COF-LZU1/3D-KSC composite became fuzzy. The findings clearly established the effective immobilization of AChE molecules on the COF-LZU1/3D-KSC electrode.

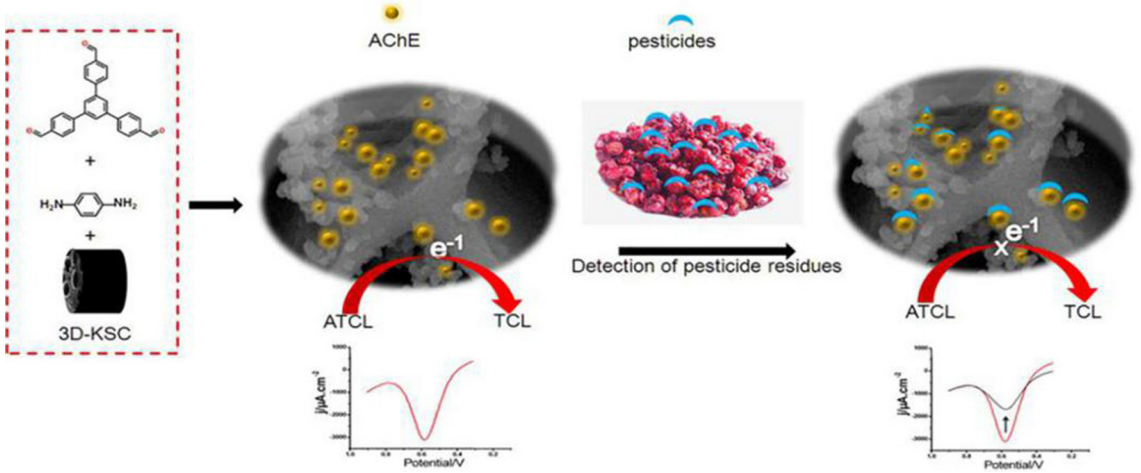

SCHEME 1 | Schematic of the AChE/COF-LZU1/3D-KSC electrochemical pesticides biosensor.

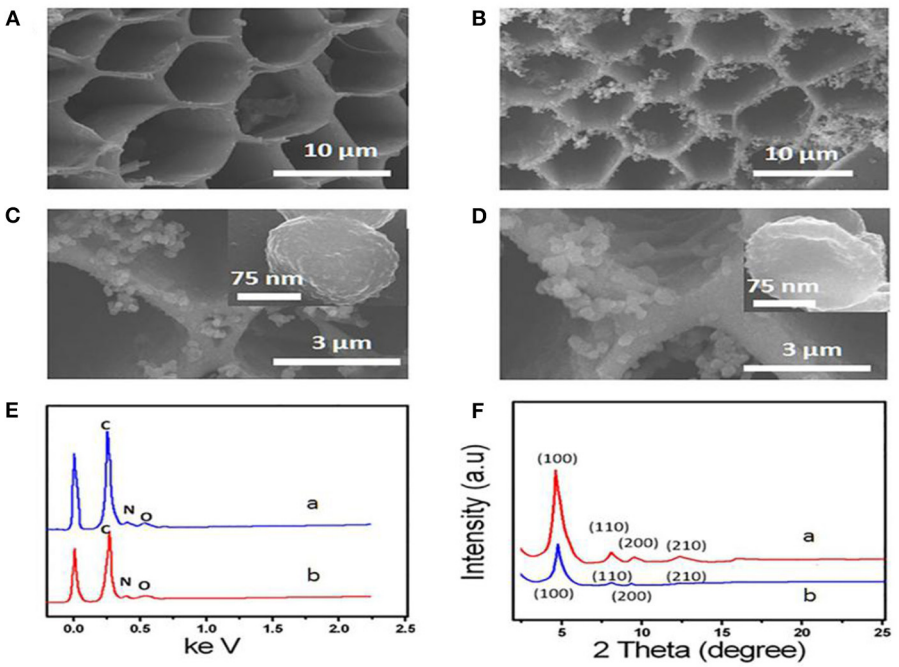

FIGURE 1 | (A) SEM image of 3D-KSC and **(B,C)** SEM images of COF-LZU1/3D-KSC. **(D)** SEM images of AChE/ COF-LZU1/3D-KSC. **(E)** EDS curve of COF-LZU1(curve a) and COF-LZU1/3D-KSC (curve b). **(F)** XRD pattern of COF-LZU1(curve a) and COF-LZU1/3D-KSC (curve b).

Electrochemical Behaviors of AChE/COF-LZU1/3D-KSC Electrodes

For exploring the electrochemical characteristics of the AChE/COF-LZU1/3D-KSCE, the CVs of multiple electrodes, particularly AChE/COF-LZU1/3D-KSCE, AChE/3D-KSCE and AChE/glass carbon electrode (AChE/GCE), were investigated (**Figures 2A–C**). **Figure 2A**, curve a, showed the CVs of AChE/COF-LZU1/3D-KSCE in PBS (pH 7) having 1 mM ATCl. The CV of the AChE/3D-EUSE presented an irreversible oxidation peak on 0.68 V (curve a), resulting from thiocholine oxidation, the hydrolyzed material of ATCl, through enzyme catalysis. Contrarily, the maximal current with AChE/glass carbon electrode (AChE/GCE) (**Figure 2C**, curve a) was much lower. The increased response might be due to the stack effect of the COF-LZU1/3D-KSC composite, possessing a higher surface area that can immobilize additional enzymes. Meanwhile, COF-LZU1/3D-KSC also has the benefit of fast electron transfer owing to its 3D-porous composite structure. Additionally, the good biocompatibility of COF-LZU1/3D-KSC could well-preserve the highest bioaction by immobilized

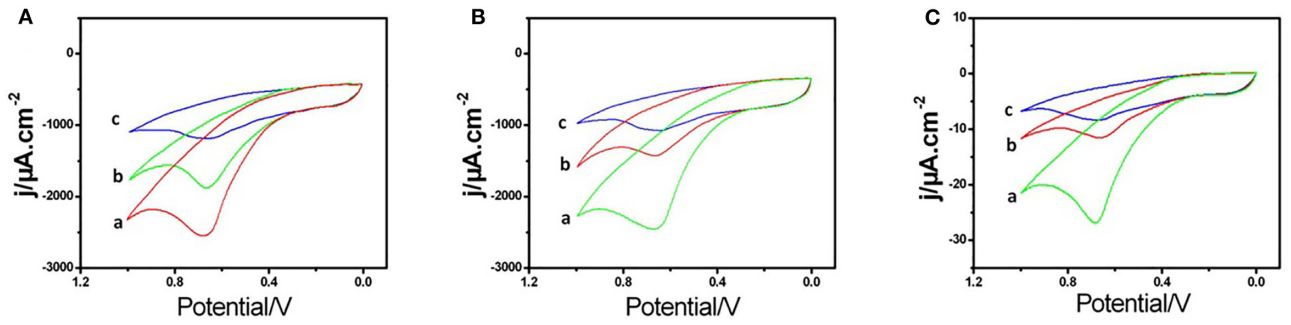

FIGURE 2 | CVs of the **(A)** AChE/COF-LZU1/3D-KSC, **(B)** AChE/3D-KSC, and **(C)** AChE/GCE in PBS (pH 7.0) containing (1.0 mM ATCl) following 10 min incubation in 0.0 (curve a), 9.0 (curve b), and 18 ng/mL (curve c) trichlorfon solution.

enzymes. Following 10 min placing in 9.0 ng/mL and 18 ng/mL trichlorfon solution, the anodic peak currents (curves b and c, **Figure 2A**) were significantly reduced compared to the control (curve a **Figure 2A**), and the reduction in peak current improved with the rising concentration of trichlorfon. It was because trichlorfon, an OP compound, displayed acute toxicity and produced an irreversible inhibitory response upon AChE, which therefore decreased enzymatic action to its substrate. However, the anodic peak currents of AChE/3D-KSCE (curves b and c, **Figure 2B**) and AChE/GCE (curves b and c, **Figure 2C**) decreased irregularly. This may be due to the decrease of enzyme modification, resulting in the narrowing of the detection range (**Figure 2B**) and could also be related to the fact that the glassy surface of the carbon electrode is smooth and the AChE can not be immobilized for a long time (**Figure 2C**). The trichlorfon concentration can be determined by changes in the voltammetric signal of the AChE/COF-LZU1/3D-KSCE. The principle of detection was pictorially illustrated by **Scheme 1**.

Influence of pH Value, ATCl, and AChE Concentration

Figure 3A showed the ampere sensitivity of AChE/COF-LZU1/3D-KSCE after adding ATCl. The usual biosensor current-time (response curve) was achieved when adding a substrate continuously in the stirred tank. By increasing ATCl concentration, the current response improved and tended to be stable at 1.0 mM. It might be due to the increase of ATCl concentration which leads to the active-sites' saturation of the enzyme by ATCl, thus reducing the binding sites of new molecules. The growth rate of peak current then shows a downward trend. Therefore, in the next pesticide analysis experiment, 1.0 mM ATCl was selected as the constant concentration.

The immobilization of AChE upon the surface electrode is another essential factor affecting the biosensor efficiency. **Figure 3B** showed the relationship between AChE concentration and the biosensor (amperometric response). With an increasing AChE concentration, a gradual increase occured in peak current and attained the highest value at around 20 U mL^{-1}. After this point, further addition of AChe will slowly weaken the current response. Its behavior may be ascribed to the presence of lesser AChE amounts, which is not enough to catalyze substrate oxidation, while too thick an AChE-modified layer may hinder mass and electron transfer, thus reducing the catalytic current. Therefore, this turning point may be due to the inhibition of COF-LZU1/3D-KSC to generate thiocholine and electron transfer by a large number of AChE. Therefore, in the next experiment, 20 U mL^{-1} AChE solution was used to build AChE/ COF-LZU1/3D-KSCE.

For electrochemical biosensors, pH value is the key factor that affects their stability and sensitiveness. Therefore, the influence of pH value was also studied. As shown in **Figure 3C**, at pH = 7, the maximum ampere response of AChE/COF-LZU1/3D-KSCE at 1 mM ATCl was obtained, which is consistent with most reported AChE biosensors (Ding et al., 2011; Su et al., 2016). Among the most influential parameters in pesticide assay is the culture time of inhibition. While increasing the incubation time period, there is also an increase in the rate of inhibition. Whereas, the required time of inhibition has been determined on various time-intervals varying from 02 to 60 min (**Figure 3D**). By prolonging the incubation timeframe, the rate of inhibition elevated to its highest value after incubating with trichlorfon 19 ng/mL for 10 min. Therefore, 10 min is used for the test.

Voltammetric Detection of Trichlorfon

In an optimized state, the inhibition stayed proportionate to varying concentrations of trichlorfon with 0.20–19 ng/mL (**Figure 4**), having a limit of detection (0.067 ng/mL). The effectiveness of AChE/COF-LZU1/3D-KSCE compared to other stated AChE biosensors is listed in **Table 1**, which indicated that the current AChE/COF-LZU1/3D-KSCE exhibited an equivalent or lower detection limit, demonstrating that COF-LZU1/3D-KSCE had multifunctions in enzyme immobilization. The high carbon content and nitrogen doted characteristics may sustain the enzymatic activity; moreover, the high specific surface-area with excellent electrical conducting potential of the composite would help a lot improvementn improving the sensitivity.

Precision, Stability, and Selectivity of Biosensor

After trichlorfon (10 ng/mL) solution was added after around 10 min, the inter-assay precision of 1.0 mM ATCl was established

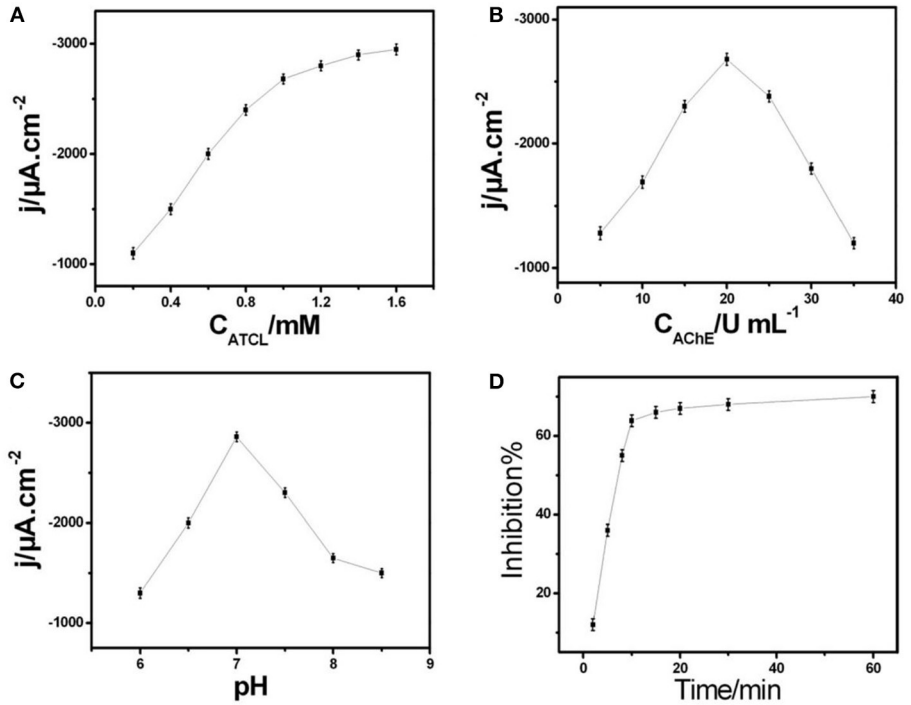

FIGURE 3 | (A) Correlation among current response to ATCl concentration in 0.1 M PBS of pH 7. **(B)** Plot of amperometric response vs. AChE concentration of AChE/COF-LZU1/3D-KSCE in 0.1 M PBS of pH 7 with 1 mM ATCl. **(C)** Effect of pH on current response of AChE/COF-LZU1/3D-KSCE to 1 mM ATCl. **(D)** Effect of inhibition time on inhibition (percentage) of AChE/COF-LZU1/3D-KSCE in 0.1 M PBS of pH 7 with 1 mM ATCl; inhibition of trichlorfon was 19 ng mL^{-1}.

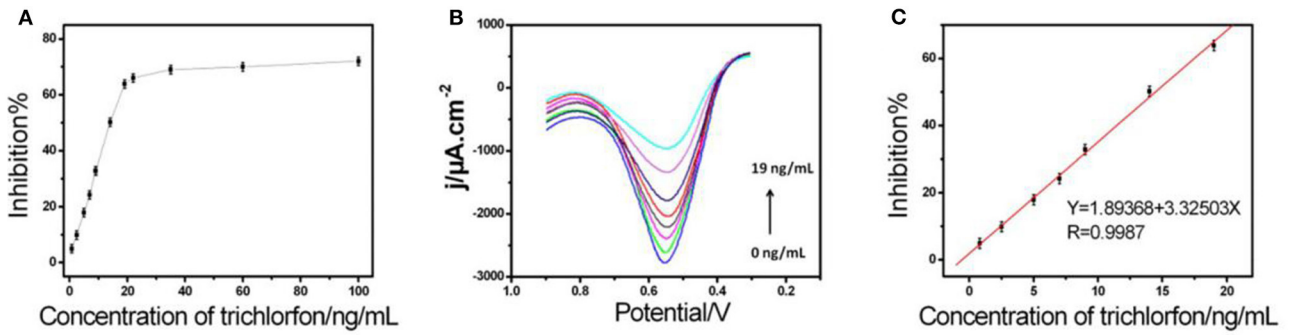

FIGURE 4 | (A) The biosensor inhibition curve with varying concentrations of trichlorfon (inhibitions corresponded to trichlorfon concentrations of 0.8, 2.5, 5, 7, 9, 14, 19, 22, 35, 60, and 100 ng mL^{-1}, respectively), in 0.1 M PBS with pH 7 consisting of 1 mM ATCl. **(B)** DPVs and **(C)** standard curve for trichlorfon assessment in 0.1 M PBS of pH 7 including 1 mM ATCl.

on five distinct electrodes; the inter-assay precision was 3.9%, which proved that the precision and repeatability were good. The interference of several electro-active phenol derivatives (like nitrophenol, catechol, and hydroquinone) and the detection ofinorganic substances containing oxygen (SO_4^{2-}, NO_3^-, sodium citrate) was also studied. As shown in **Figure S2**, when adding 2 times of nitrophenol, hydroquinone, catechol, SO_4^{2-}, NO_3^-, and $Na_3C_6H_5O_7$ in determining trichlorfon (19 ng/mL), the inhibition behavior did not change significantly. The good selectivity of the electrode is confirmed and can be utilized for determining actual amounts of trichlorfon in samples. The enzymatic electrode is placed in 4°C in a dry environment unless used. During the first 5 d of storage, the reaction of ATCl did not decrease significantly. After 30 d of storage, the current response of the sensor was still maintained (94%) at the primary response (**Figure S3**).

TABLE 1 | Comparative evaluation of various AChE biosensors' efficiency used for pesticide detection.

Process	Detected pesticide	Linear range	Limit of detection	Reference
Nafion/AChE/Chit-PB-MWNTs-HGNs/Au	Carbofuran	1.11–17.70 ng/mL	0.55	Kandimalla and Ju, 2006
AuNPs-MWCNTs-chitosan	Monocrotophos	0.1–10 μM	10 nM	Zhai et al., 2013
AChE-(xGnPs)-chitosan	Parathion	0.005–0.039 μM	0.158 nM	Norouzi et al., 2010
NF/AChE-CS/SnO_2NPs-CGR-NF/GCE	Carbofuran	2.21×10^{-4}-2.21×10^{-2} ng/mL 2.21×10^{-2}–2.21 ng/mL	1.11×10^{-4} ng/mL	Ion et al., 2010
AChE/e-GON-MWCNTs/GCE	Carbofuran Paraoxon	0.03–0.81 ng/m 0.05–1, 1–104 ng/mL	0.015 ng/mL 0.025 ng/mL	Zhou et al., 2013
AChE/Au-MWNTs/GCE	Paraoxon	0.028–1.927 ng/mL	0.028 ng/mL	Li et al., 2017
PPy-AChE-Geltn-Glut/Pt	Carbofuran Paraoxon	0.025–2, 5–60 ng/mL 0.1–12.5, 12.5–150 ng/mL	0.12 ng/mL 1.1 ng/mL	Jha and Ramaprabhu, 2010
AChE/SWCNT-Co phtalocyanine/GCE	Paraoxon	5–50 ng/mL	3 ng/mL	Dutta and Puzari, 2014
AChE/CNT-NH_2/GCE	Paraoxon	0.055–0.275 ng/mL, 0.275–8.257 ng/mL	0.022 ng/mL	Ivanov et al., 2011
AChE/ZnO-MWCNTs-sG/GCE	Paraoxon	0.275–7.156 ng/mL	2.752×10^{-4} ng/mL	Yu et al., 2015
AChE/Fe_3O_4-CH/GCE	Carbofuran	1.11–19.91 ng/mL	0.80 ng/mL	Nayak et al., 2013
AChE/PAMAMb-Au/CNTs/GCE	Carbofuran	1.06–19.91 ng/mL	0.89 ng/mL	Jeyapragasam and Saraswathi, 2014
AChE/COF-LZU1/3D-KSCE	Trichlorfon	0.2–19 ng/mL	0.067 ng/mL	Current work

Reactivity and Real Sample Analysis

Activation of AChE is a key additional component affecting the effectiveness of biosensors. Irreversible inhibiton of AChE by OPs could be fully activated by the use of nucleophilic agents like praldoximin chloride (PAM-Cl), while, 5 mM PAM-Cl PBS concentration was applied for activation. Then, the biosensor was dipped in the PAM-CL solution to inhibit trichlorfon. After 10 min of regeneration, AChE activity recovered completely. By reactivating the procedure, the biosensor can be reused up to five times with good constancy. The biosensor practicability was further proven by the addition of different amounts of trichlorfon to the Schisandra chinensis samples for the recovery test. **Table S1** provides an overview of the results. The recovery was 96.1–105%. The results show that the method has high accuracy, high precision, and good reproducibility. It can be employed for the direct detection of associated samples.

CONCLUSION

During the present project, a stable and highly sensitive biosensor was fabricated using an AChE-modified COF-LZU1/3D-KSC composite, which makes it possible to detect even trace amounts (0.067 ng/mL) of an organophosphorus compound trichlorfon. The use of COF-LZU1/3D-KSC has significantly enhanced the biosensor efficiency in three ways: (1) COF-LZU1s and porous 3D-KSC provides a synergestic response due to the fully bumpy and hollow surface area that can firmly immobilize additional enzymes; (2) COF-LZU1s significantly improves electrical signaling due to fast electron transfer; and (3) Derived nitrogen elements from COF-LZU1 and 3D-KSC show that the higher bioactivities of the immobilized enzymes are also maintained. Due to these factors, the developed biosensor exhibited tremendously high sensitivity and lower-detection limits, and thus is more reliable to detect trace residues of OP pesticide compared to other AChE biosensors.

DATA AVAILABILITY STATEMENT

The original contributions presented in the study are included in the article/**Supplementary Material**, further inquiries can be directed to the corresponding author/s.

AUTHOR CONTRIBUTIONS

YS conceived and designed the project. YL and MZ analysised experimental date and drafted the manuscript. CJ, JZ, and CH performed research. QS contributed methods and resources.

FUNDING

This research was financially supported by the National Natural Science Foundation of China (81860702), the Science and technology project of Jiangxi Provincial Department of Education (GJJ180650), Double First-class Discipline Construction Project Fund of Jiangxi Province (JXSYLXK-ZHYAO067, 069, 070, and 106), Foundation for Doctoral Research Initiation of Jiangxi University of Traditional Chinese Medicine (2018WBZR014), and the Research Fund of Zhangjiagang first people's Hospital (ZKY201852).

SUPPLEMENTARY MATERIAL

The Supplementary Material for this article can be found online at: https://www.frontiersin.org/articles/10.3389/fchem.2020.00643/full#supplementary-material

REFERENCES

Baldissera, M. D., Souza, C. F., Descovi, S. N., Zanella, R., Prestes, O. D., and da Silva, A. S. (2019). Organophosphate pesticide trichlorfon induced neurotoxic effects in freshwater silver catfish Rhamdia quelen via disruption of blood-brain barrier: Implications on oxidative status, cell viability and brain neurotransmitters. *Comp. Biochem. Physiol. C. Toxicol. Pharmacol.* 218, 8–13. doi: 10.1016/j.cbpc.2018.12.006

Ding, S. Y., Gao, J., Wang, Q., Zhang, Y., Song, W. G., and Su, C. Y., et al. (2011). Construction of covalent organic framework for catalysis: Pd/COF-LZU1 in suzuki–miyaura coupling reaction. *J. Am. Chem. Soc.* 133, 19816–19822. doi: 10.1021/ja206846p

Dutta, R. R., and Puzari, P. (2014). Amperometric biosensing of organophosphate and organocarbamate pesticides utilizing polypyrrole entrapped acetylcholinesterase electrode. *Biosens. Bioelectron* 52, 166–172. doi: 10.1016/j.bios.2013.08.050

Ion, A. C., Ion, I., Culetu, A., Gherase, D., Moldovan, C. A., and Iosub, R. (2010). Acetylcholinesterase voltammetric biosensors based on carbon nanostructure-chitosan composite material for organophosphate pesticides. *Mat. Sci. Eng. C* 30, 817–821. doi: 10.1016/j.msec

Ivanov, A. N., Younusov, R. R., Evtugyn, G. A., Arduini, F., Moscone, D., and Palleschi, G. (2011). Acetylcholinesterase biosensor based on single-walled carbon nanotubes—Co phtalocyanine for organophosphorus pesticides detection. *Talanta* 85, 216–221. doi: 10.1016/j.talanta.2011.03.045

Jeyapragasam, T., and Saraswathi, R. (2014). Electrochemical biosensing of carbofuran based on acetylcholinesterase immobilized onto iron oxide–chitosan nanocomposite. *Sensor. Actuat. B-Chem.* 191, 681–687. doi: 10.1016/j.snb.2013.10.054

Jha, N., and Ramaprabhu, S. (2010). Development of Au nanoparticles dispersed carbon nanotube-based biosensor for the detection of paraoxon. *Nanoscale* 2, 806–810. doi: 10.1039/b9nr00336c

Kandimalla, V. B., and Ju, H. (2006). Binding of acetylcholinesterase to multiwall carbon nanotube-cross-linked chitosan composite for flow-injection amperometric detection of an organophosphorous insecticide. *Chem. A Eur. J.* 12, 1074–1080. doi: 10.1002/chem.200500178

Khalilzadeh, B., Charoudeh, H. N., Shadjou, N., Mohammad-Rezaei, R., Omidi, Y., and Velaei, K., et al. (2016). Ultrasensitive caspase-3 activity detection using an electrochemical biosensor engineered by gold nanoparticle functionalized MCM-41: Its application during stem cell differentiation. *Sensor. Actuat. B-Chem.* 231, 561–575. doi: 10.1016/j.snb.2016.03.043

Li, Y., Zhao, R., Shi, L., Han, G., and Xiao, Y. (2017). Acetylcholinesterase biosensor based on electrochemically inducing 3D graphene oxide network/multi-walled carbon nanotube composites for detection of pesticides. *Rsc. Adv.* 7, 53570–53577. doi: 10.1039/c7ra08226f

Liu, K., Song, Y., Liu, Y., Peng, M., Li, H., Li, X., et al. (2017). An integrated strategy using UPLC–QTOF-MSE and UPLC–QTOF-MRM (enhanced target) for pharmacokinetics study of wine processed schisandra chinensis fructus in rats. *J. Pharm. Biomed. Anal.* 139, 165–178. doi: 10.1016/j.jpba.2017.02.043

Liu, Y., Su, D., Zhang, L., Wei, S., Liu, K., and Peng, M., et al. (2016). Endogenous Lcarnosinelevel in diabetes rat cardiac muscle. Evid. *Based Complementary Altern. Med.* doi: 10.1155/2016/6230825

Ma, Y., Li, B., Ke, Y., and Zhang, Y. (2018). Effects of low doses trichlorfon exposure on rana chensinensis tadpoles. *Environ. Toxicol.* 34, 30–36. doi: 10.1002/tox.22654

Nayak, P., Anbarasan, B., and Ramaprabhu, S. (2013). Fabrication of Organophosphorus biosensor using ZnO nanoparticle-decorated carbon nanotube–graphene hybrid composite prepared by a novel green technique. *J. Phys. Chem. C* 117, 13202–13209. doi: 10.1021/jp312824b

Norouzi, P., Pirali-Hamedani, M., Ganjali, M. R., and Faridbod, F. (2010). A novel acetylcholinesterase biosensor based on chitosan-gold nanoparticles film for determination of monocrotophos using FFT continuous cyclic … *Int. J. Electrochem. Sci.* 5, 1434–1446. doi: 10.1002/fuce.201000027

Shan, L., Zhao, M., Lu, Y., Ning, H., Yang, S., Song, Y., et al. (2019). CENPE promotes lung adenocarcinoma proliferation and is directly regulated by FOXM1. *Int. J. Oncol.* 55, 257–266. doi: 10.3892/ijo.2019.4805

Shi, X., Mackie, B., Zhang, G., Yang, S., Song, Y., and Su, D., et al. (2016a). Identification of the metabolic enzyme involved morusin metabolism and characterization of its metabolites by ultraperformance liquid chromatography quadrupole time-of-flight mass spectrometry (UPLC/Q-TOF-MS/MS). *Evid-Based Compl. Alt.* 2016, 1–10. doi: 10.1155/2016/9240103

Shi, X., Yang, S., Zhang, G., Song, Y., Su, D., Liu, Y., et al. (2016b). The different metabolism of morusin in various species and its potent inhibition against UDP-glucuronosyltransferase (UGT) and cytochrome p450 (CYP450) enzymes. *Xenobiotica* 46, 467–476. doi: 10.3109/00498254.2015.1086839

Shi, X., Zhang, G., Ge, G., Guo, Z., Song, Y., Su, D., et al. (2019). *In vitro* metabolism of auriculasin and its inhibitory effects on human cytochrome P450 and UDP-glucuronosyltransferase enzymes. *Chem. Res. Toxicol.* 32, 2125–2134. doi: 10.1021/acs.chemrestox.9b00307

Song, N. E., Lee, J. Y., Mansur, A. R., Jang, H. W., Lim, M. C., and Lee, Y. (2019a). Determination of 60 pesticides in hen eggs using the QuEChERS procedure followed by LC-MS/MS and GC-MS/MS. *Food Chem.* 298, 125050.1–125050.10. doi: 10.1016/j.foodchem.2019.125050

Song, Y., Chen, J., Liu, H., Song, Y., Xu, F., and Tan, H. (2015). Conformation, bioactivity and electrochemical performance of glucose oxidase immobilized on surface of gold nanoparticles. *Electrochim. Acta.* 158, 56–63. doi: 10.1016/j.electacta.2015.01.114

Song, Y., Gong, C., Su, D., Shen, Y., Song, Y., and Wang, L. (2016b). A novel ascorbic acid electrochemical sensor based on spherical MOF-5 arrayed on a three-dimensional porous carbon electrode. *Anal. Methods* 8, 2290–2296. doi: 10.1039/c6ay00136j

Song, Y., Shan, B., Li, H., Feng, B., Peng, H., and Xu, P. (2019b). Safety investigation of Pulsatilla chinensis saponins from chronic metabonomic study of serum biomedical changes in oral treated rat. *J. Ethnopharmacol.* 235, 435–445. doi: 10.1016/j.jep.2019.01.035

Song, Y., Su, D., Shen, Y., Liu, H., and Wang, L. (2016a). Design and preparation of open circuit potential biosensor for *in vitro* and *in vivo* glucose monitoring. *Anal. Bioanal. Chem.* 409, 161–168. doi: 10.1007/s00216-016-9982-1

Soreq, H., and Seidman, S. (2001). Acetylcholinesterase - new roles for an old actor. *Nat. Rev. Neurosci.* 2, 294–302. doi: 10.1038/35067589

Sotiropoulou, S., and Chaniotakis, N. A. (2005). Lowering the detection limit of the acetylcholinesterase biosensor using a nanoporous carbon matrix. *Anal. Chim. Acta.* 530, 199–204. doi: 10.1016/j.aca.2004.09.007

Su, D., Huang, J., Song, Y., and Feng, Y. (2014). Comparative pharmacokinetics and tissue distribution study of mono-, and di-caffeoylquinic acids isomers of ainsliaea fragrans champ by a fast UHPLC?MS/MS method. *Fitoterapia.* 99, 139–152. doi: 10.1016/j.fitote.2014.09.011

Su, D., Li, W., Xu, Q., Liu, Y., Song, Y., Feng, Y., et al. (2016). New metabolites of acteoside identified by ultra-performance liquid chromatography/quadrupole-time-of-flight MSE in rat plasma, urine, and feces. *Fitoterapia.* 112, 45–55. doi: 10.1016/j.fitote.2016.05.004

Su, D., Liao, Z., Feng, B., Wang, T., Shan, B., Zeng, Q., et al. (2020). Pulsatilla chinensis saponins cause liver injury through interfering ceramide/sphingomyelin balance that promotes lipid metabolism dysregulation and apoptosis. *Phytomedicine.* 153–265. doi: 10.1016/j.phymed.2020.153265

Su, D., Peng, M., Song, Y., Liu, Y., Li, X., Liu, K., et al. (2018). Distribution and accumulation characteristics of five pulchinenosides in tumor-bearing mice for solubilization formulations using LC-ESI-MS/MS Method. *Curr. Pharm. Anal.* 14, 175–184. doi: 10.2174/1573412913666170105164731

Wang, J., Musameh, M., and Lin, Y. (2003). Solubilization of carbon nanotubes by nafion toward the preparation of amperometric biosensors. *J. Am. Chem. Soc.* 125, 2408–2409. doi: 10.1021/ja028951v

Yu, G., Wu, W., Zhao, Q., Wei, X., and Lu, Q. (2015). Efficient immobilization of acetylcholinesterase onto amino functionalized carbon nanotubes for the fabrication of high sensitive organophosphorus pesticides biosensors. *Biosens. Bioelectron* 68, 288–294. doi: 10.1016/j.bios.2015.01.005

Zeng, Q., Liu, Y., Song, Y., Feng, B., Xu, P., and Shan, B. (2019). A UHPLC–MS/MS method coupled with simple and efficient alkaline hydrolysis for free and total determination of conjugate nanomedicine: pharmacokinetic and biodistribution study of poly (L-glutamic acid)-graft-methoxy poly (ethylene glycol)/combretastatin A4. *J. Pharm. Biomed. Anal.* 169, 215–224. doi: 10.1016/j.jpba.2019.03.001

Zhai, C., Sun, X., Zhao, W., Gong, Z., and Wang, X. (2013). Acetylcholinesterase biosensor based on chitosan/prussian blue/multiwall carbon nanotubes/hollow

gold nanospheres nanocomposite film by one-stepelectrodeposition. *Biosens. Bioelectron.* 42, 124–130. doi: 10.1016/j.bios.2012.10.058

Zhang, P., Sun, T., Rong, S., Zeng, D., Yu, H., and Zhang, Z. (2019). A sensitive amperometric AChE-biosensor for organophosphate pesticides detection based on conjugated polymer and Ag-rGO-NH2 nanocomposite. *Bioelectrochemistry* 127, 163–170. doi: 10.1016/j.bioelechem.2019.02.003

Zhou, Q., Yang, L., Wang, G., and Yang, Y. (2013). Acetylcholinesterase biosensor based on SnO2 nanoparticles–carboxylic graphene–nafion modified electrode for detection of pesticides. *Biosens. Bioelectron.* 49, 25–31. doi: 10.1016/j.bios.2013.04.037

Conflict of Interest: The authors declare that the research was conducted in the absence of any commercial or financial relationships that could be construed as a potential conflict of interest.

frontiers in Chemistry

ORIGINAL RESEARCH
published: 15 October 2020
doi: 10.3389/fchem.2020.00803

Detection of Pb(II): Au Nanoparticle Incorporated CuBTC MOFs

Gajanan A. Bodkhe[1†], Bhavna S. Hedau[1†], Megha A. Deshmukh[1], Harshada K. Patil[1], Sumedh M. Shirsat[2], Devdatta M. Phase[3], Krishan K. Pandey[4] and Mahendra D. Shirsat[1]*

[1] RUSA Center for Advanced Sensor Technology, Department of Physics, Dr. Babasaheb Ambedkar Marathwada University, Aurangabad, India, [2] Department of Electronics and Telecommunication Engineering, Jawaharlal Nehru Engineering College, Aurangabad, India, [3] UGC-DAE Consortium for Scientific Research, University Campus, Indore, India, [4] High Pressure and Synchrotron Radiation Physics Division, Bhabha Atomic Research Center, Mumbai, India

In the present investigation, copper benzene tricarboxylate metal organic frameworks (CuBTC MOF) and Au nanoparticle incorporated CuBTC MOF (Au@CuBTC) were synthesized by the conventional solvothermal method in a round bottom flask at 105°C and kept in an oil bath. The synthesized CuBTC MOF and Au@CuBTC MOFs were characterized by structure using X-ray diffraction (XRD) spectroscopic methods including Fourier Transform Infrared spectroscopy, Raman Spectroscopy, X-ray Photoelectron Spectroscopy (XPS), and Energy dispersive spectroscopy (EDS). We also characterized them using morphological techniques such as Field emission scanning electron microscopy (FE-SEM), and electrochemical approaches that included cyclic voltammetry (CV) and electrochemical impedance spectroscopy (EIS). We examined thermal stability by thermogravimetric analysis (TG/DTA) and N_2 adsorption—desorption isotherm by Brunauer-Emmett-Teller (BET) surface area method. Both materials were tested for the detection of lead (II) ions in aqueous media. Au nanoparticle incorporated CuBTC MOF showed great affinity and selectivity toward Pb^{2+} ions and achieved a lower detection limit (LOD) of 1 nM/L by differential pulse voltammetry (DPV) technique, which is far below than MCL for Pb^{2+} ions (0.03 μM/L) suggested by the United States (U.S.) Environmental Protection Agency (EPA) drinking water regulations.

Keywords: differential pulse voltammetry (DPV), electrochemical sensor, gold nanoparticles, metal organic frameworks, CuBTC MOF

OPEN ACCESS

Edited by:
Daojun Zhang,
Anyang Normal University, China

Reviewed by:
Fugang Xu,
Jiangxi Normal University, China
Xuan Zhang,
Donghua University, China

***Correspondence:**
Mahendra D. Shirsat
mdshirsat.phy@bamu.ac.in

† These authors have contributed equally to this work

Specialty section:
This article was submitted to Supramolecular Chemistry, a section of the journal Frontiers in Chemistry

Received: *27 May 2020*
Accepted: *30 July 2020*
Published: *15 October 2020*

Citation:
Bodkhe GA, Hedau BS, Deshmukh MA, Patil HK, Shirsat SM, Phase DM, Pandey KK and Shirsat MD (2020) Detection of Pb(II): Au Nanoparticle Incorporated CuBTC MOFs. Front. Chem. 8:803. doi: 10.3389/fchem.2020.00803

INTRODUCTION

Heavy metal ions are a major water pollutant caused by sewage from chemical industries and various other sources (Singh et al., 2011; Maleki et al., 2019). Some of the more toxic heavy metal ions include Pb(II), Cu(II), Hg(II), Co(II), etc. (Meena et al., 2005). The accumulation of heavy metallic ions results in severe health issues, damage to the ecosystem (Wu et al., 2010), and significant damage to the environment (Fu and Wang, 2011). It is well-known that Pb(II) is toxic for human and aquatic health (Deshmukh et al., 2018b), causing health issues which include memory damage, muscle fatigue, neurotic diseases, damage to the liver and kidneys, reduction in hemoglobin formation, infertility, and abnormalities in pregnancy, amongst other concerning side effects (Meena et al., 2005). There is an urgent need to detect and remove these pollutants from water, by introducing highly sensitive and selective sensing materials. Various technologies have been introduced for highly sensitive heavy metal ion detection, namely liquid chromatography (Ali and Aboul-Enein, 2002), solid-phase extraction coupled with atomic absorption spectroscopy

(Faraji et al., 2010), and atomic emission spectroscopy. However, these methods are very expensive, time-consuming, and require experts to operate the instruments (Quang and Kim, 2010).

Researchers are also dedicating efforts to developing heavy metal ions sensors in other modalities, such as the fluorescent (Neupane et al., 2011), Field Effect Transistors (FETs) (Cobben et al., 1992), Surface-Enhanced Raman Scattering (SERS) (Tan et al., 2012), Surface Plasmon Resonance (SPR) (Forzani et al., 2005), colorimetric (Hung et al., 2010), and electrochemical sensors (Deshmukh et al., 2018c,d). Most of these techniques are challenging due to the high cost of the laboratory facilities that they require. Modalities such as electrochemical sensors are, on the other hand, an ideal and prominent option due to advantages such as the fact that they require simple and cost-effective instruments and have faster analytical responses (Kimmel et al., 2011). Researchers have explored various materials for the detection of heavy metal ions in aqueous media in electrochemical modality, for example considering organic conducting polymers (OCPs) (Deshmukh et al., 2018e), carbon nanotubes (CNTs) (Deshmukh et al., 2018e; Maleki, 2018), metal oxides (Hwang et al., 2008), graphene (Dai et al., 2016), bioreceptors (Cui et al., 2015), metal nanoparticles (Kim et al., 2001), and metal organic frameworks (MOFs) (Roushani et al., 2016), among others.

Recently, researchers have had an interest in an efficient material called Metal Organic Frameworks (MOFs) due to versatile physical and chemical properties, high porosity, ultrahigh surface area, high electrical transfer rate, high crystallinity, evenly element doping, and abundant metal sites (Bodkhe et al., 2019), among other benefits. MOFs are generally composed of a central metal ion and organic linker resulting in crystalline and porous materials. These properties make them useful in versatile applications as a catalyst (Lee et al., 2009), potential biomedical applications (Wuttke et al., 2017), sensors (Rauf et al., 2020), gas storage (Chen et al., 2020), and separation (Lin et al., 2020).

However, the sensing properties of MOFs can be enhanced by combining them with other efficient materials (Liu et al., 2018). Nanocomposites (Maleki et al., 2016) are a combination of various materials that overcome or improve deficiencies in the parent material (Maleki et al., 2018), which makes them advantageous when used in sensors. The episodic structure of MOFs makes them an attractive candidate for the encapsulation of metal nanoparticles (such as Ag, Pt, Cu, and Au, etc.) due to increased control of the regular distribution of nanoparticles and enhancement of the stability of NPs (Butova et al., 2018). The porous structure of MOFs make NPs accessible to the environment, meaning they are good candidates for use in sensors. Among all nanoparticles, gold (Au) nanoparticles have shown better results when incorporated in MOFs, showing carbon monoxide oxidation (Jiang et al., 2009), alcohols oxidation (Ishida et al., 2008), hydrazine electrocatalytic oxidation (Han et al., 2015), and a reduction of 4-hydroxynitrobenzene (Ke et al., 2015).

Inspired by these reports, this study exploited various properties of copper benzene tricarboxylate (CuBTC) MOF to synthesize the Au nanoparticles incorporated CuBTC (henceforth referred to as Au@CuBTC). CuBTC MOF contains Cu(II) central metal ion and benzene tricarboxylic acid as an organic linker. CuBTC MOF is the most explored MOF. The CuBTC MOF shows good electrochemical performance and electro catalytic activity which makes them suitable for electrochemical sensors using hydrazine (Meng et al., 2019), nitrite (Saraf et al., 2016), hydroquinone, catechol (Zhou et al., 2015), ammonia (Travlou et al., 2015), and H_2O_2 (Zhang et al., 2013; Golsheikh et al., 2020). This study observed that pure CuBTC MOF does not show any electrochrochemical response to Pb(II) ions at 0.01 mM/L concentration. However, Au@CuBTC MOF shows an electrochemical response up to 1 nM/L concentration, which is far below the MCL level of Pb(II) ions. The porous structure of CuBTC provided maximum surface area and Au NPs enhanced electrocatalytic activity, which makes the material a highly sensitive and selective electrochemical sensor for Pb(II) ions.

EXPERIMENTAL

Materials and Chemicals

All the reagents and chemicals were analytical grade and used without purification. Benzene-1,3,5-tricarboxylic acid (BTC), Copper nitrate trihydrate ($Cu(NO_3)_2$,$3H_2O$), and N, N dimethyl formamide (DMF) purchased from Sigma Aldrich. Chloroauric acid, Hydrazine hydrate, hydrochloric acid, sodium acetate, acetic acid, sodium hydroxide, hydrochloric acid, and ethanol purchased from Molychem, India.

Synthesis of CuBTC MOF

The CuBTC MOF was synthesized as per the reported method (Marx et al., 2011). 2.252 gm of Copper nitrate trihydrate [$Cu(NO_3)_2$, $3H_2O$] was mixed with 50 ml of deionized water and benzene-1,3,5-tricarboxylic acid (BTC) (0.982 gm) in 50 ml of DMF, prepared separately and mixed with constant stirring at room temperature. The precursor solution was transferred into a 250 ml round-bottom flask and kept in an oil bath at 105°C for 4 h. After completion of the reaction, CuBTC MOF crystals were observed at the bottom of the round-bottom flask. After cooling at room temperature, CuBTC MOF crystals were washed with deionized water and ethanol three times each to remove unreacted reactants. The filtered CuBTC MOF was kept for activation at 120°C for 12 h to remove coordinated solvent molecules from the pores (Bodkhe et al., 2019). After activation, the color of CuBTC changed from faint blue to dark blue. The activated CuBTC MOF was stored in air tight sample containers for further use.

Synthesis of Au@CuBTC MOF

Gold (Au) nanoparticle precursor solution was prepared separately, as reported in other studies (Yadav et al., 2018). Chloroauric acid ($HAuCl_4$) (0.71 mM) was used as the gold (Au) source, mixed with 0.1 M hydrochloric acid (HCl) in D. I. water, with 0.71 mM hydrazine hydrate then added slowly. This solution was stirred for 30 min and sonicated for 5 min. The synthesis procedure for Au@CuBTC MOF is the same as CuBTC MOFs. In the precursor solution of CuBTC, the Au NPs precursor solution

was added slowly then stirred for 30 min and sonicated for 5 min. This solution was transferred into a 250 ml round bottom flask and kept in an oil bath for 4 h at 105°C. Au@CuBTC MOF was cooled at room temperature and washed with deionized water and ethanol three times each. The filtered Au@CuBTC MOF activated at 120°C for 12 h and stored for further use.

Preparation of CuBTC and Au@CuBTC MOF Electrode

Glassy carbon electrode (GCE) was used as an electrode for all electrochemical experiments. The GCEs were carefully polished with alumina powder slurries of 1, 0.3, and 0.05 μ, respectively, to get a mirror like surface. Then the GCE was ultrasonicated and washed with acetone and D.I. water sequentially. The preconditioning of bare GCE was performed in 0.5 M of H_2SO_4 solution using the cyclic voltammetry (CV) technique in the potential window of −0.35 to 1.5 V at a scan rate of 100 mV/s until stable voltammogram was observed.

The pure CuBTC and Au@CuBTC MOF were properly mixed in diluted nafion in acetone. The prepared suspension of pure CuBTC and Au@CuBTC MOF were drop cast on GCE electrodes and dried at room temperature, then used for electrochemical experiments.

Electrochemical Detection of Lead (Pb^{2+}) Ions

The Pb^{2+} ions solution was prepared in acetate buffer at pH 5.0 using $Pb(NO_3)_2$ (Pb^{2+} ions source), $Pb(NO_3)_2$ mixed properly, with constant stirring for 30 min. The Pb^{2+} ions solution was prepared at a higher concentration and used as a stock solution, a lower concentration was prepared by diluting it with the addition of a buffer solution. Electrochemical detection of Pb^{2+} ions was carried out on CHI 660C electrochemical workstation by the differential pulse voltammetry technique. The GCE modified electrodes of pure CuBTC and Au@CuBTC were used as the working electrode, platinum served as the counter electrode, while Ag/AgCl were used as a reference. Initially, the accumulation of Pb^{2+} ions on GCE modified electrodes was carried out by dipping the modified electrode for 5 min at constant pH of 5.0, then DPV in another buffer (pH = 5.0) was carried out in the potential from 0 to (−1) volts.

Apparatus and Instruments

Powder X-ray diffraction (XRD) measurements were performed on a Bruker D8 Advance Diffractometer with Cu kα1 radiation (λ = 1.5406). The Fourier Transform Infrared (FTIR) spectrum was recorded on Bruker Alpha FTIR in ATR mode with the ZnSe window in the range of 500 to 4,000 cm^{-1}. Nitrogen adsorption-desorption isotherm measurements were carried out on Autosorb iQ Station 1 instrument at 77 K and all samples were degassed at 150°C in a helium environment. The X-Ray Photoelectron studies were carried out on the XPS facility available at Raja Ramanna Center for Advanced Technology (RRCAT), Indore, India.

Thermogravimetric measurements were carried out on Shimadzu to take the DTG-60H model from room temperature to 1,000°C, with a scan rate of 10°C/min in the nitrogen environment. The Raman spectrum of all the samples was recorded on a Renishaw inVia reflex Raman microscope in the spectral range of 90 to 2,000 cm^{-1} at 532 nm laser excitation wavelength. Cyclic Voltammetry (CV) and Electrochemical Impedance Spectroscopy (EIS) measurements were carried out on a CHI 660C electrochemical workstation with platinum (Pt) foil, Ag/AgCl as counter and reference electrodes, respectively. The CV was recorded in the potential range of −0.8–0.5 V in 10 mM $[Fe(CN)6]^{3-/4-}$ solution containing 0.1 M KCl solution at a scan rate of 100 mV/S. EIS measurements were taken in the frequency range of 0.01–0.1 MHz in the 0.1 M KCl solution. Electrochemical sensing experiments were performed in acetate buffer at 5.0 pH by differential pulse voltammetry (DPV) technique on CHI 660C electrochemical workstation having Ag/AgCl and Pt foil as reference and counter electrodes respectively.

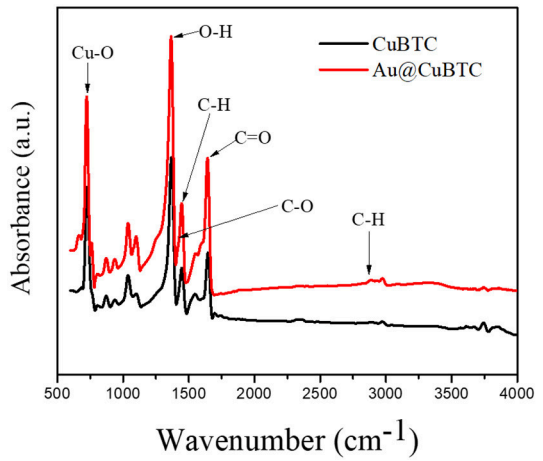

FIGURE 1 | FTIR Spectra of as-synthesized CuBTC MOF and Au@CuBTC MOF.

RESULTS AND DISCUSSION

Materials Characterization

Fourier Transform Infrared Spectroscopy Analysis

As-synthesized CuBTC MOF and Au@CuBTC MOF were characterized by FTIR spectroscopy as shown in **Figure 1**. In CuBTC MOF, the presence of asymmetric C-H stretching vibration and asymmetric stretching of the carboxylic groups confirmed by bands present at 2,890 cm^{-1} and 1,446 cm^{-1} (Dastan et al., 2016). The absorption band at 730 cm^{-1} attributed to Cu-O stretching vibration. The absorption peaks at 1,640 cm^{-1} attributed to the stretching of $V_{C=O}$ while the band at 1,446 cm^{-1} were attributed to the stretching of V_{C-O}. The band at 1,373 cm^{-1} indicated that there was a bending of O-H functional groups (Lin et al., 2014) and confirms the CuBTC MOF. The FTIR spectra of Au nanoparticle incorporated CuBTC does not show any difference in peak position in FTIR spectra, but there was an increase in absorption of the IR spectrum in Au nanoparticle incorporated CuBTC MOF. This confirms

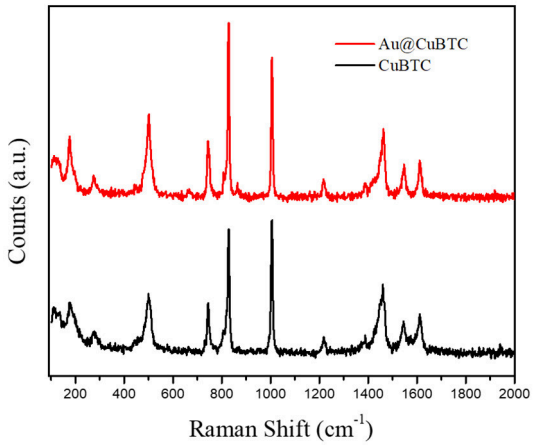

FIGURE 2 | The Raman Spectra of as-synthesized CuBTC MOF and Au@CuBTC MOF.

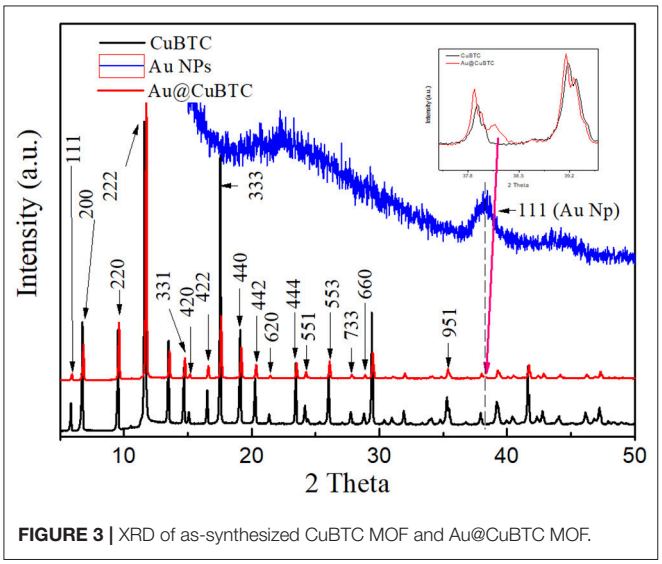

FIGURE 3 | XRD of as-synthesized CuBTC MOF and Au@CuBTC MOF.

that no vibrational bond formed between CuBTC MOF and Au nanoparticles.

Raman Spectroscopy Analysis

The Raman spectra of CuBTC MOF and Au nanoparticle incorporated CuBTC MOF are shown in **Figure 2**. The Raman spectra of CuBTC MOF shows that the Raman shift at 500 cm^{-1} corresponds to the presence of Cu(II) species, with peaks at 1,006 cm^{-1} and 1,606 cm^{-1} attributed to the ν(C=C) modes of the benzene ring. The vibrational peak at 1,457 cm^{-1} corresponds to $\nu_s(COO^-)$. This confirms the formation of CuBTC MOF (Deshmukh et al., 2018b). Au@CuBTC MOF does not show any change in the Raman spectra Au nanoparticles, does not affect the chemical bonding in CuBTC MOF, and that the Au nanoparticles are not Raman active (Worrall et al., 2016).

Structural Analysis

The structural analysis of as synthesized CuBTC and Au@CuBTC MOF carried out by X-ray diffraction is shown in **Figure 3**. All the diffraction peaks were compared and matched with the ICDD database no. PDF 00-065-1028 and reported literature (Wang et al., 2014). Both the patterns of as synthesized CuBTC and Au@CuBTC shows the same diffraction pattern and peak positions except one very small extra peak, which appeared at 2θ = 38.2°C. This confirms the presence of Au nanoparticles in the compound, while peaks in both materials represent the crystal structure of CuBTC MOF (cubic) at the 2θ angle with respective d_{hkl} planes showing 5.8° (111), 6.7° (200), 9.5° (220), 11.6° (222), 14.7° (331), 15° (420), 16.5° (422), 17.5° (333), 19,0° (440), 20.2° (442), 21.3° (620) 23.4° (444), 24.1° (551), 26.0° (553), 27.7° (733), 28.7° (660), and 35.2° (951). The crystalline size of both the compounds was calculated by classical Scherrer formula (Dastan et al., 2014) by considering peaks of the XRD patterns, as shown in **Figure 3**:

$$D = \frac{K\lambda}{\beta Cos\theta} \quad (1)$$

where D is the average crystallite size, λ is the wavelength of the X-ray radiation (λ = 1.5404 A°), K is the Scherrer constant (0.89 for cubic shape), θ is the Bragg diffraction angle, and β is the full width at half-maximum height (FWHM). The crystallinity and crystallite size of as synthesized CuBTC were found to be 74.4% and 199.94 nm, respectively, while reduction of the crystallinity and crystallite size in Au nanoparticle incorporated CuBTC MOF observed as 69.9% and 108.41 nm respectively.

Morphological Analysis

The FE-SEM images show distinct changes in morphology, particle size, and the crystalline nature of as-synthesized CuBTC, Au@CuBTC, shown in **Figures 4A,B**. **Figure 4B** indicates the presence of the Au nanoparticles in the composite on the surface, but most that the Au nanoparticles are incorporated in the MOF crystal. The elemental confirmation of the compounds was carried out using Energy-dispersive X-ray spectroscopy (EDX). Inside the CuBTC MOF structure, we recorded EDX spectra (**Figures 4C,D**) and found the presence of the Au NPs inside the CuBTC MOF, shown in **Figure 4D**. We also found the elemental concentration detail of Au@CuBTC, which is shown in **Table 1**. The CuBTC MOF has a cubic structure with a high surface area and porous morphology that provides more active sites for Au NPs inside the CuBTC MOF for the detection of Pb (II) ions sensitively.

Thermogravimetric Analysis

The thermogravimetric analysis of as-synthesized CuBTC and Au nanoparticles incorporated CuBTC is shown in **Figure 5**. In as-synthesized CuBTC, small weight loss (5.4%) started from 40 to 133°C due to the removal of H_2O molecules, while a weight loss of 29.8%, from 133 to 343°C was observed, due to the dislodgement of coordinated DMF molecules from the CuBTC MOF Structure. There was an obvious weight loss above 343°C of ∼49% in the CuBTC MOF network, which produced H_2O, CO_2, and Cu_2O, meaning that CuBTC MOF is thermally stable up to 343°C. In Au@CuBTC, a small weight loss (15.16%) started

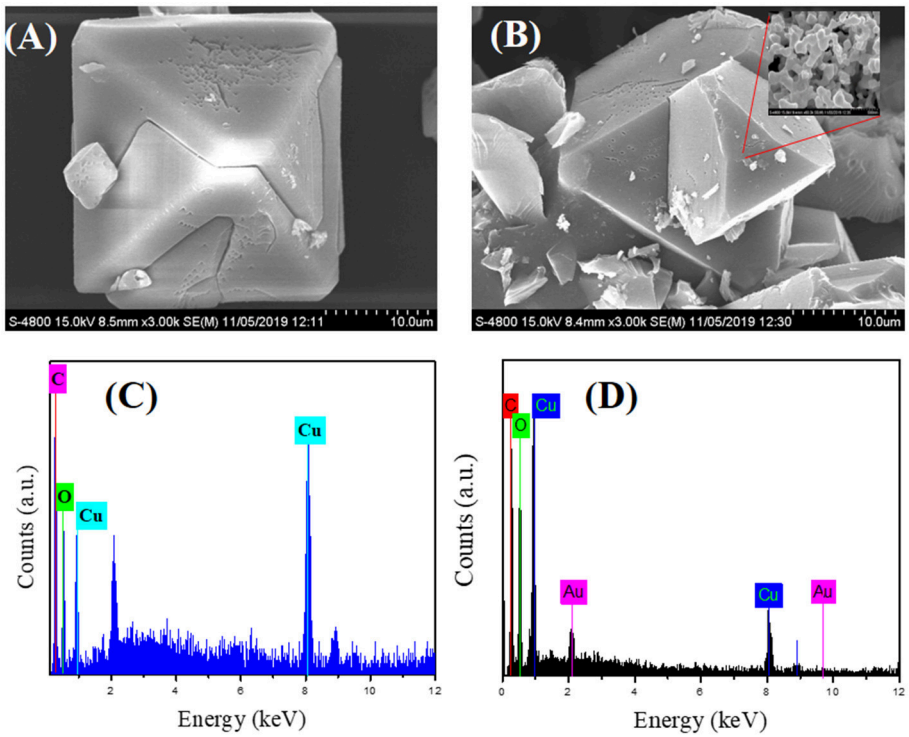

FIGURE 4 | FE-SEM images of **(A)** as-synthesized CuBTC, **(B)** Au@CuBTC, and Energy-dispersive X-ray spectroscopy (EDX) analysis of **(C)** as-synthesized CuBTC, **(D)** Au@CuBTC.

TABLE 1 | EDS elemental analysis data of as-synthesized Au@CuBTC.

Element	Atomic no.	Unnormalised concentration (wt%)	Normalized concentration (wt.%)	Atom concentration (%)	Error (wt%) (1 sigma)
Carbon (C)	6	26.05	34.19	56.28	5.50
Oxygen (O)	8	19.53	25.63	31.67	4.09
Copper (Cu)	29	28.99	38.04	11.84	1.51
Gold (Au)	79	1.63	2.14	0.22	0.16
Sum		76.21	100.00	100.00	-

from 40 to 122°C due to the removal of the H_2O molecule. A weight loss of (16.9%) from 133 to 180°C was observed, which is due to the dislodgement of coordinated DMF molecules from the Au@CuBTC MOF Structure. An obvious weight loss of ∼41.78% above 335°C was observed in Au@CuBTC MOF and produced H_2O, CO_2, and Cu_2O. These results confirm that the thermal stability of both the materials is almost the same up to ∼335°C.

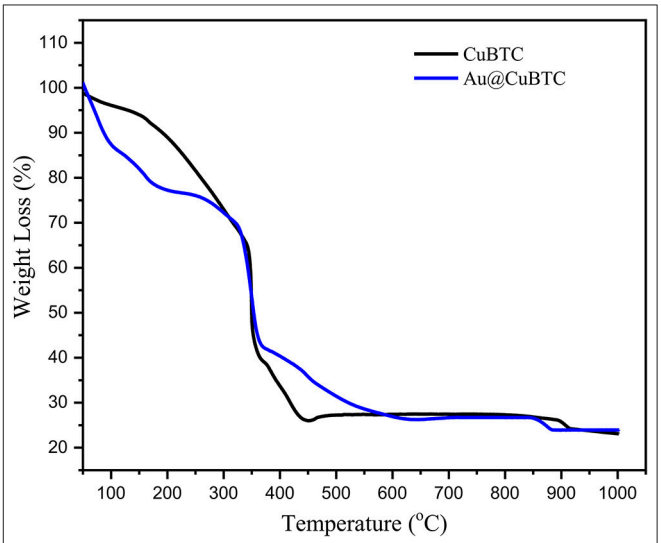

FIGURE 5 | Thermogravimetric (TGA) analysis of as synthesized CuBTC, and Au@CuBTC MOF.

Brunauer-Emmett-Teller (BET) Analysis

N_2 adsorption-desorption isotherm and BJH Pore size distribution of the as synthesized CuBTC and Au@CuBTC was studied using the Brunauer-Emmett-Teller (BET) technique, shown in **Figures 6A,B**, respectively. Both the MOFs were degassed in the Helium environment at 150°C to remove possible contaminations inside the pores. The physical adsorption of nitrogen at a temperature of 77 K was carried out for the BET surface area and pore size measurement. Both the compounds clearly show a microporous structure, having type I adsorption-desorption isotherm (Akhtar et al.,

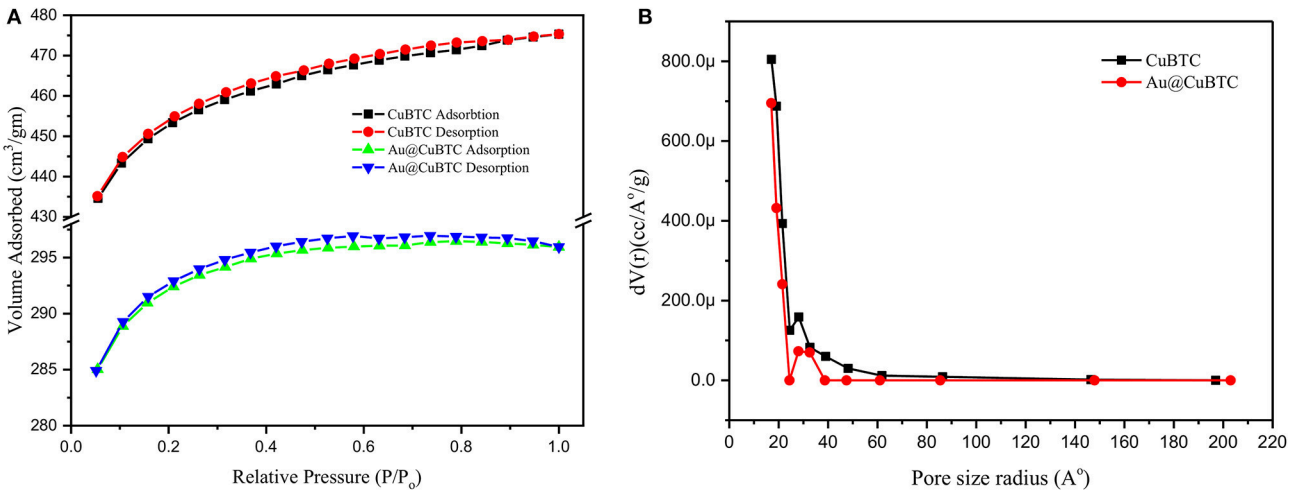

FIGURE 6 | (A) N_2 adsorption-desorption isotherm and **(B)** BJH Pore size distribution of as synthesized CuBTC and Au@CuBTC.

TABLE 2 | BET surface area details.

Compound	Surface area (m^2/gm)	Total pore volume (cc/gm)	Average pore radius (nm)
CuBTC	1374.983	0.7352	1.06942
Au@CuBTC	876.704	0.4589	1.04691

2018). The BET surface area details are shown in **Table 2**. The surface area, total pore volume, and average pore radius of Au nanoparticle incorporated CuBTC MOF reduces as compared to the synthesized CuBTC MOF.

X-ray Photoelectron Spectroscopy (XPS) Analysis

To analyze the surface chemical state of as synthesized CuBTC and Au@CuBTC, XPS measurements were performed as shown in **Figure 7**. The XPS spectra of C 1s (**Figure 7A**) shows binding energy (BE) peaks at 286.3 and 290.2 eV of as synthesized CuBTC and Au@CuBTC, with the same BE of C 1s. This indicates no interaction between Au nanoparticle and CuBTC at the carbon site. The XPS spectra at Cu 2p (**Figure 7B**) of as synthesized CuBTC and Au@CuBTC shows the same spectrum having a small decrease in peak intensity of Au@CuBTC, which may be due to the presence of Au nanoparticles inside the CuBTC. The peaks present in both the compounds at 936.2 eV and 956.3 eV correspond to Cu 2p3/2 and Cu 2p1/2, with shake-up satellite bands that confirm the +2 oxidation state (Luo et al., 2016). The spectra of O 1s (**Figure 7C** in both the compound shows no change in the chemical states of oxygen after incorporation with Au nanoparticles in CuBTC. The peak at BE of 533.4 eV indicates the presence of carboxylic species in CuBTC. **Figure 7D** shows the XPS spectra of Au@CuBTC at the binding energy edge of Au 4f and confirms the presence of Au nanoparticles in CuBTC, with the peaks at 87.30 and 94.70 eV attributed to the Au 4f5/2 and Au 4f7/2 transitions (Ghodake et al., 2010).

Electrochemical Analysis

The electrochemical activity of bare GCE, Au Np, CuBTC, and Au@CuBTC were studied by cyclic voltammetry in a 10 mM $[Fe(CN)_6]^{3-/4-}$ solution containing 0.1 M KCl solution at a scan rate of 100 mV/s, as shown in **Figure 8**. The CuBTC coated glassy carbon electrode (GCE) shows distinct oxidation and reduction peaks at 0.02 and −0.5 V versus Ag/AgCl reference electrode, indicating the reversible oxidation and reduction of Cu(II) to Cu(I) (Kumar et al., 2012). The CV curve of the Au@CuBTC coated GCE electrode shows a distinct reduction peak compared with pure CuBTC and the same oxidation peak, with an increase in oxidation current that probably an overlapping of the oxidation of Au nanoparticles over CuBTC MOF, while bare GCE and Au Np coated GCE shows higher current due to high conductivity.

Bare GCE, Au Np, CuBTC, and Au@CuBTC were characterized by EIS, which is an effective tool to study electrochemical activity by applying variable AC frequencies. The EIS spectra of bare GCE, Au Np, CuBTC, and Au@CuBTC coated films on GCE were recorded in the AC frequency range of 0.01 Hz to 0.1 MHz in a 10 mM $[Fe(CN)_6]^{3-/4-}$ solution containing 0.1 M KCl. Nyquist plot (**Figure 9**) showed a slight decrease in a semicircle of Au@CuBTC as compared to CuBTC, which is due to a slight increase in the ionic conductivity in CuBTC after the incorporation of Au nanoparticles due to the small concentration of Au NPs, and a slight difference was observed. Bare GCE and Au Np showed a very small semicircle due to the very low electron transfer resistance (Ret) of the redox probe. The increase in diameter of the semicircle in the CuBTC MOF and Au@CuBTC MOF modified GCE surface was due to the insulating nature of CuBTC MOF which acts as a barrier for the electrochemical process and slowed down the diffusion of the electrochemical probe toward the electrode surface. EIS and CV results are complementary to each other.

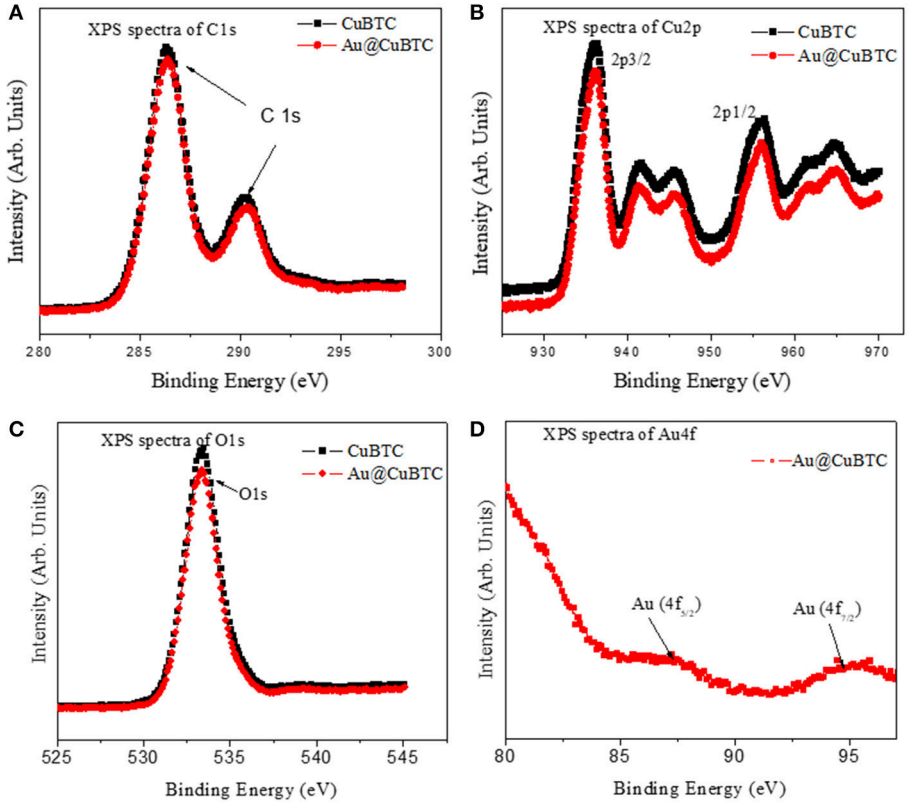

FIGURE 7 | XPS spectra of **(A)** C1s **(B)** Cu2p **(C)** O1s of CuBTC and Au@CuBTC and **(D)** Au4f of Au@CuBTC.

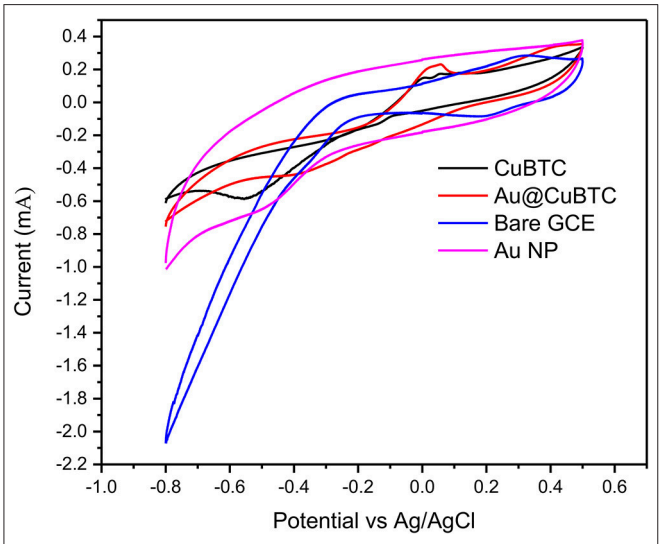

FIGURE 8 | Cyclic voltammograms (CV) of bare GCE, Au NP, CuBTC MOF, and Au@CuBTC MOF.

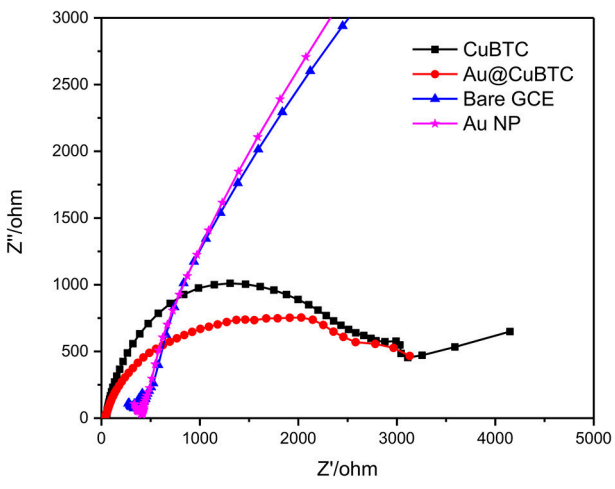

FIGURE 9 | Electrochemical Impedance Spectroscopy (EIS) Nyquist plot of bare GCE, Au NP, CuBTC MOF, and Au@CuBTC MOF.

SENSOR PERFORMANCE

The sensing experiment was carried out in two steps: (1) Accumulation in Pb^{2+} ions solution, and (2) reduction in buffer solution by applying differential pulse voltammetry (DPV), where the accumulated Pb^{2+} ions can get reduced at particular potential Pb^{2+} ions (Equation 1). As shown in **Figure 10A**, the bare GCE Au nanoparticles coated GCE and CuBTC shows lower response to the Pb^{2+} ions at a concentration of

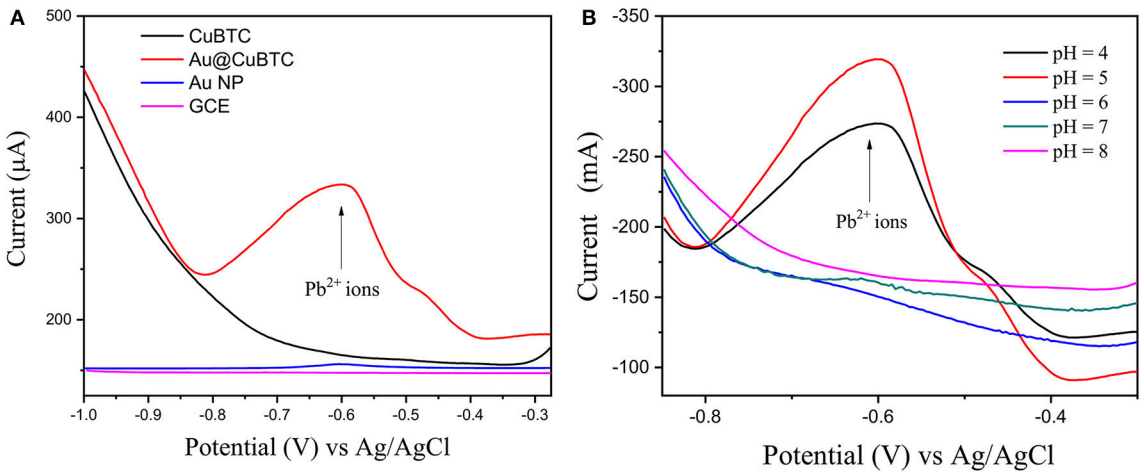

FIGURE 10 | (A) Differential pulse voltammograms (DPV) of 0.01 mMol L^{-1} Pb (II) ions in acetate buffer (pH-5) of bare GCE, Au Nps, CuBTC, and Au@CuBTC and **(B)** DPV of Au@CuBTC to 1 μM/L Pb^{2+} ions at various pH.

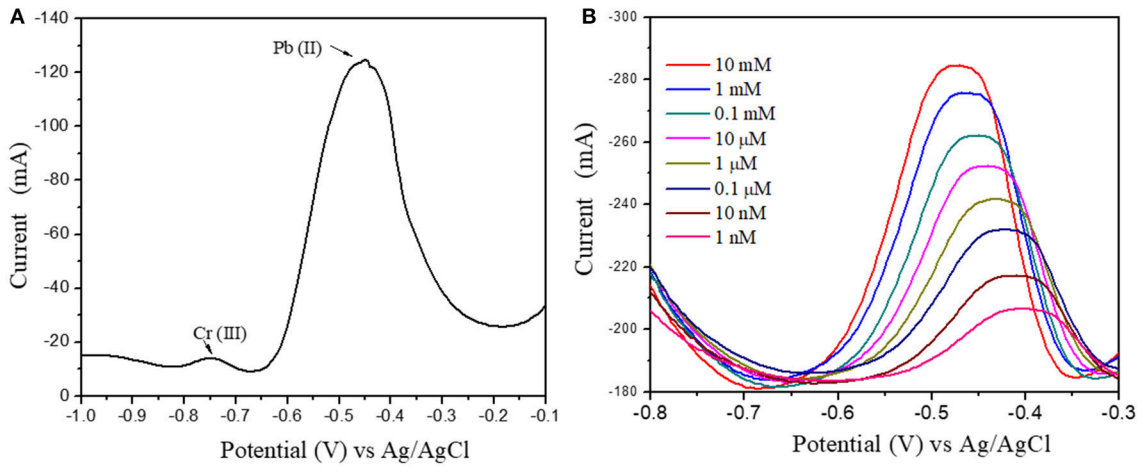

FIGURE 11 | (A) Pb(II) and Cr(III) ions DPV response at 1 μM concentration **(B)** Differential Pulse Voltammograms of Au@CuBTC modified GCE electrodes for Pb(II) ions concentration of 10 mM/L to 1 nM/L.

0.01 mM/L. However, Au@CuBTC shows a significant sensing response to the Pb^{2+} ions, which means that after incorporating Au nanoparticles in CuBTC become sensitive toward Pb^{2+} ions. The Au Np work as a catalyst while the CuBTC MOF provides more surface area and the pore provides more active sites for electrocatalytic activity, which enables highly sensitive detection of Pb^{2+} ions. Here, in the accumulation step, Pb^{2+} ions coordinate with Au@CuBTC MOF and form PbO that are trapped on the surface of Au@CuBTC MOF, while in the DPV they are reduced at the reduction potential (Equation 1) (Metzger, 2012), which results in a large flow of current through working and counter electrodes as shown in **Figures 10**, **11**.

$$PbO_{(s)} + H_2O(l) + 2e^{-1} \rightarrow Pb_{(s)} + 2OH^{-1}_{(aq)}$$
$$E^{\circ} = -0.58V \quad (1)$$

Figure 10B shows the DPV curve of Pb^{2+} ions at the concentration of 1 μM/L at the various pH (4–8) and shows the highest sensitivity at pH 5. All the sensing experiments were carried out in acetate buffer at pH 5. The Au@CuBTC modified GCE electrode was tested for Cr^{3+} ions and Pb^{2+} ions and shows a more selective response toward Pb^{2+} ions as shown in **Figure 11A**. It was also tested for various concentrations of Pb^{2+} ions in water, as shown in **Figure 11**. The Au@CuBTC shows a sensing response toward Pb^{2+} ions up to a lower detection limit of 1 nM/L, which is below the Maximum Contamination Level (MCL) of 0.03 μM/L as proposed by EPA, USA (Landmeyer et al., 2003). The comparative studies for the detection of Pb(II) ions by electrochemical method using various materials are shown in **Table 3**. This indicates that this work has a better deletion limit (LOD) compared to other reported

TABLE 3 | Comparative studies for detection of Pb(II) ions by electrochemical method using various materials.

Sr. No.	Sensing material electrode	Sensing technique	Detection limit (LOD) of Pb^{2+} ions	References
1.	Bismuth/Poly(1,8-diaminonaphthalene) modified carbon paste electrode (CPE)	Square-wave voltammetry	0.3 μg L^{-1}	Salih et al., 2017
2.	Bismuth-Carbon pate electrode (CPE)	Square-wave anodic stripping voltammetry	0.3 μg/L	Martín-Yerga et al., 2017
3.	Glassy carbon electrode modified SWNTs/Biomass electrode	Differential pulse anodic stripping voltammetry	10^{-8} M	Dali et al., 2018
4.	TAPB-DMTP-COF (TAPB, 1,3,5-tris(4-aminophenyl)benzene; DMTP, 2,5-dimethoxyterephaldehyde; COF, covalent organic framework) modified carbon paste electrode	Differential pulse anodic stripping voltammetry	1.9 nmol/L	Zhang et al., 2018
5.	Iron oxide (Fe_3O_4) nanoparticles (NPs) capped with terephthalic acid (TA)/Glassy Carbon Electrode	Square wave anodic stripping voltammetry	0.05 μM/L	Deshmukh et al., 2017
6.	EDTA-Ppy/SWNTs modified stainless steel electrode	Differential pulse voltammetry	0.15 μM/L	Deshmukh et al., 2018a
7.	Fe_3O_4@PDA@MnO_2 electrode	Differential pulse voltammetry	0.03 μg L^{-1}	Wang et al., 2020
8.	Au@CuBTC MOF modified GCE electrodes	Differential pulse voltammetry	1 nM/L	This work

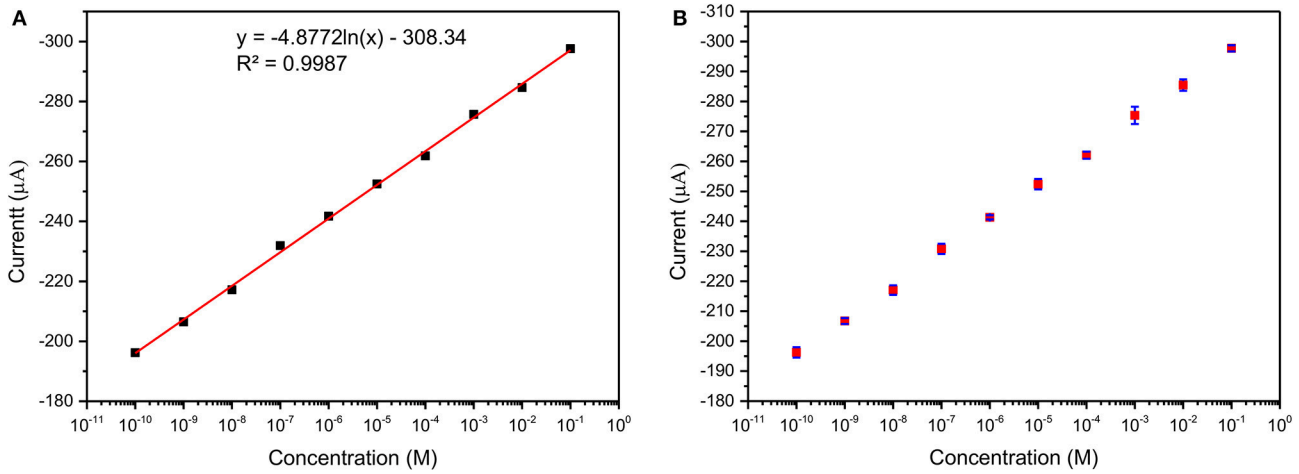

FIGURE 12 | (A) Calibration plot and **(B)** Error bar diagram of Au@CuBTC modified GCE electrodes for Pb(II) ions concentration of 10 mM/L to 1 nM/L.

data. The calibration plot and error bar diagram also show (**Figures 12A,B**) that the fabricated sensor shows good linearity and repeatability.

CONCLUSIONS

In this study successfully synthesized and rigorously characterized CuBTC MOF and Au nanoparticle incorporated CuBTC MOF (Au@CuBTC). We prepared an electrochemical sensor based on Au@CuBTC MOF that showed a significant response and sensitivity toward Pb^{2+} ions compared with pure CuBTC MOF coated on the GCE electrode. Au@CuBTC MOF shows the highest sensitivity in acetate buffer at pH 5 and shows great affinity toward Pb^{2+} ions in water media at a lower detection limit of 1 nM/L concentration at pH 5.0 by using a DPV technique which is far below the Maximum Contamination Level (MCL) as proposed by EPA, USA.

DATA AVAILABILITY STATEMENT

The raw data supporting the conclusions of this article will be made available by the authors, without undue reservation.

AUTHOR CONTRIBUTIONS

GB and BH contributed equally in experimental work, idea generation, and data analysis. MD and HP contributed for electrochemical experiment data analysis. SMS contributed in experimental work. DP and KP contributed for XPS and XRD experimental data collection analysis. MS contributed as

corresponding author (i.e., idea, experiment, data validation, and guidance). All authors contributed to the article and approved the submitted version.

ACKNOWLEDGMENTS

The authors extend their sincere thanks to the following for providing financial support: UGC—DAE CSR (RRCAT), Indore (Project No. CSR-IC-BL66/CRS- 183/2016-17/847), Inter University Accelerator Center (IUAC), New Delhi, India (UFR no. 62320), DST—SERB, New Delhi (Project No. EEQ/2017/000645), Rashtria Uchachatar Shiksha Abhiyan (RUSA), Government of Maharashtra, UGC-SAP Programme (F.530/16/DRS-I/2016 (SAP-II) Dt.16-04-2016), and DST-FIST (Project No. SR/FST/PSI-210/2016(C) dtd. 16/12/2016).

REFERENCES

Akhtar, S., Bala, S., De, A., Das, K. S., Adhikary, A., Jyotsna, S., et al. (2018). Designing multifunctional MOFs using the inorganic motif [Cu3 (μ3-OH)(μ-Pyz)] as an SBU and their properties. *Crystal Growth Design* 19, 992–1004. doi: 10.1021/acs.cgd.8b01540

Ali, I., and Aboul-Enein, H. Y. (2002). Speciation of arsenic and chromium metal ions by reversed phase high performance liquid chromatography. *Chemosphere* 48, 275–278. doi: 10.1016/S0045-6535(02)00085-1

Bodkhe, G. A., Deshmukh, M. A., Patil, H. K., Shirsat, S. M., Srihari, V., Pandey, K. K., et al. (2019). Field effect transistor based on proton conductive metal organic framework (CuBTC). *J. Phys.* 52:335105. doi: 10.1088/1361-6463/ab1987

Butova, V. V., Kirichkov, M. V., Budnyk, A. P., Guda, A. A., Soldatov, M. A., Lamberti, C., et al. (2018). A room-temperature growth of gold nanoparticles on MOF-199 and its transformation into the $[Cu_2(OH)(BTC)(H_2O)]$ n phase. *Polyhedron* 154, 357–363. doi: 10.1016/j.poly.2018.08.002

Chen, S., Li, Y., and Mi, L. (2020). Porous carbon derived from metal organic framework for gas storage and separation: the size effect. *Inorg. Chem. Commun.* 118:107999. doi: 10.1016/j.inoche.2020.107999

Cobben, P. L., Egberink, R. J., Bomer, J. G., Bergveld, P., Verboom, W., and Reinhoudt, D. N. (1992). Transduction of selective recognition of heavy metal ions by chemically modified field effect transistors (CHEMFETs). *J. Am. Chem. Soc.* 114, 10573–10582. doi: 10.1021/ja00052a063

Cui, L., Wu, J., and Ju, H. (2015). Electrochemical sensing of heavy metal ions with inorganic, organic and bio-materials. *Biosens. Bioelectr.* 63, 276–286. doi: 10.1016/j.bios.2014.07.052

Dai, H., Wang, N., Wang, D., Ma, H., and Lin, M. (2016). An electrochemical sensor based on phytic acid functionalized polypyrrole/graphene oxide nanocomposites for simultaneous determination of Cd (II) and Pb (II). *Chem. Eng. J.* 299, 150–155. doi: 10.1016/j.cej.2016.04.083

Dali, M., Zinoubi, K., Chrouda, A., Abderrahmane, S., Cherrad, S., and Jaffrezic-Renault, N. (2018). A biosensor based on fungal soil biomass for electrochemical detection of lead (II) and cadmium (II) by differential pulse anodic stripping voltammetry. *J. Electroanal. Chem.* 813, 9–19. doi: 10.1016/j.jelechem.2018.02.009

Dastan, D., Londhe, P. U., and Chaure, N. B. (2014). Characterization of TiO_2 nanoparticles prepared using different surfactants by sol–gel method. *J. Mater. Sci.* 25, 3473–3479. doi: 10.1007/s10854-014-2041-9

Dastan, D., Panahi, S. L., and Chaure, N. B. (2016). Characterization of titania thin films grown by dip-coating technique. *J. Mater. Sci.* 27, 12291–12296. doi: 10.1007/s10854-016-4985-4

Deshmukh, M. A., Bodkhe, G. A., Shirsat, S., Ramanavicius, A., and Shirsat, M. D. (2018a). Nanocomposite platform based on EDTA modified Ppy/SWNTs for the sensing of Pb (II) ions by electrochemical method. *Front. Chem.* 6:451. doi: 10.3389/fchem.2018.00451

Deshmukh, M. A., Celiesiute, R., Ramanaviciene, A., Shirsat, M. D., and Ramanavicius, A. (2018b). EDTA_PANI/SWCNTs nanocomposite modified electrode for electrochemical determination of copper (II), lead (II) and mercury (II) ions. *Electrochim. Acta* 259, 930–938. doi: 10.1016/j.electacta.2017.10.131

Deshmukh, M. A., Patil, H. K., Bodkhe, G. A., Yasuzawa, M., Koinkar, P., Ramanaviciene, A., et al. (2018c). EDTA-modified PANI/SWNTs nanocomposite for differential pulse voltammetry based determination of Cu (II) ions. *Sensors Actuat. B* 260, 331–338. doi: 10.1016/j.snb.2017.12.160

Deshmukh, M. A., Patil, H. K., Bodkhe, G. A., Yasuzawa, M., Koinkar, P., Ramanavicius, A., et al. (2018d). EDA modified PANI/SWNTs nanocomposite for determination of Ni (II) metal ions. *Colloid. Surf. A* 537, 303–309. doi: 10.1016/j.colsurfa.2017.10.026

Deshmukh, M. A., Shirsat, M. D., Ramanaviciene, A., and Ramanavicius, A. (2018e). Composites based on conducting polymers and carbon nanomaterials for heavy metal ion sensing. *Crit. Rev. Anal. Chem.* 48, 293–304. doi: 10.1080/10408347.2017.1422966

Deshmukh, S., Kandasamy, G., Upadhyay, R. K., Bhattacharya, G., Banerjee, D., Maity, D., et al. (2017). Terephthalic acid capped iron oxide nanoparticles for sensitive electrochemical detection of heavy metal ions in water. *J. Electroanal. Chem.* 788, 91–98. doi: 10.1016/j.jelechem.2017.01.064

Faraji, M., Yamini, Y., Saleh, A., Rezaee, M., Ghambarian, M., and Hassani, R. (2010). A nanoparticle-based solid-phase extraction procedure followed by flow injection inductively coupled plasma-optical emission spectrometry to determine some heavy metal ions in water samples. *Anal. Chim. Acta* 659, 172–177. doi: 10.1016/j.aca.2009.11.053

Forzani, E. S., Zhang, H., Chen, W., and Tao, N. (2005). Detection of heavy metal ions in drinking water using a high-resolution differential surface plasmon resonance sensor. *Environ. Sci. Technol.* 39, 1257–1262. doi: 10.1021/es049234z

Fu, F., and Wang, Q. (2011). Removal of heavy metal ions from wastewaters: a review. *J. Environ. Manag.* 92, 407–418. doi: 10.1016/j.jenvman.2010.11.011

Ghodake, G., Deshpande, N., Lee, Y., and Jin, E. (2010). Pear fruit extract-assisted room-temperature biosynthesis of gold nanoplates. *Colloid. Surf. B* 75, 584–589. doi: 10.1016/j.colsurfb.2009.09.040

Golsheikh, A. M., Yeap, G.-Y., Yam, F. K., and San Lim, H. (2020). Facile fabrication and enhanced properties of copper-based metal organic framework incorporated with graphene for non-enzymatic detection of hydrogen peroxide. *Synthetic Metals* 260:116272. doi: 10.1016/j.synthmet.2019.116272

Han, Y., Han, L., Zhang, L., and Dong, S. (2015). Ultrasonic synthesis of highly dispersed Au nanoparticles supported on Ti-based metal–organic frameworks for electrocatalytic oxidation of hydrazine. *J. Mater. Chem. A* 3, 14669–14674. doi: 10.1039/C5TA03090K

Hung, Y.-L., Hsiung, T.-M., Chen, Y.-Y., Huang, Y.-F., and Huang, C.-C. (2010). Colorimetric detection of heavy metal ions using label-free gold nanoparticles and alkanethiols. *J. Phys. Chem. C* 114, 16329–16334. doi: 10.1021/jp1061573

Hwang, G.-H., Han, W.-K., Park, J.-S., and Kang, S.-G. (2008). An electrochemical sensor based on the reduction of screen-printed bismuth oxide for the determination of trace lead and cadmium. *Sensors Actuat. B* 135, 309–316. doi: 10.1016/j.snb.2008.08.039

Ishida, T., Nagaoka, M., Akita, T., and Haruta, M. (2008). Deposition of gold clusters on porous coordination polymers by solid grinding and their catalytic activity in aerobic oxidation of alcohols. *Chem. Eur. J.* 14, 8456–8460. doi: 10.1002/chem.200800980

Jiang, H.-L., Liu, B., Akita, T., Haruta, M., Sakurai, H., and Xu, Q. (2009). Au@ZIF-8: CO oxidation over gold nanoparticles deposited to metal—organic framework. *J. Am. Chem. Soc.* 131, 11302–11303. doi: 10.1021/ja9047653

Ke, F., Wang, L., and Zhu, J. (2015). Multifunctional Au-Fe 3 O 4@ MOF core–shell nanocomposite catalysts with controllable reactivity and magnetic recyclability. *Nanoscale* 7, 1201–1208. doi: 10.1039/C4NR05421K

Kim, Y., Johnson, R. C., and Hupp, J. T. (2001). Gold nanoparticle-based sensing of "spectroscopically silent" heavy metal ions. *Nano Lett.* 1, 165–167. doi: 10.1021/nl0100116

Kimmel, D. W., LeBlanc, G., Meschievitz, M. E., and Cliffel, D. E. (2011). Electrochemical sensors and biosensors. *Anal. Chem.* 84, 685–707. doi: 10.1021/ac202878q

Kumar, R. S., Kumar, S. S., and Kulandainathan, M. A. (2012). Highly selective electrochemical reduction of carbon dioxide using Cu based metal organic framework as an electrocatalyst. *Electrochem. Commun.* 25, 70–73. doi: 10.1016/j.elecom.2012.09.018

Landmeyer, J., Bradley, P., and Bullen, T. (2003). Stable lead isotopes reveal a natural source of high lead concentrations to gasoline-contaminated groundwater. *Environ. Geol.* 45, 12–22. doi: 10.1007/s00254-003-0863-5

Lee, J., Farha, O. K., Roberts, J., Scheidt, K. A., Nguyen, S. T., and Hupp, J. T. (2009). Metal–organic framework materials as catalysts. *Chem. Soc. Rev.* 38, 1450–1459. doi: 10.1039/b807080f

Lin, R.-B., Xiang, S., Zhou, W., and Chen, B. (2020). Microporous metal-organic framework materials for gas separation. *Chem* 6, 337–363. doi: 10.1016/j.chempr.2019.10.012

Lin, S., Song, Z., Che, G., Ren, A., Li, P., Liu, C., et al. (2014). Adsorption behavior of metal–organic frameworks for methylene blue from aqueous solution. *Micropor. Mesopor. Mater.* 193, 27–34. doi: 10.1016/j.micromeso.2014.03.004

Liu, L., Zhou, Y., Liu, S., and Xu, M. (2018). The applications of metal–organic frameworks in electrochemical sensors. *ChemElectroChem* 5, 6–19. doi: 10.1002/celc.201700931

Luo, Q.-x., Ji, M., Park, S.-E., Hao, C., and Li, Y.-q. (2016). PdCl 2 immobilized on metal–organic framework CuBTC with the aid of ionic liquids: enhanced catalytic performance in selective oxidation of cyclohexene. *RSC Adv.* 6, 33048–33054. doi: 10.1039/C6RA02077A

Maleki, A. (2018). Green oxidation protocol: Selective conversions of alcohols and alkenes to aldehydes, ketones and epoxides by using a new multiwall carbon nanotube-based hybrid nanocatalyst *via* ultrasound irradiation. *Ultrasonics Sonochem.* 40, 460–464. doi: 10.1016/j.ultsonch.2017.07.020

Maleki, A., Hajizadeh, Z., and Firouzi-Haji, R. (2018). Eco-friendly functionalization of magnetic halloysite nanotube with SO3H for synthesis of dihydropyrimidinones. *Micropor. Mesopor. Mater.* 259, 46–53. doi: 10.1016/j.micromeso.2017.09.034

Maleki, A., Hajizadeh, Z., Sharifi, V., and Emdadi, Z. (2019). A green, porous and eco-friendly magnetic geopolymer adsorbent for heavy metals removal from aqueous solutions. *J. Clean. Prod.* 215, 1233–1245. doi: 10.1016/j.jclepro.2019.01.084

Maleki, A., Rahimi, R., and Maleki, S. (2016). Efficient oxidation and epoxidation using a chromium (VI)-based magnetic nanocomposite. *Environ. Chem. Lett.* 14, 195–199. doi: 10.1007/s10311-016-0558-2

Martín-Yerga, D., Alvarez-Martos, I., Blanco-Lopez, M. C., Henry, C. S., and Fernández-Abedul, M. T. (2017). Point-of-need simultaneous electrochemical detection of lead and cadmium using low-cost stencil-printed transparency electrodes. *Anal. Chim. Acta* 981, 24–33. doi: 10.1016/j.aca.2017.05.027

Marx, S., Kleist, W., and Baiker, A. (2011). Synthesis, structural properties, and catalytic behavior of Cu-BTC and mixed-linker Cu-BTC-PyDC in the oxidation of benzene derivatives. *J. Catalysis* 281, 76–87. doi: 10.1016/j.jcat.2011.04.004

Meena, A. K., Mishra, G., Rai, P., Rajagopal, C., and Nagar, P. (2005). Removal of heavy metal ions from aqueous solutions using carbon aerogel as an adsorbent. *J. Hazard. Mater.* 122, 161–170. doi: 10.1016/j.jhazmat.2005.03.024

Meng, Z., Li, M., Liu, X., and Lei, Z. (2019). Sensitive electrochemical sensor for hydrazine based on in situ synthesis of Cu 3 (BTC) 2/GO nanocomposite. *J. Mater. Sci.* 30, 18617–18625. doi: 10.1007/s10854-019-02214-y

Metzger, R. M. (2012). *The Physical Chemist's Toolbox.* Hoboken, NJ: John Wiley & Sons. doi: 10.1002/9781118195598

Neupane, L. N., Thirupathi, P., Jang, S., Jang, M. J., Kim, J. H., and Lee, K.-H. (2011). Highly selectively monitoring heavy and transition metal ions by a fluorescent sensor based on dipeptide. *Talanta* 85, 1566–1574. doi: 10.1016/j.talanta.2011.06.052

Quang, D. T., and Kim, J. S. (2010). Fluoro-and chromogenic chemodosimeters for heavy metal ion detection in solution and biospecimens. *Chem. Rev.* 110, 6280–6301. doi: 10.1021/cr100154p

Rauf, S., Vijjapu, M. T., Andres, M. A., Gascón, I., Roubeau, O., Eddaoudi, M., et al. (2020). A highly selective metal-organic framework textile humidity sensor. *ACS Appl. Mater. Interfaces.* 12:29999–30006. doi: 10.1021/acsami.0c07532

Roushani, M., Valipour, A., and Saedi, Z. (2016). Electroanalytical sensing of Cd2+ based on metal–organic framework modified carbon paste electrode. *Sensors Actuat. B* 233, 419–425. doi: 10.1016/j.snb.2016.04.106

Salih, F. E., Ouarzane, A., and El Rhazi, M. (2017). Electrochemical detection of lead (II) at bismuth/poly (1, 8-diaminonaphthalene) modified carbon paste electrode. *Arab. J. Chem.* 10, 596–603. doi: 10.1016/j.arabjc.2015.08.021

Saraf, M., Rajak, R., and Mobin, S. M. (2016). A fascinating multitasking Cu-MOF/rGO hybrid for high performance supercapacitors and highly sensitive and selective electrochemical nitrite sensors. *J. Mater. Chem. A* 4, 16432–16445. doi: 10.1039/C6TA06470A

Singh, R., Gautam, N., Mishra, A., and Gupta, R. (2011). Heavy metals and living systems: an overview. *Indian J. Pharmacol.* 43:246. doi: 10.4103/0253-7613.81505

Tan, E., Yin, P., Lang, X., Zhang, H., and Guo, L. (2012). A novel surface-enhanced Raman scattering nanosensor for detecting multiple heavy metal ions based on 2-mercaptoisonicotinic acid functionalized gold nanoparticles. *Spectrochim. Acta A* 97, 1007–1012. doi: 10.1016/j.saa.2012.07.114

Travlou, N. A., Singh, K., Rodríguez-Castellón, E., and Bandosz, T. J. (2015). Cu–BTC MOF–graphene-based hybrid materials as low concentration ammonia sensors. *J. Mater. Chem. A* 3, 11417–11429. doi: 10.1039/C5TA01738F

Wang, L., Lei, T., Ren, Z., Jiang, X., Yang, X., Bai, H., et al. (2020). Fe3O4@ PDA@ MnO2 core-shell nanocomposites for sensitive electrochemical detection of trace Pb (II) in water. *J. Electroanal. Chem.* 864:114065. doi: 10.1016/j.jelechem.2020.114065

Wang, Y., Ge, H., Wu, Y., Ye, G., Chen, H., and Hu, X. (2014). Construction of an electrochemical sensor based on amino-functionalized metal-organic frameworks for differential pulse anodic stripping voltammetric determination of lead. *Talanta* 129, 100–105. doi: 10.1016/j.talanta.2014.05.014

Worrall, S. D., Bissett, M. A., Hill, P. I., Rooney, A. P., Haigh, S. J., Attfield, M. P., et al. (2016). Metal-organic framework templated electrodeposition of functional gold nanostructures. *Electrochim. Acta* 222, 361–369. doi: 10.1016/j.electacta.2016.10.187

Wu, G., Kang, H., Zhang, X., Shao, H., Chu, L., and Ruan, C. (2010). A critical review on the bio-removal of hazardous heavy metals from contaminated soils: issues, progress, eco-environmental concerns and opportunities. *J. Hazard. Mater.* 174, 1–8. doi: 10.1016/j.jhazmat.2009.09.113

Wuttke, S., Zimpel, A., Bein, T., Braig, S., Stoiber, K., Vollmar, A., et al. (2017). Validating metal-organic framework nanoparticles for their nanosafety in diverse biomedical applications. *Adv. Healthcare Mater.* 6:1600818. doi: 10.1002/adhm.201600818

Yadav, D. K., Gupta, R., Ganesan, V., Sonkar, P. K., and Yadav, M. (2018). Gold nanoparticles incorporated in a zinc-based metal-organic framework as multifunctional catalyst for the oxygen reduction and hydrogen evolution reactions. *ChemElectroChem* 5, 2612–2619. doi: 10.1002/celc.201800519

Zhang, C., Wang, M., Liu, L., Yang, X., and Xu, X. (2013). Electrochemical investigation of a new Cu-MOF and its electrocatalytic activity towards H_2O_2 oxidation in alkaline solution. *Electrochem. Commun.* 33, 131–134. doi: 10.1016/j.elecom.2013.04.026

Zhang, T., Gao, C., Huang, W., Chen, Y., Wang, Y., and Wang, J. (2018). Covalent organic framework as a novel electrochemical platform for highly sensitive and stable detection of lead. *Talanta* 188, 578–583. doi: 10.1016/j.talanta.2018.06.032

Zhou, J., Li, X., Yang, L., Yan, S., Wang, M., Cheng, D., et al. (2015). The Cu-MOF-199/single-walled carbon nanotubes modified electrode for simultaneous determination of hydroquinone and catechol with extended linear ranges and lower detection limits. *Anal. Chim. Acta* 899, 57–65. doi: 10.1016/j.aca.2015.09.054

Conflict of Interest: The authors declare that the research was conducted in the absence of any commercial or financial relationships that could be construed as a potential conflict of interest.

frontiers in Chemistry

ORIGINAL RESEARCH
published: 20 October 2020
doi: 10.3389/fchem.2020.00814

A DNA Based Biosensor Amplified With ZIF-8/Ionic Liquid Composite for Determination of Mitoxantrone Anticancer Drug: An Experimental/Docking Investigation

Marzieh Alizadeh[1], *Parviz Aberoomand Azar*[1], *Sayed Ahmad Mozaffari*[2]*, *Hassan Karimi-Maleh*[3] and *Ali-Mohammad Tamaddon*[4]

[1] Department of Chemistry, Science and Research Branch, Islamic Azad University, Tehran, Iran, [2] Department of Chemical Technologies, Iranian Research Organization for Science and Technology (IROST), Tehran, Iran, [3] Laboratory of Nanotechnology, Department of Chemical Engineering, Quchan University of Technology, Quchan, Iran, [4] Center for Nanotechnology in Drug Delivery, School of Pharmacy, Shiraz University of Medical Sciences, Shiraz, Iran

An ultrasensitive DNA electrochemical biosensor based on the carbon paste electrode (CPE) amplified with ZIF-8 and 1-butyl-3-methylimidazolium methanesulfonate (BMIMS) was fabricated in this research. The DNA/BMIMS/ZIF-8/CPE was used for the selective determination of a mitoxantrone anticancer drug in aqueous solution, resulting in a good catalytic effect and a powerful ability for determining mitoxantrone. Also, the interaction of the mitoxantrone anticancer drug with guanine bases of ds-DNA was used as a powerful strategy in the suggested biosensor, which was confirmed with docking investigation. Docking study of mitoxantrone into the ds-DNA sequence showed the intercalative binding mode of mitoxantrone into the nitrogenous-based pairs of ds-DNA. The effective factors such as ds-DNA concentration, temperature, buffer types, and incubation time were also optimized for the fabricated mitoxantrone biosensor. The results showed that, under optimum conditions (T = 25°C; incubation time=12 min; pH= 4.8 acetate buffer solution and [DNA] = 50 mg/L), the DNA/BMIMS/ZIF-8/CPE could be used in mitoxantrone assay in a concentration ranging from 8.0 nM to 110 μM with a detection limit of 3.0 nM. In addition, recovery data between 99.18 and 102.08% were obtained for the determination of mitoxantrone in the injection samples using DNA/ZIF-8/BMIMF/CPE as powerful biosensors.

Keywords: mitoxantrone, ZIF-8, 1-butyl-3-methylimidazolium methanesulfonate, modified electrode, ds-DNA biosensor, drug analysis

OPEN ACCESS

Edited by:
Baiqing Yuan,
Ludong University, China

Reviewed by:
Xia Li,
Liaocheng University, China
Gennady Evtugyn,
Kazan Federal University, Russia

***Correspondence:**
Sayed Ahmad Mozaffari
mozaffari@irost.ir

Specialty section:
This article was submitted to Supramolecular Chemistry, a section of the journal Frontiers in Chemistry

Received: *28 June 2020*
Accepted: *03 August 2020*
Published: *20 October 2020*

Citation:
Alizadeh M, Azar PA, Mozaffari SA, Karimi-Maleh H and Tamaddon A-M (2020) A DNA Based Biosensor Amplified With ZIF-8/Ionic Liquid Composite for Determination of Mitoxantrone Anticancer Drug: An Experimental/Docking Investigation. Front. Chem. 8:814. doi: 10.3389/fchem.2020.00814

INTRODUCTION

Mitoxantrone (developed in the 1980's) is one of the famous anthracycline anti-cancer agents with a wide range of applications in the treatment of breast cancer, acute myelogenous leukemia, and Non-Hodgkin's lymphoma (Lenk et al., 1987; Vollmer et al., 2010). This drug stays in the body for a long time (elimination $t1/2 = 75$ h) and has various side effects such as low blood counts, nausea, vomiting, weakness, low blood pressure, and hair loss (Scott and Figgitt, 2004). Moreover,

the highest concentrations of mitoxantrone were detected in the heart, liver, and thyroid (Fox, 2004). Assay of anticancer drugs in biological samples such as blood is one of the most important strategies available to monitor the harmful effects of such drugs on the body (Bolanowska et al., 1983; Baghayeri et al., 2014, 2017, 2018a; Beitollahi et al., 2014; Veisi et al., 2015; Fouladgar, 2018). From the methods reported for measuring the pharmaceutical and biological compounds, electrochemical methods with more advantages such as simplicity of analysis method, low cost, and fast analysis are considered to be more important compared to the other methods (Yuan et al., 2013, 2017; Mozaffari et al., 2014; Eren et al., 2015; Movaghgharnezhad and Mirabi, 2019). Intercalative binding between DNA and mitoxantrone has been proven by the Li group (Li et al., 2005). Accordingly, this makes it possible to design the DNA-based electrochemical biosensors for selective analysis of the drug (Tiwari and Sharma, 2020).

Moreover, the DNA-based biosensors have been reported as powerful tools with a high selectivity for the analytical determination of many compounds, especially for anticancer drugs (Brett et al., 1998; Gooding, 2002; Ozsoz et al., 2003; Ensafi et al., 2011). In this regard, the specific interaction of anticancer drugs with adenine and guanine bases in the complex structure of DNA has been used as an appropriate analytical factor to design new biosensors in the analysis of anticancer drugs (Karimi-Maleh et al., 2018; Khodadadi et al., 2019; Yin et al., 2019). In addition, the sensitivity of the DNA-based biosensors is very low at surface of bare electrodes due to the presence of low-conductivity ds-DNA on the sensor surface (Li et al., 2017, 2020). Correspondingly, this point was introduced as one of the most important problems caused by the conventional DNA-based biosensors (Karimi-Maleh et al., 2020c). To overcome this problem, the DNA-based biosensors are typically amplified using the high-conductivity modifiers such as conductor polymers, organic and inorganic compounds, ionic liquids, and nanomaterials (Cheraghi et al., 2017; Sanati and Faridbod, 2017; Baghayeri et al., 2019; Faridbod and Sanati, 2019).

Nanomaterials such as nanoparticles, nanotubes, and nano porous compounds showed many advantages in different fields and also created a new approach to science (Rahmanian et al., 2015; Xu et al., 2018; Yuan et al., 2019, 2020; Karimi-Maleh et al., 2020a). Accordingly, Nano porous materials like zeolitic imidazolate frameworks (ZIF) are a new type of nanomaterials with a high surface area and metal ion in center and imidazolate linkers (Quang Khieu et al., 2018). Recently, many researchers focused on the usage of ZIF and especially ZIF-8 for the electrochemical applications (Wang et al., 2015). ZIF-8 is very stable in water and other aqueous solutions and could be used as mediator for the fabrication of electrochemical sensors for analysis of electroactive compound in water solution (Banerjee et al., 2008). Although the high surface area of ZIF compounds makes creating a more active surface area for electrochemical sensors possible, its low electrical conductivity is one of the most important problems of its high use in electrochemical sensors (Lu et al., 2020). Therefore, to eliminate this problem, the simultaneous usage of these materials with compounds that have a high electrical conductivity such as conductive polymers and ionic liquids, is recommended (Baghayeri et al., 2018b; Jin et al., 2018; Chen et al., 2019).

Ionic liquids are highly conductive and are a green type of organic compound with a wide range application in different scientific fields (Marr and Marr, 2016; Osada et al., 2016; Atta et al., 2019; Tahernejad-Javazmi et al., 2019; Arabali et al., 2020). Moreover, due to the high conductivity and wide electrochemical range windows, ionic liquids were used as amplifiers with a high quality in the fabrication of electrochemical sensors (Bijad et al., 2013; Beytur et al., 2018; Li et al., 2019; Hojjati-Najafabadi et al., 2020). There are many published scientific papers for the application of ionic liquid coupled with other nanomaterials to create a high quality electrochemical sensor in the environmental and biological compounds analyses (Karimi-Maleh et al., 2020b).

Based on the scientific information reported in previous studies, this study developed a high-sensitivity electrochemical biosensor in terms of the use of DNA as a recognition element for analyzing the mitoxantrone anti-cancer drug. To improve the sensitivity of the DNA-based biosensor, the electrode surface was amplified with ZIF-8 and BMIMF as the conductive modifiers with a high surface. The results showed a good selectivity for the analysis of mitoxantrone anti-cancer drug in drugs samples. The docking investigation confirmed the intercalation interaction between the guanine base and mitoxantrone anti-cancer drugs.

EXPERIMENTAL

Instrument and Materials

Electrochemical investigation was performed by electrochemical workstation model Ivium-Vertex connected to an electrochemical Cell (Azar electrode Company, Iran). Moreover, the I-V signals were displayed based on the $Ag/AgCl/KCl_{sat}$ reference electrode's potential. Mitoxantrone hydrochloride, ZIF-8, BMIMF, and DNA (Calf Thymus) were purchased from Sigma-Aldrich. Also, carbon powder and paraffin oil were obtained from Merck Company. In addition, phosphoric acid, boric acid, acetic acid, and Tris hydrochloride were purchased from Across Company. Notably, the stock solution of mitoxantrone hydrochloride (0.001 M) was prepared by dissolving 0.517 g mitoxantrone hydrochloride in 100 mL distillated water under the stirring conditions.

Preparation of BMIMS/ZIF-8/CPE

The BMIMS/ZIF-8/CPE was prepared by mixing ZIF-8 with carbon powder as the powder components in the ratio 5:95 (w/w), and paraffin oil and BMIMS as the liquid binders in the ratio 8:2 (v/v). Accordingly, these ratios of powder and binder components were optimized by recording voltammograms of solution containing 1.0 mM $[Fe(CN)_6]^{3-,4-}$ at the surface of electrodes with different ratios of the components. Also, the stability of ZIF-8 as aqueous solution helps for a repeatable electrochemical response in electroanalytical systems.

Preparation of DNA/BMIMS/ZIF-8/CPE

DNA/BMIMS/ZIF-8/CPE was perpetrated by the addition of 10 μL of ds-DNA solution (50 mg/L) prepared into acetate buffer (0.5 M, pH 4.8) using a dropwise strategy. Notably, this

value was optimized by recording ds-DNA at the surface of DNA/BMIMS/ZIF-8/CPE in the concentration ranged between 10 and 60 mg/L.

Intercalation Investigation

To study the intercalation of mitoxantrone hydrochloride with ds-DNA at the surface of DNA/BMIMS/ZIF-8/CPE, the electrode was immersed into a solution containing Tris-HCL buffer solution (pH = 7.4) with mitoxantrone hydrochloride and then remained for 12 min under the stringing condition. Afterward, the electrode was washed with the acetate buffer solution and the differential pulse voltammograms of electrode was then recorded in acetate solution (0.5 M, pH 4.8).

Molecular Docking Study

In this work, the molecular docking study is performed to evaluate the affinity of mitoxantrone drug in the active site of DNA hexamer d(CGATCG)2 containing an intercalation gap (PDB ID:1Z3F). For a comprehensive investigation of the binding orientation analysis, the best conformer with the lowest root mean square deviation (RMSD) value of 0 Å and the highest binding energy value is selected. The docking of mitoxantrone into the DNA sequence suggests the intercalation of the aromatic rings of mitoxantrone drug between cytosine and guanine base pairs of DNA with a binding energy of −6.7 kcal/mol as shown in **Figure 1**, curve a. The docked model reveals that the hydrogen and oxygen atoms of mitoxantrone drug have participated as the donor and acceptor to form four intermolecular hydrogen bonds (HBs) with base pairs of DNA (see **Figure 1**, curve b). It is found that the interaction of oxygen (O5) atoms of drug molecule with H22 atom of deoxyguanosine (DG6 of chain B) of DNA leads to O5…H22-N2 conventional HB with distance of 2.6 Å. Also, the H36 atom of drug as the proton donor interacts with O4′ atom of deoxyribose sugar moiety linked to guanine (DG6 of chain B) as a proton acceptor with a distance of 2.3 Å. Furthermore, the hydrogen atom of the hydroxyl terminal group of drug molecule is bonded to the second and forth oxygen atoms of deoxycytosine (DC5 of chain B) of hexamer of DNA, i.e., O2…H60-O6 and O4′…H60-O6 with the O…H distances of 2.4 and 2.2 Å, respectively. The hydrogen bond angles are 109.5°, 110.5°, 134.5°, and 163.6° for O5…H22-N2, O2…H60-O6, O4′…H60-O6 and O4′…H36-N8, respectively. In addition, the intermolecular interactions between carbonyl groups of mitoxantrone drug and oxygen atoms of DNA sequence, i.e., O2 atom of DC5 chain B, O4′ atom of DG6 chain B and O4′ atom of DG2 chain A with the respective O…O bond lengths of 3.3, 3.5 and 3.4 Å are observed. The docking study approves the interaction between mitoxantrone drug and guanine residues of DNA contributes in the formation of the stable mitoxantrone-DNA complex.

Real Sample Analysis

Mitoxantrone (12.5 mg/12.5 mL) was purchased from a local pharmacy and then used as a real sample with no pretreatment. The standard addition method was used for analyzing the mitoxantrone concentration in the injection sample using DNA/BMIMS/ZIF-8/CPE.

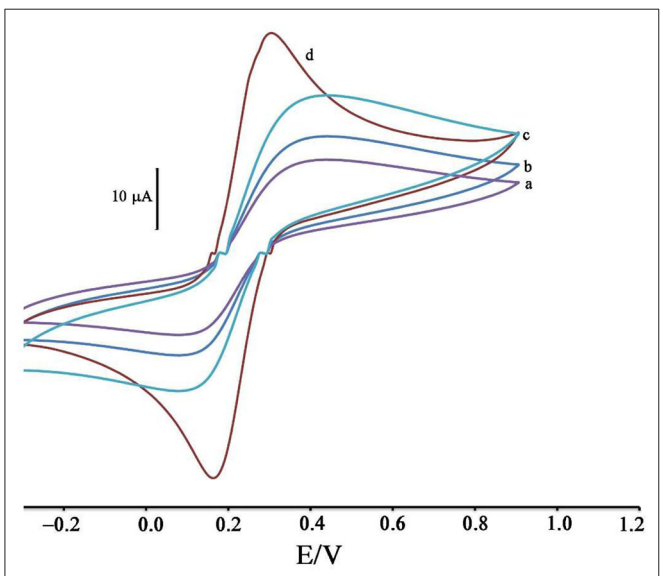

FIGURE 1 | Cyclic voltammograms of solution 1.0 mM $[Fe(CN)_6]^{3-/4-}$ in the presence of KCl 1.0 M at surface of (a) CPE, (b) ZIF-8/CPE, (c) BMIMS/CPE and (d) BMIMS/ZIF-8/CPE.

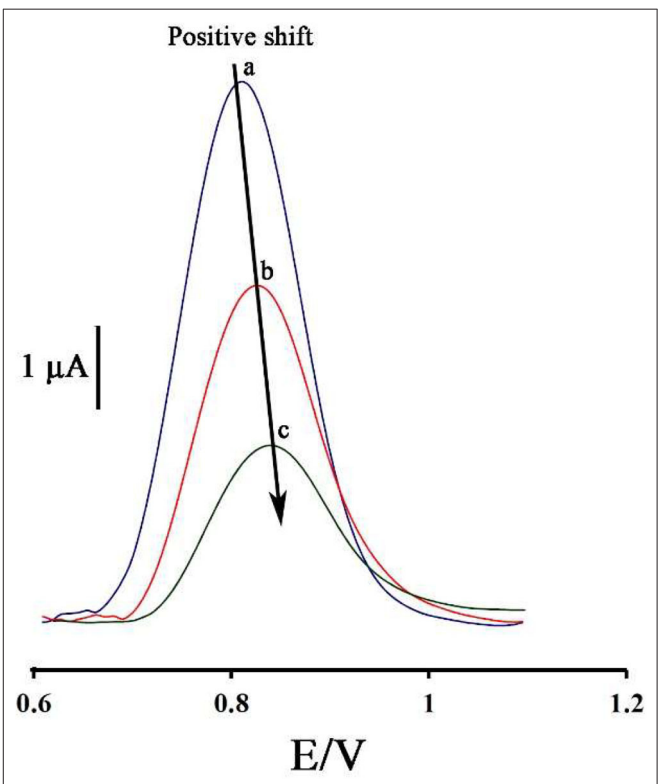

FIGURE 2 | Differential pulse voltammograms of DNA/BMIMS/ZIF-8/CPE in the absence (a) and in the presence of 35.0 μM (b) and 80.0 μM (c) mitoxantrone, respectively.

RESULTS AND DISCUSSION

Modification Process Investigation

The modification of the CPE surface with BMIMS and ZIF-8 was investigated by recording the cyclic voltammograms of the solution containing 1.0 mM $[Fe(CN)_6]^{3-,4-}$. By moving CPE (**Figure 1**, curve a) to ZIF-8/CPE (**Figure 1**, curve b), a little improvement was obtained in the oxidation signal of $[Fe(CN)_6]^{3-,4-}$ redox solution, which can be related to the creation of a high surface area of ZIF-8 at surface of CPE. After the addition of BMIMS and at a surface of BMIMS/CPE (**Figure 1**, curve c), the oxidation current of CPE was increase from 14.65 to 24.4 μA that is relative to high conductivity of IL.

After modification of CPE with ZIF-8 and BMIMS, a sharp redox signal with an oxidation current 34.8 μA was observed relative to $[Fe(CN)_6]^{3-/4-}$ that can be associated with the synergic effects of BMIMS and ZIF-8 at surface of CPE. This amplification can be created under a high sensitivity condition to determine mitoxantrone at surface of DNA/BMIMS/ZIF-8/CPE. In addition, active surface area of CPE, ZIF-8/CPE, BMIMS/CPE and BMIMS/ZIF-8/CPE were calculated about 0.121, 0.163, 0.184, and 0.22 cm^2 by solution containing 1.0 mM $[Fe(CN)_6]^{3-/4-}$ and results confirmed that mediators could be increased active surface area of CPE.

Intercalation Investigation of Mitoxantrone at Surface of DNA/BMIMS/ZIF-8/CPE

Figure 2 displays the ds-DNA signal of DNA/BMIMS/ZIF-8/CPE in the absence (curve a) and in the presence of 35.0 and 80.0 μM mitoxantrone (curves b & c), respectively. According to the data reported, the oxidation signal of ds-DNA decreased from 6.2 to 3.87 μA and 2.02 μA in the presence of 35.0 and 80.0 μM mitoxantrone, respectively. Furthermore, the peak potential related to the guanine base shifted from 816 to 825 mV and 845 mV along with the increase of mitoxantrone concentration confirming the intercalation interaction between mitoxantrone and guanine base in ds-DNA structure.

As can be seen, along with increasing of the mitoxantrone concentration, the oxidation current of ds-DNA decreased. Accordingly, this point can be selected as an analytical factor for the determination of mitoxantrone concentration in the solution.

Optimization of ds-DNA Biosensor for Mitoxantrone Detection

In order to create the best analytical conditions, it is important to optimize the significant factors in the analytical behavior of the biosensor. Therefore, the initial concentration of dsDNA, temperature, buffer types, and incubation time should be optimized.

Figure 3 displays the oxidation current of ds-DNA compared to the initial concentration of ds-DNA during the modification process.

As can be seen, along with the increase of the initial concentration of ds-DNA, the oxidation signal of DNA/BMIMS/ZIF-8/CPE increased to a concentration of

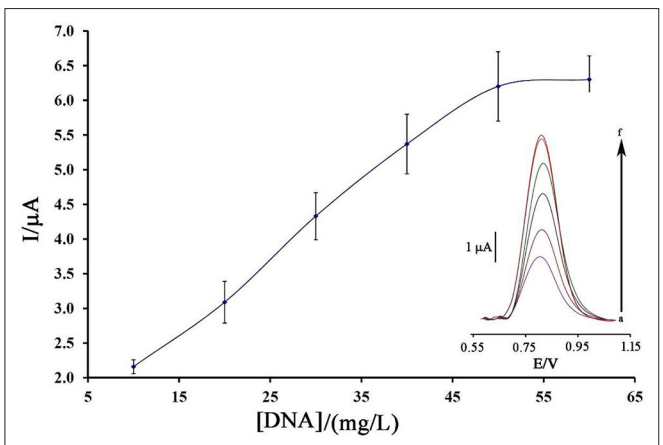

FIGURE 3 | Plot of the oxidation current of ds-DNA compared to its concentration at surface of BMIMS/ZIF-8/CPE ($n = 4$). Inset) Relative differential pulse voltammograms of ds-DNA at surface of BMIMS/ZIF-8/CPE.

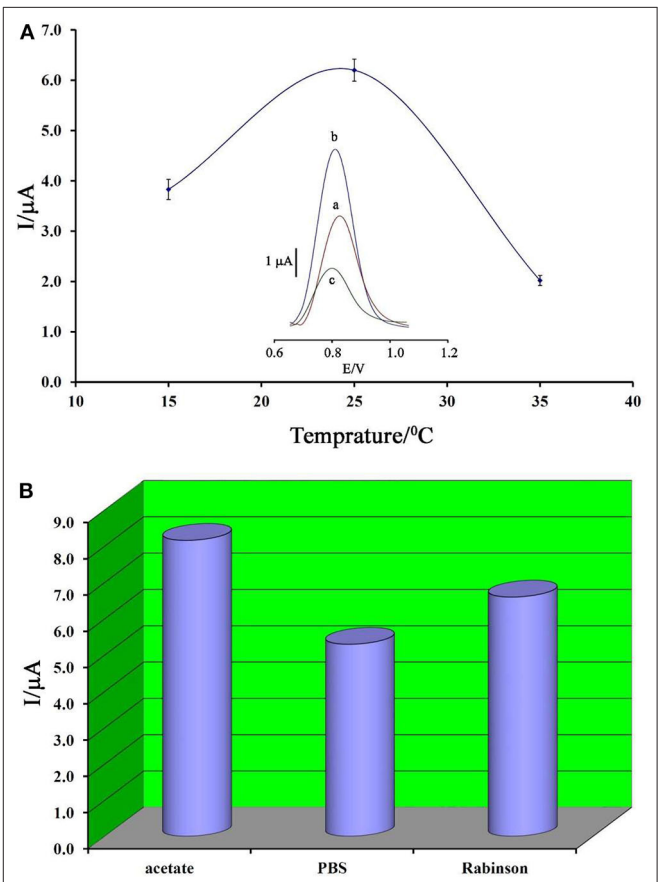

FIGURE 4 | (A) Plot of oxidation current of ds-DNA compared to changing in temperature ($n = 4$). Inset) Differential pulse voltammograms of ds-DNA/BMIMS/ZIF-8/CPE recorded at (a) 15°C, (b) 25°C, and (c) 35°C. **(B)** Diagram of oxidation current of ds-DNA compared to the type of buffer recorded under the optimum conditions.

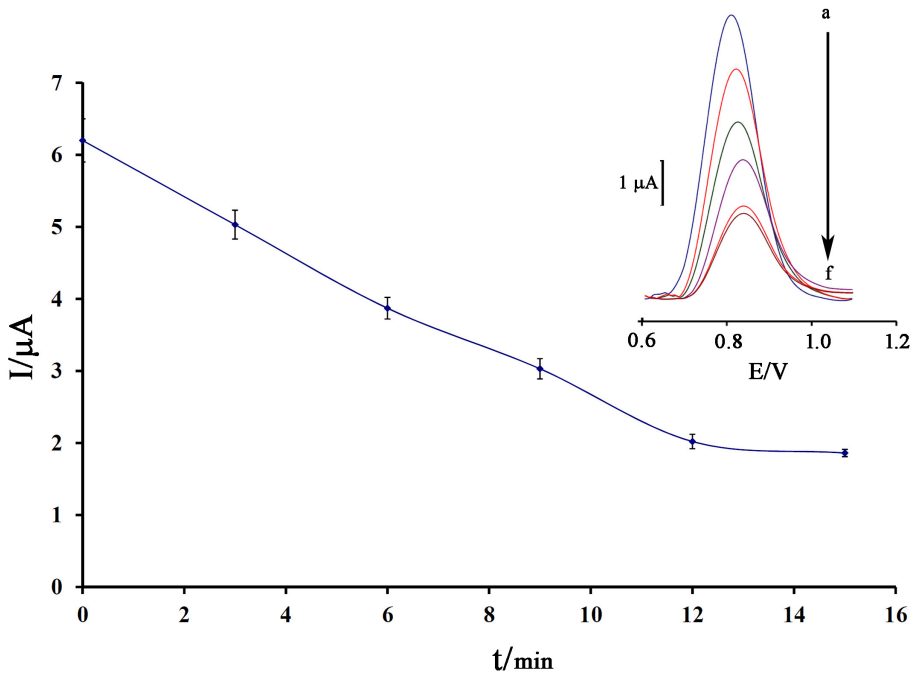

FIGURE 5 | Effect of the incubation time of 80.0 μM mitoxantrone with DNA/BMIMS/ZIF-8/CPE on the guanine oxidation signal ($n = 4$). Inset Relative DPVs in incubation time investigation.

50 mg/L, which then remained constant. Correspondingly, this point confirms that, in the solution containing 50 mg/L, the electrode surface of BMIMS/ZIF-8/CPE was saturated by ds-DNA, and also the maximum signal can be observed.

Temperature is known as one of the important factors in the fabrication of a DNA biosensor. In this regard, the changes in the ambient temperature of the test can affect the stability of the DNA at the electrode surface. Therefore, in this research, this factor was optimized. As can be seen in **Figure 4A**, by increasing the ambient temperature from 15 to 25°C, the ds-DNA signal has increased, and then, along with increasing the temperature up to 35°C, this signal has decreased. This point confirms that, in high temperatures, the electrode surface cannot keep ds-DNA at surface of BMIMS/ZIF-8/CPE.

Accordingly, the decreased viscosity of binders in the carbon paste matrix could be considered as one of the main reasons for this point. In addition, in low temperatures, the activity of ds-DNA was low and DNA/BMIMS/ZIF-8/CPE showed a low oxidation signal.

In addition, the type of buffer is one of the main factors in the deposition of ds-DNA at surface of BMIMS/ZIF-8/CPE. Therefore, the effect of acetate buffer, Britton–Robinson buffer, and phosphate buffer solutions on the deposition step of ds-DNA were investigated. As can be seen in **Figure 4B**, the best oxidation signal relative to ds-DNA can be detected in the solution containing acetate buffer solution and this buffer was selected as the best condition in the next step of the experiment. Moreover, the interference between the phosphate groups of phosphate buffers or Britton–Robinson buffer can be considered as the most important factor in the creation of a weak ds-DNA signal in these buffers.

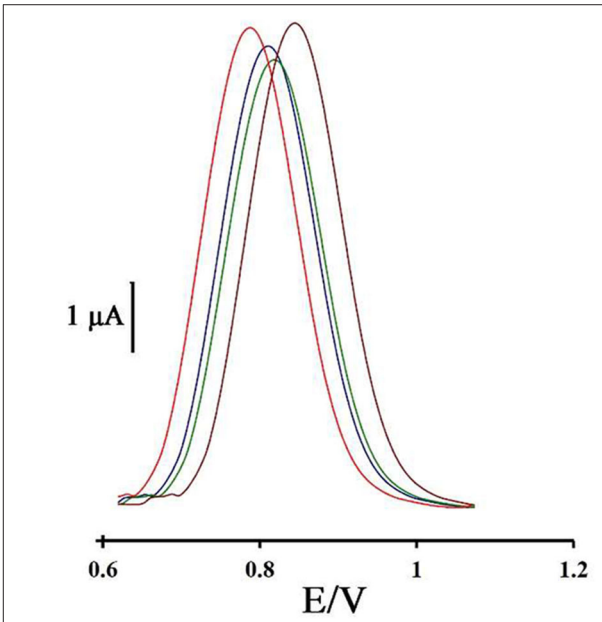

FIGURE 6 | Differential pulse voltammogram of four DNA/ZIF-8/BMIMF/CPE prepared under the same condition.

Notably, incubation time is an important factor in the final step of ds-DNA biosensor application in determining anticancer

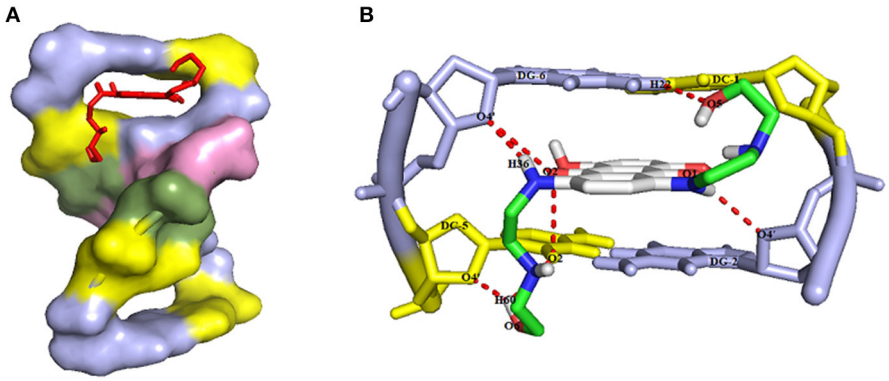

FIGURE 7 | (A) The intercalation of MTX drug (red color) into the guanine and cytosine base pairs of DNA receptor (deoxcytosine DC and deoxyguanosine DG in yellow and blue light colors, respectively), and **(B)** The intermolecular hydrogen bond interactions between MTX drug and DNA hexamer d(CGATCG)2 with the numbering atoms discussed earlier in the text.

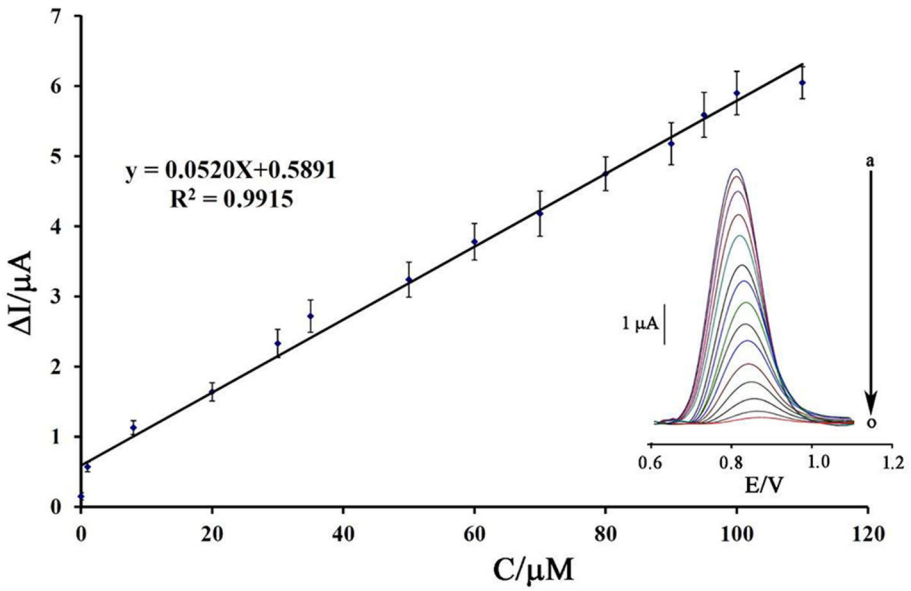

FIGURE 8 | Plot of net current vs. mitoxantrone concentration ($n = 4$). Inset) DP voltammograms of DNA/BMIMS/ZIF-8/CPE in the presence of (a) 0.0; (b) 0.008; (c) 1.0; (d) 8.0; (e) 20.0; (f) 30.0; (g) 35.0; (h) 50.0; (i) 60.0; (j) 70.0; (k) 80.0; (l) 90.0; (m) 95; (n) 100, and (o) 110 μM mitoxantrone.

drugs. Also, the low time of the intercalation step does not allow the biosensor to have a proper interaction between the guanine base and the anticancer drugs. Also, in the long term, it is possible to release the ds-DNA-drug into solution and saturation guanine sites in ds-DNA by anticancer drugs. In this regard, the recorded data showed that 12 min is a suitable incubation time for this study (**Figure 5**).

Repeatability Sensor Construction

To investigate the repeatability of the DNA biosensor, four different DNA/BMIMS/ZIF-8/CPE which were fabricated by the same procedure and oxidation signal of guanine were also recorded at the surface of fabricated electrodes (**Figure 6**). The obtained results showed the relative standard deviation of about 2.7 and 3.1% in the current and potential of guanine signal for four electrodes that are acceptable values for a novel DNA-biosensor.

Molecular Docking Study

In this research, the molecular docking study was performed to evaluate the affinity of Mitoxantrone (MTX) drug in the active site of DNA hexamer d (CGATCG) 2 containing an intercalation gap (PDB ID: 1Z3F). For conducting a comprehensive investigation on the binding orientation analysis, the best conformer with the lowest root mean square deviation (RMSD) value of 0 Å and also with the highest binding energy value, was selected. Docking of MTX into DNA sequence suggests the intercalation of the aromatic rings of Mitoxantrone

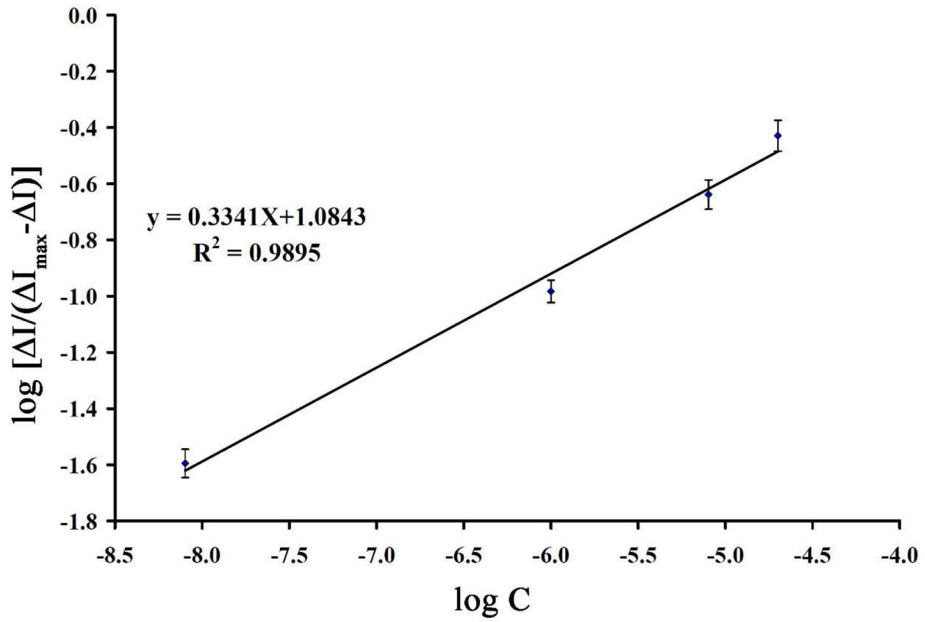

FIGURE 9 | The plot of Log [$\Delta I/(\Delta I_{max}$ - $\Delta I)$] *vs.* log ([mitoxantrone]/M) ($n = 4$).

drug between the cytosine and guanine base pairs of DNA with a binding energy of −6.7 kcal/mol, as shown in **Figure 7A**. The docked model revealed that, the hydrogen and oxygen atoms of MTX drug are participating as the donor and acceptor, to form four intermolecular hydrogen bonds (HBs) with base pairs of DNA, respectively (see **Figure 7B**). It was found that the interaction of oxygen (O5) atoms of the drug molecule with H22 atoms of deoxyguanosine (DG6 of chain B) of DNA leads to O5…H22-N2 conventional HB with a distance of 2.6 Å. Also, the H36 atom of the drug, as the proton donor, interacts with O4′ atom of deoxyribose sugar moiety linked to guanine (DG6 of chain B), as a proton acceptor with a distance of 2.3 Å. Furthermore, the hydrogen atom of the hydroxyl terminal group of drug molecule is bonded to the second and forth oxygen atoms of deoxycytosine (DC5 of chain B) of hexamer of DNA, i.e., O2…H60-O6 and O4′…H60-O6 with the O…H distances of 2.4 and 2.2 Å, respectively. Moreover, the hydrogen bond angles are 109.5°, 110.5°, 134.5°, and 163.6° for O5…H22-N2, O2…H60-O6, O4′…H60-O6, and O4′…H36-N8, respectively. In addition, the intermolecular interactions between carbonyl groups of MTX drug and oxygen atoms of DNA sequence, such as O2 atom of DC5 chain B, O4′ atom of DG6 chain B, and O4′ atom of DG2 chain A with the respective O…O bond lengths of 3.3, 3.5, and 3.4 Å were observed. The docking study approves the interaction between mitoxantrone drug and guanine residues of DNA that contributes in the formation of the stable MTX-DNA complex.

Analytical Approach

Using a decreasing trend in DNA signals and its relationship with the concentration of mitoxantrone, a linear dynamic range from 8.0 nM to 110 μM with the equation of $\Delta I_{pa} = 0.052\ C_{mitoxantrone} + 0.589$ ($R^2 = 0.991$) and a detection limit of 3.0 nM was calculated to determine mitoxantrone at surface of DNA/BMIMS/ZIF-8/CPE (**Figure 8**).

TABLE 1 | The results related to real sample analysis of mitoxantrone by DNA/BMIMS/ZIF-8/CPE ($n = 4$).

Sample	Added (μM)	Expected (μM)	Founded (μM)	Recovery%
Injection (1)	—	—	1.97 ± 0.21	—
After dilution				
	10.00	11.97	12.22 ± 0.43	102.08
Injection (2)	—	—	2.05 ± 0.28	—
After dilution				
	20.00	22.05	21.87 ± 0.87	99.18

Kinetic Investigation

Binding energy between guanine and mitoxantrone can be determined by equation 1 as follows:

$$\mathrm{Log}[\Delta I/(\Delta I_{max} - \Delta I)] = m \log(K_a/M) + m \log([\mathrm{mitoxantrone}]/M) \quad (1)$$

Where m is the binding number and K_a is the association equilibrium constant. Using the slope of recording plot in **Figure 9** and equation 1, the values of m and K_a were determined to be 0.334 and $1.737 \times 10^3\ M^{-1}$, respectively.

Real Sample Analysis and Selectivity Investigation

The selectivity of DNA/BMIMS/ZIF-8/CPE, as a new biosensor, was investigated in the presence some usual organic and inorganic interference with an acceptable error of 5% in current and potential. The obtained results

showed 1,000-fold of ions such as Na^+, Li^+, Br^-, and NO_3^-, 500-fold of methionine, alanine, and phenylalanine, and also 400-fold of vitamin C and vitamin B_2 had no interference in determination of 20 μM mitoxantrone using the suggested biosensor.

In addition, the ability of DNA/BMIMS/ZIF-8/CPE was checked as a new biosensor for determination of mitoxantrone in the injection samples using the standard addition method. The results are presented in **Table 1** and recovery data between 99.18 and 102.08% confirmed the high performance ability of DNA/BMIMS/ZIF-8/CPE for determination of mitoxantrone in real samples.

CONCLUSION

In this study, a high performance DNA biosensor amplified with ZIF-8 and 1-butyl-3-methylimidazolium methanesulfonate was made-up as a new analytical tool to determine mitoxantrone anticancer drug. The presence of ZIF-8 helps in high loading of ds-DNA and also in improving the quality of the sensor in optimum conditions (T = 25°C; incubation time = 12 min; pH = 4.8 acetate buffer solution and [DNA] = 50 mg/L). In addition, the BMIMS helped as a conductive binder for improving the sensitivity of sensor for trace level analysis of mitoxantrone anticancer drug. Moreover, the DNA/BMIMS/ZIF-8/CPE was successfully used for nano-molar determination of mitoxantrone (LOD = 3.0 nM). In addition, recovery data 99.18–102.08% confirmed the high performance ability of DNA/BMIMS/ZIF-8/CPE as a new biosensor to determine mitoxantrone in the injection samples.

DATA AVAILABILITY STATEMENT

The original contributions presented in the study are included in the article/supplementary material, further inquiries can be directed to the corresponding author/s.

AUTHOR CONTRIBUTIONS

MA: experimental part. PA and SM: characterization of electrochemical results. HK-M: written of paper and electrode modification design. A-MT: Checking the English level of paper and helping in intercalation investigation. All authors contributed to the article and approved the submitted version.

REFERENCES

Arabali, V., Malekmohammadi, S., and Karimi, F. (2020). Surface amplification of pencil graphite electrode using CuO nanoparticle/polypyrrole nanocomposite: a powerful electrochemical strategy for determination of tramadol. *Microchem. J.* 158:105179. doi: 10.1016/j.microc.2020.105179

Atta, N. F., Galal, A., and Hassan, S. H. (2019). Ultrasensitive determination of nalbuphine and tramadol narcotic analgesic drugs for postoperative pain relief using nano-cobalt oxide/ionic liquid crystal/carbon nanotubes-based electrochemical sensor. *J. Electroanal. Chem.* 839, 48–58. doi: 10.1016/j.jelechem.2019.03.002

Baghayeri, M., Alinezhad, H., Fayazi, M., Tarahomi, M., Ghanei-Motlagh, R., and Maleki, B. (2019). A novel electrochemical sensor based on a glassy carbon electrode modified with dendrimer functionalized magnetic graphene oxide for simultaneous determination of trace Pb (II) and Cd (II). *Electrochim. Acta* 312, 80–88. doi: 10.1016/j.electacta.2019.04.180

Baghayeri, M., Amiri, A., Alizadeh, Z., Veisi, H., and Hasheminejad, E. (2018a). Non-enzymatic voltammetric glucose sensor made of ternary NiO/Fe3O4-SH/para-amino hippuric acid nanocomposite. *J. Electroanal. Chem.* 810, 69–77. doi: 10.1016/j.jelechem.2018.01.007

Baghayeri, M., Mahdavi, B., Hosseinpor-Mohsen Abadi, Z., and Farhadi, S. (2018b). Green synthesis of silver nanoparticles using water extract of Salvia leriifolia: antibacterial studies and applications as catalysts in the electrochemical detection of nitrite. *Appl. Organomet. Chem.* 32:e4057. doi: 10.1002/aoc.4057

Baghayeri, M., Maleki, B., and Zarghani, R. (2014). Voltammetric behavior of tiopronin on carbon paste electrode modified with nanocrystalline Fe50Ni50 alloys. *Mater. Sci. Eng. C* 44, 175–182. doi: 10.1016/j.msec.2014.08.023

Baghayeri, M., Rouhi, M., Lakouraj, M. M., and Amiri-Aref, M. (2017). Bioelectrocatalysis of hydrogen peroxide based on immobilized hemoglobin onto glassy carbon electrode modified with magnetic poly (indole-co-thiophene) nanocomposite. *J. Electroanal. Chem.* 784, 69–76. doi: 10.1016/j.jelechem.2016.12.006

Banerjee, R., Phan, A., Wang, B., Knobler, C., Furukawa, H., O'Keeffe, M., et al. (2008). High-throughput synthesis of zeolitic imidazolate frameworks and application to CO2 capture. *Science* 319, 939–943. doi: 10.1126/science.1152516

Beitollahi, H., Tajik, S., Mohammadi, S. Z., and Baghayeri, M. (2014). Voltammetric determination of hydroxylamine in water samples using a 1-benzyl-4-ferrocenyl-1H-[1, 2, 3]-triazole/carbon nanotube-modified glassy carbon electrode. *Ionics* 20, 571–579. doi: 10.1007/s11581-013-1004-0

Beytur, M., Kardaş F., Akyildirim, O., Özkan, A., Bankoglu B, Yüksek, H., Yola, M. L., et al. (2018). A highly selective and sensitive voltammetric sensor with molecularly imprinted polymer based silver@ gold nanoparticles/ionic liquid modified glassy carbon electrode for determination of ceftizoxime. *J. Mol. Liquids* 251, 212–217. doi: 10.1016/j.molliq.2017.12.060

Bijad, M., Karimi-Maleh, H., and Khalilzadeh, M. A. (2013). Application of ZnO/CNTs nanocomposite ionic liquid paste electrode as a sensitive voltammetric sensor for determination of ascorbic acid in food samples. *Food Analy. Methods* 6, 1639–1647. doi: 10.1007/s12161-013-9585-9

Bolanowska, W., Gessner, T., and Preisler, H. (1983). A simplified method for determination of daunorubicin, adriamycin, and their chief fluorescent metabolites in human plasma by high-pressure liquid chromatography. *Cancer Chemother. Pharmacol.* 10, 187–191. doi: 10.1007/BF00255759

Brett, A. O., Macedo, T., Raimundo, D., Marques, M., and Serrano, S. (1998). Voltammetric behaviour of mitoxantrone at a DNA-biosensor. *Biosens. Bioelectron.* 13, 861–867. doi: 10.1016/S0956-5663(98)00053-0

Chen, Y., Huang, W., Chen, K., Zhang, T., Wang, Y., and Wang, J. (2019). Facile fabrication of electrochemical sensor based on novel core-shell PPy@ ZIF-8 structures: enhanced charge collection for quercetin in human plasma samples. *Sens Actuators B Chem.* 290, 434–442. doi: 10.1016/j.snb.2019.04.006

Cheraghi, S., Taher, M. A., Karimi-Maleh, H., and Faghih-Mirzaei, E. (2017). A nanostructure label-free DNA biosensor for ciprofloxacin analysis as a chemotherapeutic agent: an experimental and theoretical investigation. *N. J. Chem.* 41, 4985–4989. doi: 10.1039/C7NJ00609H

Ensafi, A. A., Taei, M., Rahmani, H., and Khayamian, T. (2011). Sensitive DNA impedance biosensor for detection of cancer, chronic lymphocytic leukemia, based on gold nanoparticles/gold modified electrode. *Electrochim. Acta* 56, 8176–8183. doi: 10.1016/j.electacta.2011.05.124

Eren, T., Atar, N., Yola, M. L., and Karimi-Maleh, H. (2015). A sensitive molecularly imprinted polymer based quartz crystal microbalance nanosensor for selective determination of lovastatin in red yeast rice. *Food Chem.* 185, 430–436. doi: 10.1016/j.foodchem.2015.03.153

Faridbod, F., and Sanati, A. L. (2019). Graphene quantum dots in electrochemical sensors/biosensors. *Curr. Anal. Chem.* 15, 103–123. doi: 10.2174/1573411014666180319145506

Fouladgar, M. (2018). CuO-CNT nanocomposite/ionic liquid modified sensor as new breast anticancer approach for determination of

doxorubicin and 5-fluorouracil drugs. *J. Electrochem. Soc.* 165, B559–B564. doi: 10.1149/2.1001811jes

Fox, E. J. (2004). Mechanism of action of mitoxantrone. *Neurology* 63, S15–S18. doi: 10.1212/WNL.63.12_suppl_6.S15

Gooding, J. J. (2002). Electrochemical DNA hybridization biosensors. *Electroanalysis* 14, 1149–1156. doi: 10.1002/1521-4109(200209)14:17<;1149::AID-ELAN1149>;3.0.CO;2-8

Hojjati-Najafabadi, A., Rahmanpour, M. S., Karimi, F., Zabihi-Feyzaba, H., Malekmohammad, S., Agarwal, S., et al. (2020). Determination of tert-Butylhydroquinone using a nanostructured sensor based on CdO/SWCNTs and ionic liquid. *Int. J. Electrochem. Sci.* 15, 6969–6980. doi: 10.20964/2020.07.85

Jin, Y. F, Ge, C. Y, Li, X. B, Zhang, M., Xu, G. R, and Li, D. H (2018). A sensitive electrochemical sensor based on ZIF-8–acetylene black–chitosan nanocomposites for rutin detection. *RSC Adv.* 8, 32740–32746. doi: 10.1039/C8RA06452K

Karimi-Maleh, H., Karimi, F., Alizadeh, M., and Sanati, A. L. (2020c). Electrochemical sensors, a bright future in the fabrication of portable kits in analytical systems. *Chem. Rec.* 20, 682–692. doi: 10.1002/tcr.201900092

Karimi-Maleh, H., Bananezhad, A., Ganjali, M. R., Norouzi, P., and Sadrnia, A. (2018). Surface amplification of pencil graphite electrode with polypyrrole and reduced graphene oxide for fabrication of a guanine/adenine DNA based electrochemical biosensors for determination of didanosine anticancer drug. *Appl. Surf. Sci.* 441, 55–60. doi: 10.1016/j.apsusc.2018.01.237

Karimi-Maleh, H., Karimi, F., Malekmohammadi, S., Zakariae, N., Esmaeili, R., Rostamnia, S., et al. (2020b). An amplified voltammetric sensor based on platinum nanoparticle/polyoxometalate/two-dimensional hexagonal boron nitride nanosheets composite and ionic liquid for determination of N-hydroxysuccinimide in water samples. *J. Mol. Liquids* 310:113185. doi: 10.1016/j.molliq.2020.113185

Karimi-Maleh, H., Shafieizadeh, M., Taher, M. A., Opoku, F., Kiarii, E. M., Govender, P. P., et al. (2020a). The role of magnetite/graphene oxide nanocomposite as a high-efficiency adsorbent for removal of phenazopyridine residues from water samples, an experimental/theoretical investigation. *J. Mol. Liquids* 298:112040. doi: 10.1016/j.molliq.2019.112040

Khodadadi, A., Faghih-Mirzaei, E., Karimi-Maleh, H., Abbaspourrad, A., Agarwal, S., and Gupta, V. K. (2019). A new epirubicin biosensor based on amplifying DNA interactions with polypyrrole and nitrogen-doped reduced graphene: experimental and docking theoretical investigations. *Sens Actuators B Chem.* 284, 568–574. doi: 10.1016/j.snb.2018.12.164

Lenk, H., Müller, U., and Tanneberger, S. (1987). Mitoxantrone: mechanism of action, antitumor activity, pharmacokinetics, efficacy in the treatment of solid tumors and lymphomas, and toxicity. *Anticancer Res.* 7, 1257–1264.

Li, N., Ma, Y., Yang, C., Guo, L., and Yang, X. (2005). Interaction of anticancer drug mitoxantrone with DNA analyzed by electrochemical and spectroscopic methods. *Biophys. Chem.* 116, 199–205. doi: 10.1016/j.bpc.2005.04.009

Li, X., Song, J., Xue, Q., Zhao, H., Liu, M., Chen, B., et al. (2017). Sensitive and selective detection of the p53 gene based on a triple-helix magnetic probe coupled to a fluorescent liposome hybridization assembly via rolling circle amplification. *Analyst* 142, 3598–3604. doi: 10.1039/C7AN01255A

Li, X., Yin, F., Xu, X., Liu, L., Xue, Q., Tong, L., et al. (2020). A facile DNA/RNA nanoflower for sensitive imaging of telomerase RNA in living cells based on "zipper lock-and-key" strategy. *Biosens. Bioelectron.* 147:111788. doi: 10.1016/j.bios.2019.111788

Li, Y., Ji, Y., Ren, B., Jia, L., Ma, G., and Liu, X. (2019). Carboxyl-functionalized mesoporous molecular sieve/colloidal gold modified nano-carbon ionic liquid paste electrode for electrochemical determination of serotonin. *Mater. Res. Bull.* 109, 240–245. doi: 10.1016/j.materresbull.2018.10.002

Lu, S., Hummel, M., Chen, K., Zhou, Y., Kang, S., and Gu, Z. (2020). Synthesis of Au@ ZIF-8 nanocomposites for enhanced electrochemical detection of dopamine. *Electrochem. Commun.* 144:106715. doi: 10.1016/j.elecom.2020.106715

Marr, P. C., and Marr, A. C. (2016). Ionic liquid gel materials: applications in green and sustainable chemistry. *Green Chem.* 18, 105–128. doi: 10.1039/C5GC02277K

Movaghgharnezhad, S., and Mirabi, A. (2019). Advanced nanostructure amplified strategy for voltammetric determination of folic acid. *Int. J. Electrochem. Sci.* 14, 10956–10965. doi: 10.20964/2019.12.79

Mozaffari, S. A., Rahmanian, R., Abedi, M., and Amoli, H. S. (2014). Urea impedimetric biosensor based on reactive RF magnetron sputtered zinc oxide nanoporous transducer. *Electrochim. Acta* 146, 538–547. doi: 10.1016/j.electacta.2014.08.105

Osada, de Vries, H., Scrosati, B., and Passerini, S. (2016). Ionic-liquid-based polymer electrolytes for battery applications. *Angew. Chem. Int. Edn.* 55, 500–513. doi: 10.1002/anie.201504971

Ozsoz, M., Erdem, A., Kara, P., Kerman, K., and Ozkan, D. (2003). Electrochemical biosensor for the detection of interaction between arsenic trioxide and DNA based on guanine signal. *Electroanalysis* 15, 613–619. doi: 10.1002/elan.200390077

Quang Khieu, D., Thi Thanh, M., Vinh Thien, T., Hai Phong, N., Hoang van, D., Dinh Du, P., et al. (2018). Synthesis and voltammetric determination of Pb (II) using a ZIF-8-based electrode. *J. Chem.* 2018, 1–12. doi: 10.1155/2018/5395106

Rahmanian, R., Mozaffari, S. A., and Abedi, M. (2015). Disposable urea biosensor based on nanoporous ZnO film fabricated from omissible polymeric substrate. *Mater. Sci. Eng. C* 57, 387–396. doi: 10.1016/j.msec.2015.08.004

Sanati, A. L., and Faridbod, F. (2017). Electrochemical determination of methyldopa by graphene quantum dot/1-butyl-3-methylimidazolium hexafluoro phosphate nanocomposite electrode. *Int. J. Electrochem. Sci.* 12, 7997–8005. doi: 10.20964/2017.09.71

Scott, L. J., and Figgitt, D. P. (2004). Mitoxantrone. *CNS Drugs* 18, 379–396. doi: 10.2165/00023210-200418060-00010

Tahernejad-Javazmi, F., Shabani-Nooshabadi, M., and Karimi-Maleh, H. (2019). 3D reduced graphene oxide/FeNi3-ionic liquid nanocomposite modified sensor; an electrical synergic effect for development of tert-butylhydroquinone and folic acid sensor. *Comp. B Eng.* 172, 666–670. doi: 10.1016/j.compositesb.2019.05.065

Tiwari, G., and Sharma, D. (2020). Electronic structure, spectra analysis and nano-range interactions of mitoxantrone with RNA base pairs: an anticancer drug. *Mater. Today Proc.* 29, 844–849. doi: 10.1016/j.matpr.2020.05.014

Veisi, H., Eshbala, F. H., Hemmati, S., and Baghayeri, M. (2015). Selective hydrogen peroxide oxidation of sulfides to sulfones with carboxylated multi-walled carbon nano tubes (MWCNTs-COOH) as heterogeneous and recyclable nanocatalysts under organic solvent-free conditions. *RSC Adv.* 5, 10152–10158. doi: 10.1039/C4RA14964E

Vollmer, T., Stewart, T., and Baxter, N. (2010). Mitoxantrone and cytotoxic drugs' mechanisms of action. *Neurology* 74, S41–S46. doi: 10.1212/WNL.0b013e3181c97f5a

Wang, Y., Zhang, Y., Hou, C., and Liu, M. (2015). Magnetic Fe_3O_4@ MOFs decorated graphene nanocomposites as novel electrochemical sensor for ultrasensitive detection of dopamine. *RSC Adv.* 5, 98260–98268. doi: 10.1039/C5RA20996J

Xu, C., Zhang, S., Zang, H., Yuan, B., Fan, R., Zhang, N., et al. (2018). A simple and facile electrochemical sensor for sensitive detection of histidine based on three-dimensional porous Ni foam. *Int. J. Electrochem. Sci.* 13, 9794–9802. doi: 10.20964/2018.10.60

Yin, F., Liu, L., Sun, X., Hou, L., Lu, Y., Xue, Q., et al. (2019). A facile deoxyuridine/biotin-modified molecular beacon for simultaneous detection of proteins and nucleic acids via a label-free and background-eliminated fluorescence assay. *Analyst* 144, 5504–5510. doi: 10.1039/C9AN01016E

Yuan, B., Sun, P., Zhao, L.-j, Zhang, D., Zhang, Y., Qi, C., Niu, Y., et al. (2020). Pd nanoparticles supported on 1, 10-phenanthroline-5, 6-dione modified graphene oxide as superior bifunctional electrocatalyst for highly sensitive sensing. *J. Electroanal. Chem.* 861:113945. doi: 10.1016/j.jelechem.2020.113945

Yuan, B., Wang, H., Cai, J., Peng, Y., Niu, Y., Chen, H., et al. (2019). A novel oxidation-reduction method for highly selective detection of cysteine over reduced glutathione based on synergistic effect of fully fluorinated cobalt phthalocyanine and ordered mesoporous carbon, *Sens. Actuators B Chem.* 288, 180–187. doi: 10.1016/j.snb.2019.02.114

Yuan, B., Xu, C., Deng, D., Xing, Y., Liu, L., Pang, H., et al. (2013). Graphene oxide/nickel oxide modified glassy carbon electrode for supercapacitor and nonenzymatic glucose sensor. *Electrochim. Acta* 88, 708–712. doi: 10.1016/j.electacta.2012.10.102

Yuan, B., Xu, C., Zhang, R., Lv, D., Li, S., Zhang, D., et al. (2017). Glassy carbon electrode modified with 7, 7, 8, 8-tetracyanoquinodimethane

and graphene oxide triggered a synergistic effect: Low-potential amperometric detection of reduced glutathione. *Biosens. Bioelectron.* 96, 1–7. doi: 10.1016/j.bios.2017.04.026

Conflict of Interest: The authors declare that the research was conducted in the absence of any commercial or financial relationships that could be construed as a potential conflict of interest.

frontiers in Chemistry

ORIGINAL RESEARCH
published: 11 November 2020
doi: 10.3389/fchem.2020.593948

Near-Infrared Phosphorescence Emission of Binuclear Mn(II) Based Metal-Organic Framework for Efficient Photoelectric Conversion

Mei-Li Zhang[1], *Zhi-Min Zhai*[2], *Xiao-Gang Yang*[2]*, *Ya-Dan Huang*[3], *Yan-Jin Zheng*[1] *and Lu-Fang Ma*[2]

[1] *Laboratory of New Energy and New Function Materials, Department of Chemistry and Chemical Engineering, Yan'an University, Yan'an, China,* [2] *Henan Province Function-Oriented Porous Materials Key Laboratory, College of Chemistry and Chemical Engineering, Luoyang Normal University, Luoyang, China,* [3] *College of Chemistry and Chemical Engineering, Henan Polytechnic University, Jiaozuo, China*

The development of metal-organic framework (MOF) based room-temperature phosphorescence (RTP) materials has raised extensive concern owing to their widespread applications in the field of anti-counterfeiting, photovoltaics, photocatalytic reactions, and bio-imaging. Herein, one new binuclear Mn(II) based 3D MOF $[Mn_2(L)(BMIB)\cdot(H_2O)]$ (**1**) (H_5L = 3,5-bis(3,5-dicarboxylphenxoy) benzoic acid, BMIB = tran-4-bis(2-methylimidazolyl)butylene) has been synthesized by a facile hydrothermal process. In **1**, the protonated BMIB cations show infinite π-stacking arrangement, residing in the channels of the 3D network extended by L ligand and binuclear Mn(II) units. The orderly and uniform host-guest system at molecular level emits intense white light fluorescence and long-lived near infrared phosphorescence under ambient conditions. These photophysical processes were well-studied by density functional theory (DFT) calculations. Photoelectron measurements reveal high photoelectron response behavior and incident photon-to-current efficiency (IPCE).

Keywords: metal-organic framework, room temperature phosphorescence, photoelectron performance, host-guest, π-stacking

OPEN ACCESS

Edited by:
Baiqing Yuan,
Ludong University, China

Reviewed by:
Wei Lu,
Southern University of Science and Technology, China
Jun-Jie Wang,
Anyang Normal University, China

***Correspondence:**
Xiao-Gang Yang
yxg2233@126.com

Specialty section:
This article was submitted to Supramolecular Chemistry, a section of the journal Frontiers in Chemistry

Received: *12 August 2020*
Accepted: *15 September 2020*
Published: *11 November 2020*

Citation:
Zhang M-L, Zhai Z-M, Yang X-G, Huang Y-D, Zheng Y-J and Ma L-F (2020) Near-Infrared Phosphorescence Emission of Binuclear Mn(II) Based Metal-Organic Framework for Efficient Photoelectric Conversion. Front. Chem. 8:593948. doi: 10.3389/fchem.2020.593948

INTRODUCTION

Room-temperature phosphorescence (RTP) materials have been widely used in a variety of optoelectronic fields such as photovoltaics, photocatalytic reactions and molecular sensing, owing to its long-lived excited states, which can increase the production of free charges (Mukherjee and Thilagar, 2015; Yang and Yan, 2016b; Yang et al., 2018, 2019a,b, 2020a; Gu et al., 2019; Yuan et al., 2019; Zhao et al., 2019; Zhou and Yan, 2019). Generally, key factors to improve the phosphorescence performance can be concluded as follows: (a) promote the intersystem crossing by increasing spin–orbit coupling through the introduction of hetero atoms, heavy atoms; (b) inhibit the non-radiative decay of triplet exciton by the formation of crystallization and the rigid matrix (Bolton et al., 2011; Gong et al., 2015; Kabe et al., 2016; Baryshnikov et al., 2017; Kabe and Adachi, 2017; Li and Li, 2017; Liu et al., 2017; Xie et al., 2017; Yang et al., 2018; Hirata, 2019; Ma and Tian, 2019; Mao et al., 2019). In this sense, metal-organic frameworks (MOFs) can be considered as a outstanding platform to achieve efficient RTP owing to their functionally

adjustable structure and various topology matrices (Wang et al., 2016, 2019; Tan et al., 2018; Qin et al., 2019; Wu et al., 2019; Chen et al., 2020; Yang et al., 2020b). As a kind of crystalline material, the spatial confinement effect of MOFs can maximally increase the rigidity of molecular conformations, suppressing the molecular motions/vibrations for the chromophore linkers or guests. For example, Adachi's group reported persistent RTP emission up 22.4 s to can be obtained by encapsulating coronene into cages of ZIF-8 (Mieno et al., 2016). The interposition and volatilization of guest solvent molecules can also result in the reversible transformation of phosphorescence emission (Yang and Yan, 2016a). Considering the variety of MOFs, it still remains a challenge to study relationships between the RTP performance and structures of such materials.

In this paper, we reported one new binuclear Mn(II) based MOF, $[Mn_2(L)(BMIB)\cdot(H_2O)]$ (**1**), by selection of polycarboxylate ligand 3,5-bis(3,5-dicarboxylphenxoy) benzoic acid (H_5L) and an N-heterocyclic ligand tran-4-bis(2-methylimidazolyl)butylene (BMIB) as shown in **Scheme 1**. The title MOF exhibits a 3D network with the π-stacking BMIB cations residing in the channels. Steady/transient state measurements indicate that the orderly and uniform arrangement of Mn-L 3D host and BMIB guests exhibits intense white light fluorescence and long lifetime of near infrared phosphorescence emission under ambient conditions. The density functional theory (DFT) calculations and photoelectron behavior have also been studied.

EXPERIMENTAL

Materials and General Methods

All reagents were of analytical grade and obtained from commercial sources without further purification. PXRD patterns were collected on a Bruker D8-ADVANCE X-ray diffractometer with Cu *Kα* radiation (λ = 1.5418 Å) with a step of 0.02° (2θ). The C, H, N analyses were carried out using a Perkin–Elmer Elementarvario elemental analysis instrument. Thermogravimetric analysis (TGA) experiments were carried out using SII EXSTAR6000 TG/DTA6300 thermal analyzer from room temperature to 800°C under a nitrogen atmosphere at a heating rate of 10°C min^{-1}. The IR spectra was recorded in the range of 4,000–400 cm^{-1} on a Nicolet 6700 (Thermo) FT-IR spectrometer with KBr pellets. Room temperature photoluminescence spectra and decay curves were measured by Edinburgh FLS1000 fluorescence spectrometer with a xenon arc lamp (Xe900), and nano/microsecond flashlamp. UV-vis absorption spectra was measured by Shimadzu UV-3600 plus UV-vis-NIR spectrophotometer.

Electrocatalytic measurements were conducted by CHI 660E electrochemical workstation in 0.5 M Na_2SO_4 solution at room temperature. Monochromatic light was generated using the Omni-λ 150 monochromator, and the output power was measured using a photodiode detector. The incident photon-to-current efficiency (IPCE) at each wavelength was measured by MPI-EO PEC analysis system (Xi'an Remex Analysis Instrument Co., Ltd., Xi'an, China) with external potential at −0.5 V vs. Ag-AgCl. The monochromatic light was generated by a 300 W Xe arc lamp assembled with a Omni-λ150 monochromator. IPCE = $(1{,}240\ I)/(\lambda\ P_{light})$, where I is the photocurrent density (mA cm^{-2}), λ is the incident light wavelength (nm), and P_{light} is the power density of monochromatic light at each wavelength (mW cm^{-2}).

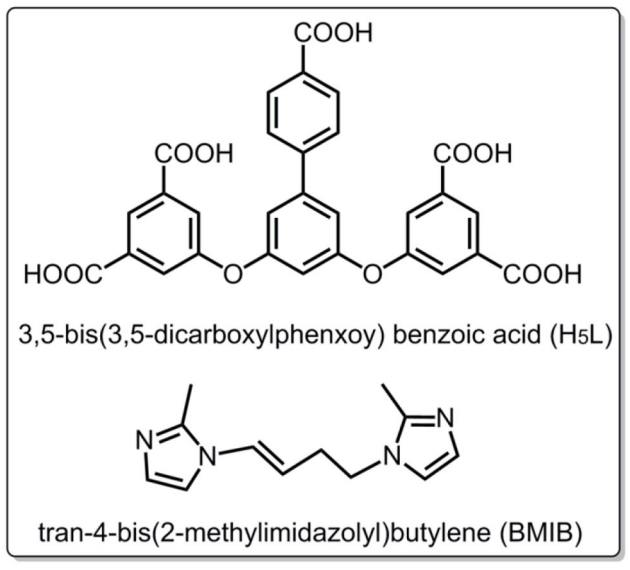

SCHEME 1 | Chemical structures of H_5L and BMIB molecules in this work.

Syntheses of $[Mn_2(L)(BMIB)\cdot(H_2O)]$ (1)

A mixture of $MnSO_4\cdot H_2O$ (0.5 mmol, 84.5 mg), 3,5-bis(3,5-dicarboxylphenxoy) benzoic acid (0.25 mmol, 119 mg), tran-4-bis(2-methylimidazolyl)butylene (0.25 mmol, 54.2 mg) and 8 mL of H_2O was stirred for 10 min. The mixture was then transferred and sealed into a Teflon reactor (23 ml), and heated at 150°C for 48 h, and then cooled to room temperature naturally. Colorless block crystals of **1** were obtained. Yield: 60% (based on Mn). Anal. Calc. (%) for $C_{35}H_{28}Mn_2N_4O_{13}$: C 51.11, H 3.43, N 6.84; found (%): C 50.97, H 3.25, N 6.69. IR (KBr pellet, cm^{-1}): 3,422 m, 1,960 w, 1,608 m, 1,545 m, 1,446 m, 1,388 s, 1,068 m, 966 w, 771 w.

X-Ray Crystal Structure

Crystal Structure was tested on Oxford Diffraction SuperNova area-detector diffractometer with the program of CrysAlisPro and solved by SHELXS-2014 and SHELXL-2014 software (Sheldrick, 2008, 2015). The crystallographic data for **1** is listed in **Table 1**. CCDC No. 2011677 contains the supplementary crystallographic data for **1**.

RESULTS AND DISCUSSION

Crystal Structure Description

Single-crystal X-ray diffraction analysis reveals that **1** crystallizes in triclinic $P\bar{1}$ space group, the asymmetric unit of which consists of two independent Mn(II) atoms, one L anion and one protonated BMIB. In **1**, the completely deprotonated

ligand polycarboxylate ligand 3,5-bis(3,5-dicarboxylphenxoy) benzoate displays twisty spatial configuration with the torsion angles between two arm benzene rings and the central one of 82.9 and 78.5°, respectively. The five carboxylate groups show monodentate, bidentate and chelate coordination modes, connecting eight Mn(II) atoms (**Figure 1A**). On the other hand, there are two kind of binuclear Mn(II) units, four bidentate carboxylates link the metal dimmer to form a paddle-wheel cluster with half-coordinated BMIB ligands loading on the axial position and short Mn···Mn distance of 3.08 Å. While the other binuclear Mn(II) unit shows longer Mn···Mn distance of 3.69 Å. The paddle-wheel cluster is surrouded by four L liagands (**Figure 1B**), the later binuclear Mn(II) unit is coordinated by six L ligands (**Figure 1C**). Based on above coordination fashion, these Mn(II) clusters are extended by L ligands giving rise to a 3D network. It is worth noting that the BMIB ligands possess one protonated and one monodentate coordinated imidazole ring, which act as guests and charge compensating units, and are fixed in the channels of the 3D network through coordination and electrostatic interactions (**Figure 1D**). Topological analysis show that the title MOF can be simplified as a (4,5,6)-connected net (**Figure 1E**). It is found that the BMIB ligands are arranged in a 1D continuous π···π stacking between imidazole rings with the centroid to centroid distance of 3.76 Å (**Figure 1F**). The above structure feature suggests that the confined π-conjugate system would provide an efficient electron delivery pathway along the channels.

TABLE 1 | Crystallographic data for **1**.

Sample	1
Chemical formula	$C_{35}H_{28}Mn_2N_4O_{13}$
Formula weight	822.5
Crystal system	triclinic
Space group	$P\bar{1}$
a (Å)	9.7440 (4)
b (Å)	10.8967 (4)
c (Å)	17.8019 (6)
α (°)	92.251 (3)
β (°)	97.727 (3)
γ (°)	114.333 (4)
V (Å^3)	1697.20 (12)
Z	2
D (g cm^{-3})	1.6093
μ (mm^{-1})	0.820
R_{int}	0.0223
Goof	1.050
R_1^a ($I>2\sigma$ (I))	0.0499
$wR_2{}^b$ ($I>2\sigma(I)$)	0.1222

$^aR_1 = \Sigma(||F_o| - |F_c||)/\Sigma|F_o|$; $^bwR_2 = [\Sigma w(|F_o|^2 - |F_c|^2)^2/\Sigma w(F_o^2)^2]^{1/2}$.

PXRD and Thermal Gravimetric Analysis

The phase purity of title MOF was characterized by powder X-ray diffraction analyses (PXRD) as shown in **Figure 2A**. The position of the main diffraction peaks of the experiment match well with the simulated one, indicating the high purity and crystalline of the as-synthesis samples. The thermo gravimetric analysis (TGA, **Figure 2B**) curve shows the first weight loss of about 2.18% in

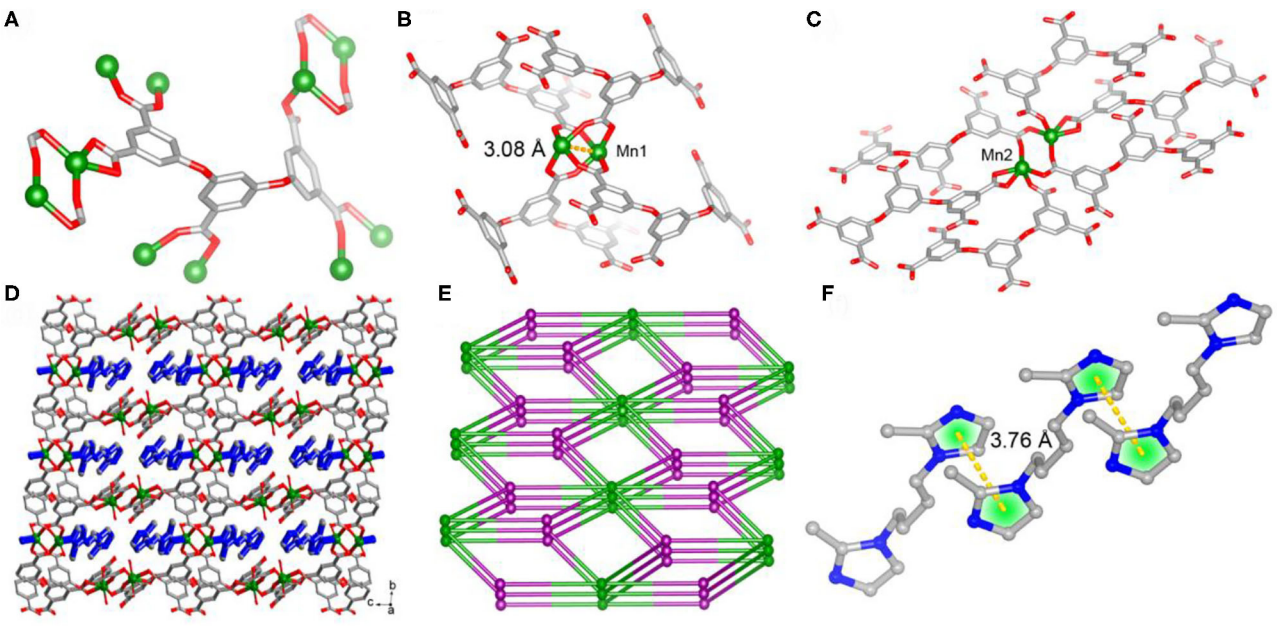

FIGURE 1 | The coordination modes of L ligand **(A)** and binuclear Mn(II) clusters **(B)** and **(C)** in **1**. **(D)** View of the 3D network of **1** with protonated BMIB ligands fixed in the channels through coordination bonds. **(E)** Schematic illustration of 3D network of **1**. **(F)** π-stacking between BMIB ligands.

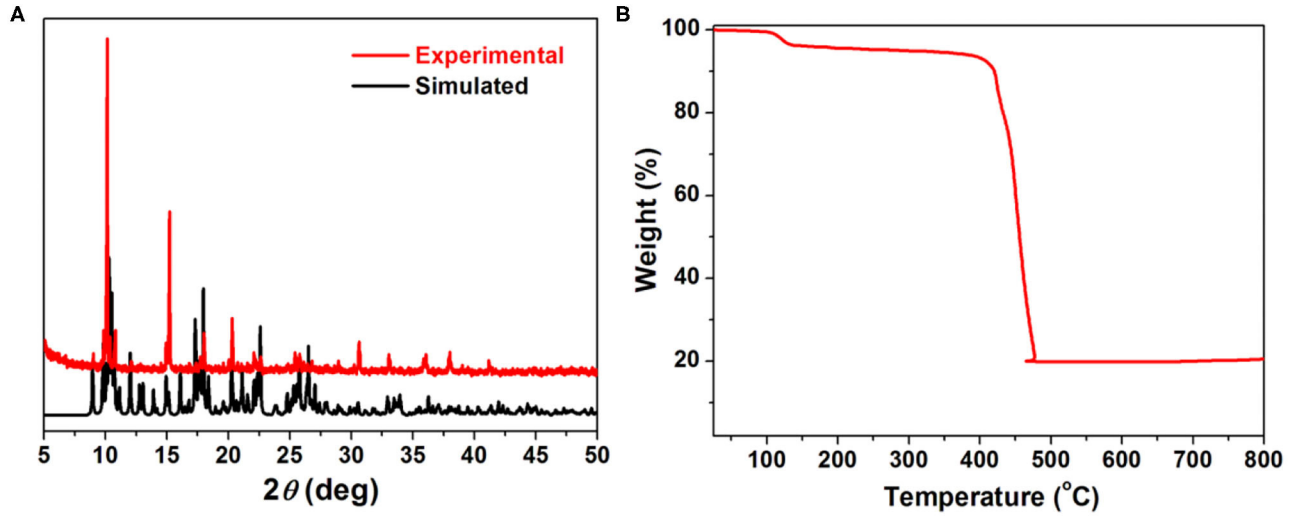

FIGURE 2 | (A) PXRD patterns of simulated (black) and as synthesized **1** (red). **(B)** Thermo gravimetric analysis curve of **1**.

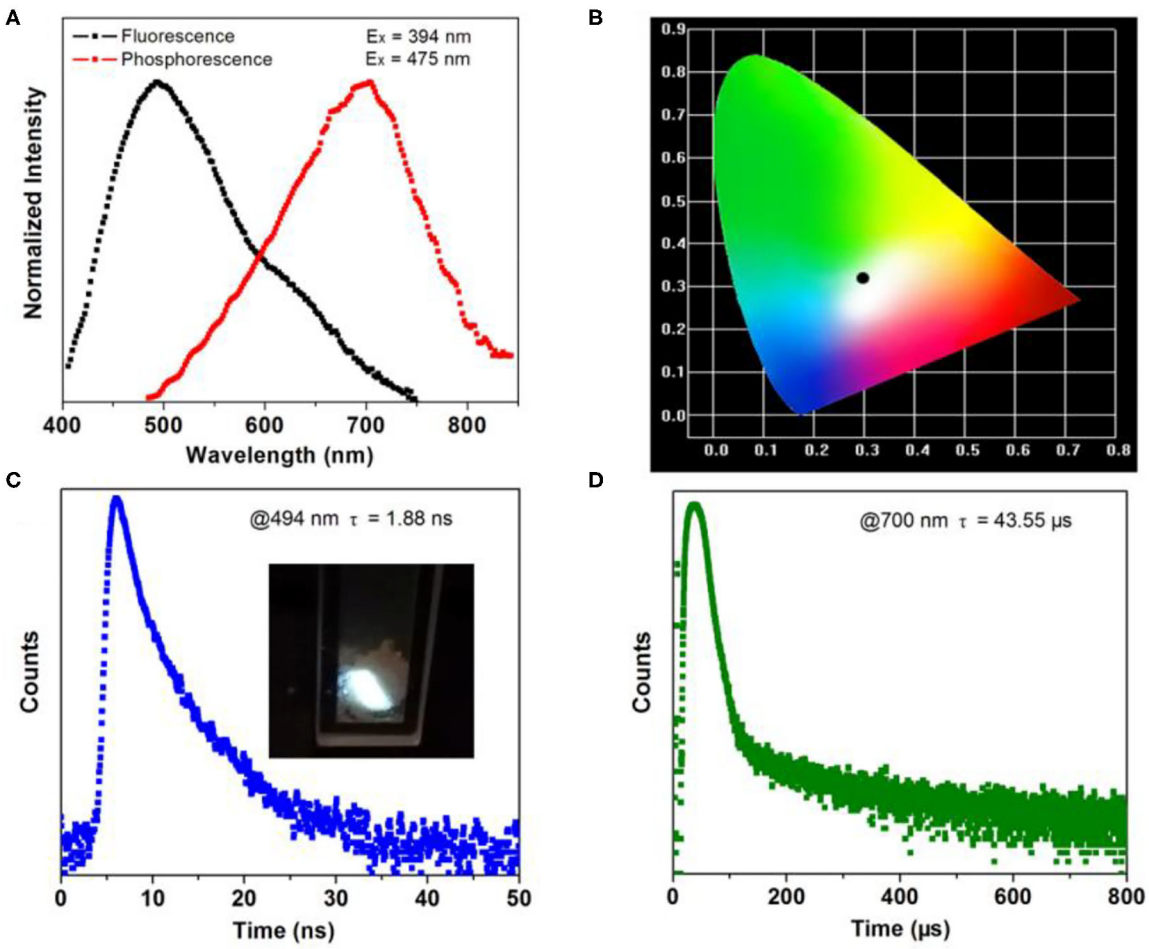

FIGURE 3 | (A) Normalized fluorescence/phosphorescence spectra of **1**. **(B)** CIE-1931 chromaticity diagram of **1**. Fluorescence **(C)** and phosphorescence **(D)** decay curves of **1** measured at room temperature. Insets show the crystal sample of **1** under UV (365 nm) light.

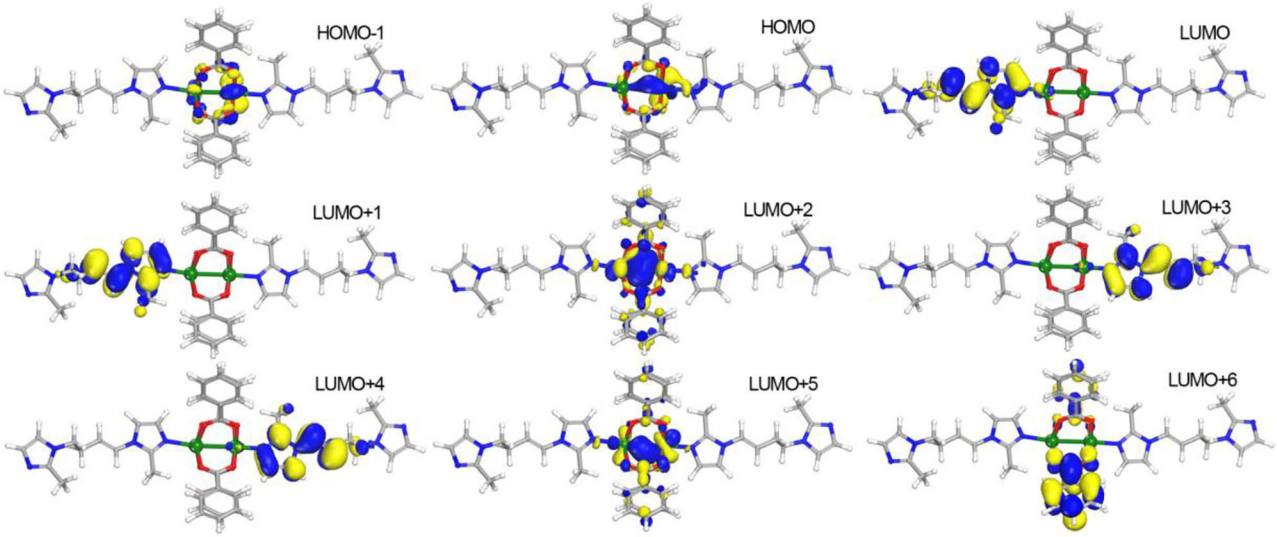

FIGURE 4 | View of the distributions of highest occupied molecular orbitals (HOMOs) and lowest unoccupied molecular orbitals (LUMOs) for **1**.

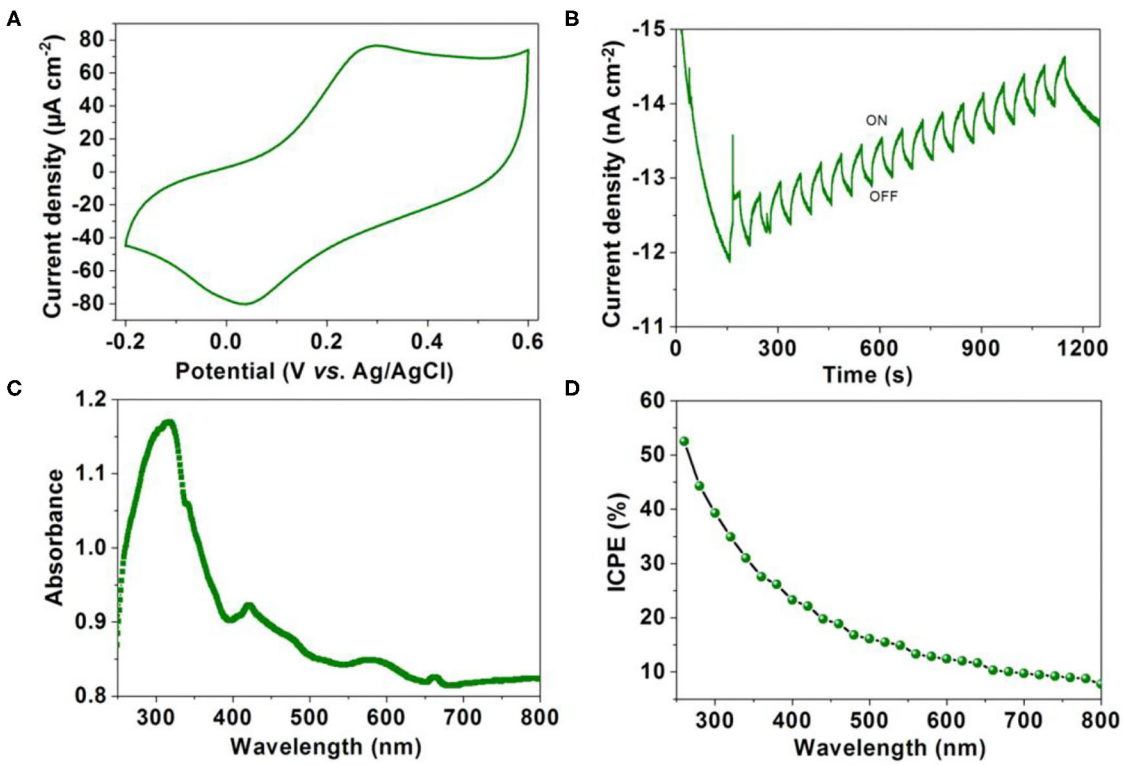

FIGURE 5 | (A) Cyclic voltammograms cuves of **1** modified ITO electrode measured in 0.5 M Na_2SO_4 aqueous solution. **(B)** Transient current density–time curve of **1** at a bias potential of −0.5 V with the periodic on-off cycles of illumination. **(C)** The UV-visible absorption spectrum of **1**. **(D)** Action spectrum for IPCE vs. wavelength of **1**.

the range of 100–130°C, which can be assigned to the loss of coordinated water molecules (calculated: 2.78%). By additional heating, the framework of **1** can be stable up to about 400°C, indicating a high thermal stability of such MOF.

Photoluminescence Properties

The photoluminescence measurement of the crystalline material was conducted at room temperature. The emission of **1** peaks at 494 nm spanning a broad range from 400 to 750 nm when

excited by 394 nm (**Figure 3A**). The chromaticity coordinate of (0.301, 0.315) indicates white emission of **1** (**Figure 3B**). From the insert in **Figure 3C**, the crystal sample of **1** emits intense white fluorescence under 365 nm UV lamp irradiation. Under the excitation of 475 nm microsecond flashlamp, long-wavelength of phosphorescence spectra peak at 700 nm can be detected. This results in a large Stocks shift of 48,543 cm^{-1} in comparison with the fluorescence emission. Further photoluminescence decay curves show a short lifetime of 1.88 ns for fluorescence emission (measured at 494 nm) and a long one of 43.55 μs for phosphorescence emission (measured at 700 nm). As a result, **1** features both energy (emission wavelength) and time (emission lifetime) scale diversity stimulated by the continuous and pulsing light source.

Density Functional Theory (DFT) Calculations

To further understand the photophysical process of **1**, density functional theory (DFT) calculations were performed by $Dmol^3$ module in Material Studio software package (Delley, 2000). The structure mode was set from the crystallographic information file (cif) of **1** by removing the symmetry and leaving the binuclear Mn(II) unit. The calculated results (**Figure 4**) show that the highest occupied molecular orbitals (HOMOs) exclusively distribute on Mn(II) atoms. The lowest unoccupied molecular orbitals (LUMOs) including LUMO, LUMO+1, LUMO+3, and LUMO+4 mainly appear on BMIB ligands. It is worth noting that the electronic isodensity surfaces are located between two Mn(II) atoms in LUMO+2 and LUMO+5, indicating the delocalization of *d* electron in the Mn(II) cluster. The LUMO+6 mainly disperse in the benzoate. Based on the above analysis, it can be concluded that the photophysical process of **1** contains the mixture of metal-centered luminescence and metal to ligand charge transfer (MLCT).

Photoelectron Performance

It has been demonstrated that long lifetime of the triplet state exciton enables the slow recombination rate of electrons and holes. Photoelectron performance was measured by a three-electrode system in Na_2SO_4 solution (0.5 M) with the MOF modified indium tin oxide (ITO) glass as the working electrode. The cyclic voltammogram curve shows that **1** has good electrochemical activity (**Figure 5A**). As shown in **Figure 5B**, the current generated by **1** modified indium tin oxide (ITO) electrode shows a gradually increasing trend at a bias potential of −0.5 V with the periodic on-off cycles of illumination, suggesting efficient photoelectron response performance. The UV-visible absorption spectrum (**Figure 5C**) reveals that the intense absorption band around 316 nm can be assigned to intra-ligand ($\pi \rightarrow \pi^*$) transitions, whereas the less intense peak at 419 nm is attributed to the metal-to-ligand charge-transfer (MLCT). Further incident photon-to-current efficiency (IPCE) vs. the wavelength curve shows a high IPCE of 53% at a bias potential of −0.5 V (**Figure 5D**). The above results indicate **1** can be used as an efficient photoelectric conversion, CO_2 reduction and H_2O oxidation material (Fu et al., 2018; Chen et al., 2020; Lu et al., 2020; Xu et al., 2020). It also provides a new idea for the application of MOF-based materials.

CONCLUSIONS

In summary, one new binuclear Mn(II) based 3D MOF host-guest material can be facilely synthesized by the assemble of flexible polycarboxylate ligand 3,5-bis(3,5-dicarboxylphenxoy) benzoic acid (H_5L) and N-heterocyclic ligand tran-4-bis(2-methylimidazolyl)butylene (BMIB). The orderly arrangement BMIB π-conjugated chains are confined in the MOF channels through coordination and electrostatic interactions, providing a structure model of molecular level heterojuction for high performance of white light fluorescence and long-lived near infrared phosphorescence emission as well as photoelectron conversion. Therefore, this work not only provides a facial process to obtain near-infrared phosphorescence emission material, but also proposes new opportunities to introduce phosphorescence MOF materials for potential optoelectronic applications.

DATA AVAILABILITY STATEMENT

The original contributions presented in the study are included in the article/supplementary material, further inquiries can be directed to the corresponding author/s.

AUTHOR CONTRIBUTIONS

X-GY and L-FM conceived the idea and designed research. M-LZ, Z-MZ, Y-DH, and Y-JZ synthesized and characterized materials. All authors analyzed data and wrote the paper. All authors contributed to the article and approved the submitted version.

FUNDING

This work was supported by the National Natural Science Foundation of China (Nos. 21971100, 21771097), Project of Central Plains Science and Technology Innovation Leading Talents of Henan Province (No. 204200510001), Key Scientific Research Projects of Higher Education of Henan Province (No. 20A150005), and Postgraduate Education Innovation Program of Yan'an University (YCX201998).

REFERENCES

Baryshnikov, G., Minaev, B., and Agren, H. (2017). Theory and calculation of the phosphorescence phenomenon. *Chem. Rev.* 117, 6500–6537. doi: 10.1021/acs.chemrev.7b00060

Bolton, O., Lee, K., Kim, H. J., Lin, K. Y., and Kim, J. (2011). Activating efficient phosphorescence from purelyorganic materials by crystal design. *Nat. Chem.* 3, 205–210. doi: 10.1038/nchem.984

Chen, Z., Li, P., Anderson, X., Wang, X., Zhang, L., Robison, L. R., et al. (2020). Balancing volumetric and gravimetric uptake in highly porous materials for clean energy. *Science* 368, 297–303. doi: 10.1126/science.aaz8881

Delley, B. (2000). From molecules to solids with the DMol3 approach. *J. Chem. Phys.* 113, 7756–7764. doi: 10.1063/1.1316015

Fu, C., Wu, X., and Yang, J. (2018). Material design for photocatalytic water splitting from a theoretical perspective. *Adv. Mater.* 30:e1802106. doi: 10.1002/adma.201802106

Gong, Y., Zhao, L., Peng, Q., Fan, D., Yuan, W., Zhang, Y., et al. (2015). Crystallization-induced dual emission from metal-and heavy atom-free aromatic acids and esters. *Chem. Sci.* 6, 4438–4444. doi: 10.1039/C5SC00253B

Gu, L., Shi, H., Bian, L., Gu, M., Ling, K., Wang, X., et al. (2019). Colour-tunable ultra-long organic phosphorescence of a single-component molecular crystal. *Nat. Photonics* 13, 406–411. doi: 10.1038/s41566-019-0408-4

Hirata, S. (2019). Recent advances in materials with room-temperature phosphorescence: photophysics for triplet exciton stabilization. *Adv. Optical Mater.* 5:1700116. doi: 10.1002/adom.201700116

Kabe, R., and Adachi, C. (2017). Organic long persistent luminescence. *Nature* 550, 384–387. doi: 10.1038/nature24010

Kabe, R., Notsuka, N., Yoshida, K., and Adachi, C. (2016). Afterglow organic light-emitting diode. *Adv. Mater.* 28, 655–660. doi: 10.1002/adma.201504321

Li, Q., and Li, Z. (2017). The strong light-emission materials in the aggregated state: what happens from a single molecule to the collective group. *Adv. Sci.* 4:1600484. doi: 10.1002/advs.201600484

Liu, J., Wang, N., Yu, Y., Yan, Y., Zhang, H., Li, J., et al. (2017). Carbon dots in zeolites: a new class of thermally activated delayed fluorescence materials with ultralong lifetimes. *Sci. Adv.* 3:e1603171. doi: 10.1126/sciadv.1603171

Lu, W., Zhang, Y., Zhang, J., and Xu, P. (2020). Reduction of gas CO_2 to CO with high selectivity by Ag nanocube-based membrane cathodes in a photoelectrochemical system. *Ind. Eng. Chem. Res.* 59, 5536–5545. doi: 10.1021/acs.iecr.9b06052

Ma, X., and Tian, H. (2019). Assembling-induced emission: an efficient approach for amorphous metal-free organic emitti ng materials with room-temperature phosphorescence. *Acc. Chem. Res.* 52, 738–748. doi: 10.1021/acs.accounts.8b00620

Mao, Z., Yang, Z., Fan, Z., Ubba, E., Li, W., Li, Y., et al. (2019). The methylation effect in prolonging the pure organic room temperature phosphorescence lifetime. *Chem. Sci.* 10, 179–184. doi: 10.1039/C8SC03019G

Mieno, H., Kabe, R., Notsuka, N., Allendorf, M. D., and Adachi, C. (2016). Long-lived room-temperature phosphorescence of coronene in zeolitic imidazolate framework ZIF-8. *Adv. Opt. Mater.* 4, 1015–1021. doi: 10.1002/adom.201600103

Mukherjee, S., and Thilagar, P. (2015). Recent advances in purely organic phosphorescent materials. *Chem. Commun.* 51, 10988–11003. doi: 10.1039/C5CC03114A

Qin, J., Huang, Y., Zhao, Y., Yang, X., Li, F., Wang, C., et al. (2019). Highly dense packing of chromophoric linkers achievable in a pyrene-based metal-organic framework for photoelectric response. *Inorg. Chem.* 58, 15013–15016. doi: 10.1021/acs.inorgchem.9b02203

Sheldrick, G. M. (2008). A short history of SHELX. *Acta Crystallogr. Sect. A* 64, 112–122. doi: 10.1107/S0108767307043930

Sheldrick, G. M. (2015). SHELXT-integrated space-group and crystal-structure determination. *Acta Cryst. A* 71, 3–8. doi: 10.1107/S2053273314026370

Tan, Y., Wang, F., and Zhang, J. (2018). Design and synthesis of multifunctional metal-organic zeolites. *Chem. Soc. Rev.* 47, 2130–2144. doi: 10.1039/C7CS00782E

Wang, H., Meng, W., Wu, J., Ding, J., Hou, H., and Fan, Y. (2016). Crystalline central-metal transformation in metal-organic frameworks. *Coor. Chem. Rev.* 307, 130–146. doi: 10.1016/j.ccr.2015.05.009

Wang, X., Liu, J., Zhang, L., Dong, L., Li, S., Kan, Y., et al. (2019). Monometallic catalytic models hosted in stable metal-organic frameworks for tunable CO_2 photoreduction. *ACS Catal.* 9, 1726–1732. doi: 10.1021/acscatal.8b04887

Wu, Y., Tian, J., Liu, S., Li, B., Zhao, J., Ma, L., et al. (2019). Bi-microporous metal–organic frameworks with Cubane $[M_4(OH)_4]$ (M=Ni, Co) clusters and pore-space partition for electrocatalytic methanol oxidation reaction. *Angew. Chem. Int. Ed.* 58, 12185–12189. doi: 10.1002/anie.201907136

Xie, Y., Ge, Y., Peng, Q., Li, C., Li, Q., and Li, Z. (2017). How the molecular packing affects the room temperature phosphorescence in pure organic compounds: ingenious molecular design, detailed crystal analysis, and rational theoretical calculations. *Adv. Mater.* 29, 1606829–1606836. doi: 10.1002/adma.201606829

Xu, P., Lu, W., Zhang, J., and Zhang, L. (2020). Efficient hydrolysis of ammonia borane for hydrogen evolution catalyzed by plasmonic Ag@Pd core–shell nanocubes. *ACS Sustain. Chem. Eng.* 8, 12366–12377. doi: 10.1021/acssuschemeng.0c02276

Yang, J., Zhen, X., Wang, B., Gao, X., Ren, Z., Wang, J., et al. (2018). The influence of the molecular packing on the room temperature phosphorescence of purely organic luminogens. *Nat. Commun.* 9, 840–849. doi: 10.1038/s41467-018-03236-6

Yang, X., Lu, X., Zhai, Z., Qin, J., Chang, X., Han, M., et al. (2020a). π-Type halogen bonding enhanced long-last room temperature phosphorescence of Zn(II) coordination polymers for photoelectron response applications. *Inorg. Chem. Front.* 7, 2224–2230. doi: 10.1039/D0QI00191K

Yang, X., Lu, X., Zhai, Z., Zhao, Y., Liu, X., Ma, L., et al. (2019a). Facile synthesis of micro-scale MOF host-guest with long-last phosphorescence and enhanced optoelectronic performance. *Chem. Commun.* 55, 11099–11102. doi: 10.1039/C9CC05708K

Yang, X., and Yan, D. (2016a). Long-afterglow metal–organic frameworks: reversible guest-induced phosphorescence tenability. *Chem. Sci.* 7, 4519–4526. doi: 10.1039/C6SC00563B

Yang, X., and Yan, D. (2016b). Strongly enhanced long-lived persistent room temperature phosphorescence based on the formation of metal–organic hybrids. *Adv. Optical Mater.* 4, 897–905. doi: 10.1002/adom.201500666

Yang, X., Zhai, Z., Liu, X., Li, J., Li, F., and Ma, L. (2020b). Sulfur heteroatom-based MOFs with long-lasting room-temperature phosphorescence and high photoelectric response. *Dalton Trans.* 49, 598–602. doi: 10.1039/C9DT04046C

Yang, X., Zhai, Z., Lu, X., Zhao, Y., Chang, X., and Ma, L., (2019b). Room temperature phosphorescence of Mn(II) and Zn(II) coordination polymers for photoelectron response applications. *Dalton Trans.* 48, 10785–10789. doi: 10.1039/C9DT02178G

Yuan, J., Wang, S., Ji, Y., Chen, R., Zhu, Q., Wang, Y., et al. (2019). Invoking ultralong room temperature phosphorescence of purely organic compounds through H-aggregation engineering. *Mater. Horiz.* 6, 1259–1264. doi: 10.1039/C9MH00220K

Zhao, Y., Yang, X., Lu, X., Yang, C., Fan, N., Yang, Z., et al. (2019). $\{Zn_6\}$ cluster based metal–organic framework with enhanced room-temperature phosphorescence and optoelectronic performances. *Inorg. Chem.* 58, 6215–6221. doi: 10.1021/acs.inorgchem.9b00450

Zhou, B., and Yan, D. (2019). Simultaneous long-persistent blue luminescence and high quantum yield within 2D organic-metal halide perovskite. *Angew. Chem. Int. Ed.* 58, 15272–15279. doi: 10.1002/ange.201909760

Conflict of Interest: The authors declare that the research was conducted in the absence of any commercial or financial relationships that could be construed as a potential conflict of interest.

frontiers in Chemistry

ORIGINAL RESEARCH
published: 25 November 2020
doi: 10.3389/fchem.2020.602752

Electrochemically Activated Conductive Ni-Based MOFs for Non-enzymatic Sensors Toward Long-Term Glucose Monitoring

Yating Chen, Yulan Tian, Ping Zhu, Liping Du, Wei Chen and Chunsheng Wu**

Department of Biophysics, School of Basic Medical Sciences, Health Science Center, Xi'an Jiaotong University, Xi'an, China

Continuous intensive monitoring of glucose is one of the most important approaches in recovering the quality of life of diabetic patients. One challenge for electrochemical enzymatic glucose sensors is their short lifespan for continuous glucose monitoring. Therefore, it is of great significance to develop non-enzymatic glucose sensors as an alternative approach for long-term glucose monitoring. This study presented a highly sensitive and selective electrochemical non-enzymatic glucose sensor using the electrochemically activated conductive Ni_3(2,3,6,7,10,11-hexaiminotriphenylene)$_2$ MOFs as sensing materials. The morphology and structure of the MOFs were investigated by scanning SEM and FTIR, respectively. The performance of the activated electrode toward the electrooxidation of glucose in alkaline solution was evaluated with cyclic voltammetry technology in the potential range from 0.2 V to 0.6 V. The electrochemical activated Ni-MOFs exhibited obvious anodic (0.46 V) and cathodic peaks (0.37 V) in the 0.1 M NaOH solution due to the Ni(II)/Ni(III) transfer. A linear relationship between the glucose concentrations (ranging from 0 to 10 mM) and anodic peak currents with R2 = 0.954 was obtained. It was found that the diffusion of glucose was the limiting step in the electrochemical reaction. The sensor exhibited good selectivity toward glucose in the presence of 10-folds uric acid and ascorbic acid. Moreover, this sensor showed good long-term stability for continuous glucose monitoring. The good selectivity, stability, and rapid response of this sensor suggests that it could have potential applications in long-term non-enzymatic blood glucose monitoring.

Keywords: electrochemical, conductive Ni-MOFs, cyclic voltammetry, non-enzymatic, glucose sensor

OPEN ACCESS

Edited by:
Baiqing Yuan,
Ludong University, China

Reviewed by:
Hassan Karimi-Maleh,
University of Electronic Science and Technology of China, China
Huan Pang,
Yangzhou University, China

****Correspondence:***
Wei Chen
weiwcchen@xjtu.edu.cn
Chunsheng Wu
wuchunsheng@xjtu.edu.cn

Specialty section:
This article was submitted to Supramolecular Chemistry, a section of the journal Frontiers in Chemistry

Received: *04 September 2020*
Accepted: *05 October 2020*
Published: *25 November 2020*

Citation:
Chen Y, Tian Y, Zhu P, Du L, Chen W and Wu C (2020) Electrochemically Activated Conductive Ni-Based MOFs for Non-enzymatic Sensors Toward Long-Term Glucose Monitoring. Front. Chem. 8:602752. doi: 10.3389/fchem.2020.602752

INTRODUCTION

Diabetes, caused by insulin deficiency or resistance, is a chronic disorder of glucose metabolism. It has become one of the most widespread diseases in the world and has profound implications for disability and mortality (Wong et al., 2013). According to the World Health Organization, it is estimated that type II diabetes patients will grow to at least 350 million worldwide by 2030 if no appropriate action is taken (Collins et al., 2011). The normal

range of blood glucose concentration is 4.4-6.6 mM, while the blood glucose concentration in patients with diabetes mellitus is out of this normal range (Chelaghmia et al., 2018). To care for diabetes, the blood glucose level of patients needs to be monitored on a regular basis daily. Thus, establishing a fast and reliable estimation method to detect blood glucose concentrations has attracted considerable interest from scientists.

Currently, an electrochemical enzyme-based glucose biosensor has been used widely because of its high selectivity, reliability, and simplicity (Caliò et al., 2016; Karimi-Maleh et al., 2020a). However, the instability, critical operating conditions, and limited lifetimes of enzymes hinder the application of this biosensor for continuous glucose monitoring (Zhang et al., 2013). To address these drawbacks, non-enzymatic electrochemical glucose biosensors, including noble metallic materials and their alloys, have been proposed and developed (Dolinska et al., 2014; Chang et al., 2015; Shen et al., 2015; Ye et al., 2015; Wei et al., 2018; Karimi-Maleh et al., 2020b). However, the cost of noble metals was high. Recently, it was found that some transition metals and their metal oxides or hydroxides, such as Cu, Co, Ni, $Cu(OH)_2$, $Co(OH)_2$, NiO, $Ni(OH)_2$, NiS_2, and ZnO, have exhibited non-enzymatic glucose sensing performance (Song et al., 2015; Wei et al., 2015; Darvishi et al., 2017; Du et al., 2019; Hayat et al., 2019; Sun et al., 2019; Padideh et al., 2020; Shi et al., 2020). Among these, nickel-based sensors show excellent electrochemical activity toward glucose oxidation (Martins et al., 2011; Gao et al., 2016).

Metal-organic frameworks (MOFs), which are constituted by organic linkers and metal ions or clusters, have rapidly been developed (Jiao et al., 2019). MOFs are a new type of crystalline material with ultrahigh surface areas up to 10,000 m^2/g, high surface area to volume ratios, tunable structures, and flexible tailorability. They have been applied in various fields including gas sorption and separation, catalysis, sensors, cancer therapy, and drug delivery (Li et al., 2009; Lu et al., 2018; Zhou et al., 2018; Liang et al., 2019; Rojas et al., 2019; Wang et al., 2020). For electrochemical glucose sensors, Cu-MOFs, Co-MOFs, Ni-MOFs, and their metal oxide composites have been developed (Sun et al., 2018; Li et al., 2020b; Liu et al., 2020; Qiao et al., 2020; Shahrokhian et al., 2020). Conductive Ni_3(2,3,6,7,10,11-hexaiminotriphenylene)$_2$ (2,3,6,7,10,11-hexaiminotriphenylene=HITP) MOFs exhibit very high electrical conductivity, exceeding those of previous semiconducting metal-organic graphene analogs and other conductive MOFs, which are even higher than some of the best organic conductors (Sheberla et al., 2014). Thus, it is suspected that the high porosity, high surface area, large pore diameter, and high conductivity of these MOFs could promote the electron transfer between the electrode and solution.

In this study, the electrochemically activated conductive Ni_3(2,3,6,7,10,11-hexaiminotriphenylene)$_2$ MOFs was utilized as sensing materials to develop electrochemical non-enzymatic glucose sensors. The morphology and structure of MOFs were characterized by scanning SEM and FTIR, respectively. In fact, after the activation of Ni-MOFs in KOH solution, the conductive MOFs exhibited stable reduction and oxidation peaks in alkaline solution, which was very sensitive to glucose concentrations. Moreover, the activated Ni-MOFs showed excellent selectivity and stability. All the obtained results suggest the promising prospects and potential applications of this sensor for non-enzymatic and long-term blood glucose monitoring.

EXPERIMENTAL SECTION

Materials

HITP·6HCl (Chemical Reagent) were brought from Shanghai TenSus Biotechnology Co., Ltd. $NiCl_2{\cdot}6H_2O$ (Analytical Reagent) and Nafion (5% solution) was brought from Sigma-Aldrich. Potassium hexacyanoferrate ($K_4Fe(CN)_6$), triethylamine, glucose, KCl, KOH, uric acid (UA), and ascorbic acid (AA) of an analytical reagent were purchased from Sinopharm Chemical Reagent Co., Ltd. All chemicals were of an analytical reagent grade and were used without further purification. All solutions were prepared by distilled water and stored at room temperature.

Preparation of $Ni_3(HITP)_2$ MOFs

The preparation of Ni-MOFs followed previous reports with some modifications (Sheberla et al., 2014). Typically, a solution of 6.6 mg of $NiCl_2{\cdot}6H_2O$ in 5 mL of water and 0.1 mL of triethylamine solution was added to a solution of 10 mg of HITP·6HCl in 5 mL of water. The mixture was stirred under an oil bath at 65°C for 3 h. The resulting black powder was centrifuged, filtered, and washed with water several times and then dried under a vacuum oven for 24 h.

Preparation of Modified Electrodes

Electrochemical experiments were performed on an electrochemical station (CHI600E). A standard three-electrode cell was applied in all the measurements. Ni-MOFs modified glass carbon electrode (GCE) and electrochemical treated Ni-MOFs electrode were used as working electrodes. The platinum rod and saturated calomel electrode (SCE) were used as counter electrodes and reference electrodes, respectively. All the electrochemical tests were performed at room temperature.

The GCE was polished with 1.5 μm, 0.5 μm, and 50 nm aluminum oxide sequentially until the P_{anodic}-$P_{cathodic}$ in 0.1 M $K_4Fe(CN)_6$/0.01M KCl below 80 mV vs. SCE. A mixture solution of 16 μL Ni-MOFs (1 mg mL^{-1}) and 4 μL Nafion was added to the polished GCE surface and dried under room temperature. To active the Ni-MOFs, the cyclic voltammogram method was performed at the potential between 0.2 V to 0.6 V vs. SCE at a scan rate of 50 mV s^{-1} for 100 cycles in a 0.1 M KOH solution until stable curves were obtained.

Electrochemical Measurements

The activated Ni-MOFs electrode was investigated as a glucose sensor in an alkaline medium. Cyclic voltammograms (CVs) measurements were processed in 0.1 M KOH in the potential range from 0.2 to 0.6 V with a scan rate of 50 mV s^{-1}. The selectivity testes were applied in the mixture glucose with 10-fold concentration of AA and UA.

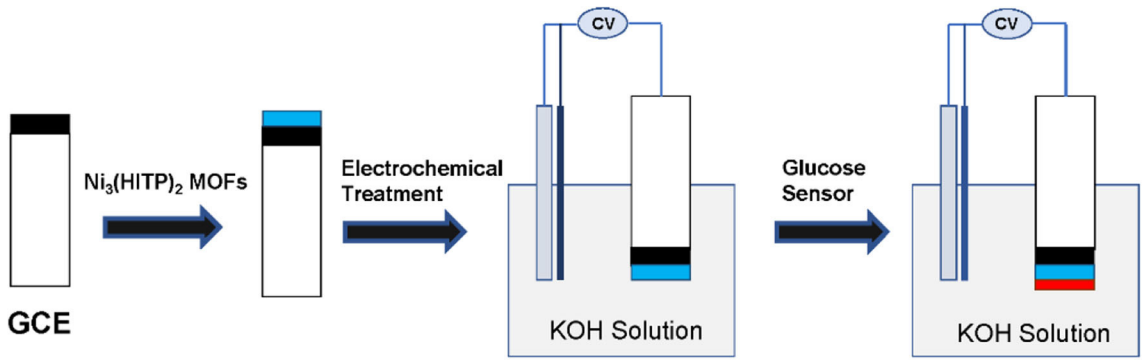

FIGURE 1 | Schematic image of electrochemical activated Ni-MOFs electrode for glucose sensor.

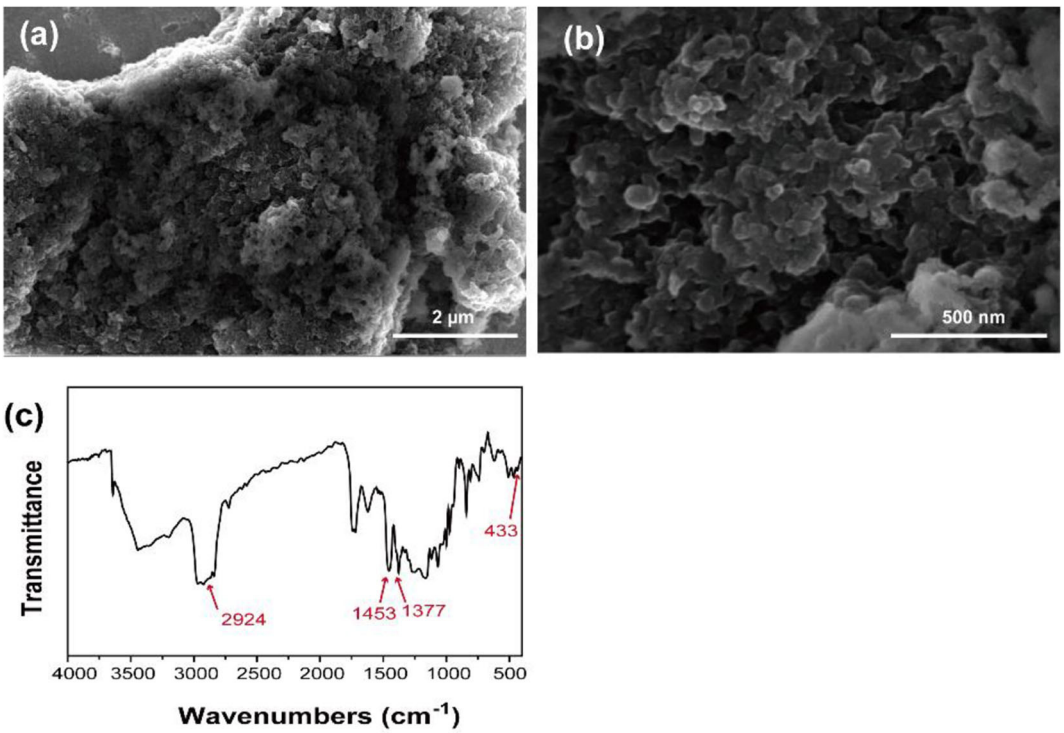

FIGURE 2 | (a,b) SEM image with different magnification, **(c)** FTIR spectra of Ni-MOFs.

Characterization

The morphology was observed by a scanning electron microscope (SEM, FEI Nova NanoSEM 450). The functional groups were tested by Fourier Transform Infrared Spectrometer (FTIR, Nicolet iS50).

RESULTS AND DISCUSSION

Characterization of Ni-MOFs

The preparation of the Ni-MOFs glucose sensor was illustrated as **Figure 1**, following the sequence of the GCE polishing, Ni-MOFs synthesis, electrochemical activation, and glucose sensing. The polished GCE exhibited an even surface and excellent electronic transfer capacity, which is indicated by the cyclic voltammogram of $K_4Fe(CN)_6$ (**Supplementary Figure 1**). After that, the synthesized $Ni_3(HITP)_2$ MOFs mixed with Nafion was dropped on the polished GCE. Then, it was activated by the electrochemical method. The treated Ni-MOFs showed obvious reduction and oxidation peaks, which were sensitive to glucose and used as a non-enzymatic glucose sensor.

The prepared Ni-MOFs exhibited a rough surface with particle sizes around 50 nm in SEM image (**Figure 2**). In the FTIR spectra, the peak at 2924 cm^{-1} is the aromatic C-H stretching vibrations. The peak at 1453 and 1377 cm^{-1} was due to the C=C

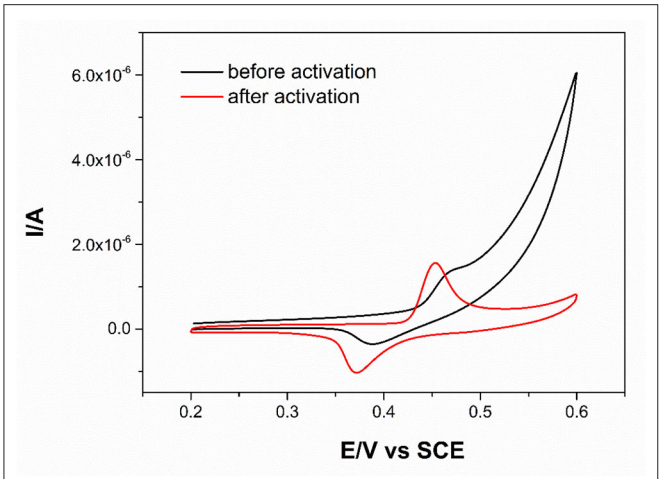

FIGURE 3 | CV curves of Ni-MOFs before and after treatment in 0.1 M KOH, scan rate 50 mV s^{-1}.

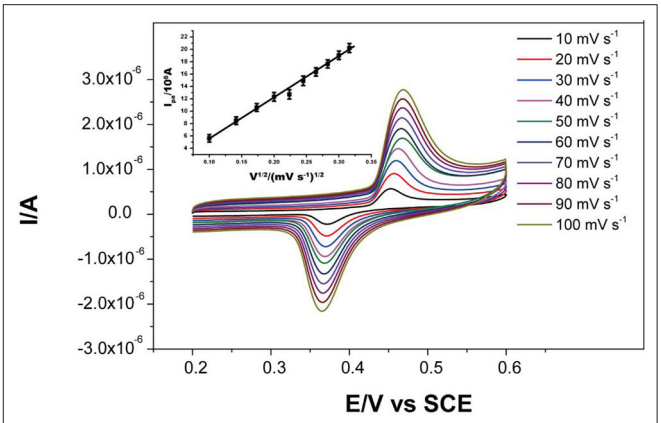

FIGURE 5 | CV curves of Ni-MOFs in the presence of 2.0 mM glucose and 0.1 M KOH solution at scan rates from 10 to 100 mV s^{-1} at 25 °C. Inset: calibration curve of anodic peak current to square root of the scan rates (10-100 mV s^{-1}).

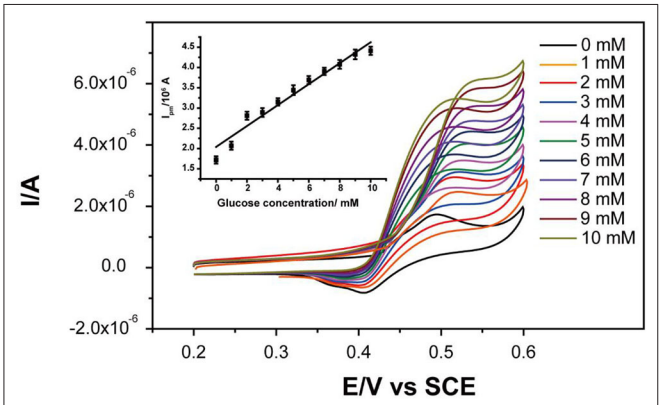

FIGURE 4 | CV curves of Ni-MOFs in the absence and presence of different concentrations of glucose. Inset: the corresponding calibration curve of anodic peak current to glucose concentrations.

vibration of the aromatic polymer chain (Su et al., 2020). The peaks at 433 cm^{-1} were assigned to Ni-N stretching vibrations (Rocchiccioli-Deltcheff et al., 1978).

Activation of Ni-MOFs Electrode

The electrochemical responses of MOFs before and after activation were studied (**Figure 3**). It can be seen that the voltammogram showed stronger anodic peaks or cathodic peaks after activation. Moreover, the anodic current and cathodic current became similar after activation. These results indicated that the activation could enhance the electrochemical reversibility. Two peaks appeared in the treated cyclic voltammogram, *i.e.*, one in the anodic direction at 0.46 V and another in the cathodic direction at 0.37 V. These peaks are caused by the conversion of Ni(II)/Ni(III) to each other in the Ni-MOFs in the alkaline solution through the following reaction:

$$Ni(II)_3(HITP)_2 \rightleftharpoons Ni(III)_3(HITP)_2 + e^- \quad (1)$$

The cyclic voltammogram of Ni-MOFs at different concentrations of KOH was also investigated (**Supplementary Figure 2**). Compared with other concentrations, the voltammogram in 0.1 M KOH showed stronger anodic and cathodic peaks. Therefore, KOH at the concentration of 0.1 M was chosen as the activation solution.

Electrocatalytic Oxidation of Glucose

Cyclic voltammetry (CV) was used to study the glucose oxidation by treated Ni-MOFs. The CV curves showed that the peak current continually increased with the increasement of glucose concentration in the range of 0 to 10 mM with a linear calibration equation:

$$I_{pa} = 0.252\ C_{glucose} + 2.076 (R^2 = 0.954)$$

Where I_{pa} is the anodic peak current and $C_{glucose}$ is the concentration of glucose (**Figure 4**).

This voltammogram indicated that Ni-MOFs could electrocatalyze the oxidation of glucose to gluconolactone *via* reaction 2, which was also in agreement with the nickel oxide-based glucose sensor (Abdel Hameed, 2013; Yang et al., 2013; Wang et al., 2015; Chelaghmia et al., 2018). It is known that diabetes mellitus is reflected by blood glucose concentrations higher or lower than the normal range of 4.4-6.6 mM (Chelaghmia et al., 2018). Therefore, the linear relationship in 1-10 mM could totally satisfy the requirement of continuous blood glucose monitoring.

$$Ni(III)_3(HITP)_2 + OH^- + glucose \rightleftharpoons Ni(II)_3(HITP)_2 + gluconolactone + H_2O + e^- \quad (2)$$

The effects of scan rate were tested in the range of 10–100 mV s^{-1} in the presence of 2 mM glucose in 0.1 M KOH (**Figure 5**).

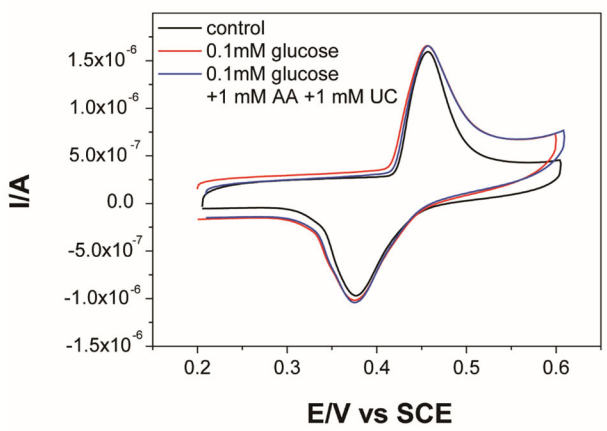

FIGURE 6 | CV curves of Ni-MOFs electrode in 0.1 M KOH and 0.1 mM glucose, 1.0 mM ascorbic acid (AA), and 1.0 mM uric acid (UC).

TABLE 1 | Comparative characteristics of the non-enzymatic MOFs based glucose sensors.

Active materials	Method	Potential (V)	Linear range (μM)	Stability	References
$Cu_2(BTC)Cl(H_2O)_4$	DPV	0.50	0.006–5000	92%	(Sun et al., 2018)
Ni-BTC	CV	0.55	5–3000; 3500–6000	–	(Chen et al., 2020)
Ni-BDC	CV	0.63	10–800	–	(Gumilar et al., 2020)
Ni/Co-TCPP	CV	0.40	1.0–3800	–	(Li et al., 2020a)
NiO/Cu-TCPP	CV	0.50	3–300	–	(Li et al., 2020a)
NiCo-MOFs nanosheets	CV	0.50	1–8000	–	(Li et al., 2019)
Ag/Co-MOFs	CV	0.55	5–550	30 times	(Liu et al., 2019)
$Ni_3(HITP)_2$	CV	0.50	0–10000	7 days	This work

**DPV, differential pulse voltammetry; CV, cyclic voltammetry; BTC, benzenetricarboxylic acid; BDC, benzene dicarboxylic acid; TCPP, tetrakis(4-carboxyphenyl)phosphonium porphyrin; HITP, 2,3,6,7,10,11-hexaiminotriphenylene.*

The anodic peak current was proportional to the square root of the scan rate ($v^{1/2}$), linearly following the linear regression equation:

$$I_{pa} = 6.631 \times 10^{-7} v^{1/2} - 1.117 (R^2 = 0.992)$$

This suggests the diffusion of the glucose to the electrode surface was the limiting step of the electrochemical reaction.

The Selectivity and Stability of Ni-MOFs Electrode

The selectivity of the activated Ni-MOFs sensor was investigated in the presence of UA and AA, which are regarded as glucose interferents in human blood (Yuan et al., 2005). Even the concentration of glucose in normal human blood is higher than the interfering concentration; the 10-folds concentration of interference is persuasive. The cyclic voltammograms of MOFs sensor in the presence of glucose and 10-fold UA and AA were shown in **Figure 6**. Compared with 0.1 mM glucose, no significant difference was observed in the detection of 0.1 mM glucose in the mixture of 1 mM AA and 1 mM UC, indicating good selectivity for glucose monitoring. The long-term stability of the activated Ni-MOFs electrode has also been evaluated (**Supplementary Figure 3**). Through 7-day tests, there was no obvious difference in the cyclic voltammograms of electrodes in the alkaline solution, indicating good stability of the sensor. Furthermore, a comparative study of $Ni_3(HITP)_2$-based glucose sensor with the reported literature (**Table 1**) revealed that this MOFs exhibited a wider linear range and higher stability.

CONCLUSIONS

In conclusion, a non-enzymatic glucose sensor was developed through electrochemical activation of the $Ni_3(HITP)_2$ MOFs on GCE in an alkaline solution. Cyclic voltammetry technology was used to study the electrocatalytic oxidation of glucose on the surface of activated Ni-MOFs. The active MOFs displayed excellent electrocatalytic activity toward the glucose oxidation in 0.1 M KOH solution and showed a good linear relationship toward 0-10 mM. The diffusion of glucose to the electrode surface was the limiting speed for the electrochemical reaction. In addition, the MOFs sensor exhibited excellent selectivity toward glucose in the presence of AA and UC. Also, the electrode exhibited long-term stability.

The conventional fabrication, high performance, excellent stability, and low cost of the activated conductive Ni-MOFs suggests its suitability as a reliable non-enzymatic glucose sensor.

DATA AVAILABILITY STATEMENT

All datasets generated for this study are included in the article/ **Supplementary Material**.

AUTHOR CONTRIBUTIONS

YC: conceptualization, methodology, validation, formal analysis, data curation, and writing original draft. YT: methodology, validation, investigation, visualization, and writing-review and editing. PZ: methodology, resources, and visualization. LD: methodology, writing-review and editing, and visualization. WC: conceptualization, methodology, validation, data curation, visualization, and writing-review and editing. CW: conceptualization, methodology, resources, writing-review and editing, supervision, project administration, and funding

acquisition. All authors contributed to the article and approved the submitted version.

FUNDING

This work was financially supported in part by grants from the National Natural Science Foundation of China (Grant Nos. 51861145307, 31700859, and 32071370), China Postdoctoral Science Foundation (Grant No. 2018M633524), and Fundamental Research Funds for the Central Universities (Grant No. xzy022019047).

SUPPLEMENTARY MATERIAL

The Supplementary Material for this article can be found online at: https://www.frontiersin.org/articles/10.3389/fchem.2020.602752/full#supplementary-material

REFERENCES

Abdel Hameed, R. M. (2013). Amperometric glucose sensor based on nickel nanoparticles/carbon Vulcan XC-72R. *Biosens. Bioelectron.* 47, 248–257. doi: 10.1016/j.bios.2013.02.044

Caliò, A., Dardano, P., Di Palma, V., Bevilacqua, M. F., Di Matteo, A., Iuele, H., et al. (2016). Polymeric microneedles based enzymatic electrodes for electrochemical biosensing of glucose and lactic acid. *Sens. Actuators B Chem.* 236, 343–349. doi: 10.1016/j.snb.2016.05.156

Chang, G., Shu, H., Huang, Q., Oyama, M., Ji, K., Liu, X., et al. (2015). Synthesis of highly dispersed Pt nanoclusters anchored graphene composites and their application for non-enzymatic glucose sensing. *Electrochim. Acta.* 157, 149–157. doi: 10.1016/j.electacta.2015.01.085

Chelaghmia, M. L., Nacef, M., Affoune, A. M., Pontié, M., and Derabla, T. (2018). Facile synthesis of $Ni(OH)_2$ modified disposable pencil graphite electrode and its application for highly sensitive non-enzymatic glucose sensor. *Electroanalysis* 30, 1117–1124. doi: 10.1002/elan.201800002

Chen, J., Yin, H., Zhao, S., Gong, J., Ji, Z., Nie, Q., et al. (2020). Construction of highly efficient non-enzymatic glucose sensors based on micro-spherical Ni-metal-organic frameworks. *Funct. Mater. Lett.* 13:2050022. doi: 10.1142/S1793604720500228

Collins, G. S., Mallett, S., Omar, O., and Yu, L. (2011). Developing risk prediction models for type 2 diabetes: a systematic review of methodology and reporting. *BMC Med.* 9:103. doi: 10.1186/1741-7015-9-103

Darvishi, S., Souissi, M., Karimzadeh, F., Kharaziha, M., Sahara, R., and Ahadian, S. (2017). Ni nanoparticle-decorated reduced graphene oxide for non-enzymatic glucose sensing: An experimental and modeling study. *Electrochim. Acta* 240, 388–398. doi: 10.1016/j.electacta.2017.04.086

Dolinska, J., Kannan, P., Sashuk, V., Kaszkur, Z., Sobczak, J. W., Jonsson-Niedziolka, M., et al. (2014). The versatile electrocatalytic oxidation of glucose on bimetallic nanoparticulate film electrode. *J. Electrochem. Soc.* 161, H3088–H3094. doi: 10.1149/2.0151413jes

Du, Y., He, Y., Zheng, Z., Shen, X., Zhou, Y., Wang, T., et al. (2019). A renewable platform for high-performance glucose sensor based on $Co(OH)_2$ nanoparticles/three-dimensional graphene frameworks. *J. Electrochem. Soc.* 166, B42–B48. doi: 10.1149/2.0481902jes

Gao, A., Zhang, X., Peng, X., Wu, H., Bai, L., Jin, W., et al. (2016). *In situ* synthesis of $Ni(OH)_2/TiO_2$ composite film on NiTi alloy for non-enzymatic glucose sensing. *Sens. Actuators B Chem.* 232, 150–157. doi: 10.1016/j.snb.2016.03.122

Gumilar, G., Kaneti, Y. V., Henzie, J., Chatterjee, S., Na, J., Yuliarto, B., et al. (2020). General synthesis of hierarchical sheet/plate-like M-BDC (M = Cu, Mn, Ni, and Zr) metal-organic frameworks for electrochemical non-enzymatic glucose sensing. *Chem. Sci.* 11:3644. doi: 10.1039/C9SC05636J

Hayat, A., Mane, S. K. B., Shaishta, N., Khan, J., Hayat, A., Keyum, G., et al. (2019). Nickel oxide nano-particles on 3D nickel foam substrate as a non-enzymatic glucose sensor. *J. Electrochem. Soc.* 166, B1602–B1611. doi: 10.1149/2.0491915jes

Jiao, L., Seow, J., Skinner, W. S., Wang, Z., and Jiang, H. (2019). Metal–organic frameworks: structures and functional applications. *Mater. Today.* 27, 43–68. doi: 10.1016/j.mattod.2018.10.038

Karimi-Maleh, H., Fatemeh, K., Marzieh, A., and Afsaneh,. L., A. (2020a). Electrochemical sensors, a bright future in the fabrication of portable kits in analytial systems. *Chem. Rec.* 20:682. doi: 10.1002/tcr.201900092

Karimi-Maleh, H., Kemal, C., Kubilay, A., Aysun, S., Fatemeh, K., and Fatih, S. (2020b). Palladium-nickel nanoparticles decorated on functionalized-MWCNT for high precision non-enzymatic glucose *sensing*. *Mater. Chem. Phys.* 250:123042. doi: 10.1016/j.matchemphys.2020.123042

Li, J. R., J., Kuppler, R., and Zhou, H. C. (2009). Selective gas adsorption and separation in metal–organic frameworks. *Chem. Soc. Rev.* 38, 1477–1504. doi: 10.1039/b802426j

Li, S., Bai, W.u., Zhang, X., and Zheng, J. (2020a). NiO/Cu-TCPP hybrid nanosheets as an efficient substrate for supercapacitor and sensing applications. *J. Electrochem. Soc.*167:027534. doi: 10.1149/1945-7111/ab6d4c

Li, S., Zhan, X., Bai, W., and Zheng, J. (2020b). Controllable synthesis of Ni/Co-TCPP MOFs with different morphologies and their application in electrochemical detection of glucose. *J. Electrochem. Soc.* 167:127506. doi: 10.1149/1945-7111/abac2a

Li, W., Lv, S., Wang, Y., Zhang, L., and Cui, X. (2019). Nanoporous gold induced vertically standing 2D NiCo bimetal-organic framework nanosheets for non-enzymatic glucose biosensing. *Sens. Actuators B Chem.* 281:652. doi: 10.1016/j.snb.2018.10.150

Liang, Z., Zhao, R., Qiu, T., Zou, R., and Xu, Q. (2019). Metal-organic framework-derived materials for electrochemical energy applications. *EnergyChem.* 1:100001. doi: 10.1016/j.enchem.2019.100001

Liu, C. S., Li, J., and Pang, H. (2020). Metal-organic framework-based materials as an emerging platform for advanced electrochemical sensing. *Coord. Chem. Rev.* 410:213222. doi: 10.1016/j.ccr.2020.213222

Liu, Y., Shi, W., Lu, Y., Liu, G., Hou, L., and Wang, Y. (2019). Nonenzymatic glucose sensing and magnetic property based on the composite formed by encapsulating ag nanoparticles in cluster-based Co-MOF. *Inorg. Chem.* 58, 16743. doi: 10.1021/acs.inorgchem.9b02889

Lu, K., Aung, T., Guo, N., Weichselbaum, R., and Lin, W. (2018). Nanoscale metal-organic frameworks for therapeutic, imaging, and sensing applications. *Adv. Mater.* 30:1707634. doi: 10.1002/adma.201707634

Martins, P. R., Rocha, M. A., Angnes, L., Toma, H. E., and Araki, K. (2011). Highly sensitive amperometric glucose sensors based on nanostructured α-$Ni(OH)_2$ electrodes. *Electroanalysis.* 23, 2541–2548. doi: 10.1002/elan.201100271

Padideh, N. A., Parviz, A. A., Mohammad, S. T., and Ahmad, M. S. (2020). Glucose oxidase/nano-ZnO/thin film deposit FTO as an innovative clinical transducer: a sensitive glucose biosensor. *Front. Chem.* 8:503. doi: 10.3389/fchem.2020.00503

Qiao, Y., Liu, Q., Lu, S., Chen, G., Gao, S., Lu, W., et al. (2020). High-performance non-enzymatic glucose detection: using a conductive Ni-MOF as an electrocatalyst. *J. Mater. Chem. B.* 8, 5411–5415. doi: 10.1039/D0TB00131G

Rocchiccioli-Deltcheff, C., Gouzerh, P., Jeannin, Y., and Valentini, F. (1978). Infrared spectra of nickel(II) complexes with hydroxyacetamidoxime and ethylnitrosolic acid. *J. Mol. Struct.* 49, 83–95. doi: 10.1016/0022-2860(78)87008-2

Rojas, S., Arenas-Vivo, A., and Horcajada, P. (2019). Metal-organic frameworks: a novel platform for combined advanced therapies. *Coord. Chem. Rev.* 388, 202–226. doi: 10.1016/j.ccr.2019.02.032

Shahrokhian, S., Ezzati, M., and Hosseini, H. (2020). Fabrication of a sensitive and fast response electrochemical glucose sensing platform based on co-based metal-organic frameworks obtained from rapid *in situ* conversion

of electrodeposited cobalt hydroxide intermediates. *Talanta* 210:120696. doi: 10.1016/j.talanta.2019.120696

Sheberla, D., Sun, L., Blood-Forsythe, M. A., Er, S., Wade, C. R., Brozek, C. K., et al. (2014). High electrical conductivity in Ni_3(2,3,6,7,10,11-hexaiminotriphenylene)$_2$, a semiconducting metal-organic graphene analogue. *J. Am. Chem. Soc.* 136, 8859–8862. doi: 10.1021/ja502765n

Shen, C., Su, J., Li, X., Luo, J., and Yang, M. (2015). Electrochemical sensing platform based on Pd–Au bimetallic cluster for non-enzymatic detection of glucose. *Sens. Actuators B Chem.* 209, 695–700. doi: 10.1016/j.snb.2014.12.044

Shi, N., Sun, S., Zhang, B., Du, Q., Liao, Y., Liao, X., et al. (2020). $Co(OH)_2$ nanosheets decorated $Cu(OH)_2$ nanorods for highly sensitive nonenzymatic detection of glucose. *Nanotechnology*, 31:325502. doi: 10.1088/1361-6528/ab8c77

Song, Y., Wei, C., He, J., Li, X., Lu, X., and Wang, L. (2015). Porous Co nanobeads/rGO nanocomposites derived from rGO/Co-metal organic frameworks for glucose sensing. *Sens. Actuators B Chem.* 220, 1056–1063. doi: 10.1016/j.snb.2015.06.052

Su, L., Xu, F., Chen, J., Cao, Y., and Wang, C. (2020). Photoresponsive 2D polymeric Langmuir–Blodgett films of 2,3,6,7,10,11-hexaiminotriphenylene. *New J. Chem.* 44, 5656–5660. doi: 10.1039/D0NJ00560F

Sun, F., Wang, S., Wang, Y., Zhang, J., Yu, X., Zhou, Y., et al. (2019). Synthesis of Ni-Co hydroxide nanosheets constructed hollow cubes for electrochemical glucose determination. *Sensors* 19:2938. doi: 10.3390/s19132938

Sun, Y., Li, Y., Wang, N., Xu, Q. Q., Xu, L., and Lin, M. (2018). Copper-based metal-organic framework for non-enzymatic electrochemical detection of glucose. *Electroanalysis* 30, 474–478. doi: 10.1002/elan.201700629

Wang, K., Xun, Q., and Zhang, Q. (2020). Recent progress in metal-organic frameworks as active materials for supercapacitors. *EnergyChem* 2:100025. doi: 10.1016/j.enchem.2019.100025

Wang, Y., Bai, W., Nie, F., and Zheng, J. (2015). A Non-enzymatic glucose sensor based on Ni/MnO_2 nanocomposite modified glassy carbon electrode. *Electroanalysis* 27, 2399–2405. doi: 10.1002/elan.201500049

Wei, C., Cheng, C., Cheng, Y., Wang, Y., Xu, Y., Du, W., et al. (2015). Comparison of NiS_2 and α-NiS hollow spheres for supercapacitors, non-enzymatic glucose sensors and water treatment. *Dalton Trans.* 44:17278. doi: 10.1039/C5DT02724A

Wei, Z., Yang, Y., Xiao, X., Zhang, W., and Wang, W. (2018). Fabrication of conducting polymer/noble metal nanocomposite modified electrodes for glucose, ascorbic acid and tyrosine detection and its application to identify the marked ages of rice wines. *Sens. Actuators B Chem.* 255, 895–906. doi: 10.1016/j.snb.2017.08.155

Wong, E., Backholer, K., Gearon, E., Harding, J., Freak-Poli, R., Stevenson, C., et al. (2013). Diabetes and risk of physical disability in adults: a systematic review and meta-analysis. *Lancet Diabetes Endocrinol.* 1, 106–114. doi: 10.1016/S2213-8587(13)70046-9

Yang, J., Yu, J., Strickler, J. J. R., Chang, W. J., and Gunasekaran, S. (2013). Nickel nanoparticle–chitosan-reduced graphene oxide-modified screen-printed electrodes for enzyme-free glucose sensing in portable microfluidic devices. *Biosens. Bioelectron.* 47, 530–538. doi: 10.1016/j.bios.2013.03.051

Ye, J., Chen, C. W., and Lee, C. L. (2015). Pd nanocube as non-enzymatic glucose sensor. *Sens. Actuators B Chem.* 208, 569–574. doi: 10.1016/j.snb.2014.11.091

Yuan, C., Hsu, C. L., Wang, S. C., and Chang, K. S. (2005). Eliminating the interference of ascorbic acid and uric acid to the amperometric glucose biosensor by cation exchangers membrane and size exclusion membrane. *Electroanalysis* 17, 2239–2245. doi: 10.1002/elan.200503359

Zhang, Y., Xiao, X., Sun, Y., Shi, Y., Dai, H., Ni, P., et al. (2013). Electrochemical deposition of nickel nanoparticles on reduced graphene oxide film for nonenzymatic glucose sensing. *Electroanalysis* 25, 959–966. doi: 10.1002/elan.201200479

Zhou, J., Tian, G., Zeng, L., Song, X., and Bian, X. (2018). Nanoscaled metal-organic frameworks for biosensing, imaging, and cancer therapy. *Adv. Health. Mater.* 7:1800022. doi: 10.1002/adhm.201800022

Conflict of Interest: The authors declare that the research was conducted in the absence of any commercial or financial relationships that could be construed as a potential conflict of interest.

frontiers in Chemistry

REVIEW
published: 26 November 2020
doi: 10.3389/fchem.2020.601044

Electrochemical Sensors Based on Covalent Organic Frameworks: A Critical Review

Sidi Chen[1], *Baiqing Yuan*[1]*, *Gang Liu*[1]* and *Daojun Zhang*[2]*

[1] School of Chemistry and Materials Science, Ludong University, Yantai, China, [2] Henan Province Key Laboratory of New Optoelectronic Functional Materials, College of Chemistry and Chemical Engineering, Anyang Normal University, Anyang, China

The metal-free cousins of metal-organic frameworks, covalent organic frameworks (COFs), are a class of pre-designable crystalline polymers composed of light elements and connected by strong covalent bonds. COFs are being given more and more attention in the electrochemical sensor field due to their fascinating properties, such as highly tunable porosity, intrinsic chemical and thermal stability, structural diversity, large specific surface area, and unique adsorption characteristics. However, there are still some key issues regarding COFs that need to be urgently resolved before they can be effectively applied in electrochemical sensing. In this review, we summarized recent achievements in developing novel electrochemical sensors based on COFs, and discussed the key fundamental and challenging issues that need to be addressed, including the mechanisms underlying charge transport, methods to improve electrical conductivity, immobilization methods on different substrates, synthesis strategies for nanoscale COFs, and the application of COFs in different fields. Finally, the challenges and outlooks in this promising field are tentatively proposed.

Keywords: electrochemical sensor, covalent organic frameworks (COFs), electrical conductivity, nanoscale COFs, conductive substrate, metal-covalent organic frameworks (MCOFs)

OPEN ACCESS

Edited by:
Carmine Gaeta, University of Salerno, Italy

Reviewed by:
Huan Pang, Yangzhou University, China
Matthew A. Addicoat, Nottingham Trent University, United Kingdom

***Correspondence:**
Baiqing Yuan
baiqingyuan1981@126.com
Gang Liu
shdliugang@163.com
Daojun Zhang
zhangdj0410@sohu.com

Specialty section:
This article was submitted to Supramolecular Chemistry, a section of the journal Frontiers in Chemistry

Received: *31 August 2020*
Accepted: *19 October 2020*
Published: *26 November 2020*

Citation:
Chen S, Yuan B, Liu G and Zhang D (2020) Electrochemical Sensors Based on Covalent Organic Frameworks: A Critical Review. Front. Chem. 8:601044. doi: 10.3389/fchem.2020.601044

INTRODUCTION

Covalent organic frameworks (COFs), a new class of multifunctional porous crystalline materials, are two- or three-dimensional (2D or 3D) porous crystalline materials built by light elements (C, B, O, Si, and N) via strong covalent bonds (C-N, C=N, C=C-N, B-O) (Xue et al., 2017; Chen et al., 2019; Wang and Zhuang, 2019; Zhu et al., 2019). Since the first report in 2005 by Cote et al. (2005), COFs have attracted more and more attention due to their fascinating properties, and many novel COFs have been synthesized (Waller et al., 2015; Lohse and Bein, 2018). Compared with other materials, COFs have many unique properties, such as highly tunable porosity, large specific surface area, unique adsorption characteristics, ordered channel structure, and intrinsic chemical and thermal stability, which make them outstanding in many fields including separation, gas adsorption, analysis, energy conversion and storage, and electrochemical sensing (Wu and Yang, 2017; Wang J. et al., 2018; Zheng et al., 2019). Ordered network configuration and multiple active acupoints give COFs a large adhesion surface, which is superior to 2D graphene nanosheets. In comparison with another class of porous crystalline material MOFs, COFs have thermal and chemical stabilities due to the involvement of covalent bonds (Li et al., 2020b; Yusran et al., 2020b).

To ensure the growth of the crystalline structures, the chemical reactions involved in the construction of COFs need to be reversible to render the self-healing ability to repair structural defects caused by mismatched covalent linkages. Up to now, researchers have proposed six synthetic methods for COFs, which refers to solvothermal, ionothermal, room-temperature, mechanochemical synthesis, interfacial synthesis, and microwave synthesis (Geng et al., 2020). Solvothermal synthesis is one of the most common methods to fabricate COFs, occurring in a sealed system at a specific temperature and pressure (Chen et al., 2019). For example, BND-TFB COFs were synthesized through the solvothermal method with improved material quality and a shorter reaction time. Ordered and amorphous microporous polytriazine networks were prepared through ionothermal synthesis by the trimerization of nitriles in a $ZnCl_2$ melt at 400°C (Vitaku and Dichtel, 2017). The material exhibited a very large surface area that can be used for gas storage, sensors, or catalyst carriers (Kuhn et al., 2008). TpBD-based COFs were prepared via room-temperature synthesis, which is an attractive way to construct COFs for the case of fragile organic units or sensitive substrates (Yang et al., 2015). Mechanochemical synthesis is a simple, economical, and green method in which building blocks are mixed in a mortar and ground under ambient conditions to yield the COFs (Geng et al., 2020). The interfacial synthetic strategy is a novel and efficient method for fabricating COF thin films with controllable thickness. For the very first time, mesoscale covalent self-assembly was explored to fabricate self-standing crystalline porous thin films without defects at the liquid-liquid (DCM-water bilayer) interface (Sasmal et al., 2019). Microwave synthesis is a simple and efficient approach to building COFs. The melamine-based porous polymeric network SNW-1 was synthesized by a microwave-assisted synthesis route (Zhang et al., 2012).

Electrochemical sensors work by reacting with analytes to produce electrical signals which are proportional to its concentration. A typical electrochemical sensor consists of a sensing electrode (or working electrode) and a counter electrode separated by a thin electrolytic layer (Karimi-Maleh et al., 2019). Recently, electrochemical sensing has gained extensive attention in multiple fields, such as pharmacy, clinical diagnosis, environmental monitoring, and food safety, because of its low cost, sensitive response, and simple operation (Yan et al., 2019; Yang et al., 2019; Liang et al., 2020). COFs have been widely exploited in electrochemical sensing due to their unique properties (Liang et al., 2019a; Sun et al., 2019a), which can improve the sensitivity of electrochemical sensors. For example, COFs possess a highly ordered porous structure, functional groups, and available holes, providing a large active surface in which to load electroactive molecules. In addition, their better biocompatibility also improves the stability of the electrochemical sensor (Ding et al., 2014; Li et al., 2020a). However, some key issues regarding COFs need to be urgently resolved before they can be effectively applied in electrochemical sensing. Herein, we present a critical review on the recent advances of COFs and their application in electrochemical sensors, with focus on the mechanism and method/strategy for improving electrical conductivity, the immobilization on different substrates, miniaturization, and application in electrochemical sensors (**Figure 1**). The challenges and outlooks toward COF-based electrochemical sensing are also discussed. We hope that the review will guide readers to design and develop COF-based materials for electrochemical sensing applications.

IMPROVING THE ELECTRICAL CONDUCTIVITY OF THE COFs

A topology design diagram can be used to guide the synthesis of 2D or 3D COFs in which the geometry of the selected organic monomers **determine** the primary-order structure **in either a 2D or** 3D manner (Geng et al., 2020), as shown in **Figure 2**. In 2D COFs, planar building blocks are covalently connected in the lateral crystallographic direction and further stacked together in the vertical direction by van der Waals. By contrast, the design of 3D COFs requires at least one building block to possess Td or orthogonal geometry that controls the development of the skeletons into a 3D structure. To ensure the growth of the crystalline structures, the chemical reactions involved in the formation of COFs need a certain reversibility which creates the self-healing ability to repair structural defects (Huang et al., 2016). However, the self-healing process is not sufficient, resulting in abundant defects in COFs. In addition, the low molecular conjugation of π-electrons cause electron localization.

Abbreviations: 2D, two-dimensional; 3D, three-dimensional; 2HP6, dihydroxylatopillar [6]arene; 3D-KSC, 3D kenaf stem-derived macroporous carbon; AA, ascorbic acid; AAO, anodic aluminum oxide; AE, Au electrode; AP, amperometric; BDBA, 1,4-phenylenebis; BDT, 2,6-benzo[1,2-b:4,5-b′]dithiophene dialdehyde; BND, N-benzidine benzophenone imine; BPA, bisphenol A; $BPPF_6$, N-butylpyridinium hexafluorophosphate; BPS, bisphenol S; BTA, 1,3,5-tricarbaldehyde; CC, catechol; CGA, chlorogenic acid; $COF_{p-porNH2-BTA}$, iron-porphyrin-based covalent organic framework; COFs, covalent organic frameworks; CP6, cationic pillar [6]arene; CTnI, cardiac troponin I; CV, cyclic voltammetry; DAAQ, 2,6-diaminoanthraquinone; DAB, p-phenylenediamine; DAT, 3,5-diamino-1,2,4-triazole; DHTA, 2,5-dihydroxyterethaldehyde; DMTP, 2,5-dimethoxyterephaldehyde; DPASV, differential pulse anodic stripping voltammetry; DPPD, 3,8-diamino-6-phenylphenanthridine; DPV, differential pulse voltammetry; EGFR, epidermal growth factor receptor; EIS, electrochemical impedance spectroscopy; ETTA, 4,4′,4″,4‴-(1,1,2,2-ethylenetetrayl)tetrakisaniline; Fe_3O_4@NHCS, Fe_3O_4/N co-doped hollow carbon spheres; FTO, fluorine doped tin oxide; GCE, glassy carbon electrode; GO, graphene oxide; GOD, glucose oxidase; HQ, hydroquinone; ITO, indium tin oxide; LOD, low detection limits; MCOFs, metal-covalent organic frameworks; MGCE, magnetic glassy carbon electrode; MIP, molecularly imprinted polymer; MOFs, metal-organic frameworks; NH_2-f-MWCNT, amino-functionalized carbon nanotube; NPs, nanoparticles; ONP, o-nitrophenol; ORR, oxygen reduction reaction; P-COFs, porphyrin-based covalent organic frameworks; PDA, 1,4-phthalaldehyde; PEDOT, poly(3,4-ethylenedioxythiophene); PNP, p-nitrophenol; POR, poly(5,10,15,20-tetrakis (4-aminophenyl)porphyrin); PQ, paraquat; PSA, prostate specific antigen; PSF, polysulfone; PVP, polyvinylpyrrolidone; RC, resorcinol; SDZ, sulfadiazine; SMR, sulfamerazine; SP, sodium picrate; SWV, square wave voltammetry; TAPB, 1,3,5-tris (4-aminophenyl) benzene; TAPP, 5,10,15,20-tetrakis(4- aminophenyl)porphyrin; TCNQ, tetracyanoquinodimethane; TFB, 1,3,5-triformylbenzene; TFP, 1,3,5-triformylphluroglucinol; TFPB, 1,3,5-tris(p-formylphenyl) benzene; Thi, thionine; TPAL, terephthalaldehyde; TpBD, 1,3,5-triformylphloroglucinol (Tp)/benzidine (BD); TTA, 4,4′,4″-(1,3,5-triazine-2,4,6-triyl)trianiline; TTF, tetrathiafulvalene; WP6, water-soluble pillar[6]arene.

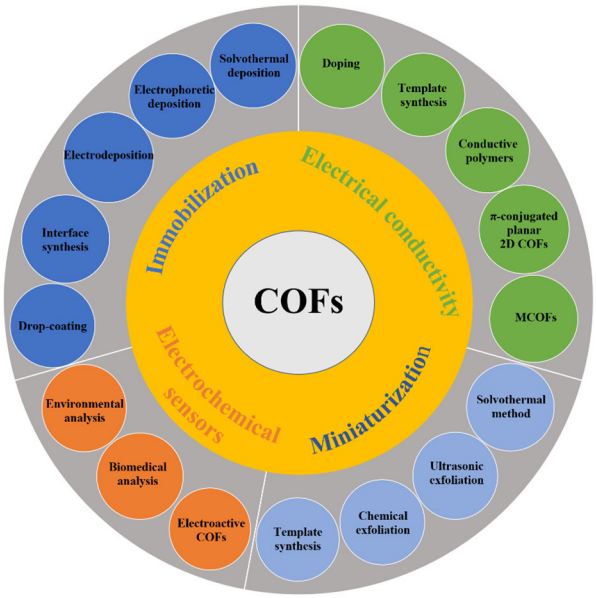

FIGURE 1 | Schematic illustration of COF-based electrochemical sensing.

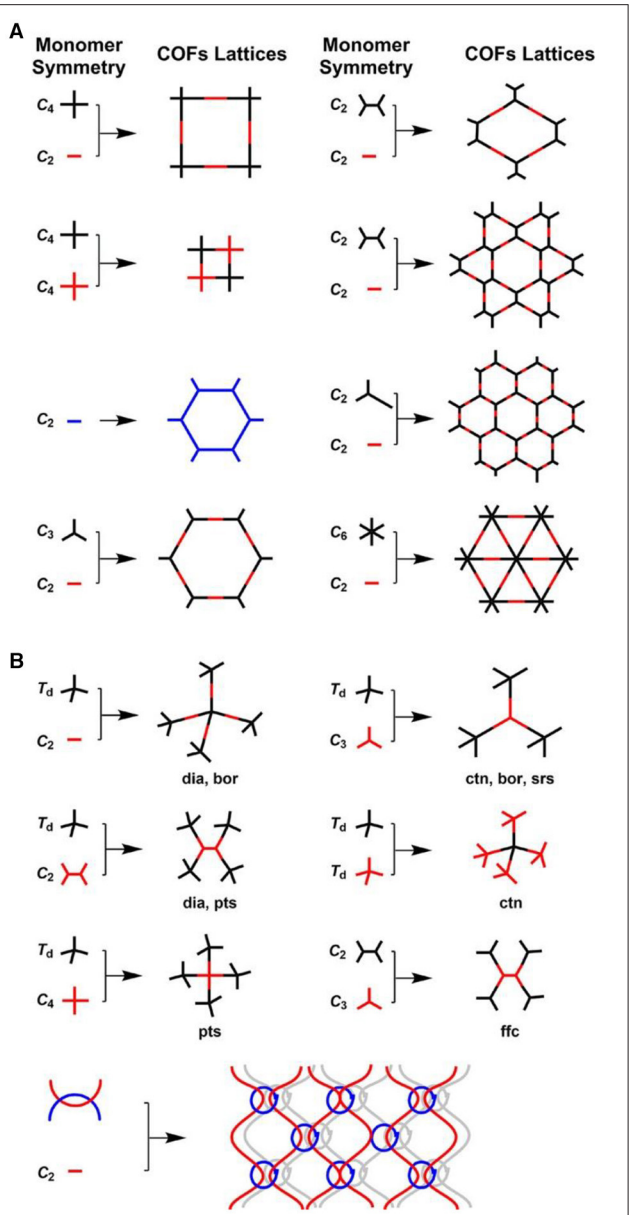

FIGURE 2 | Basic topological diagrams for the design of 2D and 3D COFs. Reproduced with permission from Geng et al. (2020). Copyright 2020, American Chemical Society.

The issues lead to the intrinsic poor conductivity of bulk COFs, which limits their application in electrochemical sensing.

There are two mechanisms for charge transport in COFs: hopping transport and ballistic (or band-like) transport (**Figure 3**) (Xie et al., 2020). In hopping mode, the charge carriers (electrons/holes) hop between isolated, non-bonded neighbor sites (donor and acceptor sites), where the charge carriers are localized. As for band transport, the charge carriers are delocalized and continuous energy bands are formed. Conductive COFs can be therefore categorized into two categories: through space and through bonds (Meng et al., 2019). Instead of a single bond connection including borate and imine linkage, full annulation of building blocks through aromatic linkages can promote efficient charge delocalization, suggesting a promising strategy for conjugated 2D structure generation to achieve a through-bond charge transport (Guo et al., 2013). Through-space charge transport relies on maximizing orbital overlap with lowered energy for charge transport through a strategic choice of building blocks. For example, π-stacking was explored to design COF-based materials with improved electrical conductivity (Wan et al., 2011). The principal strategy to guide the synthesis of conductive COFs is to obtain a highly conjugated and crystalline structure with few defects.

The low intrinsic conductivity of COFs still imposes a great challenge for their applications in electrochemical sensing (Meng et al., 2019; Wu et al., 2019; Xu L. et al., 2019). This problem could be overcome via the following methods and strategies including doping with oxidants and guest molecules, template synthesis, introducing conductive polymers, π-conjugated planar 2D structures, and the metalation of COFs.

The electrical conductivity of COFs can be improved by designing high-supply electronic blocks with electron acceptor dopants. For example, the electrical conductivity of COFs could be tuned by doping with iodine or TCNQ, resulting in high conductivity up to 0.28 S/m (Cai et al., 2014). In addition, this doping strategy is broad enough that it can be used to improve the electrical conductivity of many kinds of COFs.

Template synthesis is another powerful method to improve the conductivity of COFs on a conductive template surface. COFs with highly ordered pore channels ($COF_{TTA-DHTA}$) were synthesized on an amino-functionalized carbon nanotube (NH_2-f-MWCNT) from TTA and DHTA via imine linkages (Sun et al., 2017). The $MWCNT@COF_{TTA-DHTA}$ not only had electrical

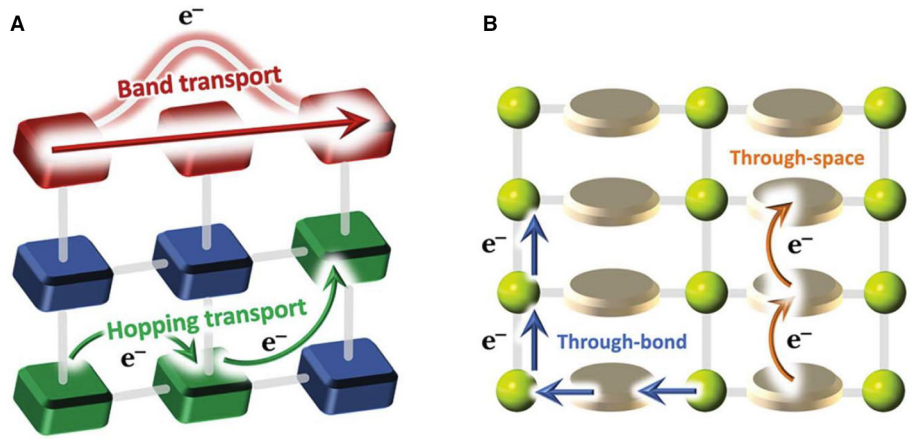

FIGURE 3 | Schematic diagrams of charge transport modes (band transport and hopping transport) **(A)** and pathways **(B)**. Reproduced with permission from Calbo et al. (2019). Copyright 2019, The Royal Society of Chemistry.

conductivity but also possessed excellent crystallinity, regular pore channels, and a high surface area. The $COF_{BTA-DPPD}$-rGO composite was also synthesized by this method at room temperature under ambient conditions (Xu L. et al., 2019). Coupling the improved conductivity from rGO, $COF_{BTA-DPPD}$-rGO exhibited an enhanced electrochemical performance, which might be attributed to the synergistic effect of the π-conjugated $COF_{BTA-DPPD}$ being fully covered on the conductive rGO surface.

Introducing a conductive polymer into the channel of COFs can also increase its conductivity. PEDOT is one of the most widely investigated conductive polymers because of its excellent electronic properties and high stability. One strategy includes electropolymerizing PEDOT into the pores of redox-active 2D COF films (Mulzer et al., 2016). PEDOT-modified COF films can accommodate high charging rates (10–1,600 C) without compromising performance and exhibit 10-fold current response relative to unmodified films and stable capacitances for at least 10,000 cycles. However, the disadvantages of electropolymerization and requirement of COF films as a precursor make it difficult to scale up to high-throughput production lines for practical application. Recently, a novel method to introduce PEDOT to improve the electrical conductivity of the COFs was reported by using an *in-situ* solid-state polymerization inside the nanochannels (Wu et al., 2019). The resulting PEDOT@AQ-COFs showed an electrical conductivity value of 11 0 S/cm at room temperature and a remarkably improved storage performance. This approach will serve as a promising strategy for increasing the electrical conductivity of COFs and extending the applications of COF materials.

The fourth method is the molecular design strategy focusing on planar 2D COFs, in which the formation of π-conjugated sheets can promote the delocalization of charge, has yielded metallic conductivities (Meng et al., 2019). A novel intrinsically conductive 2D COF was synthesized through the aromatic annulation of 2,3,9,10,16,17,23,24-octa-aminophthalocyanine nickel (II) and pyrene-4,5,9,10-tetraone. The intrinsic bulk conductivity of the COF material could be up to 0.0025 S/m, and increased by 3 orders of magnitude upon I_2 doping. In addition, 3D electroactive TTF-based COFs were reported with high crystallinity and large permanent porosity, in which these TTF-based COFs were redox active to form organic salts that exhibit outstanding electric conductivity (Li et al., 2019).

In order to further enhance the electric conductivity, metal ions were introduced into the COFs lattice to form conductive metal-covalent organic frameworks (MCOFs), which can be synthesized through either direct synthesis or post-synthetic metalation by using planar and large π-electronic macrocycles as the building and paring units for the metal (Dong et al., 2020; Xie et al., 2020). Compared with metal free COFs, MCOFs not only have higher intrinsic conduction, but also exhibit superior electrocatalytic activity due to the presence of a metal component. 2D and 3D MCOFs have been prepared by using π-electron rich building blocks, such as porphyrin (Lin et al., 2015), phthalocyanine (Spitler et al., 2012), bipyridine (Aiyappa et al., 2016), and dehydrobenzoannulene (Baldwin et al., 2016).

IMMOBILIZATION OF COFs ON DIFFERENT SUBSTRATES

It is an essential procedure to modify COFs on different electrodes for electrochemical sensing applications. The fabrication of ultrathin COF films is still very challenging, since the poor COF-substrate affinity hampers the nucleation of COF crystallites. Herein, immobilization methods and strategies for COFs on different substrates were summarized, such as solvothermal growth/deposition, electrophoretic deposition, electrochemical deposition, interfacial polymerization, and drop-coating, as shown in **Table 1**.

Solvothermal growth/deposition is found to be an efficient method to immobilize DAB-TFP COF thin films on different substrates (indium tin oxide, fluorine doped tin oxide, and

TABLE 1 | Immobilization methods and strategies for COFs on different substrates.

Substrates	COFs	Synthetic units	Immobilization methods	Thickness	References
GCE	POR-COFs	TAPP	Electrochemical deposition	/	Tavakoli et al., 2019
ITO	COF-300	Tetrakis(4-aminophenyl) methane/terephthalaldehyde	Electrophoretic deposition	0.4–24 μm	Rotter et al., 2019
ITO	COF-5	Benzene-1,4-diboronic acid/2,3,6,7,10,11-hexahydroxytriphenylene hydrate	Electrophoretic deposition	0.4–24 μm	Rotter et al., 2019
ITO	BDT-ETTA COF	BDT/ETTA	Electrophoretic deposition	0.4–24 μm	Rotter et al., 2019
AAO	Imine-based COFs	1,3,5triformylphloroglucinol/p-phenylenediamine	Solvothermal growth	/	Shi et al., 2019
PSF	TpPa-COFs	1,3,5triformylphloroglucinol/p-phenylenediamine	Interfacial polymerization	0.29–1.12 μm	Wang R. et al., 2018
α-Al_2O_3	COF-320	tetra-(4-anilyl) methane and 4,4′-biphenyldicarboxaldehyde	Solvothermal growth	4 μm	Lu et al., 2015
GO	COF-1	1,4-benzenediboronic acid	Solvothermal growth	10–250 nm	Zhang X. et al., 2019
GCE	COF	BDBA/1,4-dioxane–mesitylene	Drop-coating	/	Zhang T. et al., 2019
Au electrode	DAAQ-TFP COF	DAAQ/TFP	Solvothermal growth	60–560 nm	DeBlase et al., 2015
ITO/FTO/platinum	2D COFs	DAB/TFP	Solvothermal growth	200 nm	Gou et al., 2016

platinum substrates) (Gou et al., 2016). The oriented thin films of a redox-active 2D β-ketoenamine COF on Au was first fabricated by solvothermal growth, and the film thickness was controlled by varying the initial concentrations of the monomers (DeBlase et al., 2015). The oriented COF film modified electrode exhibit a 400% increase in capacitance scaled to the electrode area as compared to those functionalized with the randomly oriented COFs powder (**Figure 4**). Recently, COF-1 with an ordered channel structure and precise pore size was synthesized and attached onto the surface of graphene oxide (GO) by *in-situ* growth, which improves the dispersity and stability in water over COF-1 (Zhang X. et al., 2019).

The fabrication of COF film and coatings on conducting substrates was demonstrated in an electric field by electrophoretic deposition, which is suitable for depositing 2D and 3D COFs linked by imine or boronate ester bonds, such as BDT-ETTA COFs, COF-300, and COF-5 (Rotter et al., 2019). By controlling the key parameters including particle concentration, duration, and applied potential, deposition with precise thickness can be achieved. In addition, co-deposition of different COFs as well as COFs/Pt nanoparticles from mixed suspensions were also presented.

Solvent intractability and sluggish condensation kinetics have limited the synthesis and processing of 2D or 3D COFs. In order to resolve the problem, poly(5,10,15,20-tetrakis(4-aminophenyl)porphyrin)-COFs (POR-COFs) with a high crystalline order were electrochemically synthesized via the formation of phenazine linkages by controlling the temperature, potential scanning rate, and electrode materials and co-crystallization with pyridine (Tavakoli et al., 2019). The pyridine sublattice not only stabilized the Py-POR-COFs superlattice but also controlled the interlayer spacing and stacking in this class of materials, resulting in enhanced ORR activity.

A facile and simple strategy, interfacial polymerization, was developed for the direct synthesis of imine-typed COFs on polysulfone substrates to produce composite membranes (Wang R. et al., 2018). The prepared membranes exhibited superior long-term stability and stability even in highly acidic/basic conditions. The COFs/polysulfone composite membranes had the advantage of large-scale production, showing potential application for the treatment of wastewater and the removal of pharmaceutical wastes from water.

The synthesized COFs can also be dripped onto different electrodes and then dried at room temperature to achieve their modification. For example, COF nanosheets were modified on GCE by this method for signal amplification, which was applied for sensitive biomarker detection (Zhang X. et al., 2019).

NANOSCALE COFs

Large size COFs lead to low active area, low mass transfer rate, and difficult modification as well as poor stability on the electrode, which will influence the stability, reproducibility/repeatability, and sensitivity. The miniaturization of COFs will solve this problem. The existing methods for nanoscale COF preparation includes the polymer-assisted solvothermal method, high-power ultrasonic exfoliation, steric hindrance-induced chemical exfoliation, and the template synthesis. However, these procedures are usually tedious and need strict synthetic conditions. Recently, a nanoscale COF prepared via a facile synthetic approach under ambient conditions was reported (Guan et al., 2019). Imine-linked TPB-DMTP-COFs was prepared through the reaction of 1,3,5-tris (4-aminophenyl) benzene and 2,5-dimethoxyterephthaldehyde under mild conditions (CH_3CN, 25°C, 12 h) with the aid of acetic acid and polyvinylpyrrolidone (PVP). Unlike traditional solvothermal COFs synthesis, this approach does not need any vigorous reaction conditions, such as a solvothermal and inert atmosphere. More importantly, scaling up to a gram-scale nanoscale COF synthesis was easily achieved. In order to decrease the size of COFs, a template-mediated synthesis of hollow tubular COFs using a twostep strategy was reported by Pachfule et al. (2015). ZnO nanorods were wrapped with COF layers by a typical Schiff-base reaction of 1,3,5-triformylphloroglucinol and

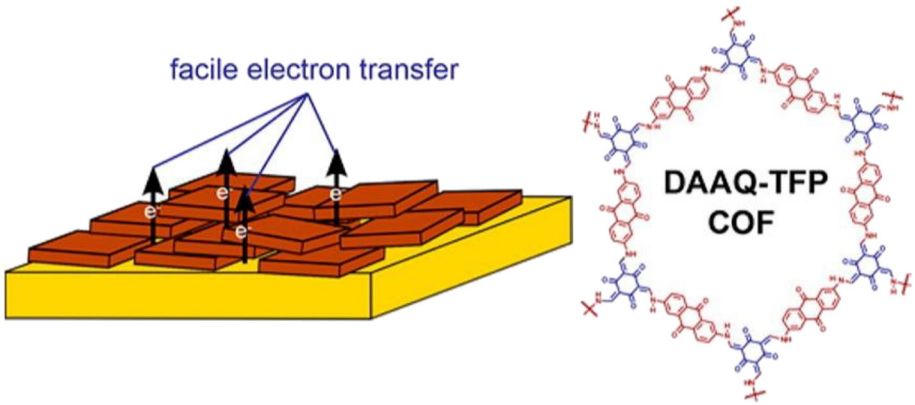

FIGURE 4 | Oriented thin film of DAAQ-TFP COFs for efficient redox processes. Reproduced with permission from DeBlase et al. (2015). Copyright 2015, American Chemical Society.

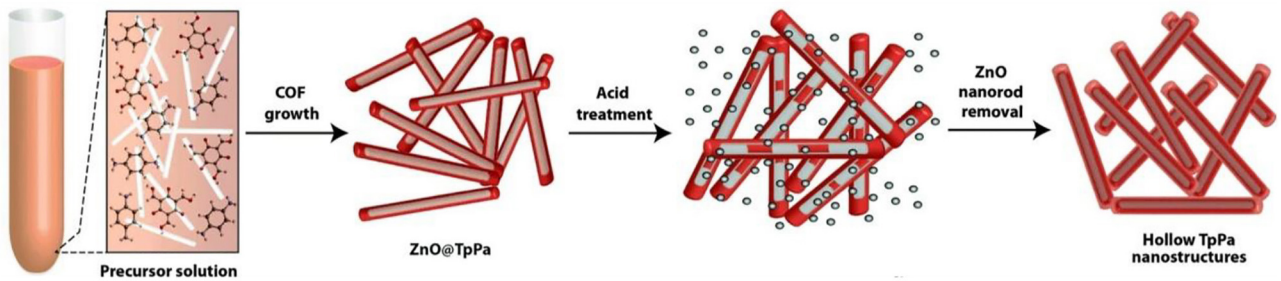

FIGURE 5 | Synthesis of COF nanotubes via a template-mediated strategy. Reproduced with permission from Pachfule et al. (2015). Copyright 2015, The Royal Society of Chemistry.

p-phenylenediamine. Then the inside templates were etched by acid to leave the hollow nanostructures in quantitative yield (**Figure 5**).

APPLICATIONS OF COFs IN ELECTROCHEMICAL SENSING

Based on their structural characteristics, COFs are endowed with unique properties, and have been successfully applied in electrochemical sensing. Nowadays, an electrochemical sensing platform based on COFs is widely used in the fields of environmental pollutant and biomedicine analysis. Herein, the applications of COFs in different fields are comprehensively summarized (**Table 2**). Furthermore, we focus the application of electroactive COFs in ratiometric electrochemical sensors which will be a promising field.

Application of COFs in Different Analytical Fields

Environmental Analysis

Endowed with an intrinsic absorption capability, COF-based electrochemical sensors have been widely used in the detection of environmental pollutants including hydrazine, explosives, catechol, nitrophenol, hydroquinone, bisphenol A, paraquat, and heavy metals. Porous and redox-active COFs were demonstrated to remove and detect hydrazine (Liang et al., 2020). Benefiting from a combination of the enhanced electron transfer and high surface area of DQ–COF, the electrochemical sensor exhibited a low detection limit, wide linear range, and high anti-interference ability. In addition, a sensitive and selective sensor was developed based on TAPB-DMTP-COFs for the detection of lead in an aqueous medium (Zhang et al., 2018b). This COFs were synthesized with 1,3,5-tris (4-aminophenyl) benzene (TAPB) and 2,5-dimethoxyterephaldehyde (DMTP). The novel sensor showed a broad linear range, low detection limit, high sensitivity, good stability and reproducibility, which may be assigned to the many active sites and high surface area of TAPB-DMTP-COFs. Under optimum conditions, the method showed an excellent linearity to the concentration of lead in the range of 0.0050–2.0 μM with a detection limit of 1.9 nM. This method not only demonstrates the feasibility of COF-based sensors for the detection of trace metal ions, but also broadens the detection range application of COF-based hybrid materials in electroanalytical chemistry. An Fe_3O_4-based magnetic COFs nanosphere (Fe_3O_4@AT-COFs) with a different surface morphologic structure is reported by facile ambient temperature synthesis, which shows the

TABLE 2 | The analytical performances of electrochemical sensors based on different COFs.

Electrode	Analyte	Technique	Potential	Detection limit	Linear range	Sensitivity	References
DQ-COF/Ni/ITO	Hydrazine	AP	0.8 V	0.07 μM	0.5–1,223 μM	1.81 μA $cm^{-2}μM^{-1}$	Liang et al., 2020
p-COF/AE	EGFR	DPV	0.2 V	5.64 × 10^{-3} pg mL^{-1}	0.05–100 pg mL^{-1}	/	Yan et al., 2019
3D-KSC/$COF_{TAPB-PDA}$/PtNPs	H_2O_2	AP	0.04 V	0.006 μM	0.0185–5.4 μM 5.4–3055.4 μM	2.58 μA $cm^{-2}μM^{-1}$ 449.33 μA cm^{-2} mM^{-1}	Yang et al., 2019
3D-KSC/$COF_{TAPB-PDA}$/CuNPs	Glucose	AP	0.5 V	1.54 μM	4.69–1,570 μM 1,570–7,070 μM	2.128 mA cm^{-2} mM^{-1} 0.829 mA cm^{-2} mM^{-1}	Yang et al., 2019
Au NPs/BPene/Fe_3O_4-COF/GCE	PSA	DPV	0.3 V	30 fg mL^{-1}	0.0001–10 ng mL^{-1}	/	Liang et al., 2019a
MIP/GO@COF/GCE	SDZ	DPV	0.9 V	0.16 μM	0.5–200 μM	/	Sun et al., 2019a
MIP/GO@COF/GCE	Acetaminophen	DPV	0.4 V	0.032 μM	0.05–20 μM	/	Sun et al., 2019a
TAPB-DMTP-COFs/AuNPs/GCE	CGA	DPV	0.17 V	0.0095 μM	0.010–40 μM	/	Zhang et al., 2018a
$COF_{DHTA-TTA}$/GCE	H_2O_2	DPV	−0.5 V −0.3 V	2.42 μM 1.70 μM	8.06–400 μM 5.66–400 μM	/	Xu M. et al., 2019
$COF_{DHTA-TTA}$/GCE	pH	DPV	−0.5–0.5 V	/	11–3	64.2 mV/pH	Xu M. et al., 2019
GOD/$COF_{DHTA-TTA}$/GCE	Glucose	DPV	−0.3 V −0.53 V	0.38 μM 0.18 μM	1.26–6,000 μM 0.60–6,000 μM	/	Xu M. et al., 2019
WP6@Ag@COF/GCE	PQ	CV	−0.755 V	0.014 μM	0.01–50 μM	/	Tan et al., 2019
TAPB-DMTP-COF/CPE	Lead	DPASV	−1.2 V	0.0019 μM	0.0050–2.0 μM	/	Zhang et al., 2018b
$COF_{ETTA-TPAL}$-Fc $(COOH)_2$/GCE	H_2O_2	DPV	−0.5/0.45 V	0.33 μM	1.1–500 μM		Liang et al., 2019b
MIP/MoS_2/NH_2-MWCNT@COF/GCE	SMR	DPV	1.03 V	0.11 μM	0.3–200 μM	/	Sun et al., 2019b
2HP6@Au@CP6@COF/GCE	SP	DPV	−0.4∼-0.1 V	0.0017 μM	0.005–120 μM	/	Tan et al., 2020
$COF_{p-FeporNH2-BTA}$/GCE	H_2O_2	DPV	−0.2 V	2.06 nM	6.85–7,000 nM	/	Xie et al., 2020a
$COF_{p-FeporNH2-BTA}$/GCE	pH	DPV	−0.9–0.15 V	/	3–9	−41.2 mV/pH	Xie et al., 2020a
$COF_{Thi-TFPB}$-CNT/GCE	pH	DPV	−0.6–0.3 V	/	1–12	54 mV/pH	Wang L. et al., 2020
$COF_{Thi-TFPB}$-CNT/GCE	AA	DPV	−0.05 V	17.68 μM	53.04–4,000 μM/ 4–8 mM	/	Wang L. et al., 2020
CTpPa-2/GCE	BPA	DPV	0.2–1.0 V	0.02 μM	0.1–50 μM	/	Pang et al., 2020
CTpPa-2/GCE	BPS	DPV	0.2–1.0 V	0.09 μM	0.5–50 μM	/	Pang et al., 2020
TB-Au-COFs-Ab_2/GCE	cTnI	SWV	−0.4 V	0.17 pg mL^{-1}	0.5–10,000 pg mL^{-1}	/	Zhang et al., 2018c
Fe_3O_4@AT-COF/MGCE	PNP	DPV	−0.772 V	0.2361 μM	10–3,000 μM	0.7588 μA $cm^{-2}μM^{-1}$	Wang Q. et al., 2020
Fe_3O_4@AT-COF/MGCE	ONP	DPV	−0.616 V	0.6568 μM	10–3,000 μM	0.7799 μA $cm^{-2}μM^{-1}$	Wang Q. et al., 2020
PtNPs@COFs-MWCNTs/GCE	Tanshinol	DPV	0.4 V	0.018 μM	0.002–1.1 mM	10.089 μA $cm^{-2}mM^{-1}$	Zhang et al., 2020
COF-3-$BPPF_6$-CPE	HQ	DPV	0.17 V	0.31 μM	1–2,000 μM	/	Xin et al., 2020
COF-3-$BPPF_6$-CPE	CC	DPV	0.26 V	0.46 μM	1–2,000 μM	/	Xin et al., 2020
GCE/DAT-COF	HQ	DPV	0.03 V	0.13 μM	0.20–500 μM	/	Arul et al., 2020
GCE/DAT-COF	CC	DPV	0.13 V	0.07 μM	0.20–500 μM	/	Arul et al., 2020
GCE/DAT-COF	RC	DPV	0.56 V	0.08 μM	0.20–500 μM	/	Arul et al., 2020
Fe_3O_4@NHCS/GCE	Dopamine	DPV	0.35 V	6.3 nM	0.01–40 μM	/	Lu et al., 2020
Fe_3O_4@NHCS/GCE	Uric acid	DPV	0.42 V	36.1 nM	0.10–40 μM	/	Lu et al., 2020
Fe_3O_4@NHCS/GCE	Guanine	DPV	0.75 V	143.2 nM	0.50–30 μM	/	Lu et al., 2020
Fe_3O_4@NHCS/GCE	Adenine	DPV	1.08 V	123.5 nM	0.50–40 μM	/	Lu et al., 2020
COF@NH_2-CNT/GCE	Furazolidone	DPV	−0.4 V	77.5 nM	0.2–100 μM	/	Sun et al., 2020
Fe_3O_4@TAPB-DMTP-COFs/GCE	Luteolin	DPV	0.2 V	7.2 nM	0.010–7 μM	/	Xie et al., 2020b

advantages of higher surface area, good water dispersity, long-term stability, excellent electrical conductivity, and pre-concentration effect (Wang Q. et al., 2020). The prepared Fe_3O_4@AT-COFs exhibited high electrocatalytic activity toward PNP and ONP, and the simultaneous detection of PNP and ONP was achieved with a wide linear detection range of 10–1,000 μM and low detection limits (LOD) of 0.2361 μM and 0.6568 μM, respectively.

Biomedical Analysis

In addition to its application in environmental pollution, an electrochemical sensing platform based on COFs also plays

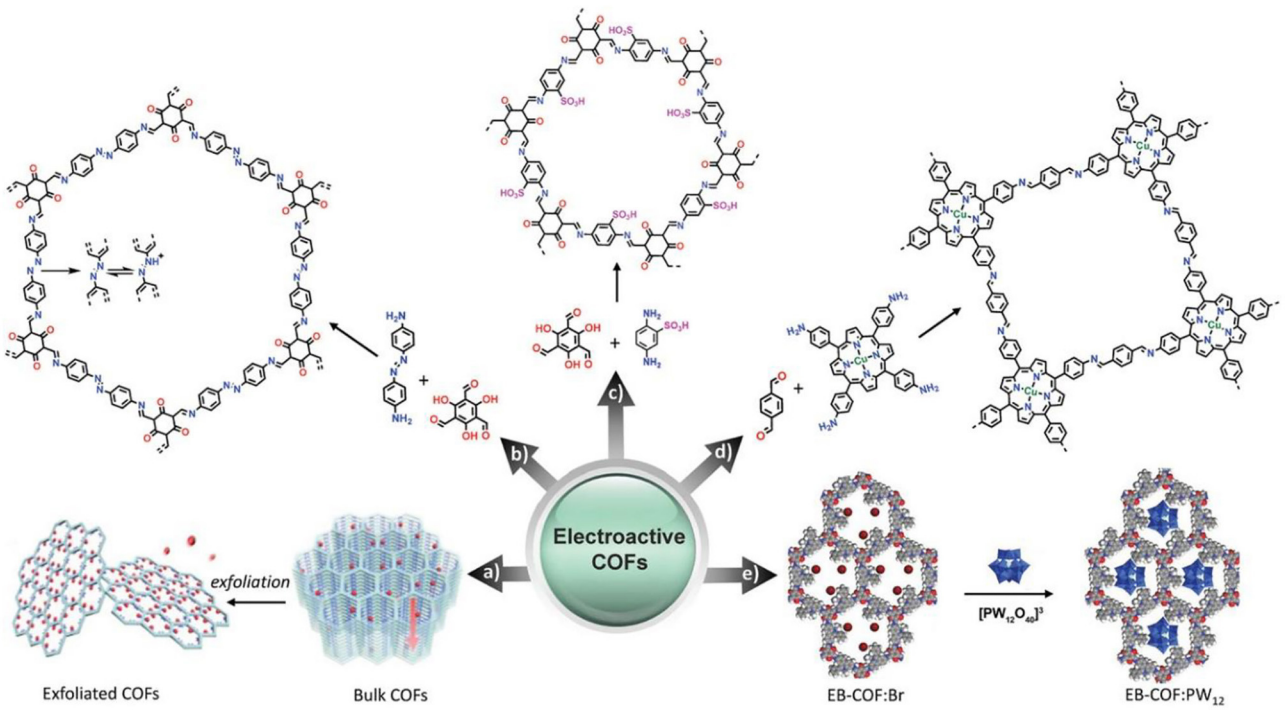

FIGURE 6 | General design of electroactive COFs. (a) Typical design of electroactive bulk COFs and exfoliated COFs. (b) Typical bottom-up design of electroactive COFs with reactive skeletons. (c) Typical bottom-up design of electroactive COFs with reactive functional groups. (d) Typical bottom-up design of electroactive COFs with reactive metals. (e) Typical design of electroactive COF hybrids. (a) Reproduced with permission. Reproduced with permission from Yusran et al. (2020a). Copyright 2020, WILEY-VCH.

a prominent role in biomedicine, such as epidermal growth factor receptors, living cancer cells, prostate specific antigens, cardiac troponin I, glucose, ascorbic acid, dopamine, uric acid, guanine, adenine, luteolin, hydrogen peroxide, chlorogenic acid, furazolidone, tanshinol, sulfadiazine, and acetaminophen. Recently, porphyrin-based COFs (P-COFs) were synthesized, which are a potential candidate for the sensitive detection of target cancer markers or living cells (EGFR and living Michigan cancer foundation-7) (Yan et al., 2019). P-COFs presented high electrochemical activity, good stability in aqueous solution, excellent bio-affinity, and this material enabled strong immobilization of the aptamer strands. The fabricated aptasensor was demonstrated for the analysis of EGFR and living cancer cells, with the advantages of good anti-interferences ability, stability, and reproducibility.

An electroactive 2D $COF_{Thi-TFPB}$ nanosheet packaged on amino-functionalized CNT was designed as a ratiometric electrochemical AA sensor, showing satisfactory selectivity, reproducibility, and stability (Wang L. et al., 2020). The $COF_{Thi-TFPB}$ was synthesized by a dehydration condensation reaction between 1,3,5-tris (p-formylphenyl) benzene (TFPB) and thionine (Thi) and this porous crystalline material was a highly ordered 2D nanosheet. A highly selective and sensitive electrochemical sensing platform based on 2HP6@Au@CP6@COFs was successfully established for the determination of dangerous and explosive sodium picrate (SP) (Tan et al., 2020), in which Au nanoparticles play an electrocatalytic role and 2HP6 as well as CP6 contribute to the aggregation and identification of SP on the electrode surface. Recently, Xu described a facile one-pot strategy to immobilize COFs on an amino-functionalized carbon nanotube (NH_2-CNT) support at room temperature via π-π interactions. The COFs-CNT composites modified electrode showed a high specific surface area (147.3 $m^2\ g^{-1}$), and excellent electrical conductivity, which exhibited an excellent analytical performance for the detection of the nitrofuran antibacterial agent furazolidone (Sun et al., 2020).

Application of Electroactive COFs in Electrochemical Sensors

The incorporation of electroactive moieties in the structure endows electroactive COFs with great potential for electroanalysis application. Electroactive COFs possess abundant accessibly active sites which contribute to the electrochemical reaction and avoid overpotential. Electroactive COFs can be designed by incorporating electroactive sites (e.g., electron-rich species and metal) in their frameworks, or hybridizing COFs with other electroactive components with following scheme in **Figure 6** (Yusran et al., 2020a).

An electroactive iron porphyrin-based covalent organic framework ($COF_{p-FeporNH2-BTA}$) was synthesized via aldehyde-ammonia condensation reaction between

1,3,5-benzenetricarboxaldehyde and 5,10,15,20-tetrakis(4-aminophenyl)-21H, 23H-porphine, followed by post-modification with Fe^{2+}. The synthesized COF*p*-Fepor NH2-BTA showed a good electrochemical redox property and electrocatalytic activity toward the reduction of hydrogen peroxide (Xie et al., 2020a). The electrochemical sensor based on $COF_{p-FeporNH2-BTA}$ showed a wide linear range from 6.85 nM to 7 μM with the detection limit of 2.06 nM (S/N = 3) for the detection of hydrogen peroxide. Recently electroactive COFs were used to construct a ratiometric electrochemical sensor. Wang reported an electroactive COF with multiple redox-active states synthesized by an amine-aldehyde condensation reaction between 4, 4′,4″-(1,3,5-triazine-2,4,6-triyl) trianiline and 2,5-dihydroxy terethaldehyde ($COF_{DHTA-TTA}$), which was applied for the construction of a ratiometric electrochemical sensor for the detection of hydrogen peroxide and pH level based on both current and potential signals (Xu M. et al., 2019). An electroactive COFs composite was also prepared by a dehydration condensation reaction between 1,3,5-tris(p-formylphenyl) benzene (TFPB) and thionine (Thi) wound with carbon nanotubes (CNT) to construct the ratiometric electrochemical sensing of ascorbic acid (Wang L. et al., 2020).

CONCLUSIONS AND OUTLOOKS

This critical review briefly summarized the key properties of COFs that influence the electroanalytical performances, and corresponding solutions were discussed in detail, which will serve as a guide for the novel design and fabrication of an electrochemical sensor. Although COFs have been used to construct an electrochemical sensing platform for the sensitive analysis of biomedicine, environmental pollutants, and others, and some intriguing developments have been made, COFs in the electrochemical sensing field is still in its initial stage. To promote the development of electrochemical sensors based on COFs, the following challenges and outlooks should be considered in future work: (1) novel synthesis strategies (for example, microfluidic synthesis) need to be developed for conductive, nanoscale, and electroactive COFs for enhanced sensitivity and electrocatalytic activity. (2) Finding a simple and efficient surface modification method/strategy on conductive substrates is an urgent problem that needs to be resolved in the future. (3) The intrinsic fragility, powdered crystalline state, and large size of COFs lead to a low active area, low mass transfer rate, and difficult modification as well as poor stability on the electrode. Therefore, simple and facile synthesis methods for nanoscale and hydrogels/aerogels COFs need to be further investigated. (4) The antifouling capability and biocompatibility of COF-based materials still need to be studied and improved for the analysis of biological samples. (5) With the enhanced thermal, chemical, and mechanical stability, biomolecules encapsulated in COFs may be further explored to broaden their operational conditions and extend their potential applications in electrochemical sensors. (6) Molecularly imprinted COFs used in electrochemical sensors need to improve in their selectivity and sensitivity. (7) It will be an efficient method to improve the performances of conduction and sensing by using COFs as nanocarriers to encapsulate organic molecules that can be released through specific stimuli (Chang et al., 2019).

AUTHOR CONTRIBUTIONS

SC writing-original draft, table preparation, copyright application, and manuscript figure. BY writing-original draft, manuscript concept and design, funding acquisition, manuscript revision/review/editing, and manuscript figure. GL and DZ review/editing/revision. All authors contributed to the article and approved the submitted version.

FUNDING

Financial support was gratefully acknowledged from the Program for Innovative Research Team of Science and Technology in the University of Henan Province (18IRTSTHN006), the National Science Foundation of China (No. 21405005), the Joint Fund for Fostering Talents of National Natural Science Foundation of China and Henan Province (No. U1404208), the Program for Science and Technology Innovation Talents at the University of Henan Province (17HASTIT001), and the Talented Scholars of Ludong University (No. 10000313).

REFERENCES

Aiyappa, H. B., Thote, J., Shinde, D. B., Banerjee, R., and Kurungot, S. (2016). Cobalt-modified covalent organic framework as a robust water oxidation electrocatalyst. *Chem. Mater.* 28, 4375–4379. doi: 10.1021/acs.chemmater.6b01370

Arul, P., Narayanamoorthi, E., and John, S. A. (2020). Covalent organic framework film as an effective electrocatalyst for the simultaneous determination of dihydroxybenzene isomers in water samples. *Sens. Actuators B* 313:128033. doi: 10.1016/j.snb.2020.128033

Baldwin, L. A., Crowe, J. W., Pyles, D. A., and McGrier, P. L. (2016). Metalation of a mesoporous three-dimensional covalent organic framework. *J. Am. Chem. Soc.* 138, 15134–15137. doi: 10.1021/jacs.6b10316

Cai, S. L., Zhang, Y. B., Pun, A. B., He, B., Yang, J., Toma, F. M., et al. (2014). Tunable electrical conductivity in oriented thin films of tetrathiafulvalene-based covalent organic framework. *Chem. Sci.* 5, 4693–4700. doi: 10.1039/C4SC02593H

Calbo, J., Golomb, M. J., and Walsh, A. (2019). Redox-active metal–organic frameworks for energy conversion and storage *J. Mater. Chem. A* 7, 16571–16597. doi: 10.1039/C9TA04680A

Chang, J., Wang, X., Wang, J., Li, H., and Li, F. (2019). Nucleic acid functionalized metal-organic frameworks-based homogeneous electrochemical biosensor for simultaneous detection of multiple tumor biomarkers. *Anal. Chem.* 91, 3604–3610. doi: 10.1021/acs.analchem.8b05599

Chen, L., Wu, Q., Gao, J., Li, H., Dong, S., Shi, X., et al. (2019). Applications of covalent organic frameworks in analytical chemistry. *TrAC Trends Anal. Chem.* 113, 182–193. doi: 10.1016/j.trac.2019.01.016

Cote, A. P., Benin, A. I., Ockwig, N. W., O'Keeffe, M., Matzger, A. J., and Yaghi, O. M. (2005). Porous, crystalline, covalent organic frameworks. *Science* 310, 1166–1170. doi: 10.1126/science.1120411

DeBlase, C. R., Hernández-Burgos, K., Silberstein, K. E., Rodríguez-Calero, G. G., Bisbey, R. P., Abruña, H. D., et al. (2015). Rapid and efficient redox processes within 2D covalent organic framework thin films. *ACS Nano* 9, 3178–3183. doi: 10.1021/acsnano.5b00184

Ding, H., Li, Y., Hu, H., Sun, Y., Wang, J., Wang, C., et al. (2014). A tetrathiafulvalene-based electroactive covalent organic framework. *Chem. Eur. J.* 20, 14614–14618. doi: 10.1002/chem.201405330

Dong, J., Han, X., Liu, Y., Li, H., and Cui, Y. (2020). Metal-covalent organic frameworks (MCOFs): a bridge between metal-organic frameworks and covalent organic frameworks. *Angew. Chem. Int. Ed.* 59, 13722–13733. doi: 10.1002/anie.202004796

Geng, K., He, T., Liu, R., Dalapati, S., Tan, K. T., Li, Z., et al. (2020). Covalent organic frameworks: design, synthesis, and functions. *Chem. Rev.* 120, 8814–8933. doi: 10.1021/acs.chemrev.9b00550

Gou, X., Zhang, Q., Wu, Y., Zhao, Y., Shi, X., Fan, X., et al. (2016). Preparation and engineering of oriented 2D covalent organic framework thin films. *RSC Adv.* 6, 39198–39203. doi: 10.1039/C6RA07417K

Guan, Q., Zhou, L. L., Li, Y. A., Li, W. Y., Wang, S., Song, C., et al. (2019). Nanoscale covalent organic framework for combinatorial antitumor photodynamic and photothermal therapy. *ACS Nano* 13, 13304–13316. doi: 10.1021/acsnano.9b06467

Guo, J., Xu, Y., Jin, S., Chen, L., Kaji, T., Honsho, Y., et al. (2013). Conjugated organic framework with three-dimensionally ordered stable structure and delocalized π clouds. *Nat. Commun.* 4, 1–8. doi: 10.1038/ncomms3736

Huang, N., Wang, P., and Jiang, D. (2016). Covalent organic frameworks: a materials platform for structural and functional designs. *Nat. Rev. Mater.* 1, 1–19. doi: 10.1038/natrevmats.2016.68

Karimi-Maleh, H., Karimi, F., Alizadeh, M., and Sanati, A. L. (2019). Electrochemical sensors, a bright future in the fabrication of portable kits in analytical systems. *Chem. Rec.* 20, 682–692. doi: 10.1002/tcr.201900092

Kuhn, P., Antonietti, M., and Thomas, A. (2008). Porous, covalent triazine-based frameworks prepared by ionothermal synthesis. *Angew. Chem. Int. Ed.* 47, 3450–3453. doi: 10.1002/anie.200705710

Li, H., Chang, J., Li, S., Guan, X., Li, D., Li, C., et al. (2019). Three-dimensional tetrathiafulvalene-based covalent organic frameworks for tunable electrical conductivity. *J. Am. Chem. Soc.* 141, 13324–13329. doi: 10.1021/jacs.9b06908

Li, X., Yang, X., Xue, H., Pang, H., and Xu, Q. (2020a). Metal–organic frameworks as a platform for clean energy applications. *EnergyChem* 2:100027. doi: 10.1016/j.enchem.2020.100027

Li, Y., Guo, X., Li, X., Zhang, M., Jia, Z., Deng, Y., et al. (2020b). Redox-active two-dimensional covalent organic frameworks (COFs) for selective reductive separation of valence-variable, redox-sensitive and long-lived radionuclides. *Angew. Chem. Int. Ed.* 59, 4168–4175. doi: 10.1002/anie.201916360

Liang, C., Lin, H., Wang, Q., Shi, E., Zhou, S., Zhang, F., et al. (2020). A redox-active covalent organic framework for the efficient detection and removal of hydrazine. *J. Hazard. Mater.* 381:120983. doi: 10.1016/j.jhazmat.2019.120983

Liang, H., Xu, H., Zhao, Y., Zheng, J., Zhao, H., Li, G., et al. (2019a). Ultrasensitive electrochemical sensor for prostate specific antigen detection with a phosphorene platform and magnetic covalent organic framework signal amplifier. *Biosens. Bioelectron.* 144:111691. doi: 10.1016/j.bios.2019.111691

Liang, H., Xu, M., Zhu, Y., Wang, L., Xie, Y., Song, Y., et al. (2019b). H_2O_2 Ratiometric electrochemical sensors based on nanospheres derived from ferrocence-modified covalent organic frameworks. *ACS Appl. Nano Mater.* 3, 555–562. doi: 10.1021/acsanm.9b02117

Lin, S., Diercks, C. S., Zhang, Y. B., Kornienko, N., Nichols, E. M., Zhao, Y., et al. (2015). Covalent organic frameworks comprising cobalt porphyrins for catalytic CO_2 reduction in water. *Science* 349, 1208–1213. doi: 10.1126/science.aac8343

Lohse, M. S., and Bein, T. (2018). Covalent organic frameworks: structures, synthesis, and applications. *Adv. Funct. Mater.* 28:1705553. doi: 10.1002/adfm.201705553

Lu, H., Wang, C., Chen, J., Ge, R., Leng, W., Dong, B., et al. (2015). A novel 3D covalent organic framework membrane grown on a porous α-Al_2O_3 substrate under solvothermal conditions. *Chem. Commun.* 51, 15562–15565. doi: 10.1039/C5CC06742A

Lu, Z., Shi, Z., Huang, S., Zhang, R., Li, G., and Hu, Y. (2020). Covalent organic framework derived Fe_3O_4/N co-doped hollow carbon nanospheres modified electrode for simultaneous determination of biomolecules in human serum. *Talanta* 214:120864. doi: 10.1016/j.talanta.2020.120864

Meng, Z., Stolz, R. M., and Mirica, K. A. (2019). Two-dimensional chemiresistive covalent organic framework with high intrinsic conductivity. *J. Am. Chem. Soc.* 141, 11929–11937. doi: 10.1021/jacs.9b03441

Mulzer, C. R., Shen, L., Bisbey, R. P., McKone, J. R., Zhang, N., Abruña, H. D., et al. (2016). Superior charge storage and power density of a conducting polymer-modified covalent organic framework. *ACS Cent. Sci.* 2, 667–673. doi: 10.1021/acscentsci.6b00220

Pachfule, P., Kandmabeth, S., Mallick, A., and Banerjee, R. (2015). Hollow tubular porous covalent organic framework (COF) nanostructures. *Chem. Commun.* 51, 11717–11720. doi: 10.1039/C5CC04130A

Pang, Y., Huang, Y., Wang, L., Shen, X., and Wang, Y. (2020). Determination of bisphenol A and bisphenol S by a covalent organic framework electrochemical sensor. *Environ. Pollut.* 263:114616. doi: 10.1016/j.envpol.2020.114616

Rotter, J. M., Weinberger, S., Kampmann, J., Sick, T., Shalom, M., Bein, T., et al. (2019). Covalent organic framework films through electrophoretic deposition-creating efficient morphologies for catalysis. *Chem. Mater.* 31, 10008–10016. doi: 10.1021/acs.chemmater.9b02286

Sasmal, H. S., Halder, A., Kunjattu, H., S., Dey, K., Nadol, A., et al. (2019). Covalent self-assembly in two dimensions: connecting covalent organic framework nanospheres into crystalline and porous thin films. *J. Am. Chem. Soc.* 141, 20371–20379. doi: 10.1021/jacs.9b10788

Shi, X., Xiao, A., Zhang, C., and Wang, Y. (2019). Growing covalent organic frameworks on porous substrates for molecule-sieving membranes with pores tunable from ultra-to nanofiltration. *J. Membr. Sci.* 576, 116–122. doi: 10.1016/j.memsci.2019.01.034

Spitler, E. L., Colson, J. W., Uribe-Romo, F. J., Woll, A. R., Giovino, M. R., Saldivar, A., et al. (2012). Lattice expansion of highly oriented 2D phthalocyanine covalent organic framework films. *Angew. Chem.* 124, 2677–2681. doi: 10.1002/ange.201107070

Sun, B., Liu, J., Cao, A., Song, W., and Wang, D. (2017). Interfacial synthesis of ordered and stable covalent organic frameworks on amino-functionalized carbon nanotubes with enhanced electrochemical performance. *Chem. Commun.* 53, 6303–6306. doi: 10.1039/C7CC01902E

Sun, Y., He, J., Waterhouse, G. I., Xu, L., Zhang, H., Qiao, X., et al. (2019a). A selective molecularly imprinted electrochemical sensor with GO@ COF signal amplification for the simultaneous determination of sulfadiazine and acetaminophen. *Sens. Actuators, B* 300:126993. doi: 10.1016/j.snb.2019.126993

Sun, Y., Waterhouse, G. I., Xu, L., Qiao, X., and Xu, Z. (2020). Three-dimensional electrochemical sensor with covalent organic framework decorated carbon nanotubes signal amplification for the detection of furazolidone. *Sens. Actuators B* 321:128501. doi: 10.1016/j.snb.2020.128501

Sun, Y., Xu, L., Waterhouse, G. I., Wang, M., Qiao, X., and Xu, Z. (2019b). Novel three-dimensional electrochemical sensor with dual signal amplification based on MoS_2 nanosheets and high-conductive NH_2-MWCNT@ COF for sulfamerazine determination. *Sens. Actuators B* 281, 107–114. doi: 10.1016/j.snb.2018.10.055

Tan, X., Fan, Y., Wang, S., Wu, Y., Shi, W., Huang, T., et al. (2020). Ultrasensitive and highly selective electrochemical sensing of sodium picrate by Dihydroxylatopillar [6] arene-Modified gold nanoparticles and cationic Pillar [6] arene functionalized covalent organic framework. *Electrochim. Acta* 335:135706. doi: 10.1016/j.electacta.2020.135706

Tan, X., Zhang, Z., Cao, T., Zeng, W., Huang, T., and Zhao, G. (2019). Control assembly of pillar [6] arene-modified Ag nanoparticles on covalent organic framework surface for enhanced sensing performance toward paraquat. *ACS Sustainable Chem. Eng.* 7, 20051–20059. doi: 10.1021/acssuschemeng.9b05804

Tavakoli, E., Kakekhani, A., Kaviani, S., Tan, P., Ghaleni, M. M., Zaeem, M. A., et al. (2019). *In situ* bottom-up synthesis of porphyrin-based covalent organic frameworks. *J. Am. Chem. Soc.* 141, 19560–19564. doi: 10.1021/jacs.9b10787

Vitaku, E., and Dichtel, W. R. (2017). Synthesis of 2D imine-linked covalent organic frameworks through formal transimination reactions. *J. Am. Chem. Soc.* 139, 12911–12914. doi: 10.1021/jacs.7b06913

Waller, P. J., Gándara, F., and Yaghi, O. M. (2015). Chemistry of covalent organic frameworks. *Acc. Chem. Res.* 48, 3053–3063. doi: 10.1021/acs.accounts.5b00369

Wan, S., Gándara, F., Asano, A., Furukawa, H., Saeki, A., Dey, S. K., et al. (2011). Covalent organic frameworks with high charge carrier mobility. *Chem. Mater.* 23, 4094–4097. doi: 10.1021/cm201140r

Wang, J., Li, J., Gao, M., and Zhang, X. (2018). Recent advances in covalent organic frameworks for separation and analysis of complex samples. *TrAC Trends Anal. Chem.* 108, 98–109. doi: 10.1016/j.trac.2018.07.013

Wang, J., and Zhuang, S. (2019). Covalent organic frameworks (COFs) for environmental applications. *Coord. Chem. Rev.* 400:213046. doi: 10.1016/j.ccr.2019.213046

Wang, L., Xie, Y., Yang, Y., Liang, H., Wang, L., and Song, Y. (2020). Electroactive covalent organic frameworks/carbon nanotubes composites for electrochemical sensing. *ACS Appl. Nano Mater.* 3, 1412–1419. doi: 10.1021/acsanm.9b02257

Wang, Q., Li, R., Zhao, Y., Zhe, T., Bu, T., Liu, Y., et al. (2020). Surface morphology-controllable magnetic covalent organic frameworks: a novel electrocatalyst for simultaneously high-performance detection of p-nitrophenol and o-nitrophenol. *Talanta* 219:121255. doi: 10.1016/j.talanta.2020.121255

Wang, R., Shi, X., Xiao, A., Zhou, W., and Wang, Y. (2018). Interfacial polymerization of covalent organic frameworks (COFs) on polymeric substrates for molecular separations. *J. Membr. Sci.* 566, 197–204. doi: 10.1016/j.memsci.2018.08.044

Wu, M. X., and Yang, Y. W. (2017). Applications of covalent organic frameworks (COFs): From gas storage and separation to drug delivery. *Chin. Chem. Lett.* 28, 1135–1143. doi: 10.1016/j.cclet.2017.03.026

Wu, Y., Yan, D., Zhang, Z., Matsushita, M. M., and Awaga, K. (2019). Electron highways into nanochannels of covalent organic frameworks for high electrical conductivity and energy storage. *ACS Appl. Mater. Interfaces* 11, 7661–7665. doi: 10.1021/acsami.8b21696

Xie, L. S., Skorupskii, G., and Dinc,a, M. (2020). Electrically conductive metal–organic frameworks. *Chem. Rev.* 120, 8536–8530. doi: 10.1021/acs.chemrev.9b00766

Xie, Y., Xu, M., Wang, L., Liang, H., Wang, L., and Song, Y. (2020a). Iron-porphyrin-based covalent-organic frameworks for electrochemical sensing H_2O_2 and pH. *Mater. Sci. Eng. C* 112:110864. doi: 10.1016/j.msec.2020.110864

Xie, Y., Zhang, T., Chen, Y., Wang, Y., and Wang, L. (2020b). Fabrication of core-shell magnetic covalent organic frameworks composites and their application for highly sensitive detection of luteolin. *Talanta* 213:120843. doi: 10.1016/j.talanta.2020.120843

Xin, Y., Wang, N., Wang, C., Gao, W., Chen, M., Liu, N., et al. (2020). Electrochemical detection of hydroquinone and catechol with covalent organic framework modified carbon paste electrode. *J. Electroanal. Chem.* 877:114530. doi: 10.1016/j.jelechem.2020.114530

Xu, L., Wang, F., Ge, X., Liu, R., Xu, M., and Yang, J. (2019). Covalent organic frameworks on reduced graphene oxide with enhanced electrochemical performance. *Microporous Mesoporous Mater.* 287, 65–70. doi: 10.1016/j.micromeso.2019.05.054

Xu, M., Wang, L., Xie, Y., Song, Y., and Wang, L. (2019). Ratiometric electrochemical sensing and biosensing based on multiple redox-active state $COF_{DHTA-TTA}$. *Sens. Actuators B* 281, 1009–1015. doi: 10.1016/j.snb.2018.11.032

Xue, R., Guo, H., Wang, T., Gong, L., Wang, Y., Ai, J., et al. (2017). Fluorescence properties and analytical applications of covalent organic frameworks. *Anal. Methods* 9, 3737–3750. doi: 10.1039/C7AY01261F

Yan, X., Song, Y., Liu, J., Zhou, N., Zhang, C., He, L., et al. (2019). Two-dimensional porphyrin-based covalent organic framework: a novel platform for sensitive epidermal growth factor receptor and living cancer cell detection. *Biosens. Bioelectron.* 126, 734–742. doi: 10.1016/j.bios.2018.11.047

Yang, C. X., Liu, C., Cao, Y. M., and Yan, X. P. (2015). Facile room-temperature solution-phase synthesis of a spherical covalent organic framework for high-resolution chromatographic separation. *Chem. Commun.* 51, 12254–12257. doi: 10.1039/C5CC03413B

Yang, Y., Shen, Y., Wang, L., Song, Y., and Wang, L. (2019). Three-dimensional porous carbon/covalent-organic framework films integrated electrode for electrochemical sensors. *J. Electroanal. Chem.* 855:113590. doi: 10.1016/j.jelechem.2019.113590

Yusran, Y., Fang, Q., and Valtchev, V. (2020a). Electroactive covalent organic frameworks: design, synthesis, and applications. *Adv. Mater.* 2002038. doi: 10.1002/adma.202002038

Yusran, Y., Li, H., Guan, X., Fang, Q., and Qiu, S. (2020b). Covalent organic frameworks for catalysis. *EnergyChem* 2:100035. doi: 10.1016/j.enchem.2020.100035

Zhang, C., Cui, M., Ren, J., Xing, Y., Li, N., Zhao, H., et al. (2020). Facile synthesis of novel spherical covalent organic frameworks integrated with Pt nanoparticles and multiwalled carbon nanotubes as electrochemical probe for tanshinol drug detection. *Chem. Eng. J.* 401:126025. doi: 10.1016/j.cej.2020.126025

Zhang, T., Chen, Y., Huang, W., Wang, Y., and Hu, X. (2018a). A novel AuNPs-doped COFs composite as electrochemical probe for chlorogenic acid detection with enhanced sensitivity and stability. *Sens. Actuators B* 276, 362–369. doi: 10.1016/j.snb.2018.08.132

Zhang, T., Gao, C., Huang, W., Chen, Y., Wang, Y., and Wang, J. (2018b). Covalent organic framework as a novel electrochemical platform for highly sensitive and stable detection of lead. *Talanta* 188, 578–583. doi: 10.1016/j.talanta.2018.06.032

Zhang, T., Ma, N., Ali, A., Wei, Q., Wu, D., and Ren, X. (2018c). Electrochemical ultrasensitive detection of cardiac troponin I using covalent organic frameworks for signal amplification. *Biosens. Bioelectron.* 119, 176–181. doi: 10.1016/j.bios.2018.08.020

Zhang, T., Song, Y., Xing, Y., Gu, Y., Yan, X., Liu, H., et al. (2019). The synergistic effect of Au-COF nanosheets and artificial peroxidase Au@ZIF-8 (NiPd) rhombic dodecahedra for signal amplification for biomarker detection. *Nanoscale* 11, 20221–20227. doi: 10.1039/C9NR07190C

Zhang, W., Qiu, L. G., Yuan, Y. P., Xie, A. J., Shen, Y. H., and Zhu, J. F. (2012). Microwave-assisted synthesis of highly fluorescent nanoparticles of a melamine-based porous covalent organic framework for trace-level detection of nitroaromatic explosives. *J. Hazard. Mater.* 221, 147–154. doi: 10.1016/j.jhazmat.2012.04.025

Zhang, X., Li, H., Wang, J., Peng, D., Liu, J., and Zhang, Y. (2019). In-situ grown covalent organic framework nanosheets on graphene for membrane-based dye/salt separation. *J. Membr. Sci.* 581, 321–330. doi: 10.1016/j.memsci.2019.03.070

Zheng, W., Tsang, C. S., Lee, L. Y. S., and Wong, K. Y. (2019). Two-dimensional metal-organic framework and covalent-organic framework: synthesis and their energy-related applications. *Mater. Today Chem.* 12, 34–60. doi: 10.1016/j.mtchem.2018.12.002

Zhu, R., Ding, J., Jin, L., and Pang, H. (2019). Interpenetrated structures appeared in supramolecular cages, MOFs, COFs. *Coord. Chem. Rev.* 389, 119–140. doi: 10.1016/j.ccr.2019.03.002

Conflict of Interest: The authors declare that the research was conducted in the absence of any commercial or financial relationships that could be construed as a potential conflict of interest.

frontiers in Chemistry

ORIGINAL RESEARCH
published: 08 December 2020
doi: 10.3389/fchem.2020.594093

Conductive Metal-Organic Frameworks for Amperometric Sensing of Paracetamol

Jing Wang[1,2], *Sen Liu*[1], *Jiahuan Luo*[1]*, *Shaogang Hou*[1]*, *Haixiang Song*[1], *Yongsheng Niu*[1] *and Chuanxiang Zhang*[2]*

[1] Henan Joint International Research Laboratory of Nanocomposite Sensing Materials, School of Chemical and Environmental Engineering, Anyang Institute of Technology, Anyang, China, [2] Henan Key Laboratory of Coal Green Conversion, College of Chemistry and Chemical Engineering, Henan Polytechnic University, Jiaozuo, China

An electrochemical sensor for paracetamol is executed by using conductive MOF (NiCu-CAT), which is synthesized by 2, 3, 6, 7, 10, 11-hexahydroxytriphenylene (HHTP) ligand. The utility of this 2D NiCu-CAT is measured by the detection of paracetamol, p-stacking within the MOF layers is essential to achieve high electrical conductivity, redox activity, and catalytic activity. In particular, NiCu-CAT demonstrated detection Limit of determination near 5μM for paracetamol through a wide concentration range (5–190 μM). The NiCu-CAT/GCE exhibits excellent reproducibility, stability, and interference for paracetamol.

Keywords: sensor, conductive MOF, NiCu-CAT, amperometric, paracetamol detection

OPEN ACCESS

Edited by:
Baiqing Yuan,
Ludong University, China

Reviewed by:
Matthew A. Addicoat,
Nottingham Trent University, United Kingdom
Hao Huang,
Taiyuan University of Technology, China

***Correspondence:**
Jiahuan Luo
luojiahuan2008@ayit.edu.cn
Shaogang Hou
aydxhsg@163.com
Chuanxiang Zhang
zcx223@hpu.edu.cn

Specialty section:
This article was submitted to Supramolecular Chemistry, a section of the journal Frontiers in Chemistry

Received: *12 August 2020*
Accepted: *06 November 2020*
Published: *08 December 2020*

Citation:
Wang J, Liu S, Luo J, Hou S, Song H, Niu Y and Zhang C (2020) Conductive Metal-Organic Frameworks for Amperometric Sensing of Paracetamol. Front. Chem. 8:594093. doi: 10.3389/fchem.2020.594093

INTRODUCTION

Paracetamol (PA) is a high effective antipyretic and analgesic drug, which is generally used to relieve moderate pain, such as headache caused by influenza or joint pain, migraine, etc. It regulates the synthesis and release of central prostaglandins by controlling the body temperature in the hypothalamus, improves the pain threshold and plays the role of antipyretic and analgesic (Wan et al., 2009; Ghadimi et al., 2013). The normal dose of paracetamol is harmless to the human body, but excessive or long-term use will lead to liver poisoning, leukemia, or even central nervous system poisoning (Fan et al., 2011). Therefore, it is necessary to develop a sensitive, simple, and rapid detection technology for paracetamol. The existing detection methods include spectrophotometry, titration analysis, chemiluminescence, capillary electrophoresis, fluorescence spectrum, high-performance liquid chromatography (Easwaramoorthy et al., 2001; Bosch et al., 2006). However, it is not suitable for the rapid detection of PA in daily life due to the complex pretreatment, large equipment, time-consuming and expensive of these existing detection methods. On the contrary, electrochemical methods have the advantages of being simple and convenient, highly sensitive, quickly responsive, low in cost and highly selective (Yan et al., 2019; Yuan et al., 2019, 2020; Ma et al., 2020; Wang et al., 2020). In addition, PA is an electroactive substance that is prone to electrochemical oxidation, so the detection of PA by electrochemical sensors has aroused great interest. However, the redox reaction of PA on the bare electrode is slow. As a result, researchers have developed high catalytic activity nanomaterials for the design of highly sensitive paracetamol electrochemical sensors (Ejaz and Jeon, 2017; Raymundo-Pereira et al., 2017; Zhao et al., 2019).

In recent decades, nanomaterials have attracted worldwide attention and have been widely used to modify electrochemical sensing electrodes. As one of the most popular materials at present,

the conductive nano-Metal Organic Framework (MOFs) (Campbell and Dincă, 2017; Biswas et al., 2020; Ko et al., 2020; Suwannakot et al., 2020) have many advantages, such as simple synthesis process, environmental friendliness, adjustable structure and so on, especially its excellent conductivity, which has attracted extensive attention (Ko et al., 2017; Fang et al., 2018; Xie et al., 2020). Metal-catecholates (M-CATs) are a kind of conductive MOF composed of HHTP ligands and central metal ions (Miner et al., 2018; Zhang et al., 2018, 2019; Guo et al., 2019). The good conductivity of M-CATs is mainly due to its special structure, in which oxygen atoms in an HHTP ligand can also combine with axial water ligands to form hydrogen bonds. M-CATs show two accumulation modes: one kind, a two-dimensional layered framework with a hexagonal hole and honeycomb structure, is formed by oxygen and p-p interaction, where metal nodes and organic ligands serving as charge carriers enable full charge delocalization in the two-dimensional (2D) plane, so as to produce good electrical conductivity, and the other is along the c axis through hydrogen bonding accumulation, which is easy to form one-dimensional (1D) structures between layers. Because of their special porous structure and good electrical conductivity, M-CATs have great prospects for related applications such as catalysis, supercapacitors and electrical analysis.

In this paper, the 2D conductive nano-MOFs are first systematically studied for the detection of PA in multi-component aqueous solutions. The sensor has the characteristics of fast electronic transfer, good catalytic performance, and good detection limit of determination for paracetamol. Hence this work opens up a new method for electrochemical detection of paracetamol, which is beneficial to the study of the redox metabolism of paracetamol in aqueous solution and expands the application of MOF nanomaterials in electroanalytical chemistry.

METHODS AND MATERIALS

Materials and Reagents

The chemical 2, 3, 6, 7, 10, 11-heahydroxytriphenylene (HHTP) was purchased from Innochem Reagents (Shanghai, China); Nickel (II) acetate tetrahydrate ($Ni(OAc)_2{\cdot}4H_2O$), Copper (II) acetate tetrahydrate ($Cu(OAc)_2{\cdot}4H_2O$), standard paracetamol, dopamine (DA), and ascorbic acid (AA) were purchased from Aladdin (Shanghai, China). All other chemicals were analytical reagent grade. Deionized water was prepared from a Milli-Q water purification system. Different pH phosphate buffers (0.1 mol L^{-1}) were prepared by mixing KH_2PO_4 (0.1 mol L^{-1}) and Na_2HPO_4 (0.1 mol L^{-1}) solutions.

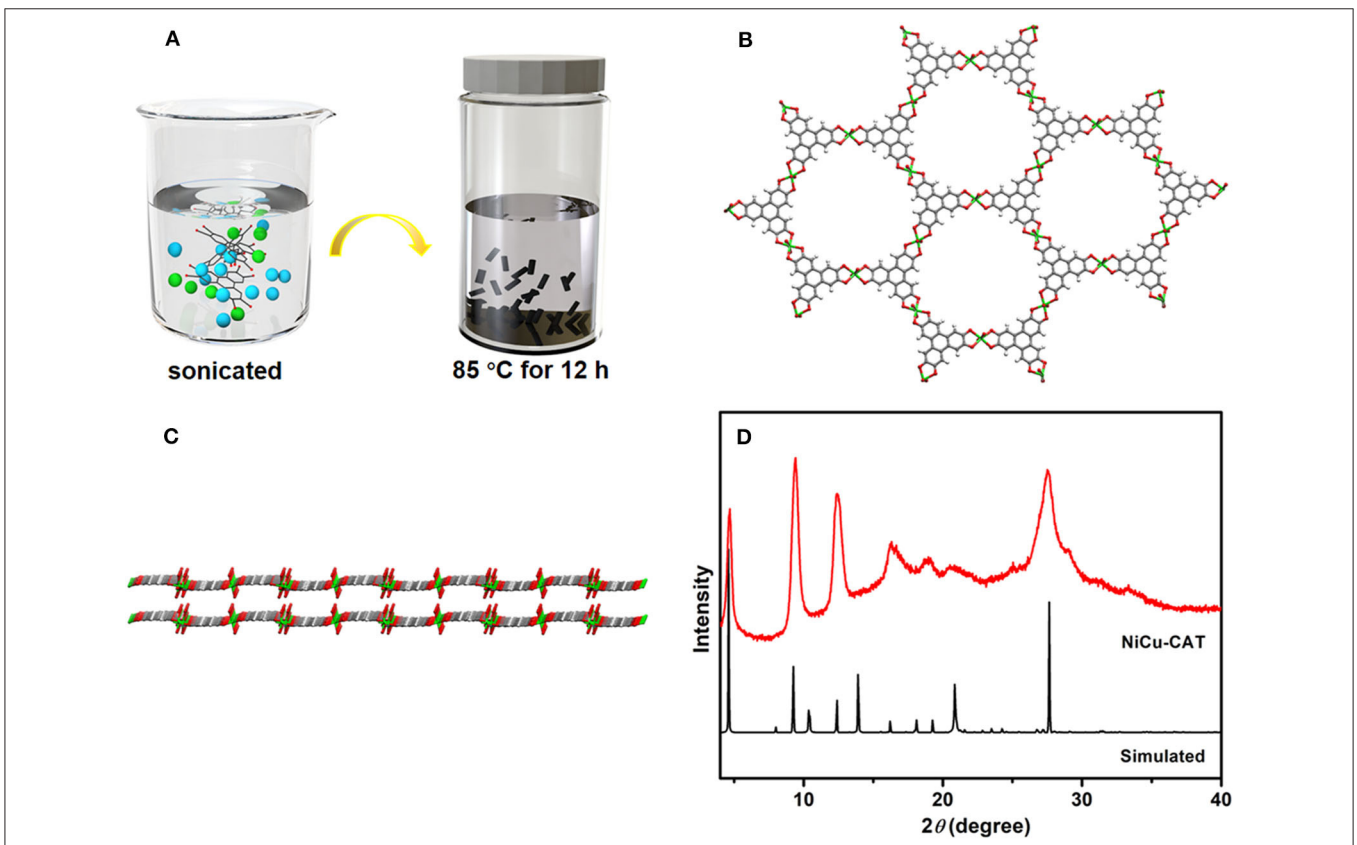

FIGURE 1 | (A) Schematic illustration of the preparation of NiCu-CAT. **(B)** Connecting mode of HHTP molecules and Ni^{2+} and Cu^{2+} ions. **(C)** View of the two extended corrugated layers along the [110] direction. **(D)** XRD pattern of NiCu-CAT nanocrystal and simulated.

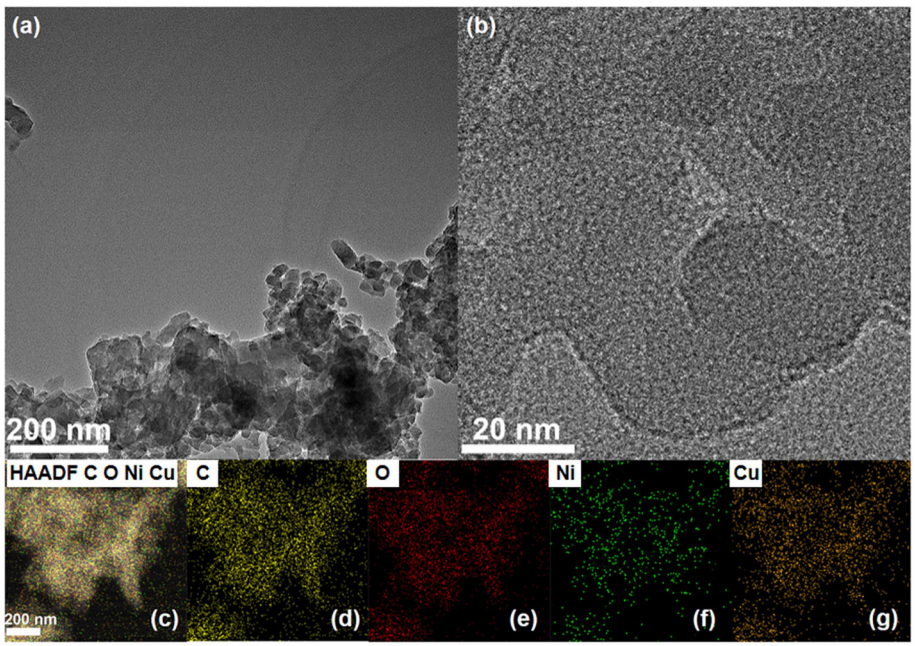

FIGURE 2 | (a,b) TEM images of the NiCu-CAT nanocrystal. **(c–g)** The distribution images of various elements of NiCu-CAT nanocrystal.

Instrumentation

All chemicals were obtained from commercial sources and used without further purification. Powder X-ray diffraction (PXRD) data were collected on a Rigaku D/max-2,550 diffractometer with CuKα radiation (λ = 1.5418 Å). The infrared (IR) spectra were recorded within the 4,000–500 cm^{-1} region on a Nicolet Impact 410 FTIR spectrometer with KBr pellets. TEM, HAADF-STEM, HRTEM, and EDX were carried out on a FEI Talos F200S TEM (200 kV). The structure for NiCu-CAT was simulated by Materials Studio 8.0 and using the Crystallographic Information File (CIF) of Ni-CAT (Ko et al., 2020) as mode.

Synthesis of the NiCu-CAT Nanocomposite

Typically, 30 mg of $Ni(OAc)_2{\cdot}4H_2O$, 20 mg of $Cu(OAc)_2{\cdot}4H_2O$, and 42 mg of HHTP ligands were dissolved in 9 mL of a solvent mixture of deionized water. The vial was capped and sonicated for 30 min until the solid was dissolved, and after that 0.5 mL of NMP was added drop-wise into this solution, and then this solution continue was sonicated for 10 min, the reaction mixture was transferred into an isothermal oven at 85°C for 12 h. After the crystals were washed with deionized water and acetone, the NiCu-CAT was obtained.

Preparation of the Modified Electrodes

First of all, glassy carbon electrode (GCE) was mechanically polished on a velvet cloth with 0.05 μM alumina slurry. Secondly, then electrochemical polishing was carried out in a potential window of 0–1 V at a scanning speed of 100 mV/s in 0.1 M H_2SO_4. Thirdly, GCE was ultrasonicated in deionized water and ethanol for 5 s respectively. One milligram of NiCu-CAT was dispersed in 1 mL of distilled water and Nafion (5 wt%) and ultrasonicated by cell disrupter for 30 min to ensure a uniform dispersion. Then, 6 μL of this dispersion was dropped on cleaned GCE and dried at room temperature to obtain a suitable coating (NiCu-CAT/GCE).

Electrochemical Measurements

Cyclic voltammetry (CV), electrochemical impedance spectroscopy (EIS) and differential pulse voltammetry (DPV) were carried out with a CHI760E electrochemical workstation (Shanghai Chenhua Instrument Co. Ltd., China) using a three-electrode system, with a bare or modified glassy carbon electrode (GCE, 3.0 mm in diameter) as the working electrode. A platinum (Pt) wire and Ag/AgCl were the counter and reference electrodes, respectively. All electrochemical experiments were conducted at room temperature (25°C).

RESULTS

Characterization

Typically, NiCu-CAT constructed from a 2D hexagonal lattice in the *ab*-plane, which configurations along the [001] direction, are synthesized by solvothermal method (**Figure 1A**). As shown in **Figures 1B,C**, the divalent metal ions (M^{2+}) are matched to adjacent deprotonated HHTP ligands to form an extended 2D P-conjugation honeycomb framework. Each ligand can be oxidized to achieve charge balance with the metal ion centers, which is very important to improve the charge density of the $M_3(HHTP)_2(H_2O)_{12}$ (**Supplementary Figures 1a,b**).

The X-ray diffraction (XRD) patterns of NiCu-CAT that matched reported characterization are shown in **Figure 1D**. The XRD pattern of NiCu-CAT clearly reveals three sharp intense

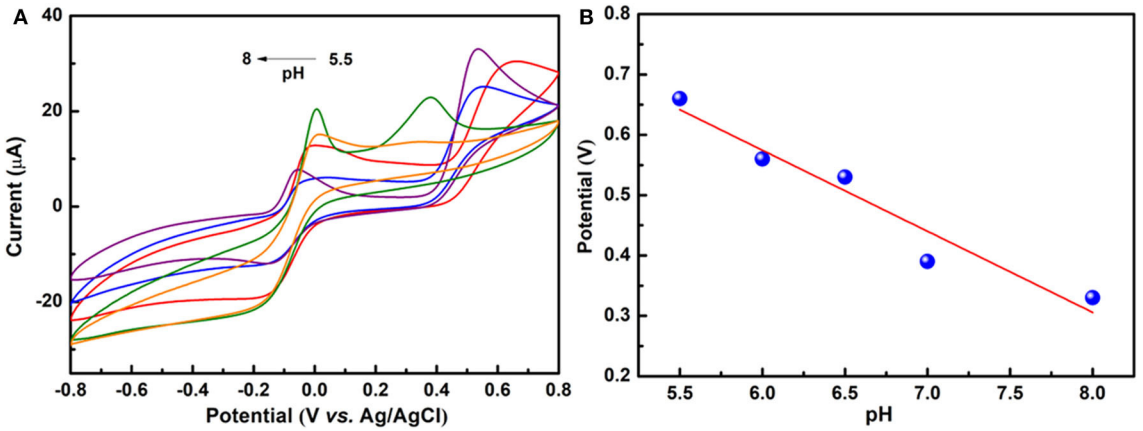

FIGURE 3 | (A) CV curves of 50 μM paracetamol at the NiCu-CAT/GCE in 0.1 M PBS under 5.5, 6, 6.5, 7, 8 pH values. **(B)** The relationship between pH and peak potential.

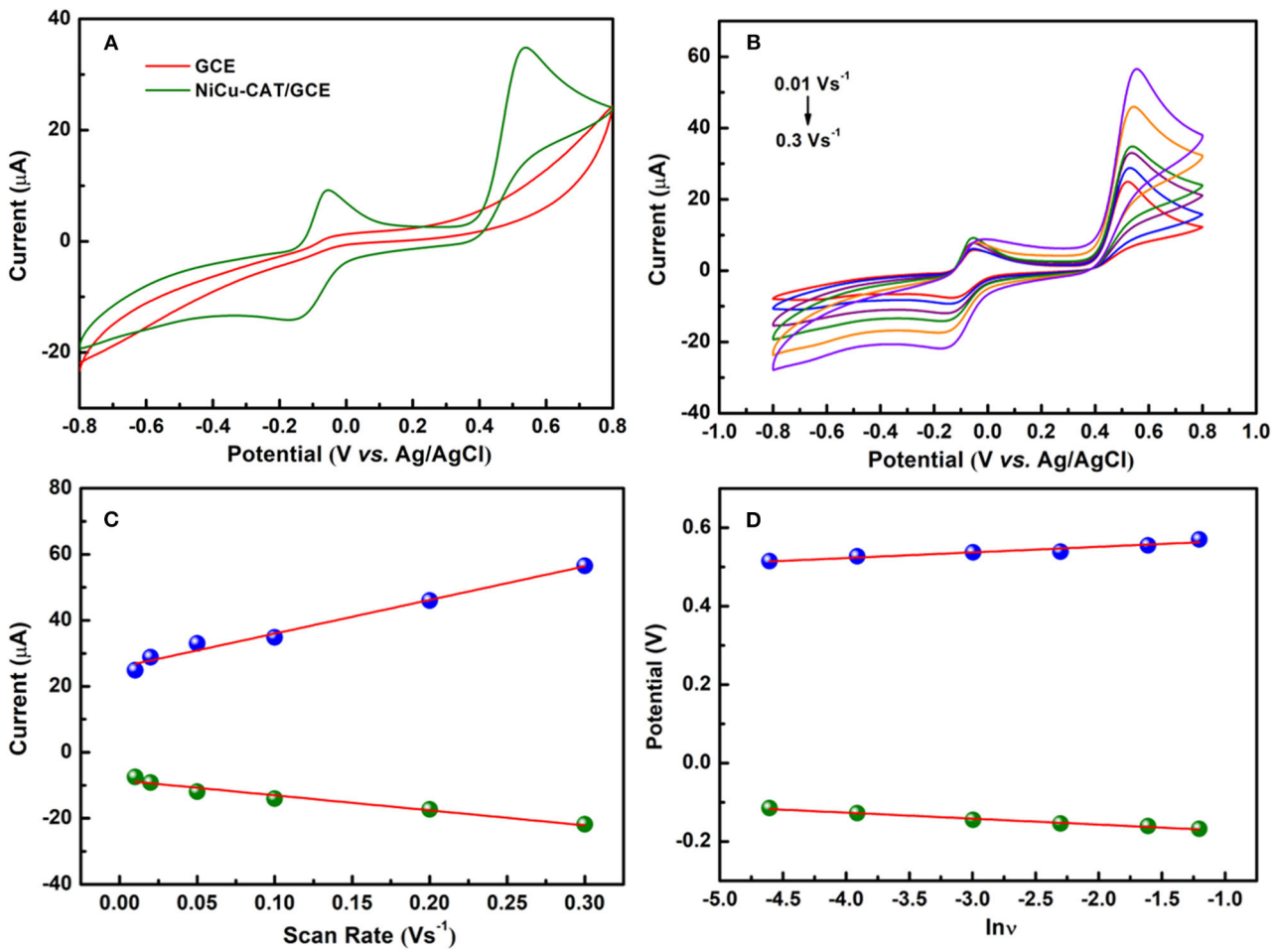

FIGURE 4 | (A) CVs of GCE and NiCu-CAT/GCE in presence of 40 μM paracetamol. **(B)** CVs of 40 μM paracetamol on NiCu-CAT/GCE at scan rates of 10, 20, 50, 100, 200, and 300 mVs^{-1}. **(C)** Displays the plot of the peak current vs. scan rates. **(D)** Displays the plot of the peak potential vs. Inν.

peaks of (100), (200) and (210) planes at 2θ = 4.7°, 9.5°, and 12.4°, respectively. The peaks indicate the long-range order of the nanocrystal in the *ab*-plane (Miner et al., 2018; Guo et al., 2019; Ko et al., 2020). Fourier transform infrared spectroscopy (FT-IR) is conducted, as showed in **Supplementary Figure 2**. Typically, the bonds at 1,118, 1,430, and 3,099 cm^{-1} are attributed to the -C = C- stretching, -C-O- stretching vibration, and -O-H, respectively. The bands at 672 and 804 cm^{-1} represent the out-of-plane C-H bending modes, fully manifesting the existence of organic HHTP.

Transmission electron microscopy (TEM), high-angle annular dark-field scanning TEM (HAADF-STEM), and high-resolution transmission electron microscopy (HRTEM) were executed to characterize the morphology of NiCu-CAT. As shown in **Figures 2a,b**, NiCu-CAT is made up of nanocrystals with the diameter of 20–50 nm. The corresponding energy dispersive X-ray spectroscopy (EDX) mapping images (**Figures 2c–g** and **Supplementary Figure 4**) evidence the even distribution of elemental Ni, Cu, C, and O throughout the nanocrystal.

Effect of the pH Values

Electrochemical properties were investigated with the conventional three-electrode system, as mentioned in the Methods and Materials section. The effect of pH on the peak potential of PA using cyclic-voltammetry in 0.1 M PBS at pH values of 5.5 to 8.0 is presented in **Figure 3A**. The effect of the pH value of the PBS on peak potential of 50 μM PA at NiCu-CAT/GCE is also investigated. It can be seen that with the pH increased, the oxidation peak shifted to a negative potential, indicating that this observation can be interpreted by observing the protons in the electrochemical reactions. The pH value 6.5 is chosen for further PA detection, with the highest sensitivity. In addition, **Figure 3B** shows that for a linear relationship between the peak potential (E_{pa}) and pH value, the regression equation is shown by the following expression (Afkhami et al., 2004):

$$\mathbf{Epa\ (V) = Epa\ (pH=0)\ -\ (2.303}m\mathbf{RT/}n\mathbf{F)\ ^{*}\ pH} \qquad (1)$$

where E_{pa}(pH = 0) is the oxidation potential for paracetamol, R is the gas constant (8.314 J·K mol^{-1}), F is Faraday's constant (96485 C mol^{-1}), T is the Kelvin temperature (298.15 K), n is the number of electrons transferred, and m is the number of protons involved in the reaction. From **Figure 3B**, E_{pa} decreased with a slope of −47.5 mV/pH (R = 0.98802). Furthermore, from this equation, according to $dE_{pa}/dpH = -2.303\ mRT/nF$ (Kang et al., 2010). Obviously, the redox reaction involves the same protons and number of electrons with a ratio of 1:1 (Fanjul-Bolado et al., 2009; Kalambate et al., 2015).

Electrocatalytic Behavior of Paracetamol

Cyclic voltammetry for NiCu-CAT/GCE is performed to investigate the electrochemical behavior of 40 μM paracetamol, electrodes are cycled between −0.8 and 0.8 V at a scan rate of 100 mV/s. **Figure 4A** shows CV responses of GCE and NiCu-CAT /GCE in PBS (pH = 6.5). No redox peaks are observed at GCE, which means that GCE is not electroactive in the studied potential region. In contrast, the redox peaks of NiCu-CAT/GCE appeared at −0.14 and 0.53 V, respectively, which can be attributed to the electrochemical redox process of the NiCu-CAT nanocrystals, and the current is larger than that of the bare glassy carbon electrode. The results show that NiCu-CAT has a good electrocatalytic effect on PA. Due to the special mesoporous structure of NiCu-CAT, the conductivity of the electrode is improved and the electrocatalytic effect of the electrode on PA is enhanced.

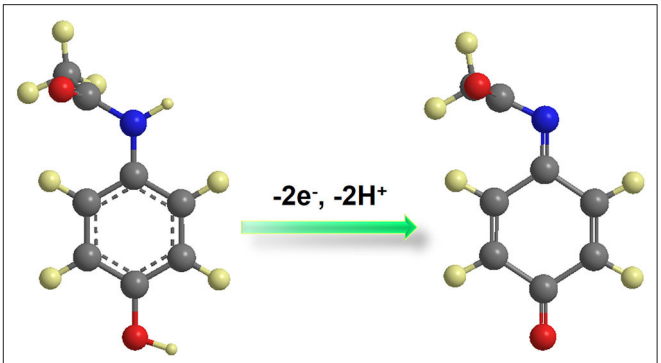

SCHEME 1 | Redox mechanisms of NiCu-CAT/GCE.

Effect of the Potential Scan Rate

In order to investigate the mechanisms responsible for the oxidation of PA at NiCu-CAT/GCE, cyclic voltammograms of PA were recorded at various scan rates. It was observed that the cathodic peak current (I_{pc}) and anodic peak current (I_{pa}) increase linearly with the scan rate over the range of 10–300 mVs^{-1} for and PA. **Figure 4B** shows that the peak potential shifts forward with the increase of scanning rate. The linear relationship between the scan rate and peak current can be expressed by a linear regression equation (Raymundo-Pereira et al., 2016) as I_{pa}[μA] = 101.88 ν[Vs^{-1}] −0.25, (R^2 = 0.980) and I_{pc}[μA] = −45.45 ν[Vs^{-1}] −8.471 (R^2 = 0.957) for the NiCu-CAT/GCE electrode, respectively (**Figure 4C**). The results show that PA undergoes an adsorption-controlled reaction (Goyal et al., 2010; Arvand and Gholizadeh, 2012; Kutluay and Aslanoglu, 2013).

To investigate the reaction kinetics, as shown in **Figure 4D**, the anodic and cathodic peak potentials have linear relationships with the natural logarithm of the scan rate (lnν). The linear regression equations are found to be:

$$\mathbf{Epa\ (V) = 0.020ln}\nu\left(\frac{\mathbf{V}}{\mathbf{s}}\right) + \mathbf{0.580,\ (R^2=0.9535)} \qquad (2)$$

$$\mathbf{Epc\ (V) = -0.019ln}\nu\left(\frac{\mathbf{V}}{\mathbf{s}}\right) - \mathbf{0.580,\ (R^2=0.9859)} \qquad (3)$$

According to Laviron's model (Laviron, 1974, 1979), the number of the electron–transfer (n) and charge-transfer coefficient (α)

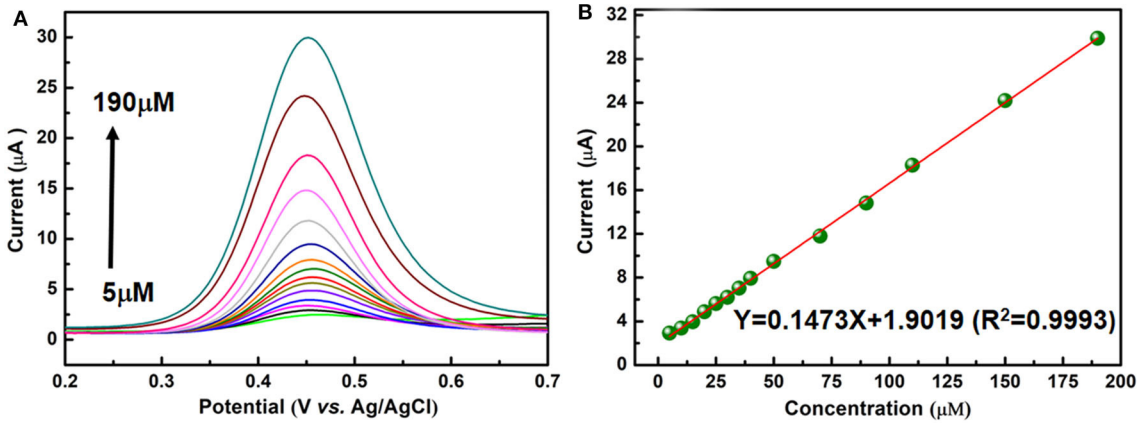

FIGURE 5 | (A) DPV responses for different paracetamol concentrations (5, 10, 15, 20, 25, 30, 35, 40, 50, 70, 90, 110, 150, and 190 μM) on a NiCu-CAT/GCE. **(B)** The linear relationship between the peak current and paracetamol concentration.

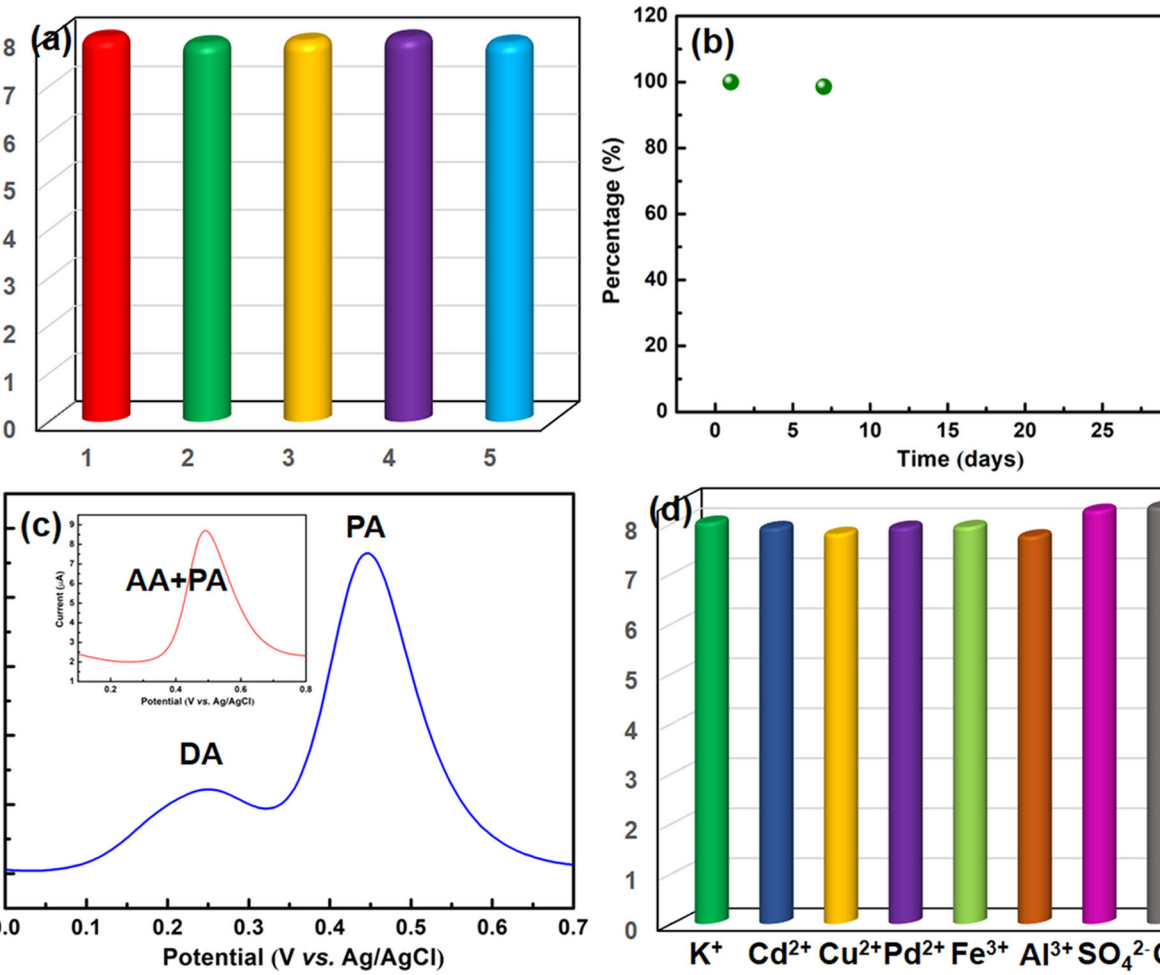

FIGURE 6 | (a) Evaluation of repeatability. **(b)** Stability of the NiCu-CAT/GCE after pretreatment during 30 days. **(c)** DPV responses of the NiCu-CAT/GCE in PBS (0.1 M, pH 6.5) containing 40 μM PA and 200 μM DA; inset is the containing 40 μM PA and 200 μM AA, respectively. **(d)** Effects of the presence of inorganic ions on the voltammetric responses of 40 μM paracetamol using the NiCu-CAT/GCE.

can be calculated to be 2 and 0.50, respectively. According to the above equations, results show that there is a two-proton and two-electron process for the PA electro-oxidation at NiCu-CAT/GCE. The possible redox mechanisms are as follows in **Scheme 1**.

Analytical Performance Characteristics

DPV is utilized to measure the PA peak current on the present electrochemical sensor. This method has the advantages of high sensitivity and good resolution. Under optimized experimental conditions, the anodic peak current is directly proportional to the concentration of PA from 5 to 190 μM as shown in **Figure 5A**. From **Figure 5B**, it can be seen that the peak current of PA is in a linear dynamic range with its concentration. The regression equation (Goyal and Singh, 2006; Krampa et al., 2018; Xu et al., 2019) for the region is $I_{pa}(\mu A) = 0.1473c(\mu M) + 1.9019$ ($R^2 = 0.9993$), the limit of determination is near 5μM. The limit of determination of the NiCu-CAT/GCE is similar to some electrochemical sensors reported using electrochemical method for detecting paracetamol (Fu et al., 2015, 2018a,b). As shown in **Supplementary Figure 7**, the diameter of the paracetamol is 8.3 Å* 3.7 Å, and the pore size of the Ni/Cu CAT is 13 Å. The paracetamol could easily go into the channel; consequently, we expected that the effects between the Ni/Cu CAT and paracetamol were based on host-guest interaction (Ko et al., 2017; Fang et al., 2018; Xie et al., 2020).

DISCUSSION

Reproducibility, Stability and Interference

The peak currents of five tests were recorded to study the reproducibility of the NiCu-CAT/GCE by DPV, and the same electrode was modified five times for PA detection at the same concentration of 40 μM (**Figure 6a**). Under the optimized conditions, the relative standard deviation (RSD) is 1.01%, indicating that NiCu-CAT/GCE can obtain satisfactory repeatability.

In order to study the stability of the modified GCE, the NiCu-CAT/GCE is used to measure 40 μM paracetamol in PBS (0.1 mol L^{-1}, pH = 6.5) after being stored in the air for 7 days and 30 days, respectively (**Figure 6b** and **Supplementary Figure 5**). The fabricated sensors retain more than 95.8% of their original responses, indicating that NiCu-CAT/GCE has good stability. This stability is helpful to the application of chemically modified electrode in electroanalysis.

To investigate the sensor selectivity, the modified GCE is used to detect paracetamol in the presence of interferents. In addition, it was found that the peak current of 40 μM PA is not affected in the presence of 5-folds of dopamine (DA) and ascorbic acid (AA) (**Figure 6c**), and 100-fold excess concentrations of K^+, Cd^{2+}, Cu^{2+}, Pb^{2+}, Fe^{3+}, Al^{3+}, SO_4^{2-}, and Cl^- (**Figure 6d**). The results demonstrated that the potential interfering substances did not interfere with the 40 μM paracetamol signals, indicating that the present assay offers good sensitivity for determining paracetamol.

Real Sample Analysis

In this paper, the NiCu-CAT electrochemical sensor was prepared to detect paracetamol in actual samples. The commercial tablet (Tylenol, produced in Shanghai, China) with a nominal value of 650 mg was used for the analysis of paracetamol. The tablets were pre-treated by grinding, dissolving with ethanol, filtering, and then diluting them with a phosphate buffer solution. The test results are shown in **Supplementary Table 1**. The recoveries of the tests were in the range from 97.23 to 103.8%. indicating that the modified electrode has a good detection performance for the actual samples containing PA, which is expected to be used for the detection of PA in real life.

CONCLUSION

In summary, we have successfully constructed 2D conductive metal–organic frameworks as efficient electrocatalysts to achieve electrochemical detection of PA in aqueous solutions. The NiCu-CAT possesses a specifically big pore, numerous potential active sites, good electrical conductivity and water stability. The electrochemical properties of NiCu-CAT/GCE for PA were studied by cyclic voltammetry and the differential pulse method, under the optimal experimental conditions, the modified electrode has a wide linear range (5–190 μm) for the electrochemical detection of PA with good reproducibility and stability, and it also achieved the limit of determination near 5 μM. The research on the electrochemical detection of PA provides a platform for the application of MOF composites in electroanalysis, which is an excellent electrochemical method for pharmaceutical analysis.

DATA AVAILABILITY STATEMENT

All datasets generated for this study are included in the article/**Supplementary Material**.

AUTHOR CONTRIBUTIONS

JW executed the whole synthesis progress and paper writing. SL tested the samples of XRD and TEM. JL, SH, HS, YN, and CZ charged for data processing and result discussion. All authors contributed to the article and approved the submitted version.

FUNDING

This work was financed by the National Natural Science Foundation of China (Grant No. 21801005, 21901008), the key scientific research project plan of Henan Province Colleges and universities (19A150012, 19A480003), the scientific and technological project of Henan province (192102310232), the Henan postdoctoral Foundation (1901020), Innovation Practice Base for Post-doctoral of Anyang Institute of Technology (402010), and Huanshui Scholars development plan of Anyang Institute of Technology.

ACKNOWLEDGMENTS

Thanks to the Test Center of the School of Chemical and Environmental Engineering, Anyang Institute of Technology and the editors and reviewers.

SUPPLEMENTARY MATERIAL

The Supplementary Material for this article can be found online at: https://www.frontiersin.org/articles/10.3389/fchem.2020.594093/full#supplementary-material

REFERENCES

Afkhami, A., Nematollahi, D., Khalafi, L., and Rafiee, M. (2004). Kinetic study of the oxidation of some catecholamines by digital simulation of cyclic voltammograms. *Int. J. Chem. Kinet.* 37, 17–24. doi: 10.1002/kin.20046

Arvand, M., and Gholizadeh, T. M. (2012). Simultaneous voltammetric determination of tyrosine and paracetamol using a carbon nanotube-graphene nanosheet nanocomposite modified electrode in human blood serum and pharmaceuticals. *Colloid. Surfaces B.* 103, 84–93. doi: 10.1016/j.colsurfb.2012.10.024

Biswas, S., Chen, Y., Xie, Y., Sun, X., and Wang, Y. (2020). Ultrasmall Au (0) inserted hollow PCN-222 MOF for the high-sensitive detection of estradiol. *Anal. Chem.* 92, 4566–4572. doi: 10.1021/acs.analchem.9b05841

Bosch, M. E., Sánchez, A. J. R., Rojas, F. S., and Ojeda, C. B. (2006). Determination of paracetamol: historical evolution. *J. Pharmaceut. Biomed.* 42, 291–321. doi: 10.1016/j.jpba.2006.04.007

Campbell, M. G., and Dincă M. (2017). Metal-organic frameworks as active materials in electronic sensor devices. *Sensors* 17:1108. doi: 10.3390/s17051108

Easwaramoorthy, D., Yu, Y.-C., and Huang, H.-J. (2001). Chemiluminescence detection of paracetamol by a luminol-permanganate based reaction. *Anal. Chim. Acta* 439, 95–100. doi: 10.1016/S0003-2670(01)00968-0

Ejaz, A., and Jeon, S. (2017). A highly stable and sensitive GO-XDA-Mn_2O_3 electrochemical sensor for simultaneous electrooxidation of paracetamol and ascorbic acid. *Electrochim. Acta* 245, 742–751. doi: 10.1016/j.electacta.2017.05.193

Fan, Y., Liu, J.-H., Lu, H.-T., and Zhang, Q. (2011). Electrochemical behavior and voltammetric determination of paracetamol on Nafion/TiO_2-graphene modified glassy carbon electrode. *Colloid. Surfaces B.* 85, 289–292. doi: 10.1016/j.colsurfb.2011.02.041

Fang, X., Zong, B., and Mao, S. (2018). Metal-organic framework-based sensors for environmental contaminant sensing. *Nano-Micro Lett.* 10:64. doi: 10.1007/s40820-018-0218-0

Fanjul-Bolado, P., Lamas-Ardisana, P. J., and Hernández-Santos, D., and Costa-García A. (2009). Electrochemical study and flow injection analysis of paracetamol in pharmaceutical formulations based on screen-printed electrodes and carbon nanotubes. *Anal. Chim. Acta* 638, 133–138. doi: 10.1016/j.aca.2009.02.019

Fu, L., Lai, G., and Yu, A. (2015). Preparation of β-cyclodextrin functionalized reduced graphene oxide: application for electrochemical determination of paracetamol. *RSC Adv.* 5, 76973–76978. doi: 10.1039/C5RA12520K

Fu, L., Wang, A., Lai, G., Lin, C. T., Yu, J., Yu, A., et al. (2018a). A glassy carbon electrode modified with N-doped carbon dots for improved detection of hydrogen peroxide and paracetamol, *Mikrochim Acta* 185:87. doi: 10.1007/s00604-017-2646-9

Fu, L., Xie, K., Zheng, Y., Zhang, L., and Su, W. (2018b). Graphene ink film based electrochemical detector for paracetamol analysis. *Electronics* 7:15. doi: 10.3390/electronics7020015

Ghadimi, H. M. A., Tehrani, R., Ali, A. S. M., Mohamed, N., and Ab Ghani, S. (2013). Sensitive voltammetric determination of paracetamol by poly (4-vinylpyridine)/multiwalled carbon nanotubes modified glassy carbon electrode. *Anal. Chim. Acta* 765, 70–76. doi: 10.1016/j.aca.2012.12.039

Goyal, R. N., Gupta, V. K., and Chatterjee, S. (2010). Voltammetric biosensors for the determination of paracetamol at carbon nanotube modified pyrolytic graphite electrode. *Sens. Actuators B Chem.* 149, 252–258. doi: 10.1016/j.snb.2010.05.019

Goyal, R. N., and Singh, S. P. (2006). Voltammetric determination of paracetamol at C60-modified glassy carbon electrode. *Electrochim. Acta* 51, 3008–3012. doi: 10.1016/j.electacta.2005.08.036

Guo, L., Sun, J., Sun, X., Zhang, J., Hou, L., and Yuan, C. (2019). Construction of 1D conductive Ni-MOF nanorods with fast Li^+ kinetic diffusion and stable high-rate capacities as an anode for lithium ion batteries. *Nanoscale Adv.* 1, 4688–4691. doi: 10.1039/C9NA00616H

Kalambate, P. K., Sanghavi, B. J., Karna, S. P., and Srivastava, A. K. (2015). Simultaneous voltammetric determination of paracetamol and domperidone based on a graphene/platinum nanoparticles/nafion composite modified glassy carbon electrode. *Sensor. Actuators B Chem.* 213, 285–294. doi: 10.1016/j.snb.2015.02.090

Kang, X., Wang, J., Wu, H., Liu, J., Aksay, I. A., and Lin, Y. (2010). A graphene-based electrochemical sensor for sensitive detection of paracetamol. *Talanta* 81, 754–759. doi: 10.1016/j.talanta.2010.01.009

Ko, M., Aykanat, A., Smith, M. K., and Mirica, K. A. (2017). Drawing sensors with ball-milled blends of metal-organic frameworks and graphite. *Sensors* 17:2192. doi: 10.3390/s17102192

Ko, M., Mendecki, L., Eagleton, A. M., Durbin, C. G., Stolz, R. M., Meng, Z., et al. (2020). Employing conductive metal-organic frameworks for voltammetric detection of neurochemicals. *J. Am. Chem. Soc.* 142, 11717–11733. doi: 10.1021/jacs.9b13402

Krampa, F. D., Aniweh, Y., Kanyong, P., and Awandare, G. A. (2018). Graphene nanoplatelet-based sensor for the detection of dopamine and N-acetyl-p-aminophenol in urine. *Arab. J. Chem.* 13, 3218–3225. doi: 10.1016/j.arabjc.2018.10.006

Kutluay, A., and Aslanoglu, M. (2013). Modification of electrodes using conductive porous layers to confer selectivity for the voltammetric detection of paracetamol in the presence of ascorbic acid, dopamine and uric acid. *Sensor. Actuators. B Chem.* 185, 398–404. doi: 10.1016/j.snb.2013.05.025

Laviron, E. (1974). Adsorption, autoinhibition and autocatalysis in polarography and in linear potential sweep voltammetry. *J. Electroanal. Chem. Interfacial Electrochem.* 52, 355–393. doi 10.1016/S0022-0728(74)80448-1

Laviron, E. (1979). General expression of the linear potential sweep voltammogram in the case of diffusionless electrochemical systems. *J. Electroanal. Chem. Interfacial Electrochem.* 101, 19–28. doi: 10.1016/S0022-0728(79)80075-3

Ma, B., Martín, C., Kurapati, R., and Bianco, A. (2020). Degradation-by-design: how chemical functionalization enhances the biodegradability and safety of 2D materials. *Chem. Soc. Rev.* 49, 6224–6247. doi: 10.1039/C9CS00822E

Miner, E. M., Wang, L., and Dincă M. (2018). Modular O_2 electroreduction activity in triphenylene-based metal-organic frameworks. *Chem. Sci.* 9, 6286–6291. doi: 10.1039/C8SC02049C

Raymundo-Pereira, P. A., Campos, A. M., Mendonça, C. D., Calegaro, M. L., Machado, S. A. S., and Oliveira, O. N. (2017). Printex 6L carbon nanoballs used in electrochemical sensors for simultaneous detection of emerging pollutants hydroquinone and paracetamol. *Sensor. Actuators B Chem.* 252, 165–174. doi: 10.1016/j.snb.2017.05.121

Raymundo-Pereira, P. A., Campos, A. M., Prado, T. M., Furini, L. N., Boas, N. V., Calegaro, M. L., et al. (2016). Synergy between printex nano-carbons and silver nanoparticles for sensitive estimation of antioxidant activity. *Anal. Chim. Acta* 926, 88–98. doi: 10.1016/j.aca.2016.04.036

Suwannakot, P., Lisi, F., Ahmed, E., Liang, K., Babarao, R., Gooding, J. J., et al. (2020). Metal-organic framework-enhanced solid-phase microextraction mass spectrometry for the direct and rapid detection of perfluorooctanoic acid in environmental water samples. *Anal. Chem.* 92, 6900–6908. doi: 10.1021/acs.analchem.9b05524

Wan, Q., Wang, X., Yu, F., Wang, X., and Yang, N. (2009). Poly(taurine)/MWNT-modified glassy carbon electrodes for the detection of acetaminophen. *J. Appl. Electrochem.* 39, 785–790. doi: 10.1007/s10800-008-9721-1

Wang, H., Yuan, B., Yin, T., and Qin, W. (2020). Alternative coulometric signal readout based on a solid-contact ion-selective electrode for detection of nitrate. *Anal. Chim. Acta* 1129, 136–142. doi: 10.1016/j.aca.2020.07.019

Xie, L. S., Skorupskii, G., and Dincă M. (2020). Electrically conductive metal-organic frameworks. *Chem. Rev.* 120, 8536–8580. doi: 10.1021/acs.chemrev.9b00766

Xu, Z., Teng, H., Song, J., Gao, F., Ma, L., Xu, G., et al. (2019). A nanocomposite consisting of MnO_2 nanoflowers and the conducting polymer PEDOT for highly sensitive amperometric detection of paracetamol. *Microchim. Acta* 186:499. doi: 10.1007/s00604-019-3614-3

Yan, M., Ye, J., Zhu, Q., Zhu, L., Huang, J., and Yang, X. (2019). ultrasensitive immunosensor for cardiac troponin I detection based on the electrochemiluminescence of 2D Ru-MOF nanosheets. *Anal. Chem.* 91, 10156–10163. doi: 10.1021/acs.analchem.9b02169

Yuan, B., Sun, P., Zhao, L.-j., Zhang, D., Zhang, Y., Qi, C., et al. (2020). Pd nanoparticles supported on 1,10-phenanthroline-5,6-dione modified graphene oxide as superior bifunctional electrocatalyst for highly sensitive sensing. *J. Electroanal. Chem.* 861:113945. doi: 10.1016/j.jelechem.2020.113945

Yuan, B., Wang, H., Cai, J., Peng, Y., Niu, Y., Chen, H., et al. (2019). A novel oxidation-reduction method for highly selective detection of cysteine over reduced glutathione based on synergistic effect of fully fluorinated cobalt phthalocyanine and ordered mesoporous carbon. *Sens. Actuators B Chem.* 288, 180–187. doi: 10.1016/j.snb.2019.02.114

Zhang, M., Wang, G., Zheng, B., Li, L., Lv, B., Cao, H., et al. (2019). 3-layer conductive metal-organic nanosheets as electrocatalysts to enable an ultralow detection limit of H_2O_2. *Nanoscale* 11, 5058–5063. doi: 10.1039/C8NR08686A

Zhang, M., Zheng, B.-H., Xu, J., Pan, N., Yu, J., Chen, M., et al. (2018). Fewer-layer conductive metal-organic nanosheets enable ultrahigh mass activity for the oxygen evolution reaction. *Chem. Comm.* 54, 13579–13582. doi: 10.1039/C8CC08156E

Zhao, P., Ni, M., Chen, C., Zhou, Z., Li, X., Li, C., et al. (2019). Stimuli-enabled switch-like paracetamol electrochemical sensor based on thermosensitive polymer and MWCNTs-GQDs composite nanomaterial. *Nanoscale* 11, 7394–7403. doi: 10.1039/C8NR09434A

Conflict of Interest: The authors declare that the research was conducted in the absence of any commercial or financial relationships that could be construed as a potential conflict of interest.

Advantages of publishing in Frontiers

OPEN ACCESS
Articles are free to read for greatest visibility and readership

FAST PUBLICATION
Around 90 days from submission to decision

HIGH QUALITY PEER-REVIEW
Rigorous, collaborative, and constructive peer-review

TRANSPARENT PEER-REVIEW
Editors and reviewers acknowledged by name on published articles

Frontiers
Avenue du Tribunal-Fédéral 34
1005 Lausanne | Switzerland

Visit us: www.frontiersin.org
Contact us: frontiersin.org/about/contact

REPRODUCIBILITY OF RESEARCH
Support open data and methods to enhance research reproducibility

DIGITAL PUBLISHING
Articles designed for optimal readership across devices

FOLLOW US
@frontiersin

IMPACT METRICS
Advanced article metrics track visibility across digital media

EXTENSIVE PROMOTION
Marketing and promotion of impactful research

LOOP RESEARCH NETWORK
Our network increases your article's readership